

## AN ABSTRACT OF THE DISSERTATION OF

Thi Bich Truong for the degree of Doctor of Philosophy in Geology presented on  
May 26, 2023.

Title: Revisiting Lō‘ihī: Geochemistry of Kama‘ehuakanaloa Lavas Reveals Complexities in the Pre-Shield to Shield Transition and Hawaiian Mantle Plume Source

Abstract approved:

---

Adam J.R. Kent

Studies of Hawaiian volcanoes contribute valuable insights about Earth processes and mantle evolution, and are fundamental for understanding the construction of the largest volcanoes on terrestrial planets. The pre-shield stage exists in every Hawaiian volcano, but is usually blanketed by high volume tholeiitic lava flows during the main shield stage. Submarine Kama‘ehuakanaloa (formerly Lō‘ihī) Seamount represents the elusive pre-shield stage, but shows a transition to early shield-type tholeiitic eruptions. In this dissertation, the evolutionary history of Kama‘ehuakanaloa lavas in Hawaii was revisited to understand the lesser understood transition occurring between pre-shield and shield phases of intraplate volcanoes. Broad trends on the volcano indicate that different processes affect observed compositions at Kama‘ehuakanaloa. Helium isotopes, which are

central to geochemical assessment of deep mantle plume origin, show coherence with major elements and trace elements. Spatial variation can be examined with the highly constrained location metadata of this sample suite. South Rift suite shows consistent evolution within suite, similar to variation observed in East Flank stratigraphic section. Volatile and Helium isotopes of major rock groups shows evidence of increasing  ${}^3\text{He}/{}^4\text{He}$  of with higher volumes of melting, but not towards increased mid-ocean ridge source contribution with volcano age, as predicted by most Hawaiian evolution models. Evidence for a distinct mantle source for North Rift tholeiites suggests the North and South rift zones sample different mantle sources. This has not been previously proposed at Kama'ehuakanaloa. Radiogenic Pb isotopes provide additional support for the origin of two rift zones from different mantle sources, and suggest derivation from the Loa component in a bilaterally zoned plume. The combination of radiogenic isotopes with Helium is central to geochemical assessment of deep mantles plume origin, as this shows evidence of gases with lithophile elements. Overall, variation in the mantle source can be confirmed by close studies of well-constrained samples on a single volcano.

©Copyright by Thi Bich Truong  
May 26, 2023  
All Rights Reserved

Revisiting Lō‘ihī: Geochemistry of Kama‘ehuakanaloa Lavas Reveals  
Complexities in the Pre-Shield to Shield Transition and Hawaiian Mantle  
Plume Source

by

Thi Bich Truong

A DISSERTATION

submitted to

Oregon State University

in partial fulfillment of  
the requirements for the  
degree of

Doctor of Philosophy

Presented May 26, 2023  
Commencement June 2024

Doctor of Philosophy dissertation of Thi Bich Truong presented on May 26, 2023.

APPROVED:

---

Major Professor, representing Geology

---

Dean of the College of Earth, Ocean, and Atmospheric Sciences

---

Dean of the Graduate School

I understand that my dissertation will become part of the permanent collection of Oregon State University libraries. My signature below authorizes release of my dissertation to any reader upon request.

---

Thi Bich Truong, Author

## ACKNOWLEDGEMENTS

Thank you to all who have helped me in this journey, especially my advisor, Adam Kent. The analytical work was not possible without the intellectual guidance and mentorship of David Graham in the Noble Gas Laboratory and Chris Russo of the Keck Laboratory, and samples from Michael Garcia. Thank you to CEOAS graduate support superstars Robert Allan and Lori Hartline for your hard work. Thank you to Jenny Engels and Flaxen Conway for your mentorship and for sharing your insights with me during the last six years!

I am so grateful to have met so many fun, creative, and supportive graduate students during my time here. I am most grateful for Jennifer Wong-Ala, who has been present and supportive during this whole journey, and was the catalyst to my introduction to R and the tidyverse, just in time to write the dissertation. Thank you Kali Melby, for your encouragement to transform my enthusiasm for clean room techniques into the final project for my dissertation, and for always grounding me in reality during sticky periods. I am lucky to have learned from Unpacking Diversity co-founders Melva, Ale, and Melissa, who created a brave space and allowed me to join and cultivate the space for many more years. Thank you to the post-doctoral scholars who validated my struggles, made time to listen, shared wisdom and strategies generously: Penny Wieser for motivating me to explore Python again, for generously listening to my research ideas, and Emily Cahoon for sharing my enthusiasm for basalts, intraplate volcanism, and pedagogy. Thank you to Glenn Dolphin for the thoughtful discussions about teaching hotspot volcanism in a historically and philosophically engaged context.

I am grateful for the support of my virtual community, who I feel close to, despite our distance! I am grateful for Luan Heywood and Rebecca Morris, who generously listened to my ideas and provided feedback for AGU abstracts and other important documents at a moment's notice. Thank you to Val Finlayson and Rita Parai for the thoughtful discussions about my work, for advocating for me, and for reminding me to think about xenon. Thank you to everyone in Asian Americans and Pacific Islanderess (AAPIiG) for providing the community that I always wanted to see at conferences, and throughout the entire research process. Thank you to Katy Peplin for being an excellent source of advice and comfort during the last few years!

Finally, thank you to my partner Alan Nguyen and my family for the emotional support and for celebrating my accomplishments with me. A heartfelt thanks to the best furry animal companion, Bosco ("bót-cô"), whose time only overlapped for part of my PhD, but provided great emotional support.

## CONTRIBUTION OF AUTHORS

Dr. David W. Graham assisted with data collection and the design of Chapter 2 and Chapter 3. Dr. Peter J. Michael contributed FTIR data in Chapter 3 and Dr. Michael O. Garcia contributed samples for the dissertation (all chapters). Dr. Christopher J. Russo assisted with data collection of Chapter 2 and 4. Dr. Aaron Pietruszka contributed reference materials for Chapter 4. Dr. Adam J.R. Kent assisted in the interpretation of the data for all chapters.

## TABLE OF CONTENTS

	<u>Page</u>
1 The Hawaiian Islands and Conceptual Development of Mantle Plume Model	1
1.1 Introduction . . . . .	1
1.2 Mantle Plumes and OIB . . . . .	3
1.2.1 The Hawaiian Islands . . . . .	8
1.3 Geologic Setting: Kama‘ehuakanaloa Seamount . . . . .	13
1.3.1 Comment on Place Name . . . . .	13
1.3.2 Key Volcanic Features . . . . .	14
1.3.3 Insights from Geochemistry . . . . .	15
1.4 This Study: Revisiting Kama‘ehuakanaloa, 40 years later . . . . .	19
1.4.1 Samples . . . . .	19
1.4.2 Methods . . . . .	25
1.4.3 Dissertation Aims . . . . .	27
1.4.4 Broader Implications . . . . .	29
2 Trace element signature and petrogenesis from primordial and depleted mantle sources of Kama‘ehuakanaloa lavas	32
2.1 Introduction . . . . .	32
2.1.1 Study Aims and Research Questions . . . . .	35
2.2 Samples . . . . .	37
2.3 Methods . . . . .	37
2.4 Results . . . . .	40
2.4.1 Major Elements . . . . .	40
2.4.2 Trace Elements . . . . .	43
2.5 Discussion . . . . .	55
2.5.1 Classification . . . . .	55
2.5.2 Shallow Compositional Controls . . . . .	58
2.5.3 Deep Source Compositional Controls . . . . .	60
2.5.4 Diagnostic Features of Kama‘ehuakanaloa Sample Suite . . . . .	84
2.6 Conclusion . . . . .	89
3 Helium and Volatile ( $H_2O$ , $CO_2$ ) Geochemistry of Deep Rift Zone Lavas from Kama‘ehuakanaloa Seamount	91

## TABLE OF CONTENTS (Continued)

	<u>Page</u>
<b>3.1 Introduction . . . . .</b>	91
<b>3.1.1 Study Aims and Research Questions . . . . .</b>	93
<b>3.2 Methods . . . . .</b>	94
<b>3.2.1 Vesicle Helium and CO<sub>2</sub> . . . . .</b>	94
<b>3.2.2 Dissolved Helium . . . . .</b>	95
<b>3.2.3 Dissolved H<sub>2</sub>O and CO<sub>2</sub> . . . . .</b>	96
<b>3.2.4 F, S, Cl . . . . .</b>	96
<b>3.3 Results . . . . .</b>	97
<b>3.3.1 Helium . . . . .</b>	97
<b>3.3.2 Major Volatiles: CO<sub>2</sub> and H<sub>2</sub>O . . . . .</b>	104
<b>3.3.3 Other Volatiles (Cl, F) . . . . .</b>	112
<b>3.4 Discussion . . . . .</b>	113
<b>3.4.1 Helium Isotope Variability . . . . .</b>	113
<b>3.4.2 Causes of Major Volatile Variations . . . . .</b>	120
<b>3.4.3 Helium and Petrogenesis . . . . .</b>	136
<b>3.5 Conclusion . . . . .</b>	141
 <b>4 Pb isotope variability at Kama‘ehuakanaloa Seamount: Constraints on pre-shield</b>	
<b>and shield stage lava distribution . . . . .</b>	143
<b>4.1 Introduction . . . . .</b>	143
<b>4.1.1 Study Aims and Research Questions . . . . .</b>	148
<b>4.2 Samples . . . . .</b>	149
<b>4.3 Analytical Methods . . . . .</b>	149
<b>4.3.1 Reference Materials/Interlaboratory Comparison . . . . .</b>	153
<b>4.4 Results . . . . .</b>	157
<b>4.4.1 Previous Studies and Replicates . . . . .</b>	159
<b>4.5 Discussion . . . . .</b>	165
<b>4.5.1 Aspects of Pb Isotope Variation . . . . .</b>	165
<b>4.5.2 Radiogenic Sources and Loa/Kea Divide . . . . .</b>	168
<b>4.5.3 Integrating <sup>3</sup>He/<sup>4</sup>He Isotopes to understand volcanic evolution . . . . .</b>	171
<b>4.6 Conclusions . . . . .</b>	176
 <b>5 Conclusions</b>	178

## TABLE OF CONTENTS (Continued)

	<u>Page</u>
Appendices	182
A    Chapter 0 . . . . .	183
B    Chapter 2 . . . . .	196
C    Chapter 3 . . . . .	199
Bibliography	201

## LIST OF FIGURES

<u>Figure</u>		<u>Page</u>
1.1 Aerial view of the main Hawaiian Islands . . . . .	2	
1.2 Schematic cross-section and 3 types of plumes . . . . .	7	
1.3 Aerial view of the main Hawaiian Islands . . . . .	9	
1.4 Schematic showing relationship of basalt chemical composition with estimated Hawaiian eruptive volumes with volcanic stage . . . . .	12	
1.5 Notable Features on Kama'ehuakanaloa Seamount . . . . .	16	
1.6 Range ${}^3\text{He}/{}^4\text{He}$ values of different Hawaiian stages and volcanoes . . . . .	18	
1.7 Map of Kama'ehuakanaloa whole rock data from GEOROC . . . . .	20	
1.8 Sample locations from expeditions between 1981-1999 . . . . .	21	
1.9 Sample locations on contour map . . . . .	23	
1.10 Sample locations with names . . . . .	24	
1.11 Analytical Flowchart . . . . .	25	
2.1 Total Alkalies vs. Silica (TAS) Diagram . . . . .	41	
2.2 Ne-Ol-Q with Kama'ehuakanaloa South and North Rift glass compositions	42	
2.3 Spidergram of trace element compositions normalized by primitive mantle	49	
2.4 Spidergram of trace element compositions normalized by primitive mantle, shown for each rock type . . . . .	51	
2.5 Rare Earth Element compositions normalized by C1 chondrite from (Sun and McDonough, 1989) . . . . .	52	
2.6 Rare Earth Element (REE) concentrations of major rock types . . . . .	53	
2.7 Rare Earth Element (REE) concentrations of North Rift Compared to South Rift Basalts . . . . .	54	
2.8 Total Alkalies vs. Silica (TAS) Diagram . . . . .	56	
2.9 Total Alkalies vs. Silica and Transitional/Overlap Samples . . . . .	57	

## LIST OF FIGURES (Continued)

<u>Figure</u>		<u>Page</u>
2.10 Whole Rock and Glass Major Element Comparison . . . . .	63	
2.11 Ni (ppm) vs. Mg # (%) . . . . .	64	
2.12 Fractional crystallization modeling . . . . .	65	
2.13 K <sub>2</sub> O/P <sub>2</sub> O <sub>5</sub> and K/Ti vs. MgO wt. (%) . . . . .	66	
2.14 Boxplots showing t-test results and statistics for various trace element ratios that are effective discriminants of South Rift lava types . . . . .	67	
2.15 Nb/U vs. Nb (ppm) . . . . .	69	
2.16 K <sub>2</sub> O/P <sub>2</sub> O <sub>5</sub> vs. Rb/Sr . . . . .	70	
2.17 K <sub>2</sub> O/P <sub>2</sub> O <sub>5</sub> vs. Sm/Yb . . . . .	71	
2.18 La/Sm vs. La (ppm) compositions . . . . .	73	
2.19 Dy/Yb <sub>N</sub> vs. La/Yb <sub>N</sub> concentrations and estimates of batch partial melting from garnet and spinel lherzolite sources . . . . .	76	
2.20 W (ppb) vs. MgO wt. (%) . . . . .	87	
2.21 W/U vs. MgO wt. (%) . . . . .	88	
3.1 Histogram showing distribution of total <sup>3</sup> He/ <sup>4</sup> He values from combined glass crushing and melting experiments . . . . .	102	
3.2 <sup>3</sup> He/ <sup>4</sup> He ratio vs. concentration of <sup>4</sup> He comparison between vesicles and glass . . . . .	103	
3.3 Total CO <sub>2</sub> concentrations vs. collection depth . . . . .	109	
3.4 CO <sub>2</sub> / <sup>3</sup> He (vesicle and total) vs. <sup>4</sup> He concentration . . . . .	110	
3.5 Vesicle <sup>3</sup> He/ <sup>4</sup> He (R <sub>A</sub> ) vs. Alkalinity Index . . . . .	114	
3.6 Boxplot of mean vesicle <sup>3</sup> He/ <sup>4</sup> He among South Rift lavas . . . . .	116	
3.7 Comparison Helium isotopes in vesicles and in glass . . . . .	119	
3.8 Modeling assimilation with Brine-Lava mixture and <sup>3</sup> He/ <sup>4</sup> He-Cl/K . . . . .	124	

## LIST OF FIGURES (Continued)

<u>Figure</u>		<u>Page</u>
3.9 Cl (ppm) vs. K (ppm) . . . . .	125	
3.10 CO <sub>2</sub> / <sup>3</sup> He (vesicle and total) vs. <sup>4</sup> He concentration . . . . .	126	
3.11 Total CO <sub>2</sub> (ppm) vs. Ba (ppm) . . . . .	128	
3.12 Histogram of Total Saturation Pressures from MagmaSat (MELTS) and VolatileCalc . . . . .	130	
3.13 Compositional parameter vs. SiO <sub>2</sub> using Dixon (1997) equation . . . . .	131	
3.14 Vesicle He/Glass He vs. Vesicle CO <sub>2</sub> /Glass CO <sub>2</sub> and Equilibrium Partitioning Field . . . . .	133	
3.15 Total CO <sub>2</sub> / <sup>3</sup> He vs. Depth (meters below sea level) . . . . .	134	
3.16 Total CO <sub>2</sub> (ppm) vs. glass H <sub>2</sub> O (wt.%) composition of glasses plotted with basalt isobars and degassing models . . . . .	135	
3.17 Ta/Ta* anomaly vs. Vesicle <sup>3</sup> He/ <sup>4</sup> He . . . . .	137	
4.1 Potential lower mantle origin of Hawaiian geochemical groups . . . . .	144	
4.2 Volcanoes of the Main Hawaiian Islands and Loa/Kea Affinities . . . . .	145	
4.3 Bathymetric Map and <sup>3</sup> He/ <sup>4</sup> He isotope distribution . . . . .	147	
4.4 <sup>208</sup> Pb/ <sup>204</sup> Pb- <sup>207</sup> Pb/ <sup>204</sup> Pb- <sup>206</sup> Pb/ <sup>204</sup> Pb Plot for Reference Materials . . . . .	155	
4.5 <sup>207</sup> Pb/ <sup>204</sup> Pb vs. <sup>206</sup> Pb/ <sup>204</sup> Pb of BHVO-1 standard . . . . .	156	
4.6 <sup>208</sup> Pb/ <sup>204</sup> Pb- <sup>207</sup> Pb/ <sup>204</sup> Pb- <sup>206</sup> Pb/ <sup>204</sup> Pb Plot . . . . .	160	
4.7 <sup>207</sup> Pb/ <sup>204</sup> Pb- <sup>206</sup> Pb/ <sup>204</sup> Pb and <sup>208</sup> Pb/ <sup>204</sup> Pb- <sup>206</sup> Pb/ <sup>204</sup> Pb Plot of study and literature values for TUNE04WT samples . . . . .	163	
4.8 <sup>208</sup> Pb/ <sup>204</sup> Pb- <sup>207</sup> Pb/ <sup>204</sup> Pb- <sup>206</sup> Pb/ <sup>204</sup> Pb and Mantle Endmembers . . . . .	164	
4.9 <sup>206</sup> Pb/ <sup>204</sup> Pb vs. Latitude and Depth . . . . .	166	
4.10 Major and Trace Element ratios K/Ti and La/Sm vs. <sup>206</sup> Pb/ <sup>204</sup> Pb . . . . .	167	
4.11 Radiogenic <sup>208</sup> Pb*/ <sup>206</sup> Pb*, grouped by rock type . . . . .	169	

## LIST OF FIGURES (Continued)

<u>Figure</u>	
	<u>Page</u>
4.12 Vesicle ${}^3\text{He}/{}^4\text{He}$ ( $R_A$ ) vs. ${}^{206}\text{Pb}/{}^{204}\text{Pb}$ - ${}^{207}\text{Pb}/{}^{204}\text{Pb}$ - ${}^{208}\text{Pb}/{}^{204}\text{Pb}$ . . . . .	172
4.13 Vesicle ${}^3\text{He}/{}^4\text{He}$ ( $R_A$ ) vs. ${}^{206}\text{Pb}/{}^{204}\text{Pb}$ . . . . .	174
4.14 ${}^{208}\text{Pb}/{}^{204}\text{Pb}$ vs. ${}^{206}\text{Pb}/{}^{204}\text{Pb}$ compared to Loa and Kea shield to post-shield trends . . . . .	175

## LIST OF TABLES

<u>Table</u>		<u>Page</u>
1.1 Summary Characteristics of Hawaiian Eruptive Stages . . . . .	11	
1.2 This Study Suite and Expeditions Information . . . . .	22	
1.3 Summary of chapters, methods, data products . . . . .	26	
2.1 Trace element concentrations in ppm . . . . .	44	
2.2 Trace element (rare earth elements La-Lu) concentrations, in ppm . . .	47	
2.3 Trace Element Ratios that do correlate for South Rift lavas . . . . .	61	
2.4 Trace Element Ratios that do not correlate for South Rift lavas . . . . .	62	
2.5 Partition Coefficients for Melting Model . . . . .	74	
2.6 Modal Abundances and Melt Reaction Coefficients for Melting Model . .	75	
2.7 Parental/Primary Melt Compositions for South and North Rift Tholeiites	80	
2.8 Literature Estimates for Parental Melts . . . . .	80	
2.9 Mantle Source Compositions for South and North Rift Tholeiites . . . . .	82	
3.1 Helium measurements from crushing and melting . . . . .	98	
3.2 CO <sub>2</sub> , H <sub>2</sub> O, Cl, S, K, Ti, F Measurements . . . . .	106	
3.3 Mean Vesicle <sup>3</sup> He/ <sup>4</sup> He ratios among rock types in South Rift . . . . .	115	
3.4 Results from two-sided t-test of mean vesicle <sup>3</sup> He/ <sup>4</sup> He among South Rift lavas . . . . .	115	
3.5 Estimated eruption ages calculated from <sup>3</sup> He/ <sup>4</sup> He disequilibrium . . . . .	120	
3.6 Endmember compositions for brine assimilation model . . . . .	122	
3.7 Parental Melt and Mantle Source Volatile Concentrations . . . . .	139	
4.1 <sup>206</sup> Pb/ <sup>204</sup> Pb- <sup>207</sup> Pb/ <sup>204</sup> Pb- <sup>208</sup> Pb/ <sup>204</sup> Pb Isotope Compositions . . . . .	158	

## LIST OF APPENDIX FIGURES

<u>Figure</u>	<u>Page</u>
A.1 Grain Mount Photographs of MIR2335-5 and TUNE-04B . . . . .	194

## LIST OF APPENDIX TABLES

<u>Table</u>	<u>Page</u>
A.1 Electron Microprobe Measurements of Major Elements . . . . .	185
A.2 Location Metadata for Dive/Submersible Collected Samples . . . . .	186
A.3 Location Metadata for Dredge Samples . . . . .	189
A.4 CIPW Normative Compositions . . . . .	191
A.5 LA-ICP-MS Standards . . . . .	194
A.6 Summary of LA-ICP-MS Analytical Accuracy and Reproducibility . . . . .	195
B.1 Summary of Volatiles Instrumentation . . . . .	196
B.2 Summary of Volatiles Reference Materials . . . . .	197
B.3 Model Results for ${}^3\text{He}/{}^4\text{He}$ and Cl/K for Lava, Seawater, Brine Mixtures	198
C.1 Pb Isotope Compositions of Reference Materials . . . . .	200

# Chapter 1: The Hawaiian Islands and Conceptual Development of Mantle Plume Model

## 1.1 Introduction

The majority of Earth’s volcanism occurs underwater, beneath the sea surface, away from direct observation. Notably, rocks obtained from Earth’s oceans provided vital evidence for seafloor spreading (Langseth et al., 1966; Pitman and Heirtzler, 1966; Vine, 1966) heralded the Plate Tectonics Revolution in the late 1960s and the work of Morgan (1968), following decades of vigorous and multicontinental debates about lateral movements on the Earth’s surface (Menard, 2014; Oreskes, 2018). Concurrent geologic studies of volcanic islands allowed the study of oceanic rocks similar to those at tectonic boundaries, generally of a similar composition as basalt (Yoder and Tilley, 1962). However, observations at isolated, linear volcanic island chains did not yield similarly unifying interpretations under Plate Tectonics. Despite more than a century of studies about the morphology distribution of volcanoes and volcanic chains in the Pacific and Atlantic Oceans (Dana, 1849; Darwin, 1891; Daly, 1925), their origin remained unsolved after the Plate Tectonics Revolution.

The two major types are basalts are broadly assigned according to their origins, which differ in the influence of plate tectonics (Fig 1.1). The more common type are called mid-ocean ridge basalt (**MORB**). MORB are volumetrically dominant on Earth, and account

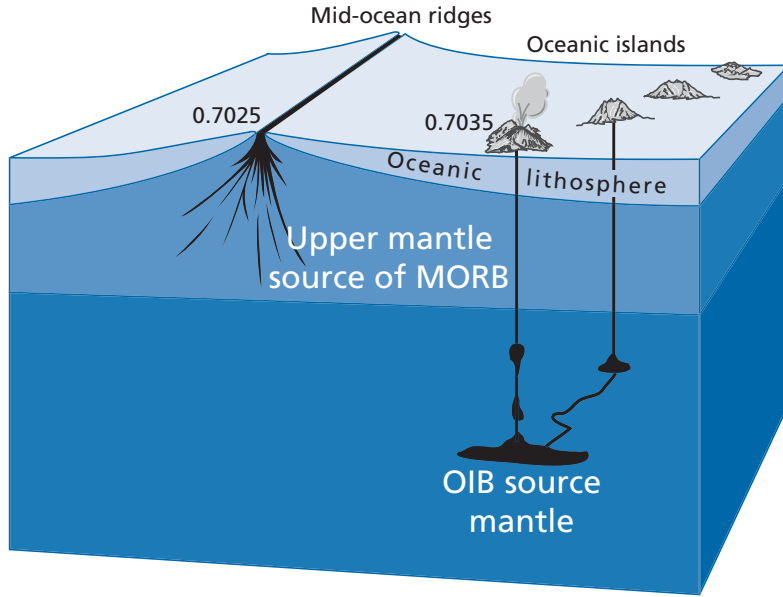


Figure 1.1: The origins of mid-ocean-ridge basalt (MORB) and ocean-island basalt (OIB) from Allègre (2008).  $^{87}\text{Sr}/^{86}\text{Sr}$  ratios of representative samples are shown.

for 75% of yearly magmatic output, with an average erupted volume of  $3 \text{ km}^3$  erupted at the per year (Crisp, 1984). They originate at divergent plate tectonic boundaries, and the discovery of symmetric spreading of ridges from a central axis was key to the success of Plate Tectonics theory to explain the construction of the world's ocean basins. The minor variety are referred to as ocean island volcanics (OIV) or ocean island basalts, (**OIB**, however, technically may be a misnomer of official chemical classification, e.g., Le Maitre et al., 2004). The surface expression of OIB eruptions have been called "hotspots", and are often designated as hotspot or intraplate volcanoes. The lower melting extents of intraplate magmas contributes to about 5% of global inventories of magma production, producing an eruptive volume of  $\sim 0.20 \text{ km}^3$  per year (Crisp, 1984).

## 1.2 Mantle Plumes and OIB

The proposed relationship between hotspots and a “mantle plume” origin was first proposed by Wilson (1963) to explain the origin of the Hawaiian Islands. Wilson (1963) posited that intraplate volcanoes are formed by magmas erupted through oceanic plates moving over stationary heat sources situated in the deep mantle (Wilson, 1963). Morgan (1972) further expanded the role of mantle convection in plumes, proposing the separation of MORB source in the upper mantle, and OIB in the lower mantle. In summary, the mechanism of mantle plumes involves a convection pattern where anomalously high temperature mantle buoyantly rises from deep in the Earth’s lower mantle to shallower mantle depths where melting occurs (Wilson, 1963; Morgan, 1972; Sleep, 1990).

Deformable fluids (e.g. corn syrup, glycerin, oils) have been used to simulate the production of buoyancy-driven plumes in laboratory tank experiments, producing flow dynamics consistent with hot, solid material rising through the mantle, providing support for thermal buoyancy-driven mantle plumes (Whitehead Jr. and Luther, 1975; Campbell, 2005). Early laboratory simulations displayed diapirs rising with a large plume head, which suggested an initial period of impinging the lithosphere, the largest amount of partial melting, and the possibility of entraining the deep mantle material within a vertical conduit from the deep mantle to the sub-lithospheric melting region Campbell (2005). The mantle plume model has also been applied to the origin of large igneous provinces (LIPs), formed by rapid outpourings of enormous volumes ( $>10^6$  km $^3$ ) of basaltic lava erupted rapidly over millions of years (Richards et al., 1989). The massive outpourings of lava at oceanic LIPs could be the result of elevated melting flux with the arrival of

the plume head (Richards et al., 1989; Campbell, 2005), followed by “tail” volcanism of lower melting, in which buoyant material is transferred within the conduit, and produces a linear volcanic island chain due to movement of a tectonic plate overlying a stationary plume (Richards et al., 1989; Campbell and Griffiths, 1990).

It has been hypothesized that thermochemical heterogeneities control the amount of entrained ambient mantle in the upwelling plume (Campbell, 2007). Thus, the proportion and vertical distribution of components in a plume sources both change with time. The thermochemical origin for a plume with buoyant rise of heterogeneous material can produce volcanic flux variations and secondary volcanism. A proposed classification of lavas from mantle plumes, e.g. from Courtillot et al. (2003) include primary plumes from near the core-mantle boundary and impinging the base of the lithosphere (e.g. Hawai‘i and Iceland), while secondary plumes emanate from a plume head from the transition zone (e.g., Polynesian Island tracks like Tahiti and Cook-Australs), and shallower plumelets contributing to observed volcanism, and tertiary plumes are produced by processes at shallower, crustal depths (localities without evidence of typical plume or hotspot indicators).

## Geochemistry and Geophysical origins

Studies of MORB and OIB type have together provided information about the evolution of Earth’s oceanic basins and major island edifices (Kay et al., 1970; Zindler and Hart, 1986). However, OIB are more likely to preserve information about the mantle source (Fig. 1.1), and represent a type of window to the long-term evolution of Earth’s mantle

(Koppers and Watts, 2010). Early geochemical studies of Hawaiian OIB revealed elevated incompatible lithophile elements compared to mid-ocean ridge basalts (Schilling and Winchester, 1966), suggesting sources with different convective histories. Specifically, enriched trace element compositions suggested derivation from a mantle source that was not yet homogenized by processing like the MORB source mantle (Fig. 1.1). Studies of Icelandic trace element and Sr-Pb isotope compositions provided support for an enriched OIB source separate from the upper mantle, despite proximity to a mid-ocean ridge (Schilling, 1973b). Radiogenic isotope characteristics of lavas from several hotspots like Hawai‘i and Afar (Schilling, 1973a) provided support for derivation from different mantle components with long-lived ( $> 10^6$  yr) histories. Noble gas isotopes, specifically Helium isotopes, provided further evidence of a distinct, deep mantle origin of OIB, particularly at Hawai‘i. High  ${}^3\text{He}/{}^4\text{He}$  ratios observed in basalts sampled from the main Hawaiian Islands ranged from 8 R<sub>A</sub> up to  $>30$  R<sub>A</sub> (R<sub>A</sub> is the atmospheric  ${}^3\text{He}/{}^4\text{He} = 1.39 \times 10^{-6}$ ) (Lupton, 1983). A major interpretation of the high  ${}^3\text{He}/{}^4\text{He}$  values poses undegassed mantle sources with high He/(Th+U) since formation from the lower mantle (Kurz et al., 1982; Allègre et al., 1983).

Models of Earth’s interior suggesting that hotspot volcanism arises from thermal upwellings formed in some generative zone in the lower mantle are supported by seismic tomographic observations of low shear wave velocity beneath the African and Pacific plates (Williams and Garnero, 1996). Seismic tomography has revealed the presence of compositional and temperature differences in warm piles residing at the core-mantle boundary. These Large Low Shear Wave Velocity Provinces (LLSVPs) are hypothesized to be large-scale anomalies in the deep mantle revealed by global tomography (Helmburger

et al., 2000). Courtillot et al. (2003) catalogued global hotspot characteristics and found a small number of localities that exhibit characteristics of primary plumes ascending from the lowermost mantle, and are located near the edges of lower mantle, upwelling domes underlying the Pacific and African continent. Courtillot et al. (2003) additionally proposed the existence of “secondary” plumes originating from the transition zone, and “tertiary” hotspots created by decompression melting due to shallow, lithospheric stress (Fig. 1.2).

Further seismic imaging studies have supported the geographic association of high- $^3\text{He}/^4\text{He}$  hotspots at the edge of underlying LLSVPs to 2800 km depth. For example, these studies have shown that the activity at the Hawaiian hotspot is consistent with a plume that samples a high- $^3\text{He}/^4\text{He}$  deep mantle source (Lay and Garnero, 2011; Weis et al., 2011). Such LLSVP anomalies could indicate dense chemical heterogeneities (potentially primordial material or recycled mafic material), inducing thermochemical plume upwelling (Farnetani and Samuel, 2005). According to Courtillot et al. (2003), the criteria to classify hotspots for potentially deep plume origin are high buoyancy flux  $> 10^3 \text{ kg s}^{-1}$ ,  $^3\text{He}/^4\text{He}$  consistently above 10 R<sub>A</sub>, low  $V_S$  between -2‰ to +2‰ of reference velocity at a given depth, presence of a linear volcanic track, and presence of a flood basalt or oceanic plateau.

Overall, the plume model offers a systematic view of studying the evolution of intraplate hotspot regions, and utilizes advances in geophysics and geochemistry to understand the geodynamic evolution and makeup of Earth’s mantle. Volcanic island chains have been used to establish an understanding of global Earth processes (Wilson, 1963; Gast et al., 1964; Schilling, 1973b; Tatsumoto, 1978; Zindler and Hart, 1986), but re-

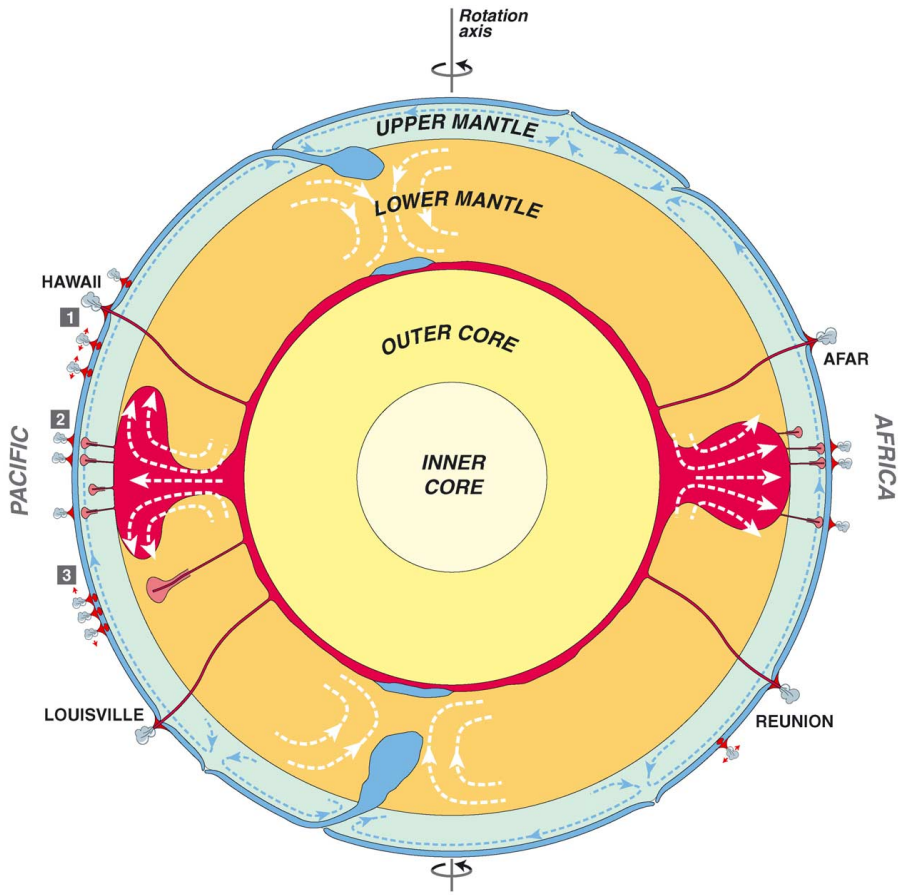


Figure 1.2: Schematic cross-section and 3 types of plumes from Courtillot et al. (2003) showing a dynamic Earth going through its rotation axis. 3 types of plumes are seen in a cross-section through the interior showing sources of the three types of plumes/hotspots: primary (1), secondary (2), and tertiary (3).

solving the origin of a diverse global catalogue of ocean island volcanoes similar to that of mid-ocean ridge basalts has revealed difficulties to produce a similarly unifying, coherent, and consilient theory with the success of Plate Tectonics model. A combination of multi-proxy geochemical constraints, radiometric dating, numerical modeling, whole Earth imaging paleoseismology have elucidated the nature of the deep interior over geo-

logic time (Koppers et al., 2021). The combined efforts within the fields of geophysics, mineral physics, geochemistry, and geodynamics are poised to continue to provide major advances to produce an integrated picture of the spatiotemporal configuration of long-lived mantle plumes.

### 1.2.1 The Hawaiian Islands

#### Intraplate Volcanic Origin

The Hawaiian Islands are among the most studied intraplate volcanic system on Earth. Collectively, the Hawaiian-Emperor-Seamount chain comprises over 80 million years of construction (Clague and Dalrymple, 1987). The volcanic history of the Emperor seamount chain bears great importance on understanding global plate motion (Konrad et al., 2018b), models of past mantle flow and circulation (Tarduno et al., 2009), and overall mantle convection modes and cycles (Koppers and Watts, 2010). The more recent main Hawaiian Islands, erupted in the last 5 million years, bear great importance on the mechanisms responsible for generating large volumes of magma until the present day. The range of activity observed at the main Hawaiian Islands is related to volcano age, where the volcanic shield is constructed over a duration on the order of a million years.

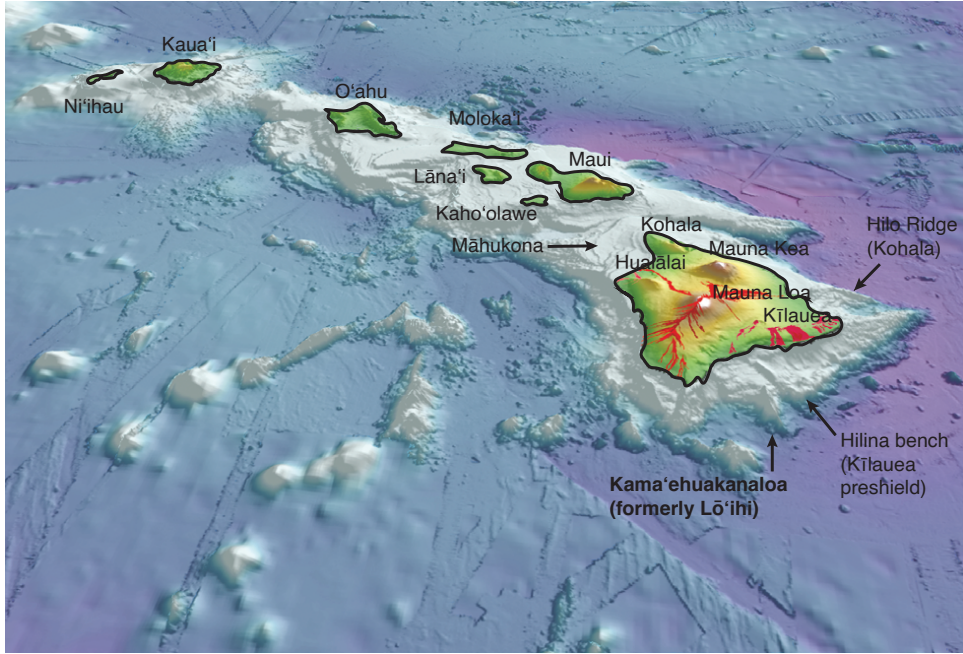


Figure 1.3: Oblique aerial view of the main Hawaiian islands, modified from [Clague and Sherrod \(2014\)](#). Locations of major volcanoes are labeled. Kama'ehuakanaloa is shown in bold font. Original illustration by J.E. Robinson.

## Volcanic Evolutionary Model

An idealized model of Hawaiian volcano evolution involves four eruptive stages: pre-shield, shield, postshield, and the rejuvenated stages (or post-erosional stage) ([Clague and Dalrymple, 1987](#); [Clague and Sherrod, 2014](#)) with varied amounts of time during each stage and between stages. Approximately 5 km of submarine growth contributes to the earliest pre-shield stage, and comprises the core of tholeiitic shields, and produces a range of alkali and subalkaline lavas. The most productive phase of voluminous growth occurs in the shield stage, which lasts for an average duration of one or more million years and produces the typical gently sloping shield volcano as seen in Mauna Loa and

Mauna Kea, with more uniform lava composition on average due to extents of melting similar to MORB (Fig. 1.4). The shield stage will account for up to 95% of total erupted volume of a Hawaiian shield volcano.

Table 1.1: Summary Characteristics of Hawaiian Eruptive Stages, simplified from Table 1 in Clague and Dixon (2000), except for relative eruptive volume percentage, which is from Clague and Sherrard (2014). Relative volume percentage is an estimate for entire pre-shield, shield, post-shield, and rejuvenated (post-erosional) submarine and subaerial combined. Stage names are bolded at rows with this volume estimate.

Stage	Example Location	Relative Eruptive Volume (%)	Duration (Ma)	Typical Lava Types			
				Nephelinite	Basanite	Alkalic Basalt	Tionnal Basalt
Precursory Pre-Shield (submarine)	South Arch	unknown		X	X		
<b>Pre-Shield</b> (submarine)	Kama'ehu	<3	0.2		X	X	X
Shield (submarine)	Kama'ehu, nascent		0.1				X
Shield-explosive phase (shallow submarine to low elevation subaerial)	Kilauea		0.3				X
<b>Shield</b> effusive phase (subaerial)	Mauna Loa	95-98	0.3				X
<b>Post-Shield</b> (subaerial)	Hualālai	1	0-0.2			X	
Peripheral (submarine)	North Arch		1.6	X	X		
<b>Rejuvenated</b> (subaerial, some submarine)	Haleakalā	<1	0-3.2	X	X	X	

The main stages of Hawaiian shield volcano construction are shown in with volumetric estimates and timescales in Figure 1.4. No single volcano on the main islands have exposures of all four stages. Due to the voluminous coverage during the prolific shield construction phase, the buried core pre-shield stage is unlikely to be exposed even after deep dissection and erosion over time.

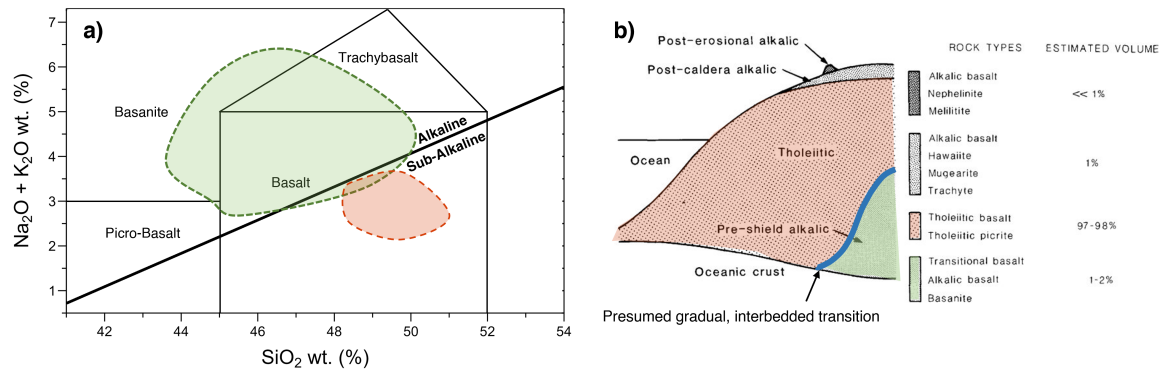


Figure 1.4: Schematic showing relationship of basalt chemical composition with estimated Hawaiian eruptive volumes with volcanic stage. (a) Shows range of major element composition of this study, matching the range in [Garcia et al. \(1993, 1995\)](#). Basanites, Alkalic Basalt and Transitional Basalt samples plot in the green field, whereas Tholeiitic Basalts plot in the red field. Reference boundaries for classification on Silica-Total Alkalies diagram from [Le Maitre et al. \(2004\)](#) and alkaline/subalkaline dividing line from [Macdonald and Katsura \(1964\)](#). (b) Schematic of Hawaiian volcanic growth stages, representative rock types, and estimated eruptive volume from [Clague \(1987\)](#). The volumes representing chemical compositions is shaded as in (a), where alkaline rocks are shaded in green and tholeiitic rocks is shaded as red.

Hawaiian volcanoes show patterns of sequential growth throughout their lifetime (Clague and Dalrymple, 1987), high magmatic productivity over the last 5 million years (Ribe and Christensen, 1999), and evidence of thickening of the surrounding Hawaiian swell (Laske et al., 1999). They are a useful case study for connecting surface observations to a hypothesized mantle plume. However, systematic spatial and temporal variations are difficult to constrain in the pre-shield stage into the early shield stage, due to large volume tholeiitic lavas obscuring the relatively minor eruptives of earlier stages (Fig. 1.4). The diversity of early alkaline and subalkaline lavas may reflect mantle signatures that are less likely to have been diluted by high volume mixing. This dissertation focuses on the most accessible exposure of the pre-shield stage, which occurs at Kama‘ehuakanaloa Seamount.

### 1.3 Geologic Setting: Kama‘ehuakanaloa Seamount

Located 20 km off the coast of Hawai‘i, Kama‘ehuakanaloa is a seamount near Hawai‘i Island. The volcano developed on the apron of Mauna Loa, in close proximity to Kilauea volcano, though the volcano’s origin is unrelated to either of the nearby volcanoes (Malahoff et al., 1982). This single volcano is the focus of this dissertation.

#### 1.3.1 Comment on Place Name

The volcano was originally known to the scientific community as Lō‘ihī. Scientific literature since the late 1970s, and current GEOROC (<http://georoc.mpchmainz.gwdg.de/>

[georoc/](#)) and Earthchem (<http://portal.earthchem.org/>) geochemical databases list the volcano as "Loihi". A name change in July 2021 was reported in an announcement by the USGS ([Hawaiian Volcano Observatory, 2022](#)), following 7 years of community discussion and meetings with the Hawai'i Board on Geographic Names ([Hawai'i Board on Geographic Names, 2021](#)). Though there are USGS regulations on naming Hawaiian volcanoes in publications consistent with spelling and diacritical marks ([Sherrod et al., 2007](#)), there is no clear official guidance on using the new name, Kama'ehuakanaloa in the future publications. According to community leaders of the name change and Advisory Committee on Undersea Features (ACUF), "Kama'ehu" is a valid variant of the name ([Hawai'i Board on Geographic Names, 2021](#)). Hence, concerns about name length can be clarified while remaining consistent with such recommendations. Future efforts to combine datasets would benefit from unique volcano identification numbers, or additional measures to filter via geographic coordinates, which are possible in tools like the open-source DashVolcano ([Oggier et al., 2023](#)). The volcano is referred to as Kama'ehuakanaloa in this dissertation, and in some figures/tables, shortened to Kama'ehu.

### 1.3.2 Key Volcanic Features

The discovery of seismic activity and fresh basalts at Kama'ehuakanaloa Seamount in the late 1970s provided an opportunity to study the mantle input at Hawaii's youngest active volcano ([Moore et al., 1979](#)). The diversity of rock types not yet observed on shield volcanism elsewhere on Hawai'i, from picrites to basanitoids ([Moore et al., 1982](#)) also permitted a comparison of different volatile contents with composition ([Moore and Clague,](#)

1981). Seawater interactions have modified the volcano's structure, where steam-driven collapse formed pit craters, in contrast to subaerial caldera formation (Clague et al., 2003). Studies at Kama'ehuakanaloa enable understanding the processes responsible for submarine explosive eruptions and construction of the largest volcanoes on terrestrial planets.

Two volcanic rift zones extend away from the summit region to the north and south-southeast directions. They are likely to have formed early in the volcano's construction (Fornari et al., 1988). The shorter, northern rift is continuous for  $\sim$ 11 km and may consist of two subparallel segments, while the southern rift zone is  $\sim$ 20 km long, curved in shape, and reaches depths of 5000 m (Garcia et al., 2006; Clague et al., 2019). Lava flows occur above 1400 m and include pillow lavas and knobby a'a-like blocky flows (Garcia et al., 1995). The morphology of Kama'ehuakanaloa has evidently been modified by landslides, which variably steepened the volcano's slopes along the east flanks. The western flank shows a more gradual slope and accumulation of debris, blocks and talus. Mapping of the southern rift has revealed talus and downslope mass wasting of volcanic rock (Malahoff et al., 1987). Figure 1.5 shows features associated with major volcanic construction (South Rift and North Rifts), and possible features from slope accumulation and erosion processes (Western Ridge and East Flank).

### 1.3.3 Insights from Geochemistry

K-Ar ages yield an estimate of 150-200,000 years for the duration of the alkalic, pre-shield phase (Guillou et al., 1997) at Kama'ehuakanaloa. The transition from pre-

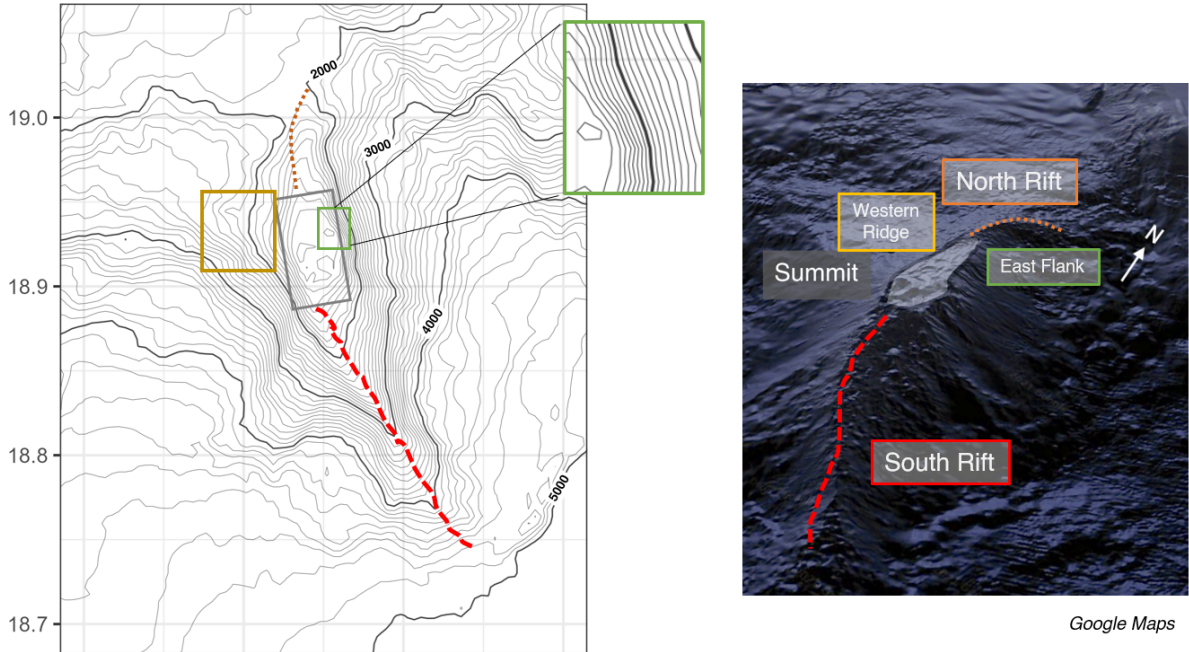


Figure 1.5: Notable Features on Kama'ehuakanaloa Seamount. Left shows bathymetric contour map described in Fig 1.9. Right side shows Google Maps generated oblique view from the Southeast of Kama'ehuakanaloa Seamount. Rift zones shown in dashed lines.

shield alkalic to tholeiitic volcanism was estimated to have occurred between 17,000–40,000 years ago, thus resulting in a total duration of activity at Kama'ehuakanaloa for around 250,000 years (Guillou et al., 1997). Observations at a real pre-shield locality of Kama'ehuakanaloa revealed that the transition from pre-shield alkalic to tholeiitic volcanism was longer than the predicted timescales of transitioning from shield to post-shield melting models (Frey et al., 1990). Hence, the pre-shield transition was not simply a reverse of the more commonly observed post-shield transition on other Hawaiian volcanoes. A duration of up to 200,000 years exceeds estimates for Kīlauea 's pre-shield to

shield transition occurring after 130,000-150,000 years (Lipman et al., 2000; Calvert and Lanphere, 2006).

The high  ${}^3\text{He}/{}^4\text{He}$  in Kama‘ehuakanaloa lavas and the overall temporal trend showing a decrease in ratio with age has led to the hypothesis that Kama‘ehuakanaloa is close to the present-day center of the Hawaiian hotspot (Kurz et al., 1983, 2004; Kaneko, 1987). Mauna Loa and Kīlauea are similarly active volcanoes in close proximity to Kama‘ehuakanaloa and the hotspot center, but have not produced  ${}^3\text{He}/{}^4\text{He}$  values comparable to Kama‘ehuakanaloa. Radiogenic isotope compositions at the other active volcanoes reflect two distinct trends of Loa (Mauna Loa) and Kea (Kīlauea) (Weis et al., 2020). The geographic configuration of Kama‘ehuakanaloa on the flanks of Mauna Loa would be consistent with Loa trend, but Kama‘ehuakanaloa radiogenic isotope compositions overlaps for both trends, neither strongly Loa nor Kea-like (Weis et al., 2020).

There appears to be a relationship with shield volcano age, as the highest  ${}^3\text{He}/{}^4\text{He}$  has been observed at pre-shield Kama‘ehuakanaloa, with lower values observed at shield-stage Kīlauea and Mauna Kea, and even lower values in the post-shield stages Lupton (1983). The overall temporal trend of decreasing  ${}^3\text{He}/{}^4\text{He}$  with volcano age, is consistent with waning thermal influence from a plume over time as Pacific plate moves overhead, and can be seen in volcanoes representing successive constructive stages (Fig. 1.6 and Table 1.1). Further efforts to integrate radiogenic isotope observations with individual volcanic localities led to devising mantle compositional endmembers with potential origins of primordial mantle, upper/MORB source mantle, as well as crustal and sediment input from subduction (Hofmann and White, 1982; Zindler and Hart, 1986; Hofmann, 1997; White, 2015).

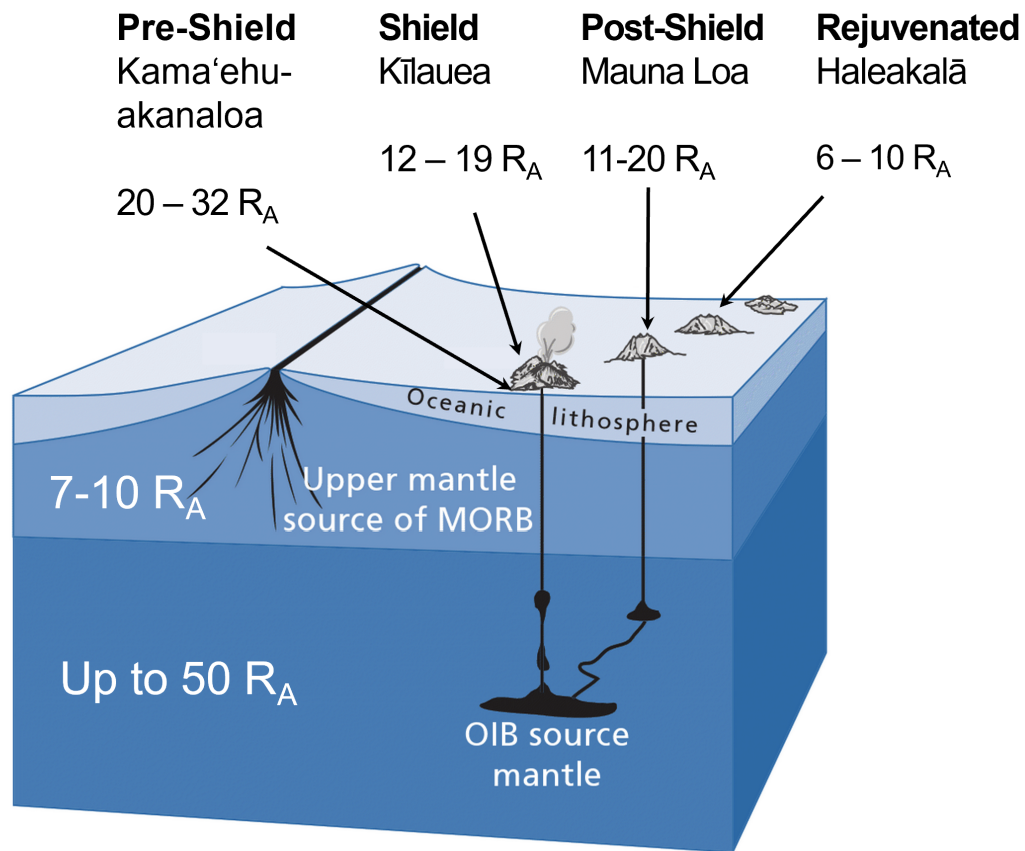


Figure 1.6: Range of  ${}^3\text{He}/{}^4\text{He}$  values of different Hawaiian stages and volcanoes on cross-section of OIB and MORB source, adapted from Allègre (2008). Helium isotope values for Kama'ehuakanaloa from Kurz et al. (1983), Kīlauea and Haleakalā from DePaolo et al. (2001), Mauna Loa from GEOROC <http://georoc.mpchmainz.gwdg.de/georoc/>)

## 1.4 This Study: Revisiting Kama‘ehuakanaloa, 40 years later

The existence of magmatic series in pre-shield, shield, post-shield, and post-eruptive or rejuvenated volcanoes are a recurring pattern observed in the trail of new and extinct Hawaiian volcanoes (Clague and Sherrod, 2014). There is general agreement about the evolution of Hawaiian magmas through alkaline and subalkaline series, and the general decline of Helium isotopes with the aging of each volcano. There has not yet been a study evaluating the coherence of trace elements, Helium isotopes, and radiogenic isotopes, to the pre-shield to early shield stage. To account for the diverse processes involved in the origin of Kama‘ehuakanaloa lavas, I evaluated how groups of samples and individual samples are related on the basis of new empirical trace element, Helium isotope, volatile, Pb isotope data, with existing compositional and location metadata to construct possible sequences of Kama‘ehuakanaloa growth based on basalt characteristics.

### 1.4.1 Samples

The present study utilizes samples from 5 different expeditions between 1981 to 1999, described in the following sections in chronological order. Sample collections according to expedition year and type (submersible dive or dredge) are shown on Figure 1.8. Table 1.2 shows a summary of collection information for this study’s sample set. Further information about expeditions in Appendix A. Sample locations primarily occur as a roughly NW-SE transect from  $18^{\circ}42'N$  to  $19^{\circ}N$  and  $155^{\circ}9'W$  to  $155^{\circ}15' W$ , representing the extent of the deep south rift zone, with depths ranging from 1300-5000 m below sea level. Exposures of fresh material along the narrow rift zone have enabled sampling of

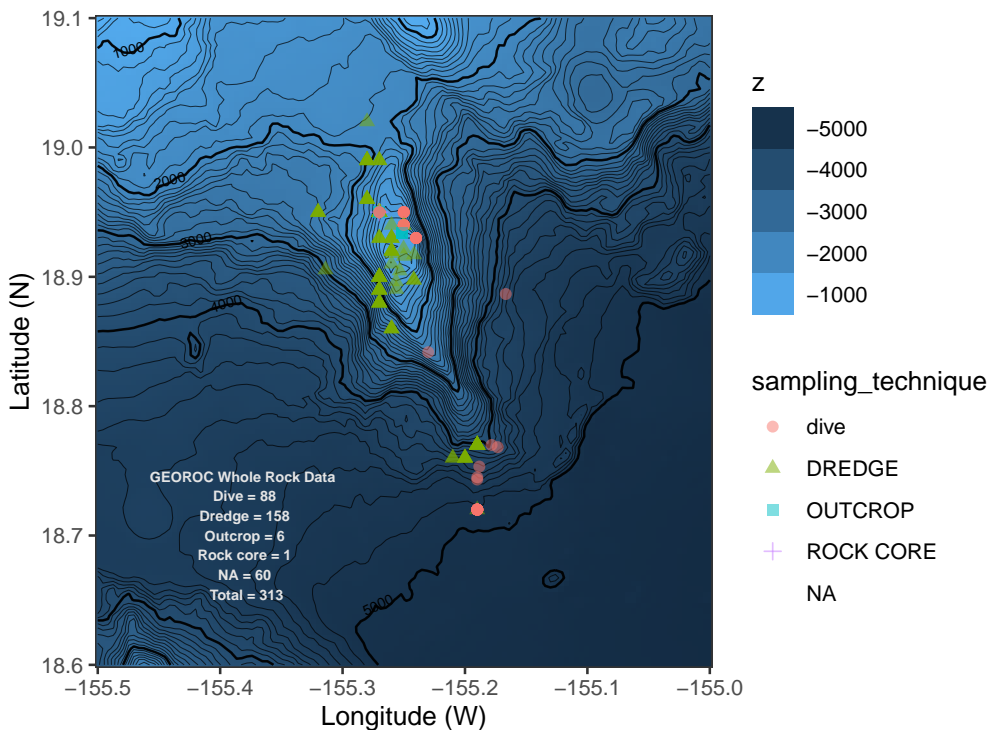


Figure 1.7: Map of existing GEOROC (<http://georoc.mpchmainz.gwdg.de/georoc/>) whole rock data from Kama'ehuakanaloa Seamount. Bathymetric Contour Map with Shaded Relief of Kama'ehuakanaloa Seamount ETOPO 2022 15 Arc-Second Global Relief Model for R (National Oceanic and Atmospheric Administration National Centers for Environmental Information, 2022). Contour interval is 100-m with index every 1000-m. Samples recovered by dredges shown in green triangle, samples collected by dives in pink circle.

glassy pillow lavas which comprise a wide range of compositions that include tholeiite, transitional and alkali basalt (Moore et al., 1982; Malahoff et al., 1987; Valbracht et al., 1997).

The study benefits from a sample set that was primarily collected by crewed submersible dives, and hence, are accompanied by precise location data which enables a comparison of the geographic extent of unique geochemical signatures. A map of all

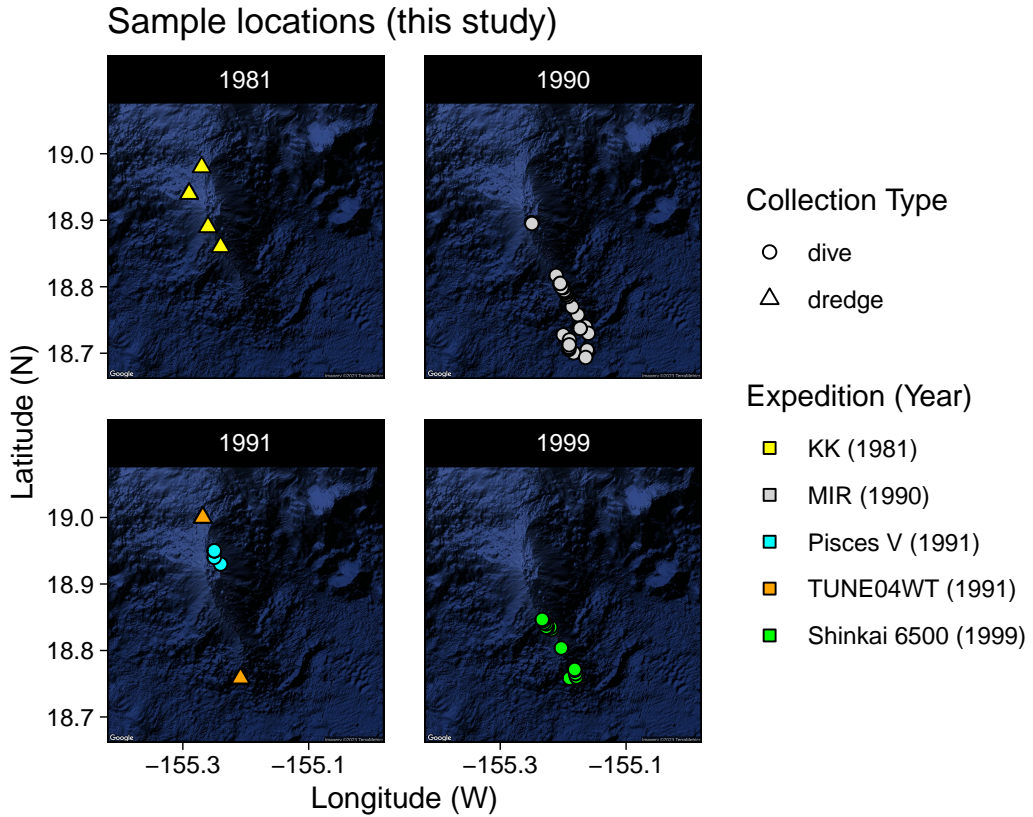


Figure 1.8: Sample locations shown on Google Map satellite view. Subfigures show sample collection metadata (Tables 1.2,A.2,A.3) and are coded according to collection by submersible dive or dredge haul

sample locations and classification of rock type (from glass composition) is shown in Figure 1.9. In this study, the on-bottom (starting) coordinates and depths for dredge samples were used for maps and other assessments of location. The majority of this study's samples were collected by manned submersible, which enables retrieval from specific locations of interest. MIR 1990 samples represent a significant proportion of samples collected by submersible along Kama'ehuakanaloa's South Rift. Coordinates from MIR submersible dives (Graham et al., 2023, 2024) were adjusted to show a closer fit to the

Table 1.2: This Study Suite and Expeditions

Year	Expedition	Type	Reference <sup>[1]</sup>	Number of Samples (This Study) <sup>[2]</sup>
1981	KK1-HW-81	Dredge	Moore et al. (1982)	5
1990	MIR	Dive	Matvenkov and Sorokhtin (1998) Garcia, unpublished	30
1991	Pisces V	Dive	Garcia et al. (1995)	7
1991	TUNE04WT	Dredge	SIO Geological Data Center (2018)	6
1999	Shinkai YK 99-07	Dive	Shipboard Scientists (1999)	15

<sup>[1]</sup> Either cruise report, ship log, or first instance of publication with location metadata. Not all references contain complete information about sampling.

<sup>[2]</sup> Number of individual samples in this study, which are not all collections or samples in the expedition

South Rift, based on sample depths, dive track locations (Garcia, unpublished) and an existing map of a subset of samples (Valbracht et al., 1997). The adjusted coordinates are shown in Appendix Table A.2 and Figure 1.10. Pre-existing literature data of MIR sample locations are limited to few samples (6 from Valbracht et al., 1994), or appearing to overlap due to the imprecise coordinates in the decimal system.

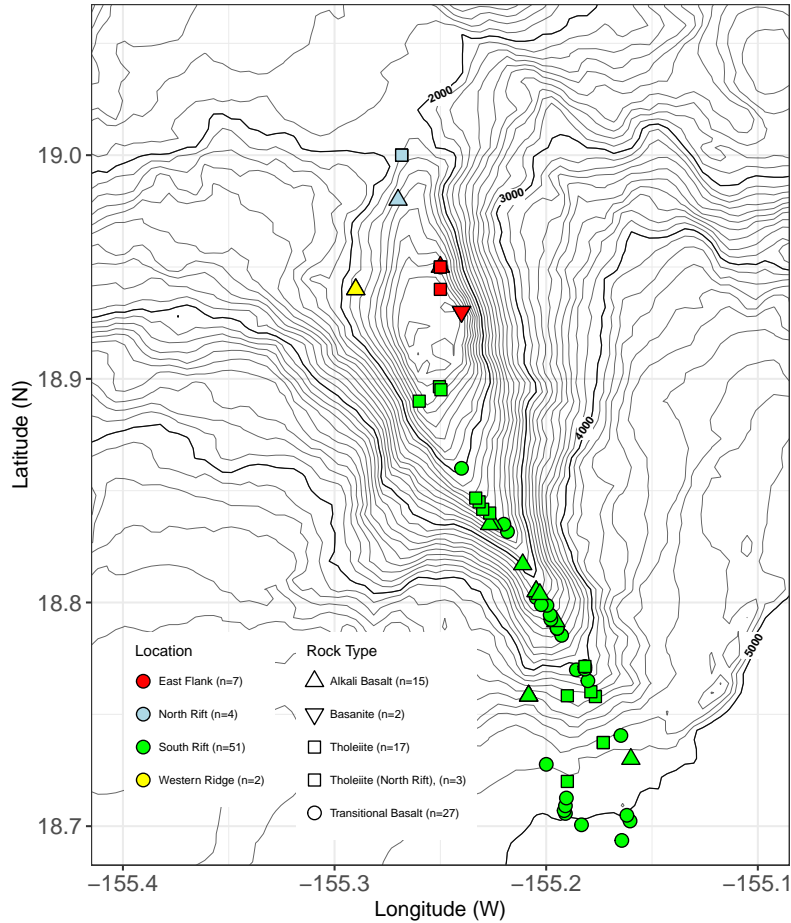


Figure 1.9: All sample locations shown on contour map of Kama'ehuakanaloa Seamount. Samples are color coded for location along the South Rift, North Rift, East Flank and Western Ridge. Shape of symbols corresponds to rock classification based on glass major element composition. Contour interval is 100-m with index every 1000-m. Bathymetric data from ETOPO 2022 15 Arc-Second Global Relief Model for R (National Oceanic and Atmospheric Administration National Centers for Environmental Information, 2022)

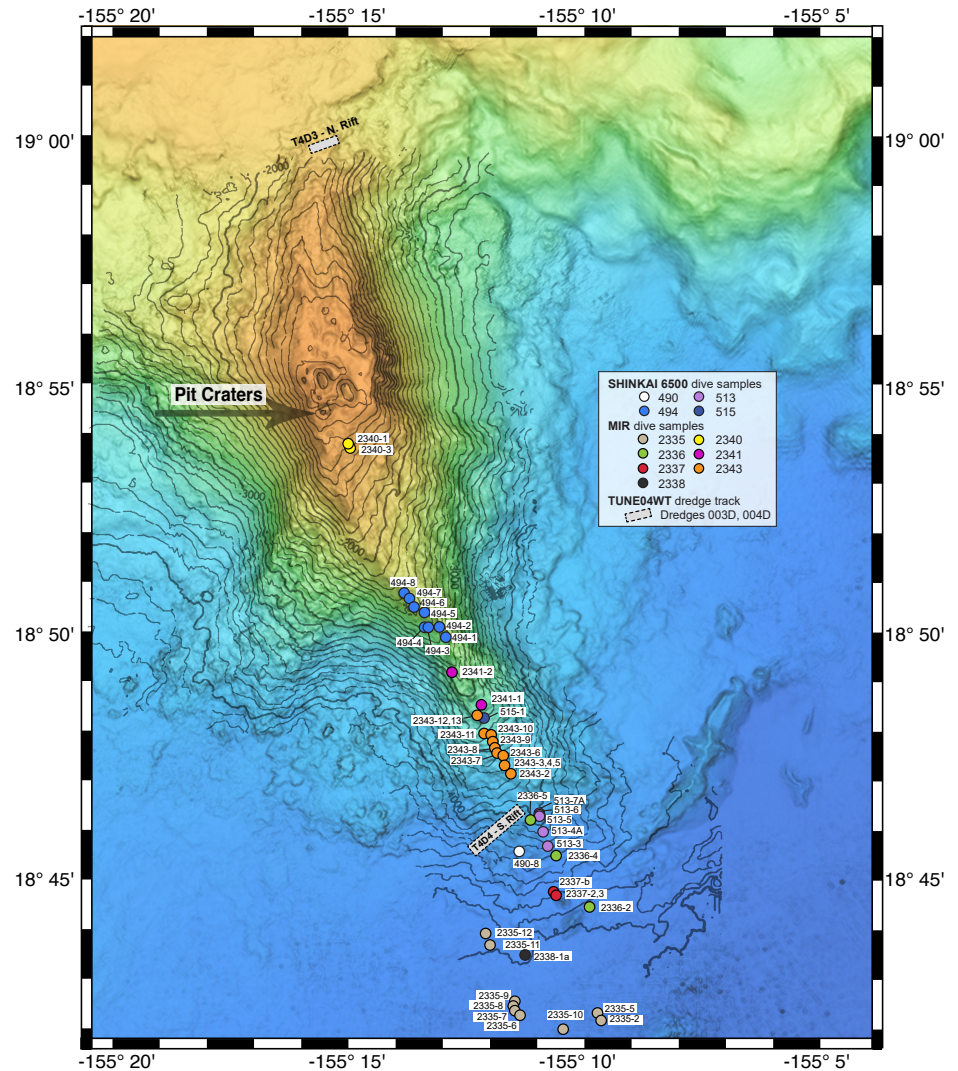


Figure 1.10: Sample locations for MIR and Shinkai dives and two TUNE04WT dredge tracks shown on map of Kama'ehuakanaloa Seamount. Approximate location for MIR samples is estimated based on depth and dive tracks

### 1.4.2 Methods

Up to 63 samples from Kama‘ehuakanaloa locations were analyzed by a range of techniques, including noble gas mass spectrometry, capacitance manometry, Fourier Transform Infrared Raman (FTIR) spectroscopy, electron microprobe analysis (EMP), and laser ablation inductively-coupled plasma mass spectrometry (LA-ICP-MS), and multi-collector inductively-coupled plasma mass spectrometry (MC-ICP-MS). Methods and sample statistics are summarized in Table 1.3. An advantage to this study is the analysis of the same glass aliquots to ensure complementary analysis on the same lava. The methods are summarized in the flowchart in Figure 1.11.

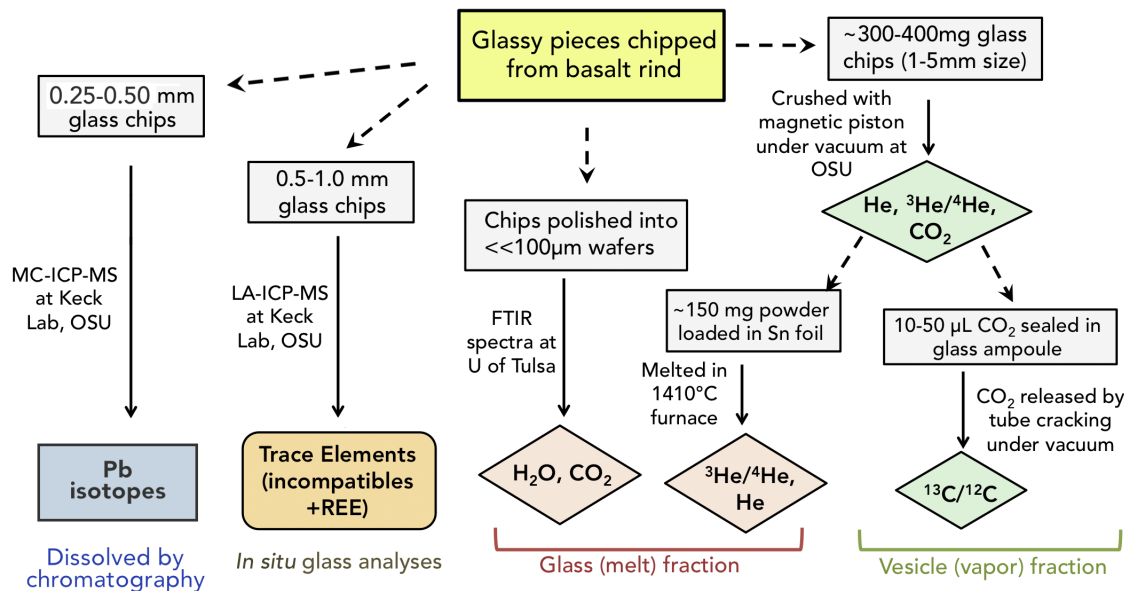


Figure 1.11: Analytical flowchart showing the sequence of analyses from aliquots of glass samples and resulting products. Data products from each chapter shown at the bottom of flowchart.

Table 1.3: Summary of chapters, methods, data products

Chapter	Methods	Data Products	Sample replicates
2	LA-ICP-MS [1]	Trace element concentrations in glass (n=63)	1 in Wieser et al. (2020b), 1 SIMS in Dixon and Clague (2001), 1 INAA-XRF in Dixon and Clague (2001)
	EMP [2]	Major element oxide concentrations (n=11)	
3	Noble Gas ICP-MS <sup>[3]</sup>	Helium concentrations and isotopes in vesicles (n=62), Helium concentrations and isotopes in glass (n=51)	1 in Kaneoka et al. (1983); Honda et al. (1993); Kent et al. (1999a), 3 in Kaneoka et al. (2002), 6 in Valbracht et al. (1996, 1997)
	Manometry [4]	CO <sub>2</sub> concentrations in vesicles (n=62)	
	FTIR [5]	CO <sub>2</sub> concentrations in glass (n=62)	3 in Dixon and Clague (2001), 1 SIMS in Pietruszka et al. (2011)
		H <sub>2</sub> O concentrations in glass (n=63)	2 in Dixon and Clague (2001), 1 SIMS in Pietruszka et al. (2011)
4	EMP [2]	Major volatiles (F, S, Cl) in glass (n=63)	4 in Dixon and Clague (2001), 1 SIMS in Kent et al. (1999a); Pietruszka et al. (2011)
	MC-ICP-MS [6]	<sup>206</sup> Pb/ <sup>204</sup> Pb, <sup>207</sup> Pb/ <sup>204</sup> Pb, <sup>208</sup> Pb/ <sup>204</sup> Pb in glass (n=28)	2 TIMS in Abouchami et al. (2005)

<sup>[1]</sup> LA-ICP-MS - Laser Ablation Inductively Coupled Plasma Mass Spectrometry at W.M. Keck Laboratory, Oregon State University. <sup>[2]</sup> EMP - Electron Microprobe at University of Tulsa. <sup>[3]</sup> ICP-MS - Inductively Coupled Plasma Mass Spectrometry at Noble Gas Laboratory, Oregon State University. Vesicle analyses performed on gas extracted from crushing. Glass analyses performed on melted powders in furnace. <sup>[4]</sup> Manometry on gas extracted from crushing, at Noble Gas Laboratory, Oregon State University. <sup>[5]</sup> FTIR - Fourier Transform Infrared Spectroscopy. <sup>[6]</sup> MC-ICP-MS - Multi-Collector Inductively Coupled Plasma Mass Spectrometry at W.M. Keck Laboratory, Oregon State University.

### 1.4.3 Dissertation Aims

#### Chapter 1

In this chapter, I investigated the major and trace element geochemistry of 62 basaltic glasses from rock samples collected at various topographic features of Kama‘ehuakanaloa Seamount to uncover consistent patterns in petrogenetic series, parental melts, and mantle source. Overall, I contribute a trace element perspective to understanding the pre-shield to shield volcanic transition in the context of typical Hawaiian volcano evolution models, which are usually based on major elements. Overall, contributions from this chapter provides valuable insights into the early stage volcanic processes and magma evolution occurring at a single volcano with exposures of the pre-shield to main shield transitional stage of oceanic island construction.

#### Chapter 2

In this chapter, I present new volatile results for >40 submarine basalts from various regions of Kama‘ehuakanaloa Seamount. TThe sample suite should be representative of the geographic extent of Kama‘ehuakanaloa Seamount away from the commonly studied summit region. Samples have been analyzed for  ${}^3\text{He}/{}^4\text{He}$  and He and CO<sub>2</sub> concentration in both the vesicle and glass phase of the basalts. All glasses were also analyzed for H<sub>2</sub>O, Cl, F and S. This new data set provides a means to evaluate the causes of volatile and helium isotope variations at Kama‘ehuakanaloa Seamount and how they relate to deep and shallow level volcanic processes.

## Chapter 3

In this chapter, I contribute Pb isotopes measured by multi-collector inductively coupled plasma mass spectrometry (MC-ICP-MS) to evaluate the distribution of rock types, isotopic signatures of basalts erupted along the 20-km long rift zone from depths of 1800 m to >5000 m. The deep South Rift has lacked coverage of Pb isotope data in geologic databases, and the majority of previous measurements have been made on samples collected from the shallower, summit region. Insights from Pb isotopes, in combination with empirical results from Chapters 2 and 3 allow an assessment of heterogeneity within Kama‘ehuakanaloa volcano, and possible indicators of the pre-shield to shield transition in context of Hawaiian volcanic systems and global OIB trends.

#### 1.4.4 Broader Implications

##### Contributions of Geochemistry to the Mantle Plume Debate

Identifying geochemical endmembers and mantle origins for ocean islands aids in volcano-level or regional data interpretation. However, there is still uncertainty about how local observations and variability relate to global patterns of deep mantle/plume source effects vs. shallow crustal and lithospheric processes at intraplate volcanoes. Arguments against plume model have been present since the decades following Plate Tectonics acceptance (O’Hara, 1973; Dziewonski and Anderson, 1981; Presnall and Gudfinnsson, 2011). Generally, plume skeptics approach intraplate volcanic phenomena from an explanation of shallow, decompression-related mechanisms of melting and as a manifestation of the global plate tectonic cycle. Early geochemical studies of the Hawaiian Islands, (e.g. Kurz et al., 1983) responded to the alternative hypothesis, that the islands formed from shallow fracture zone melting, sampling the ambient MORB source mantle, instead of tapping into a deeper source containing less processed mantle material. Hence, they argue for the “plate” model, opposed to plume model, to explain intraplate volcanism by similar controls at plate boundaries (Foulger, 2011).

Alternative hypotheses about large igneous province formation involve shallow mantle melting facilitated by plate breakups or plume-ridge interaction or mantle melting mixed with recycled oceanic crust, in which flux melting and fusible lithologies in the shallow upper mantle cause anomalous melting (Meibom and Anderson, 2004). The identification of the magma sources and their evolution relating to processes in the shallow lithosphere, plume head and/or lower mantle sources would provide key information that could also

constrain the existing models for the origin of oceanic LIPs.

## Geoscience Education

Common visual misconceptions about basic volcanic phenomena were noted by geologists of the previous century [Judd \(1881\)](#). Despite the well-established theory of plate tectonics, misconceptions related to physical structure, scale, time, and process regarding volcanoes still persist today among students and educators ([Smith and Bermea, 2012](#); [Francek, 2013](#)). One way to address misconceptions is to incorporate case studies of past field-wide debates in geology ([Dolphin and Dodick, 2014](#)). Disentangling the assumptions and claims of the plume model and Hawaiian volcanic evolution can be one way to integrate scientific controversy while developing student comparative skills about the distinct origins of basaltic volcanoes at MORB and/or OIB settings.

While the mantle plume model is popular in broader public science media and textbooks, the opposing plate model is often disseminated to non-specialist audiences, for example, in textbooks ([Foulger, 2011](#)), scientific conference presentations ([Foulger, 2020b](#)), and public websites like [mantleplumes.org](http://mantleplumes.org) ([Foulger, 2020a](#)). Since 2003, the website has been a consistent source of free articles about hotspots, plumes, and large igneous provinces and often appears in the top results for web searches about hotspot volcanoes. Plume skeptics have broadened their impacts over the last 20 years, but there is a persistent lack of counterarguments or specific response from mantle geochemists in settings where broader audiences are engaged.

Scientific curation is essential for public belief formation but pre-existing errors in

readers and common curation practices can distort information and lead to belief polarization (O'Connor et al., 2023). Mantle geochemists are well-positioned to educate students about debated topics such as the plume model, and can begin by curating information from a variety of formats and perspectives. Geochemists can follow the approach used in journalistic reporting of natural disasters and climate change events, where information is presented truthfully, while being pluralistic and reflexive in order to engage the audience in ambiguous or dynamic situations (Peeters and Maeseele, 2023).

While the geology of the Hawaiian Islands is often covered in introductory geology classes, the distinction between the geochemistry of the Hawaiian Islands and other oceanic basalts is rarely covered. However, geochemical data from active Hawaiian volcanoes like Kama‘ehuakanaloa, Kīlauea, and Mauna Loa can serve as valuable case studies for educators aiming to incorporate authentic scientific data towards students' understanding of local processes and global-scale events. Hawaiian volcano research can be a platform to address misconceptions, engage broader audiences, and foster critical thinking about volcanic evolution and plate tectonics models.

Overall, the thesis seeks to provide a comprehensive analysis of the geochemistry of a specific Hawaiian volcano, by emphasizing insights from the development of the mantle plume concept and its interplay between oceanic sampling expeditions, noteworthy samples and observations that have since supported or motivated modifications towards the mantle plume concept. This dissertation also attempts to examine primary literature and data provenance in order to promote reuse of previous and new geochemical data (Wilkinson et al., 2016), and offer a starting point to incorporate pre-shield or alkaline type intraplate volcanoes in introductory geoscience materials.

## Chapter 2: Trace element signature and petrogenesis from primordial and depleted mantle sources

### 2.1 Introduction

The Hawaiian Islands are among the most studied intraplate volcanic system on Earth. The Hawaiian-Emperor-Seamount chain records over 80 million years of construction over the Pacific Plate ([Clague and Dalrymple, 1987](#)). The volcanic history of the Emperor seamount chain is of great importance on understanding global plate motion ([Konrad et al., 2018b](#)), models of past mantle flow and circulation ([Tarduno et al., 2009](#)), and overall mantle convection modes and cycles ([Koppers and Watts, 2010](#)). The more recent main Hawaiian Islands, erupted in the last 5 million years, bear great importance on the mechanisms responsible for generating large volumes of magma until the present day. The range of activity observed at the main Hawaiian Islands is related to volcano age, where the volcanic shield is constructed over a duration on the order of a million years.

The main volcanic shield of a Hawaiian volcano typically is constructed over a duration on the order of less than a million years ([Clague and Dalrymple, 1987](#)). Hiatuses and transitions between main volcanic activity occur on shorter 10-100 kyr timescales. Post-shield eruptions can occur over millions of years, and eventually, activity ceases due to continued displacement from the hotspot source ([Clague and Sherrod, 2014](#)). Constraints from stratigraphic sequences, K-Ar and  $^{40}\text{Ar}$ - $^{39}\text{Ar}$  dating of individual Hawaiian volcanoes

enabled the development of a generalized growth model for intraplate oceanic volcanoes (see references in [Clague and Sherrod, 2014](#)).

On Hawai‘i, two volcanoes have developed rift zones on the flanks of Mauna Loa with independent magmatic plumbing systems. Subaerial Kīlauea, and submarine Kama‘ehuakanaloa (formerly Lō‘ihī Seamount) are historically active and in close proximity to the presumed radius of the Hawaiian hotspot influence. The conduit of the Hawaiian plume is likely influenced by the larger volcanoes, and deep earthquakes at Kama‘ehuakanaloa are likely to occur on existing fractures in mantle fault zones ([Merz et al., 2019](#)). Both are entering similar stages of early growth, though Kama‘ehuakanaloa represents one of the rare exposures of the pre-shield stage. The pre-shield stage is now believed to exist underneath the shield of all Hawaiian islands, inaccessible from the overlying shield lavas that comprise 95% of the total volcano volume ([Clague and Dalrymple, 1987](#)). Estimated lava accumulation rates from K-Ar dating and radiocarbon dating of fossil-rich sections yield estimates of 5 meters upward growth per 1000 years ([Guillou et al., 1997](#)), similar to the lower range of shield accumulation rates of 6 meters per 1000 years ([Robinson and Eakins, 2006; Clague and Sherrod, 2014](#)). Calculations of Kama‘ehuakanaloa’s total volume is estimated to be  $1.7 \times 10^3$  m<sup>3</sup>, more than 15X lower than Kīlauea’s volumetric estimates, with most of the growth occurring during the pre-shield stage ([Robinson and Eakins, 2006; Clague and Sherrod, 2014](#)).

The peak of sampling expeditions at Kama‘ehuakanaloa Seamount with manned submersibles and collection of deep (>1 km water depth) basaltic samples occurred between the late 1970s to 1990s ([Malahoff et al., 2006; Garcia et al., 2006](#)). Early studies described the pre-shield stage, its flux of primordial Helium-3, and the volcano’s relationship to a hy-

pothesized mantle plume (Moore et al., 1982; Rison and Craig, 1983). Other observations included interbedded alkalic and tholeiitic flows (Moore et al., 1982), deep explosive eruptions (Malahoff et al., 1982), and high chemical variability in major elements (DePaolo and Stolper, 1996). Hydrothermal activity is common on the summit, and the relative ages and locations of recent pit craters would be consistent with a southward transition in volcanic activity (Garcia et al., 2006). The presence of tholeiites at Kama‘ehuakanaloa has been interpreted as evidence of an ongoing transition to tholeiitic volcanism (Moore et al., 1982; Garcia, 1996). Increasing accumulation rates for uppermost tholeiitic lavas have also been used to propose that Kama‘ehuakanaloa is entering the more productive shield stage of volcanism by moving closer to the hotspot center (Garcia et al., 1995).

The exact length scale of isotopically heterogeneous components in Earth’s mantle, and in the resulting melts overlying OIB and MORB mantle sources, is unknown, but presumably smaller than the scale of melting in the shallow mantle (Stracke, 2021). Consistent high  ${}^3\text{He}/{}^4\text{He}$  suggests that the contributions of the plumes are evident even in the earliest stages of volcanic construction. Though the majority of samples collected at Kama‘ehuakanaloa have been alkaline or transitional, and often display moderately high  ${}^3\text{He}/{}^4\text{He}$ , Kama‘ehuakanaloa tholeiites comprise a larger proportion of data used towards mantle models, particularly for characterizing the highest  ${}^3\text{He}/{}^4\text{He}$  sources. Overlapping compositions between individual Hawaiian volcanoes are both indicative of variable source contributions and common plume or ambient mantle sources (Weis et al., 2020; Jackson et al., 2008), though within-shield chemical differences have been observed at Hawaiian volcanoes (Mukhopadhyay et al., 2003; Ren et al., 2009; Weis et al., 2020). The assumption that tholeitic compositions are reliable indicators of a shield-like source

is difficult to test.

In this study, I present new trace element results for 64 basaltic glasses from five expeditions collected over the span of 18 years. Basaltic glasses were targeted for the purpose of characterizing magmatic compositions. This data set includes samples that have previously been measured in several studies but have rarely been assessed in the context of geographic location and petrogenetic relationships across Kama‘ehuakanaloa. The majority of samples are from the South Rift Zone and collected by submersible dives targeting a well-developed thin edge of likely recent lava (Malahoff et al., 1982). Additional samples from the less studied North Rift zone and Western Ridge complement the insights gained from exposed stratigraphic sequences at the East Flank/summit region (Garcia, 1996) to build a more complete understanding of processes occurring across Kama‘ehuakanaloa. Geochemical groupings in relation to geographic location can be used to understand the alkalic to tholeiitic transition at Kama‘ehuakanaloa, sensitive trace element variations can reveal new scales of mantle heterogeneity within the growing volcano (Stracke, 2021).

### 2.1.1 Study Aims and Research Questions

The goal of this study is to use trace element compositions of Kama‘ehuakanaloa basaltic glasses to identify groupings of related lavas and identify source characteristics and processes involved in the construction of a an early shield volcano. The following research questions are addressed:

1. Are there multiple petrogenetic series present at Kama‘ehuakanaloa? Is variation

present depending on geographic distribution (location along major rift zones or other regions) and/or rock type?

2. Are trace element compositions consistent with the classification of rock types, based on major element analyses?
3. How does the range of shallow processes (crystallization, assimilation) affect glass compositions across Kama‘ehuakanaloa Seamount?
4. Do trace elements of alkalis vs. subalkaline/tholeiite samples correspond to aspects of pre-shield or shield stage at Kama‘ehuakanaloa? Are there differences between alkalic and subalkalic/tholeiite parental melts and representative mantle source compositions?

## 2.2 Samples

This study includes measurements of basaltic glass chipped from pillow lava rinds collected at Kama‘ehuakanaloa’s North Rift, South Rift, Eastern Flank, and Western Ridge. For collection and expedition details, see Appendix A. The compositional range is representative of the range of lavas observed at Kama‘ehuakanaloa and the Hawaiian Islands (Garcia et al., 1993, 1995).

Samples were often fresh with high luster and homogeneous surfaces which are favorable for *in situ* trace element analyses. The basalt glassy rinds ranged from <1 mm to 2-3 mm thick. Some of the original exposed pillow surfaces exhibited dusty brown or yellow-orange oxide staining pervading the outer portions of the rind, possibly as palagonite or nontronite (Malahoff et al., 1987). The basalts range from non-vesicular to ~20% vesicles by volume, typically with round bubbles <0.5 mm. Samples are occasionally aphyric, but more commonly they are sparsely olivine-phyric to picrotic (containing up to ~20% olivine microphenocrysts). Major element compositions show that the samples range from tholeiite to alkaline series.

## 2.3 Methods

Trace element concentrations were analyzed by laser ablation inductively coupled plasma mass spectrometry (LA-ICP-MS) on the same samples that were studied for volatiles and Pb isotopes (Ch. 3,4. Analytical procedures were adapted from Loewen and Kent (2012); Michael and Graham (2015). Glass chips of 0.25-1.0 mm grain size were selected for their lack of phenocrysts at the surface. Surface alteration was examined under a petrographic

microscope, and fresh samples were selected for mounting. Glass chips were mounted in 1-inch diameter epoxy mounts and cured overnight in a 60°C oven. Mounts were ground in successive stages of 240, 320, 400, and 600 grit silicon carbide paper followed by ultrasonic cleaning in Milli-Q water, before final polishing with 1 $\mu\text{m}$  alumina paste on a ceramic wheel. Mounts were inspected for a fine polish on the glass chips and then ultrasonically cleaned for 15 minutes in Milli-Q water and with a final ultrasonic cleaning for 15 minutes in ethanol. Most commonly, olivine was present as phenocrysts and microphenocrysts, but the presence of olivine did not limit the availability of analyzing crystal-free portions during laser ablation (Appendix Fig. A.1).

Laser ablation Inductively-Coupled Plasma Mass Spectrometry (LA-ICP-MS) analyses were performed in the W.M. Keck Laboratory for Plasma Spectrometry at Oregon State University. Three lines each 200  $\mu\text{m}$  long were analyzed per sample using a Photon Machines 193-nm excimer laser. Samples were pre-ablated just before analysis to remove any trace contaminants at the sample surface. Pre-ablation settings were 110  $\mu\text{m}$  spot size, 3 Hz repetition rate, 50  $\mu\text{m}/\text{s}$  scan speed, and an energy output of 10%/0.85 J/cm<sup>2</sup>. Ablation settings for sample analysis were 85  $\mu\text{m}$  spot size, repetition rate of 15 Hz, energy/output of 75%/6.35 J/cm<sup>2</sup>, and a scan speed of 5  $\mu\text{m}/\text{s}$  leading to an ablation interval of 40 seconds.

BCR-2G basalt standard glass from the United States Geological Survey (USGS) was used as reference material to calibrate the analytical data for this study. Secondary standards analyzed as unknowns included USGS glasses GSD-1G, GSA-1G, and BHVO-2G. BHVO-2G was used as the reference value for reproducibility and accuracy (Appendix Table A.6. Analyses utilized  $^{43}\text{Ca}$  from CaO contents of electron microprobe

and XRF data (Table A.1, Graham et al., 2023; Garcia, unpublished), for internal normalization to adjust for any variations in sample and standard ablation rate. The secondary standards were analyzed twice at the beginning and end of each experiment, and were interspersed as single runs between every 15 unknowns during an analytical session. Standard glass reference values were taken from the GeoReM database (<http://georem.mpch-mainz.gwdg.de/>). Group 1 consists of incompatible element data (K, Rb, Sr, Y, Zr, Nb, Mo, Sn, Cs, Ba, Hf, Ta, W, Tl, Pb, Th, U) which were collected during the first (morning) analytical session, followed by an instrument tuning/performance report. Group 2 elements from a second (afternoon) analytical session include rare earth elements plus Sc, Ti, V, Mn and Ni.

Raw data were processed using in-house LaserTRAM 2.3 and LaserCalc 2.0 software Kent et al. (2004). Uncertainties were calculated by repeated measurements (n=12) of standard BHVO-2G. A summary of BHVO-2G reference values, measured mean values, uncertainties, and instrument detection limits are in Appendix Table A.6. Reproducibility of the trace element analyses was better than 5% based on repeated analyses of rock standards analyzed as unknowns, except for W and Tl. The accuracy of the standard is within 10% of the suggested values (BHVO-2G, n=12) except for Sn, Ni, and Tm.

## 2.4 Results

### 2.4.1 Major Elements

In this study, electron microprobe compositions for 7 samples were determined at The University of Tulsa (UT). Major element compositions of new basalt glass compositions are reported in Table A.1. Major element compositions for glasses were compiled from this study and previous sources (Ren et al., 2009; Graham et al., 2023, Garcia, unpublished).

A Total Alkalies-Silica diagram of Kama‘ehuakanaloa compositions (Fig. 2.1) shows a range of compositions from basanite to tholeiites. Kama‘ehuakanaloa lavas generally show a negative slope and decreasing alkalis with increasing  $\text{SiO}_2$ , an uncommon trend for Hawaiian volcanoes, but commonly observed in previous Kama‘ehuakanaloa samples, including South Rift and East Flank glasses (Moore et al., 1982; Garcia et al., 1995). Alkali basalts are Si-undersaturated while transitional basalts are  $\text{SiO}_2$  oversaturated at  $\text{SiO}_2 = 48$  wt.%. Tholeiites have  $\text{Na}_2\text{O} + \text{K}_2\text{O} < 3.5$  wt.%.  $\text{SiO}_2$  ranges from 47.0-50.7 wt.%, while  $\text{Na}_2\text{O} + \text{K}_2\text{O}$  ranges from 2.7-5.0 wt. %. These compositions correspond to tholeiitic, transitional, and alkali basalts on the basis of field boundaries from (Le Bas et al., 1986), and proximity to the Macdonald-Katsura (M-K) line (Macdonald and Katsura, 1964).

Glass MgO ranges from 5-10 wt.%, and varies among the same rock type at the different rift zones. The North Rift tholeiites ( $\text{MgO} \sim 8.3$  wt.%) are slightly higher MgO than the South Rift tholeiites (mean MgO wt.% = 6.6). Helz and Thornber (1987) showed that tholeiitic glasses are likely to be derived from a narrow range of parental melts, over a temperature range estimated to lie between  $1139^\circ\text{C}$ - $1183^\circ\text{C}$  for an olivine-saturated magma.

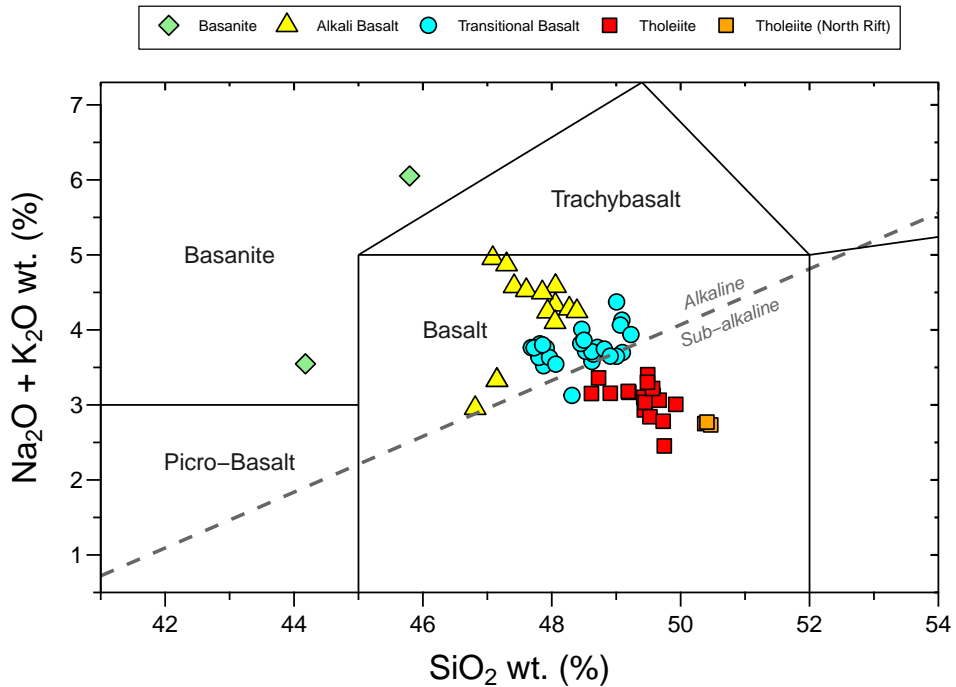


Figure 2.1: Total Alkalies vs. Silica (TAS) Diagram with major element oxides calculated to 100% on a volatile-free basis. The dividing line by Macdonald and Katsura (1964) is shown in a grey dashed line, indicating alkaline compositions above the line, transitional basalt compositions near the line, and tholeiite compositions below the line. Fields for classification are from Le Maitre et al. (2004). Samples in the basanite field have normative olivine >10%.

The relative proportions of expected minerals can be distinguished with major elements proportions, based on normative nepheline or enstatite. Results of CIPW normative compositions are in Appendix Table A.4 and displayed on Figure 2.2. Comparing the previously assigned rock classification to CIPW norms shows silica-saturation of tholeiitic lavas which are strongly En-normative (>8%). Transitional basalts are both weakly En-normative (<8%) to Ne-normative (<3%), and alkalic basalts are Ne-normative (>3%). Alkali basalts are separated from En-normative subalkaline rocks, with

transitional basalts plotting in an overlapping middle region. A subset of the transitional basalts gave Ne-norm = 0 and hence reside in the subalkaline region on the CIPW plot, similar to positions on the M-K line (Fig. 2.1). Silica-undersaturated basanite compositions are not plotted on Figure 2.2 but have Ol-norm >10% and Ne-norm>5%.

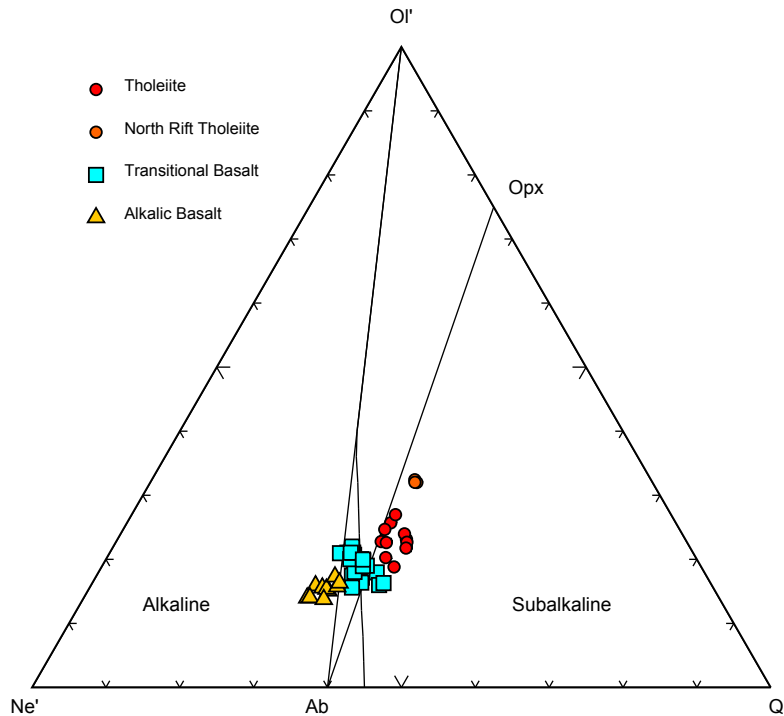


Figure 2.2: Ne-Ol-Q base of basalt tetrahedron after [Yoder and Tilley \(1962\)](#) with alkaline fields, subalkaline fields, and dividing line from [Irvine and Baragar \(1971\)](#) Kama'ehuakanaloa compositions from South and North Rift are shown. Note that "Enstatite" (En) is used in place of the term "Hypersthene" in the main text.

## 2.4.2 Trace Elements

A total of 64 samples were analyzed by LA-ICP-MS. Results are shown for the incompatible trace element (e.g. K, Rb, Sr) and minor element (Sc, V, Mn, Ni) concentrations in Table 2.1. Rare earth element (REE) concentrations are shown in Table 2.2.

Table 2.1: Trace element concentrations in ppm

ID Sample	K	Rb	Sr	Y	Zr	Nb	Mo	Sn	Cs	Ba	Hf	Ta	W	Tl	Pb	Th	U	Sc	Ti	V	Mn	Ni
1 MIR 2335-2	5506	13.2	479	25.6	165	21.7	1.04	1.84	0.140	186	4.19	1.41	0.24	0.038	1.74	1.32	0.38	28.8	17693	363	1219	132.0
2 MIR 2335-5	5906	13.9	521	28.5	186	23.4	1.07	1.88	0.149	199	4.73	1.55	0.27	0.037	1.69	1.49	0.40	29.4	18107	370	1236	131.0
3 MIR 2335-6	6360	15.2	534	26.9	179	24.4	1.18	2.03	0.164	213	4.59	1.55	0.29	0.044	1.97	1.50	0.44	27.4	18583	381	1268	108.0
4 MIR 2335-7	5991	14.2	515	24.5	164	22.9	1.08	1.97	0.144	199	4.01	1.39	0.27	0.038	1.74	1.31	0.42	28.6	18295	373	1260	121.0
5 MIR 2335-8	5821	13.6	508	26.6	175	22.8	1.03	1.87	0.137	194	4.38	1.48	0.26	0.037	1.70	1.44	0.39	27.9	18517	388	1295	128.0
6 MIR 2335-9	6117	14.5	551	29.2	192	24.6	1.11	1.91	0.154	210	4.91	1.65	0.27	0.038	1.74	1.58	0.42	29.1	19868	394	1318	110.0
7 MIR 2335-10	5734	13.5	509	25.7	167	22.5	1.04	1.83	0.143	197	4.31	1.43	0.24	0.035	1.68	1.35	0.40	28.3	18493	389	1300	130.0
8 MIR 2335-11	6468	15.4	549	27.1	187	25.5	1.14	1.94	0.162	226	4.62	1.61	0.28	0.040	1.93	1.61	0.44	26.6	18175	370	1289	99.8
9 MIR 2335-12	4776	11	391	18.5	117	18.0	0.96	1.87	0.107	145	2.91	1.00	0.24	0.034	1.53	0.97	0.37	30.9	15408	385	1431	172.0
10 MIR 2336-2	6292	14.7	518	27.3	184	23.7	1.06	1.85	0.155	212	4.72	1.55	0.26	0.039	1.80	1.56	0.41	27.8	18353	377	1323	117.0
11 MIR 2336-4	4342	9.93	405	25.4	153	19.1	0.89	1.81	0.101	142	3.98	1.26	0.21	0.030	1.33	1.08	0.33	31.6	18369	375	1379	116.0
12 MIR 2336-5	7010	16.9	473	28.1	181	25.3	1.28	2.23	0.179	218	4.35	1.50	0.29	0.042	1.95	1.41	0.49	25.6	19163	405	1399	88.5
14 MIR 2337-2	4554	10	421	24.9	144	16.5	0.81	1.60	0.109	154	3.76	1.09	0.18	0.028	1.33	1.03	0.29	29.0	16181	362	1420	63.0
15 MIR 2337-3	4152	9.4	395	29.7	168	17.1	0.83	1.75	0.085	134	4.31	1.15	0.18	0.027	1.29	1.12	0.30	28.9	17293	366	1379	66.4
16 MIR 2338-1a	6247	14.6	528	27.7	187	24.0	1.08	1.88	0.154	214	4.78	1.59	0.26	0.039	1.81	1.59	0.41	26.6	18637	381	1317	105.0
17 MIR 2340-1	4320	9.45	413	22.9	132	15.8	0.81	1.58	0.098	148	3.43	1.02	0.19	0.029	1.32	0.97	0.28	28.2	16069	356	1372	82.2
18 MIR 2340-3	3941	8.58	390	23.2	132	14.6	0.73	1.50	0.091	135	3.43	0.98	0.16	0.025	1.22	0.92	0.26	31.5	15118	338	1323	109.0
19 MIR 2341-1	5864	13.6	487	29.4	182	24.2	1.05	2.17	0.148	195	4.65	1.52	0.26	0.039	1.75	1.39	0.43	26.9	20115	401	1444	72.7
20 MIR 2341-2	8297	20.1	643	28.4	216	31.1	1.44	2.02	0.214	291	5.20	2.04	0.35	0.053	2.47	2.10	0.52	21.3	19480	399	1412	68.3
21 MIR 2343-2	5957	14	487	28.7	196	25.9	1.15	2.20	0.138	196	4.94	1.68	0.28	0.044	1.80	1.48	0.44	23.4	21935	402	1497	51.3
22 MIR 2343-3	5759	13.8	501	25.8	167	23.4	1.01	1.73	0.155	198	4.20	1.54	0.25	0.039	1.57	1.46	0.39	24.9	18637	383	1400	79.3
23 MIR 2343-4	5887	13.8	505	26.0	170	23.3	0.99	1.84	0.158	198	4.14	1.49	0.25	0.040	1.76	1.41	0.39	28.8	18312	387	1385	97.6
24 MIR 2343-5	5812	13.7	498	25.1	165	23.1	0.99	1.80	0.154	199	4.02	1.47	0.25	0.037	1.68	1.43	0.39	25.1	18394	378	1388	78.9
25 MIR 2343-6	8126	19.5	655	24.8	199	28.6	1.32	2.08	0.193	283	4.85	1.77	0.34	0.050	2.26	1.81	0.47	21.5	19970	375	1287	82.5
26 MIR 2343-7	6066	14.5	529	27.3	181	24.8	0.99	1.92	0.161	210	4.41	1.58	0.26	0.046	1.87	1.53	0.40	26.9	17810	372	1364	87.3

Trace Element Concentrations in ppm (Continued)

ID	Sample	K	Rb	Sr	Y	Zr	Nb	Mo	Sn	Cs	Ba	Hf	Ta	W	Tl	Pb	Th	U	Sc	Ti	V	Mn	Ni
27	MIR 2343-8	5538	13.2	498	26.9	174	226	0.93	1.82	0.149	189	4.27	1.50	0.26	0.037	1.66	1.42	0.36	27.1	17978	374	1366	102.0
28	MIR 2343-10	5434	12.9	478	26.2	169	21.9	0.92	1.71	0.144	185	4.23	1.45	0.24	0.037	1.65	1.40	0.35	29.6	17732	367	1329	108.0
29	MIR 2343-11	5888	14	503	26.3	173	23.6	0.99	1.78	0.160	201	4.20	1.55	0.27	0.042	1.71	1.49	0.39	24.5	18577	371	1393	74.4
30	MIR 2343-12	7553	18.8	586	30.3	209	28.3	1.33	2.06	0.195	261	5.02	1.82	0.32	0.052	2.18	1.81	0.47	20.9	19719	387	1328	60.2
31	MIR 2343-13	7425	18	551	28.3	191	26.9	1.28	2.22	0.191	250	4.72	1.68	0.32	0.047	2.18	1.63	0.48	26.6	19562	394	1321	89.9
32	S 490-8	4806	10.8	427	27.7	169	20.6	0.92	1.83	0.113	147	4.10	1.35	0.19	0.031	1.41	1.19	0.36	28.5	18552	362	1296	79.2
33	S 494-1	6801	15.2	514	26.5	196	26.8	1.33	2.23	0.160	208	4.62	1.60	0.29	0.044	2.16	1.50	0.50	24.3	21995	406	1442	51.9
34	S 494-2	6416	14.5	516	27.6	203	26.4	1.27	2.20	0.151	207	4.93	1.68	0.30	0.041	2.11	1.56	0.47	25.3	21045	379	1364	55.8
35	S 494-3	9488	23	665	28.8	233	36.0	1.74	2.16	0.256	312	5.30	2.28	0.41	0.064	2.76	2.26	0.65	19.7	21240	402	1383	51.4
36	S 494-4	8979	21.7	647	28.0	224	34.6	1.66	2.15	0.234	298	5.14	2.20	0.39	0.055	2.61	2.17	0.63	20.9	20885	411	1365	61.3
37	S 494-5	3985	8.95	400	28.7	156	16.5	0.81	1.84	0.096	129	4.18	1.09	0.18	0.029	1.37	0.98	0.28	30.1	17597	363	1406	71.1
38	S 494-6	3602	8.09	374	27.1	148	15.2	0.77	1.74	0.082	118	3.80	1.00	0.16	0.029	1.18	0.87	0.26	31.0	16696	369	1397	82.6
39	S 494-7	3498	7.99	370	26.8	144	15.1	0.79	1.75	0.079	117	3.82	0.95	0.16	0.024	1.14	0.85	0.26	30.8	16232	361	1345	79.5
40	S 494-8	4119	9.45	400	27.5	155	17.2	0.87	1.91	0.093	134	4.05	1.10	0.19	0.028	1.32	0.97	0.30	27.6	17734	376	1393	63.2
41	S 513-3	4448	10.1	431	26.9	164	20.6	0.92	1.78	0.104	145	4.19	1.37	0.22	0.028	1.29	1.19	0.35	25.6	19183	389	1447	81.4
42	S 513-4A	7001	17.3	497	32.0	206	27.1	1.30	2.19	0.173	235	5.30	1.71	0.31	0.047	1.84	1.62	0.48	25.3	19624	395	1349	86.4
43	S 513-5	4907	11.6	423	29.3	169	19.5	0.92	1.74	0.121	162	4.30	1.31	0.21	0.030	1.46	1.21	0.32	29.6	17525	364	1273	107.0
44	S 513-6	5037	12	428	29.5	172	19.8	0.93	1.79	0.126	166	4.38	1.31	0.22	0.029	1.54	1.24	0.33	30.1	17489	364	1268	124.0
45	S 513-7A	4510	10.7	389	28.4	156	18.6	0.87	1.83	0.105	149	4.03	1.21	0.20	0.028	1.31	1.06	0.31	29.7	16962	349	1297	87.0
46	S 515-1	8023	19.9	592	28.2	197	29.7	1.46	2.08	0.204	284	4.82	1.82	0.35	0.048	2.19	1.75	0.52	23.2	20536	401	1347	66.3
47	TUNE 3-a	2565	4.85	298	24.2	123	10.6	0.49	1.39	0.049	74	3.20	0.73	0.11	0.016	0.82	0.61	0.17	30.9	13515	334	1342	161.0
48	TUNE 3-b	2661	5	293	22.5	114	10.5	0.50	1.43	0.052	74	2.99	0.69	0.10	0.017	0.87	0.58	0.18	30.6	13595	343	1362	161.0
49	TUNE 3-c	2593	4.87	297	23.9	122	10.5	0.50	1.37	0.051	74	3.18	0.71	0.10	0.017	0.84	0.61	0.17	30.8	13491	336	1347	158.0
50	TUNE 4-a	7329	17.7	571	23.1	178	26.3	1.26	2.11	0.177	240	4.27	1.60	0.30	0.047	2.03	1.51	0.47	24.2	18710	358	1278	80.8
51	TUNE 4-b	7354	18.2	586	23.2	178	26.7	1.32	2.15	0.176	252	4.55	1.63	0.32	0.049	2.05	1.51	0.46	24.6	18669	352	1248	77.8

Trace Element Concentrations in ppm (Continued)

ID Sample	K	Rb	Sr	Y	Zr	Nb	Mo	Sn	Cs	Ba	Hf	Ta	W	Tl	Pb	Th	U	Sc	Ti	V	Mn	Ni
52 TUNE 4-c	7439	18.1	577	23.1	175	26.2	1.32	2.17	0.181	242	4.38	1.59	0.29	0.045	2.05	1.52	0.48	23.5	19351	375	1324	78.7
53 KK 17-2	6817	15.6	595	26.7	193	27.5	1.23	2.04	0.168	228	4.84	1.75	0.31	0.045	2.00	1.75	0.47	25.4	20031	370	1392	74.5
54 KK 20-14	3864	8.4	393	22.7	124	14.4	0.68	1.44	0.091	133	3.33	0.93	0.16	0.025	1.22	0.91	0.25	31.8	14774	335	1382	112.0
55 KK 25-4	5122	11.1	445	28.3	161	19.5	0.84	1.82	0.128	159	4.07	1.23	0.20	0.033	1.53	1.13	0.31	27.9	17993	352	1370	73.6
56 KK 31-9	5628	13.6	425	22.7	129	16.7	0.84	1.43	0.143	207	3.36	1.04	0.20	0.036	1.72	1.14	0.28	31.6	13202	364	1446	140.0
57 KK 31-12	5532	13.5	403	21.6	120	15.7	0.83	1.34	0.142	200	3.15	0.96	0.17	0.033	1.66	1.06	0.27	32.5	12644	330	1394	141.0
58 Pisces 158-4	14410	36.4	904	26.0	216	46.4	2.22	2.14	0.401	528	4.71	2.83	0.56	0.087	3.65	2.87	0.76	13.8	20356	387	1537	42.4
59 Pisces 158-5	6209	14.6	513	27.2	163	23.2	1.03	2.04	0.152	216	4.34	1.48	0.25	0.039	2.03	1.41	0.36	28.3	23891	628	1701	41.9
60 Pisces 186-3	3061	6.37	334	24.5	133	12.6	0.59	1.74	0.063	87	3.57	0.85	0.12	0.019	1.02	0.69	0.21	35.6	16152	349	1469	79.6
61 Pisces 187-1A	5495	13.2	413	20.3	117	17.4	0.82	1.38	0.143	197	3.13	1.11	0.20	0.037	1.63	1.09	0.28	35.3	14072	354	1449	222.0
62 Pisces 187-5B	4719	10.5	449	22.5	142	18.3	0.86	1.71	0.112	160	3.71	1.19	0.22	0.032	1.53	1.12	0.30	33.5	15923	334	1292	99.6
63 Pisces 187-8	3676	8.05	382	23.8	131	16.6	0.77	1.53	0.078	117	3.50	1.06	0.17	0.025	1.21	0.96	0.27	32.0	16100	363	1466	117.0
64 Pisces 187-9	3801	8.36	385	24.6	133	16.6	0.72	1.66	0.078	117	3.56	1.07	0.16	0.025	1.25	0.97	0.27	33.2	15958	331	1392	100.0

Table 2.2: Trace element (rare earth elements La-Lu) concentrations, in ppm

ID	Sample	La	Ce	Pr	Nd	Sm	Eu	Gd	Tb	Dy	Ho	Er	Tm	Yb	Lu
1	MIR 2335-2	17.2	41.3	5.50	24.9	5.89	2.01	5.89	0.86	5.09	0.93	2.53	0.32	2.01	0.29
2	MIR 2335-5	17.8	42.2	5.64	25.4	5.97	2.03	5.93	0.88	5.23	0.93	2.51	0.34	2.09	0.29
3	MIR 2335-6	18.4	45.2	5.86	26.1	6.09	2.08	6.00	0.88	5.09	0.94	2.48	0.33	2.02	0.28
4	MIR 2335-7	18.5	43.5	5.79	25.7	6.14	2.06	6.09	0.90	5.25	0.96	2.51	0.34	2.10	0.29
5	MIR 2335-8	18.4	44.7	5.83	26.0	6.11	2.06	5.91	0.86	5.04	0.92	2.48	0.32	2.07	0.28
6	MIR 2335-9	20.3	47.4	6.38	28.6	6.78	2.26	6.56	0.96	5.72	1.04	2.76	0.37	2.26	0.32
7	MIR 2335-10	18.4	45.0	5.87	26.1	6.18	2.07	5.90	0.88	5.07	0.94	2.47	0.32	2.04	0.28
8	MIR 2335-11	19.6	45.8	6.07	27.3	6.35	2.11	6.20	0.90	5.28	0.97	2.54	0.33	2.08	0.28
9	MIR 2335-12	13.9	36.2	4.50	20.1	4.62	1.67	4.70	0.68	4.10	0.74	1.97	0.26	1.60	0.22
10	MIR 2336-2	19.6	46.6	6.10	27.2	6.28	2.10	6.25	0.87	5.22	0.94	2.54	0.33	2.03	0.28
11	MIR 2336-4	14.5	35.4	4.85	22.6	5.57	1.91	5.77	0.85	5.12	0.92	2.52	0.32	1.99	0.28
12	MIR 2336-5	18.7	47.6	6.05	26.9	6.43	2.18	6.46	0.94	5.72	1.05	2.81	0.37	2.41	0.33
14	MIR 2337-2	13.5	32.6	4.48	21.0	5.22	1.78	5.35	0.79	4.80	0.87	2.37	0.31	1.95	0.27
15	MIR 2337-3	14.4	35.2	4.84	23.2	5.71	1.99	6.11	0.93	5.59	1.04	2.87	0.39	2.36	0.34
16	MIR 2338-1a	20	47.8	6.28	27.6	6.45	2.16	6.27	0.89	5.34	0.94	2.55	0.33	2.12	0.28
17	MIR 2340-1	13.4	32.6	4.42	20.5	5.12	1.79	5.22	0.78	4.72	0.84	2.31	0.30	1.87	0.26
18	MIR 2340-3	12.2	29.4	4.03	19.1	4.81	1.68	5.08	0.75	4.51	0.82	2.25	0.29	1.81	0.25
19	MIR 2341-1	19.4	45.5	6.20	28.5	6.91	2.31	7.37	1.03	6.19	1.14	3.06	0.40	2.48	0.34
20	MIR 2341-2	25.6	57.9	7.50	32.4	7.13	2.34	6.85	0.97	5.49	0.98	2.58	0.32	2.06	0.29
21	MIR 2343-2	19.2	44.9	6.20	28.2	6.73	2.29	6.67	0.96	5.65	1.02	2.67	0.34	2.12	0.29
22	MIR 2343-3	18	42.2	5.66	25.6	5.99	2.03	5.99	0.86	5.09	0.94	2.47	0.32	2.00	0.27
23	MIR 2343-4	17.8	42.5	5.69	25.4	6.07	2.01	6.03	0.87	5.06	0.93	2.48	0.31	2.00	0.28
24	MIR 2343-5	18.2	42.3	5.72	25.8	5.93	2.03	6.01	0.86	5.09	0.93	2.52	0.32	2.00	0.29
25	MIR 2343-6	23.9	54.3	7.04	31.1	7.00	2.31	6.64	0.92	5.12	0.90	2.30	0.29	1.79	0.25
26	MIR 2343-7	17.2	40.4	5.43	24.5	5.75	1.95	5.78	0.85	5.04	0.91	2.46	0.32	1.98	0.28
27	MIR 2343-8	17.6	41.5	5.56	24.8	5.90	2.00	5.77	0.84	4.92	0.91	2.38	0.31	1.95	0.27
28	MIR 2343-10	17.3	39.7	5.39	24.6	5.92	1.97	6.00	0.85	5.05	0.92	2.46	0.32	1.99	0.27
29	MIR 2343-11	18.4	42.5	5.71	26.0	6.06	2.02	6.02	0.88	5.13	0.93	2.53	0.32	2.02	0.29
30	MIR 2343-12	22	52.7	6.71	29.5	6.88	2.28	6.54	0.95	5.53	0.99	2.68	0.34	2.19	0.31
31	MIR 2343-13	22.6	52.2	6.97	31.1	7.19	2.38	7.33	1.05	6.09	1.10	2.94	0.38	2.42	0.33
32	Shinkai 490-8	15.9	37.6	5.22	24.4	5.93	2.02	6.26	0.92	5.57	1.04	2.75	0.36	2.24	0.32
33	Shinkai 494-1	21	52.5	6.91	30.6	7.16	2.41	6.88	0.99	5.68	1.03	2.72	0.34	2.17	0.29
34	Shinkai 494-2	20.7	49.1	6.58	30.2	7.11	2.36	7.04	1.00	5.85	1.05	2.78	0.36	2.16	0.31
35	Shinkai 494-3	28.5	62.5	8.21	35.9	7.78	2.53	7.45	1.04	5.99	1.06	2.77	0.35	2.19	0.30
36	Shinkai 494-4	26.7	62.5	7.96	34.3	7.51	2.45	7.10	0.99	5.64	0.99	2.65	0.33	2.09	0.28
37	Shinkai 494-5	13.9	34.0	4.84	23.2	5.83	2.04	6.36	0.95	5.66	1.08	2.84	0.38	2.38	0.35
38	Shinkai 494-6	12.2	30.3	4.26	20.7	5.38	1.87	5.81	0.89	5.45	1.00	2.78	0.36	2.27	0.32

## Trace Element concentrations in ppm, Rare Earth Elements (continued)

ID	Sample	La	Ce	Pr	Nd	Sm	Eu	Gd	Tb	Dy	Ho	Er	Tm	Yb	Lu
39	Shinkai 494-7	11.7	29.3	4.14	19.9	5.23	1.80	5.62	0.86	5.11	0.95	2.61	0.34	2.17	0.30
40	Shinkai 494-8	13.8	34.0	4.79	22.4	5.82	1.99	6.08	0.93	5.51	1.04	2.86	0.37	2.29	0.33
41	Shinkai 513-3	15.1	38.2	5.15	23.1	5.72	1.98	5.71	0.86	5.01	0.94	2.51	0.33	2.03	0.28
42	Shinkai 513-4A	20.6	49.5	6.45	29.4	6.92	2.31	6.97	1.03	6.18	1.14	3.08	0.40	2.60	0.36
43	Shinkai 513-5	15.6	37.4	5.10	23.6	5.85	1.99	6.13	0.91	5.59	1.02	2.78	0.36	2.30	0.32
44	Shinkai 513-6	15.8	38.0	5.15	23.4	5.80	1.99	6.14	0.91	5.46	1.01	2.76	0.36	2.31	0.32
45	Shinkai 513-7A	13.8	32.9	4.55	21.5	5.52	1.87	5.88	0.89	5.43	1.03	2.77	0.36	2.29	0.33
46	Shinkai 515-1	23.6	54.7	7.16	31.5	7.24	2.39	7.20	1.04	5.91	1.10	2.96	0.38	2.38	0.33
47	TUNE 003D-A	8.74	22.4	3.26	15.9	4.31	1.54	4.72	0.73	4.55	0.86	2.33	0.30	1.92	0.27
48	TUNE 003D-B	8.58	22.7	3.20	15.6	4.21	1.53	4.51	0.71	4.39	0.83	2.22	0.29	1.90	0.26
49	TUNE 003D-C	8.8	22.7	3.24	15.8	4.32	1.53	4.65	0.72	4.48	0.84	2.26	0.30	1.89	0.26
50	TUNE 004D-A	19.6	47.3	6.19	26.8	6.30	2.10	5.96	0.83	4.72	0.83	2.17	0.28	1.71	0.23
51	TUNE 004D-B	20.1	45.5	6.18	27.8	6.53	2.17	6.26	0.86	5.04	0.87	2.30	0.29	1.77	0.24
52	TUNE 004D-C	20.3	49.1	6.32	27.9	6.50	2.18	6.14	0.86	4.88	0.86	2.23	0.28	1.75	0.23
53	KK 17-2	23	54.7	7.17	31.4	6.88	2.36	6.85	0.97	5.54	0.96	2.52	0.33	1.95	0.27
54	KK 20-14	12.2	30.2	4.19	19.5	4.60	1.70	4.91	0.74	4.51	0.81	2.16	0.28	1.71	0.24
55	KK 25-4	16.4	38.4	5.46	25.5	6.09	2.07	6.28	0.95	5.70	1.04	2.83	0.37	2.34	0.33
56	KK 31-9	14.9	35.8	4.67	21.0	4.85	1.69	5.07	0.74	4.37	0.82	2.24	0.29	1.82	0.26
57	KK 31-12	14.5	32.8	4.42	20.3	4.73	1.64	4.97	0.74	4.43	0.82	2.25	0.29	1.82	0.26
58	Pisces 158-4	35.8	80.8	10.00	41.3	8.17	2.66	7.33	1.00	5.61	0.94	2.41	0.30	1.92	0.26
59	Pisces 158-5	18.5	44.5	5.85	26.5	6.22	2.17	6.31	0.89	5.28	0.96	2.41	0.31	1.98	0.27
60	Pisces 186-3	10.3	27.1	3.86	19.0	4.96	1.74	5.25	0.81	5.00	0.88	2.43	0.31	1.93	0.25
61	Pisces 187-1A	14	33.4	4.50	19.8	4.69	1.59	4.56	0.68	3.99	0.71	1.92	0.24	1.56	0.21
62	Pisces 187-5B	15.2	36.3	5.12	22.4	5.39	1.85	5.60	0.82	4.88	0.87	2.23	0.27	1.78	0.24
63	Pisces 187-8	13.5	33.8	4.49	20.3	4.95	1.76	5.26	0.79	4.70	0.85	2.30	0.30	1.86	0.26
64	Pisces 187-9	13.8	32.8	4.46	21.0	5.11	1.79	5.52	0.82	4.90	0.92	2.40	0.32	1.91	0.28

The primitive mantle (PM)-normalized trace element spidergram shows the entire lava suite exhibits sub-parallel patterns that are enriched in highly incompatible elements (Fig. 2.3). All rock types have similar abundance patterns with considerable overlap, and show relative enrichment in Rb, Ba, Th, Nb, Ta, and depletion in W, K, and Pb. Large ion lithophile element (LILE) enrichment occurs across the compositional groups, with

the lowest concentrations observed in tholeiites and highest concentrations in basanites (Fig 2.4).

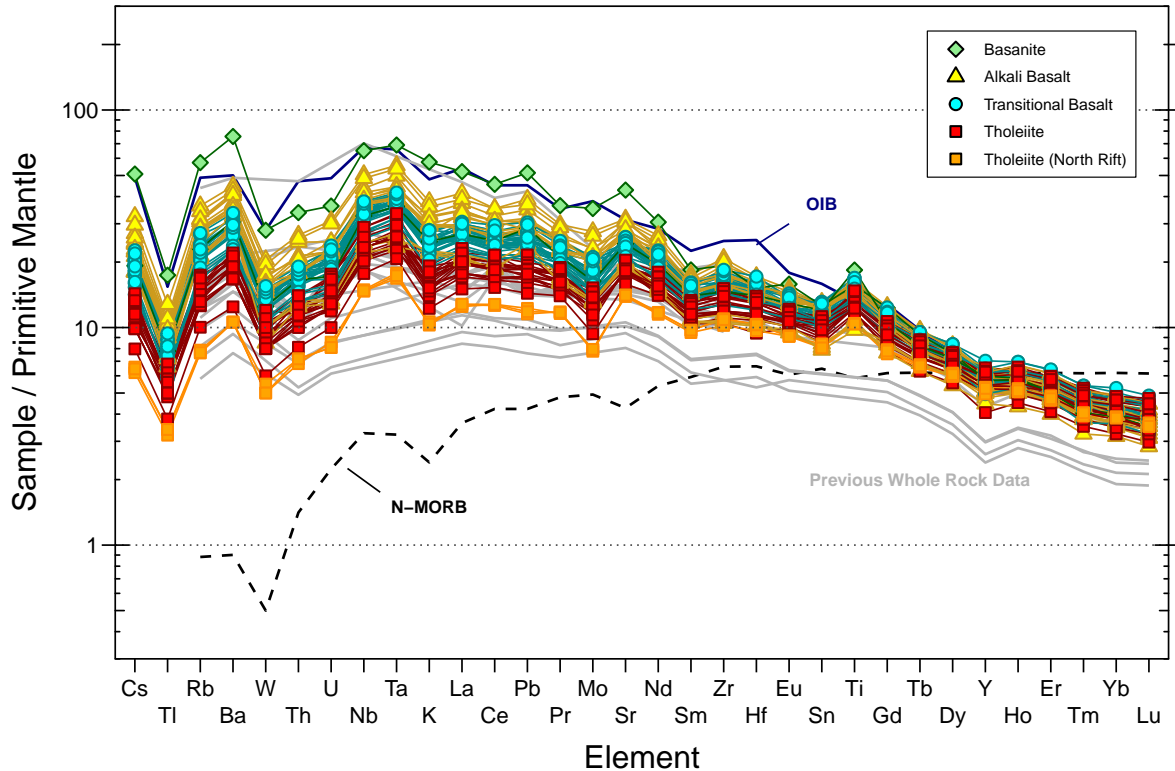


Figure 2.3: Spidergram of trace element compositions normalized by primitive mantle (Sun and McDonough, 1989). Previous whole rock data for similar samples from MIR/Shinkai dives at Kama'ehuakanaloa from Ren et al. (2009) and Garcia (unpub). Compositions for mantle endmembers ocean island basalt (OIB) and normal type MORB (N-MORB) (Sun and McDonough, 1989) shown.

Separation by rock types (but not by location, except for the North Rift) is shown in Figure 2.4. A basanite sample collected at the East Flank, P158-4, shows the largest enrichment of highly incompatible elements compared to primitive mantle (e.g. by a factor of 75 for Ba and 65 for Nb). Another basanite sample from the East Flank, P158-5

is  $\sim$ 30X enriched in Ba and Nb. Alkali basalts, transitional basalts, and tholeiites generally follow similar patterns, with decreasing enrichment in highly incompatible elements. North Rift tholeiite samples from TUNE-003D show the least enrichment in highly incompatible elements, by a factor of 10 for Ba and 15 for Nb compared to primitive mantle.

Trace element anomalies can be quantified by comparing concentrations with expected values (McLennan, 1989). Niobium (Nb), Tantalum (Ta), and Titanium (Ti) anomalies of primitive mantle normalized (pm) values (Sun and McDonough, 1989), are defined as  $Nb/Nb^* = Nb_{pm}/(Th_{pm} \times La_{pm})^{0.5}$ ,  $Ta/Ta^* = Ta_{pm}/(Th_{pm} \times La_{pm})^{0.5}$ , and  $Ti/Ti^* = Ti_{pm}/(Sm_{pm} \times Tb_{pm})^{0.5}$ , normalized to primitive mantle. Kama‘ehuakanaloa samples display positive Nb, Ta, Ti anomalies, with similar  $Nb/Nb^*$  (1.5-1.6),  $Ta/Ta^*$  (1.7-1.8), and  $Ti/Ti^*$  ( $\sim$ 1.3), consistent with positive “TITAN” anomalies observed at high- ${}^3\text{He}/{}^4\text{He}$  OIB localities (Jackson et al., 2008). Tholeiites generally exhibit the highest TITAN anomalies and alkali basalts exhibit the lowest values, although on average the highest  $Ti/Ti^*$  anomalies are observed in transitional basalts. The details are described further in light of Helium isotope correlations in Chapter 3.

Chondrite-normalized REE patterns of Kama‘ehuakanaloa glasses show light-REE (LREE) enrichment, between 35 and 130 times chondrites (Fig. 2.5). All samples show sub-parallel patterns that are consistent and overlap with previous studies of Kama‘ehuakanaloa basalts (Frey and Clague, 1983; Garcia et al., 1995, 1998; Wieser et al., 2020a). Figure 2.6 shows differences among major rock types. Basanites and alkali basalts show the highest enrichment in LREE relative to chondrites, while transitional basalts shows less (overlapping heavily with tholeiites). Heavy REE abundances span a narrower range

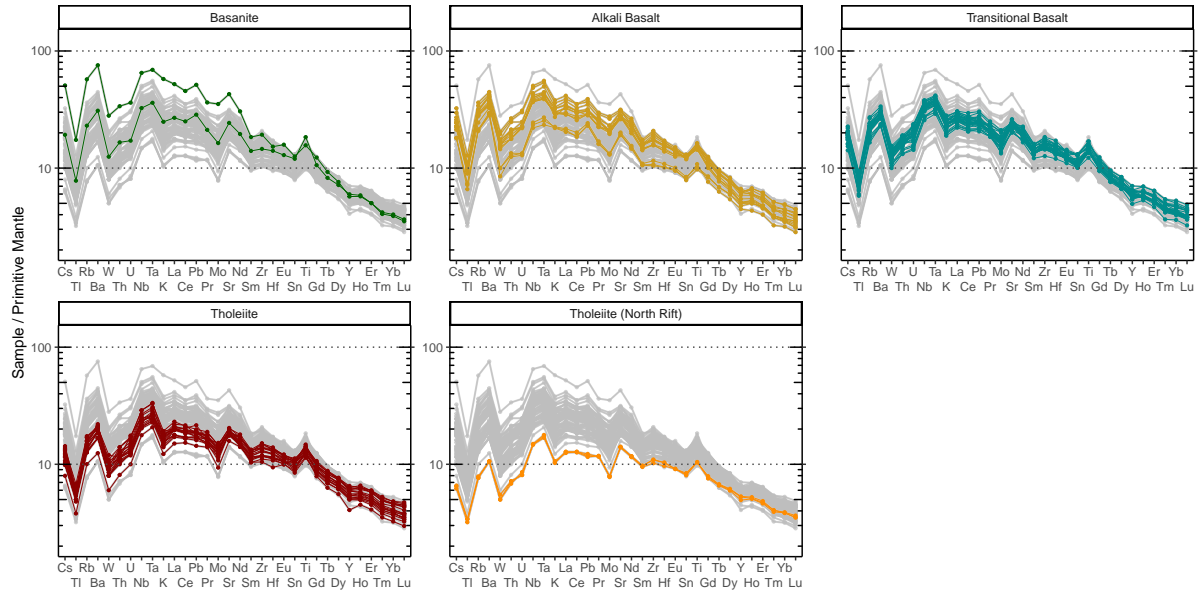


Figure 2.4: Spidergram of trace Element compositions normalized by primitive mantle (Sun and McDonough, 1989), shown for each rock type

of enrichment between  $\sim 8$  and 15 times chondritic abundances. Transitional basalts vary across the whole range of heavy rare earth elements.

In the following discussion about REE ratios, the subscript of "N" denotes chondrite-normalized values from Sun and McDonough (1989). All lavas are enriched in light REEs over heavy REEs with a range of  $(\text{La/Yb})_N$  ratios from  $\sim 5.0$ -8.5. More differentiated (lower MgO) alkali basalts show progressively steeper patterns, where tholeiites have average  $\text{La/Yb}_N = 4.8 \pm 1.0$  compared to transitional basalts ( $6.2 \pm 0.6$ ) and alkali basalts ( $8.5 \pm 0.9$ ). Average light to medium-REE slopes also slightly vary, with tholeiites having  $(\text{La/Sm})_N = 1.6 \pm 0.2$ , transitional basalts  $(\text{La/Sm})_N = 1.9 \pm 0.1$ , and alkalic basalts  $(\text{La/Sm})_N = 2.2 \pm 0.3$ . All samples show a slight positive  $\text{Eu/Eu}^*$  anomaly (McLennan, 1989), similar to the patterns for tholeiites and breccia glasses reported in

Garcia et al. (1995, 1998).

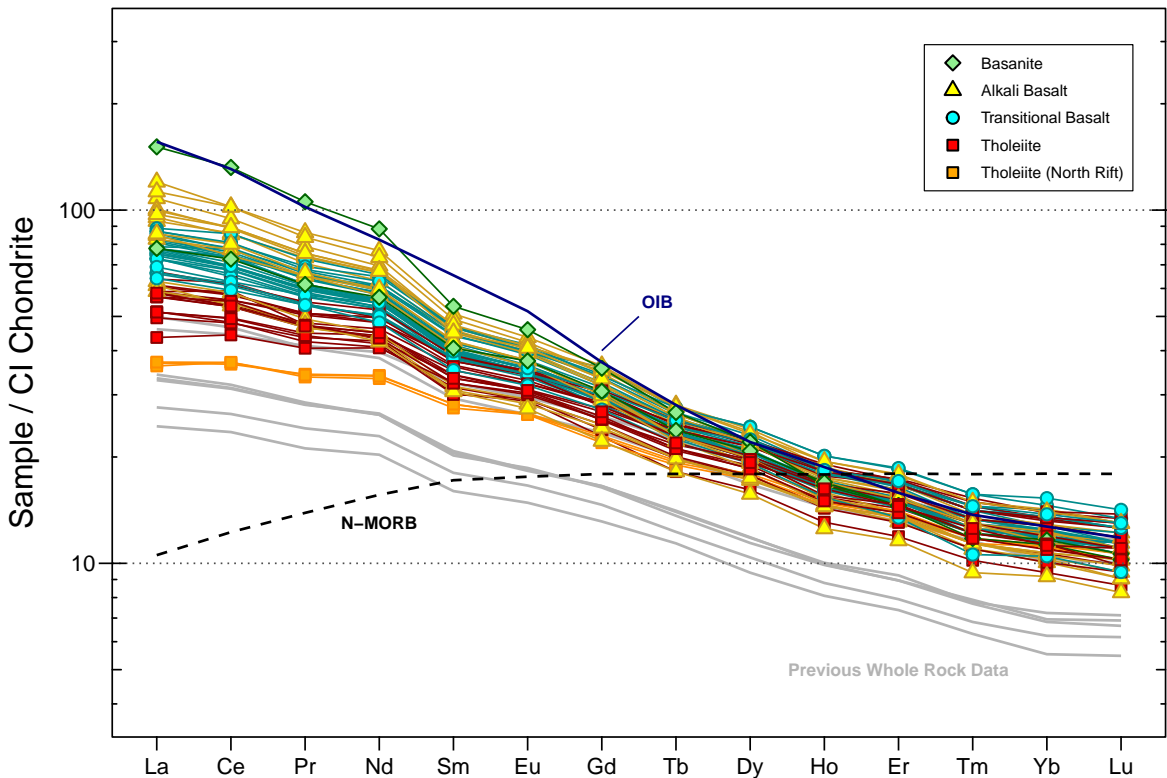


Figure 2.5: Rare Earth Element compositions normalized by C1 chondrite from (Sun and McDonough, 1989). Previous whole rock data for matching glass samples from Kama'ehuakanaloa MIR and Shinkai dives from Ren et al. (2009); Matvenkov and Sorokhtin (1998) and Garcia (unpublished). Compositions for mantle endmembers ocean island basalt (OIB) and normal type MORB (N-MORB) (Sun and McDonough, 1989) shown.

A comparison of North Rift tholeiites to the range of all other South rift basalts also reveals noticeably lower light rare earth elements compared to the least enriched South rift tholeiites (Fig 2.7).

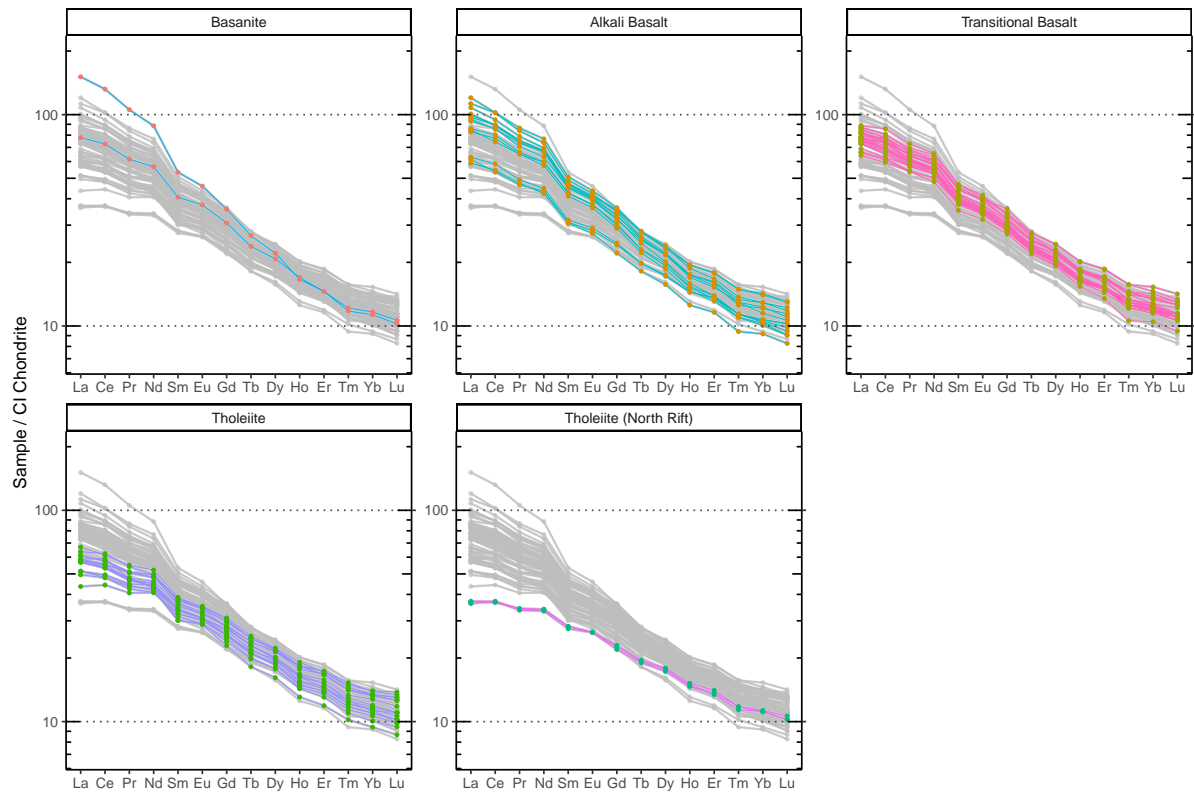


Figure 2.6: Rare Earth Element (REE) Values are normalized to C1 chondrite values from [Sun and McDonough \(1989\)](#). South Rift, Western Ridge, and East Flank samples are summarized as the major rock types (basanite, alkali basalt, transitional basalt, and tholeiites),

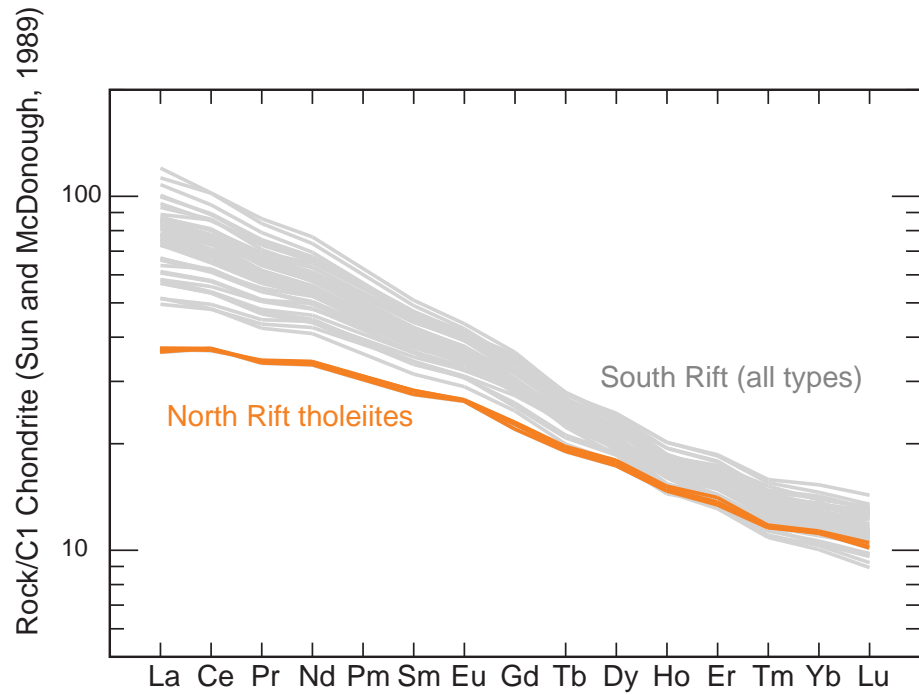


Figure 2.7: Rare Earth Element (REE) Values are normalized to C1 chondrite values from [Sun and McDonough \(1989\)](#). North Rift Tholeiites (TUNE dredge 3) are shown in orange compared to all South rift basalts shown in grey.

## 2.5 Discussion

### 2.5.1 Classification

#### 2.5.1.1 Alkaline vs. Transitional vs. Tholeiitic

Notably, previous whole rock data from the same rock samples as glass typically shows more subalkaline compositions (Figure 2.8). Tholeiites and alkali basalts typically show similar patterns. Whole rock values of transitional basalts differ from the glass compositions and rarely cross over to alkaline compositions. Glass compositions intersect with the line or higher. The whole rock values form an array parallel to the dividing line, trending from Si-undersaturated to Si-saturated, suggesting a similar magma series evolution as the alkali basalts. Studies at other early stage alkaline volcanoes like Mt. Etna (Clocchiatti et al., 1998) reveal similar differences between glass major element compositions and whole rock major elements.

Another confirmation of most transitional basalts having similar origins to alkali basalts comes from Bellieni et al. (1983) who defined fields to show percentages of likely classification in a given field of Total Alkalies vs. Silica. According to (Bellieni et al., 1983), transitional basalt samples in the overlap region (Fig 2.9) are 3X more likely to be alkali basalts than tholeiitic basalts. However, some attention is paid to transitional basalts that are on/near the border with tholeiitic basalts, especially Pisces 187-5B and some MIR 2335 dive samples. Hence, the most common rock type, transitional basalt, are likely to share petrogenetic origins with alkali basalts and are useful for evaluating the range of differentiation processes that have influenced tholeiite and alkalic basalt lava

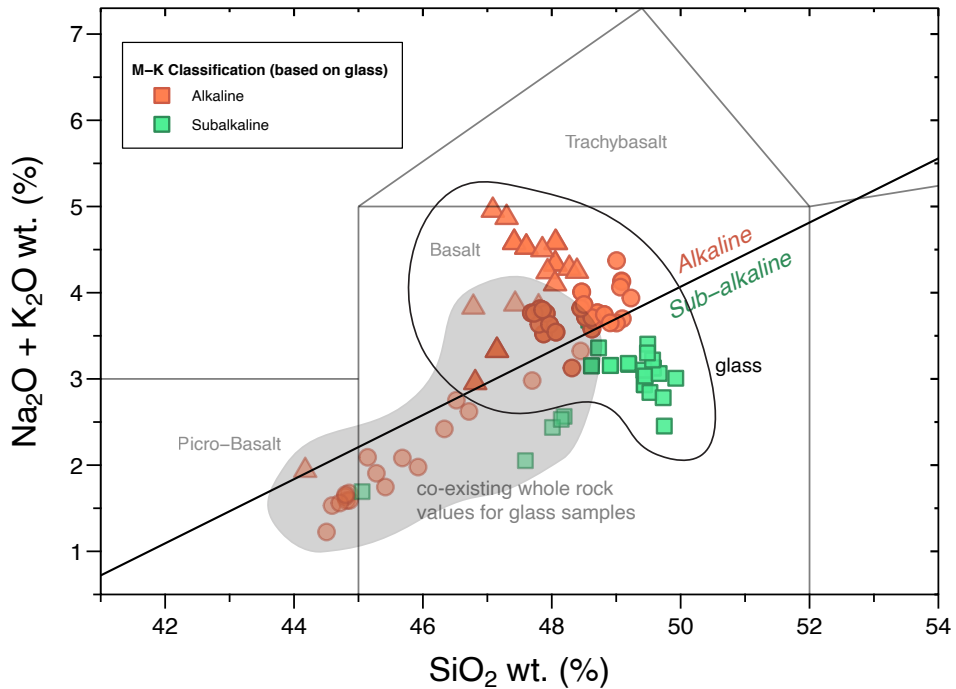


Figure 2.8: Total Alkalies vs. Silica (TAS) Diagram with major element oxides calculated to 100% on a volatile-free basis. The dividing line by Macdonald and Katsura (1964) is shown in a grey dashed line, indicating alkaline compositions above the line, transitional basalt compositions near the line, and tholeiite compositions below the line. Fields for classification are from Le Maitre et al. (2004). Samples in the basanite field have normative olivine >10%.

compositions at Kama‘ehuakanaloa.

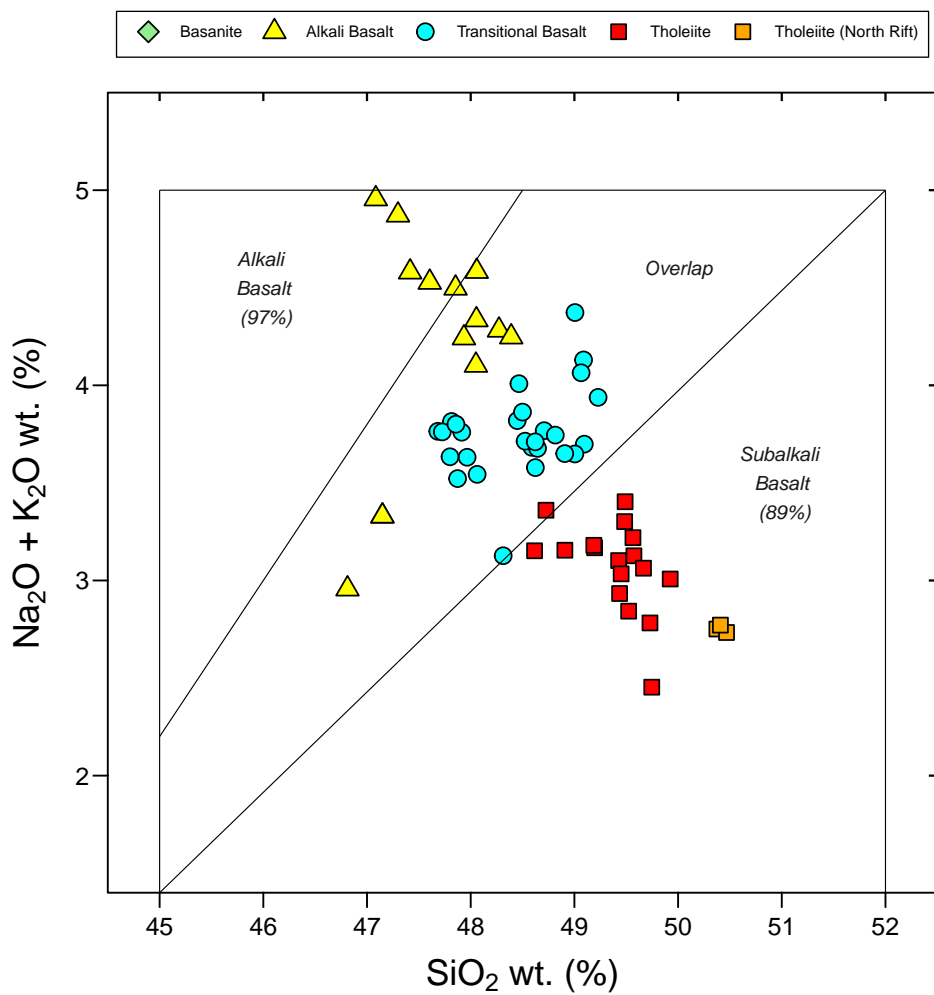


Figure 2.9: Total Alkalies vs. Silica and Transitional/Overlap Samples. Values are the same as Figure 2.1. Percentages in fields [Bellieni et al. \(1983\)](#) indicate the probability of classification of a sample in a given field. Samples in the “Overlap” region are 3X more likely to be alkali basalts than tholeiites.

## 2.5.2 Shallow Compositional Controls

### 2.5.2.1 Insights from whole rock vs. glass data

The differences observed between whole rock and glass major element data (Fig. 2.8 and 2.10) show likely crystallization effects between whole rock and glass, with the glass values being more evolved, higher in SiO<sub>2</sub> and lower in MgO. The relatively flat slope with MgO is consistent with the process of olivine removal from glass to whole rock. The patterns of CaO-Al<sub>2</sub>O<sub>3</sub> are consistent with clinopyroxene removal at MgO<6 wt. (%).

### 2.5.2.2 Crystal Fractionation

The deeply erupted south rift basalts at Kama‘ehuakanaloa seamount have witnessed a significant degree of crystallization during their evolution. Concentrations of Ni and Sc correlate with MgO, consistent with their removal by crystallization of olivine (Fig. 2.11). Olivine crystallization is a major control on melt compositional variation. Stratigraphically controlled datasets show mixing between crystallized olivines and host melts on sub-aerial and submarine Hawaiian shields (DePaolo and Stolper, 1996; Blichert-Toft et al., 2003). Few primitive samples have been found at Kama‘ehuakanaloa, and possible fractionation processes present a challenge to reconstructing the elemental concentrations in Kama‘ehuakanaloa parental magmas.

Magma crystallization is discussed through a framework of major element variations modeled using PETROLOG (Danyushevsky and Plechov, 2011). Fractional crystallization models for South Rift and North Rift samples were generated using PETROLOG

software (v. 3.1.1.3) from Danyushevsky and Plechov (2011). The Hawaiian primary tholeiitic melt composition ( $\text{MgO}=18$  wt.%) of Clague et al. (1991) and an initial/constant pressure of 2 kbar were used for the calculation. In-software parameters include olivine and clinopyroxene mineral-melt models from Weaver and Langmuir (1990), QFM buffer of oxygen fugacity from Kress and Carmichael (1988), melt density model from Lange and Carmichael (1987), and melt viscosity model from Bottinga and Weill (1972). Results were generated in 5% increments until stopping calculations at 50% crystallization.

Crystal fractionation has extensively modified Kama‘ehuakanaloa submarine basalts. Comparing calculated liquid lines of descent for multi-phase systems (olivine, clinopyroxene, plagioclase) to model results shows that this study’s sample compositions cannot be produced by fractionation of olivine alone (Garcia et al., 2006). According to the model, olivine crystallizes beginning at  $1445^{\circ}\text{C}$ , with clinopyroxene joining at  $\text{MgO} \sim 6.1$  wt.% at  $1141^{\circ}\text{C}$ , similar to temperatures determined by clinopyroxene-melt thermobarometry by Garcia et al. (1998) for breccia glass from the 1996 summit eruption. The least evolved South Rift basalt glasses of this study ( $\text{MgO}=7.5$  wt.%) are consistent with  $\sim 30\%$  crystallization of a primary tholeiite magma (Fig. 2.12), whereas the more evolved compositions between  $\text{MgO} = 5.0\text{-}7.5$  wt.%, have an estimated total crystallization of 35%. Overall, samples showing the best fit with the model are tholeiite samples (especially from the North Rift), whereas transitional basalt samples from the South Rift variably show agreement for some oxides.

In detail, many South Rift samples show elevated  $\text{CaO}$ ,  $\text{FeO}$ ,  $\text{TiO}_2$  and  $\text{K}_2\text{O}$  compared to the model calculations. Elevated  $\text{FeO}$  in low  $\text{SiO}_2$  lavas was also observed in submarine Mauna Kea samples from HSDP2 (Stolper et al., 2004). A slight inflection

at  $\text{MgO} < 7$  wt.% and a positive  $\text{CaO}/\text{Al}_2\text{O}_3 - \text{MgO}$  trend (Fig. 2.12) is consistent with co-precipitation of plagioclase and clinopyroxene, although they are not observed as phenocrysts. Overall, major element abundances suggest the glasses likely experienced higher pressure fractionation of pyroxene (Garcia et al., 1995).

The difference of crystallization between  $\text{MgO} = 7.5$  wt% to 5.0 wt. % encompasses an additional 20% crystallization of olivine, and to a lesser extent, clinopyroxene. Crystallization accounts for a fraction of the observed range in some oxides, especially  $\text{K}_2\text{O}$ ,  $\text{TiO}_2$  and  $\text{P}_2\text{O}_5$ , but does not account of the observed range in ratios such as  $\text{K}/\text{Ti}$  (Fig. 2.17). The lavas overall form an apparent negative trend between  $\text{K}/\text{Ti}$  vs.  $\text{MgO}$ , but the individual rock types do not. There is evidence of  $\text{K}/\text{Ti}$  ratios to discriminate for different degrees of partial melting, potentially from a range of mantle source compositions (Frey and Clague, 1983), e.g. enrichment in OIB relative to MORB, with higher  $\text{K}/\text{Ti}$  in OIB because of the presence of enriched mantle components in the source region. The next section will evaluate indicators of mantle source composition in the study suite.

### 2.5.3 Deep Source Compositional Controls

In contrast the major/minor elements discussed above, ratios of highly incompatible elements should not be significantly influenced by the crystallization that has occurred in the lavas, and therefore provide reliable indicators of mantle source values. Strong correlations between incompatible element pairs are present, e.g. Rb-Ba ( $r=0.994$ ) and Nb-Ta ( $r=0.990$ ). Other examples of highly correlated trace element pairs ( $r>0.96$ ) include Rb, Ba, Th, Tl, W and La with Nb, Cs, K, La with Rb, and Mo with Pb.

Table 2.3 displays selected pairs of incompatible elements in South Rift lavas and group statistics: Rb/Sr, Nb/Zr, Zr/Y, Rb/Nb, Ba/Nb, La/Sm, La/Yb and Tb/Yb. Box plots show how trace element ratios discriminate among three rock types in South Rift lavas (Fig 2.14).

Table 2.3: Trace Element Ratios that do correlate for South Rift lavas

Rock		Rb/Sr		Rb/Nb		Ba/Nb		La/Sm		La/Yb		Tb/Yb	
Type <sup>[1]</sup>	n	$\bar{x}$ <sup>[2]</sup>	$2\sigma$ <sup>[3]</sup>	$\bar{x}$	$2\sigma$								
AB	10	0.03	0.003	0.66	0.04	9.24	0.76	3.31	0.44	11.50	2.78	0.47	0.05
TB	26	0.03	0.005	0.60	0.05	8.45	0.68	2.95	0.24	8.67	1.66	0.43	0.04
TH	14	0.02	0.004	0.56	0.08	8.13	1.64	2.54	0.39	6.66	1.84	0.41	0.03

Rock		Nb/Zr		Nb/Y		Zr/Hf		Zr/Ti		Zr/Y	
Type	n	$\bar{x}$	$2\sigma$								
AB	10	0.15	0.01	1.11	0.21	41.4	3.00	0.010	0.001	7.53	0.98
TR	26	0.13	0.01	0.86	0.17	40.0	2.03	0.010	0.001	6.54	0.78
TH	14	0.12	0.03	0.67	0.22	38.7	2.15	0.009	0.001	5.74	0.60

<sup>[1]</sup> Rock types are abbreviated to AB = Alkali Basalt, TR = Transitional Basalt, and TH = Tholeiite Basalt

<sup>[2]</sup> Value for the mean, computed for each rock group

<sup>[3]</sup> Value for  $2\times$  computed standard deviation.

Though some ratios show distinct values across rock types, other trace element ratios, e.g. with U and high field strength elements do not effectively discriminate among the major rock types in South Rift lavas (n=50), where the range of alkali, transitional, and tholeiite basalt compositions often overlap. For example, Th/U, Nb/U, Ce/Pb and Ba/Rb are poor discriminants between the rock types (Table 2.4).

Table 2.4: Trace Element Ratios that do not correlate for South Rift lavas

Rock		Th/U		Ce/Pb		Nb/U		Nb/Ta		La/Nb		Th/La	
Type [1]	n	$\bar{x}$ [2]	$2\sigma$ [3]	$\bar{x}$	$2\sigma$								
AB	10	3.51	0.60	23.7	1.59	57.3	4.65	16.0	0.84	0.79	0.06	0.08	0.007
TB	26	3.57	0.59	25.0	2.70	58.4	5.64	15.6	1.06	0.78	0.07	0.08	0.009
TH	14	3.38	0.53	25.6	3.06	57.1	5.32	15.5	1.55	0.80	0.08	0.07	0.006

Rock		Ba/Rb		Rb/K		Mo/W		Ba/W		Rb/Tl		Pb/Tl	
Type	n	$\bar{x}$	$2\sigma$										
AB	10	13.9	0.80	0.002	0	4.17	0.35	802	55.3	383	34.7	44.7	4.03
TR	26	14.2	0.76	0.002	0	4.09	0.45	765	73.4	362	47.9	45.5	6.61
TH	14	14.6	1.63	0.002	0	4.47	0.55	743	142.0	337	49.4	46.3	4.22

[1] Rock types are abbreviated to AB = Alkali Basalt, TR = Transitional Basalt, and TH = Tholeiite Basalt

[2] Value for the mean, computed for each rock group

[3] Value for  $2 \times$  computed standard deviation.

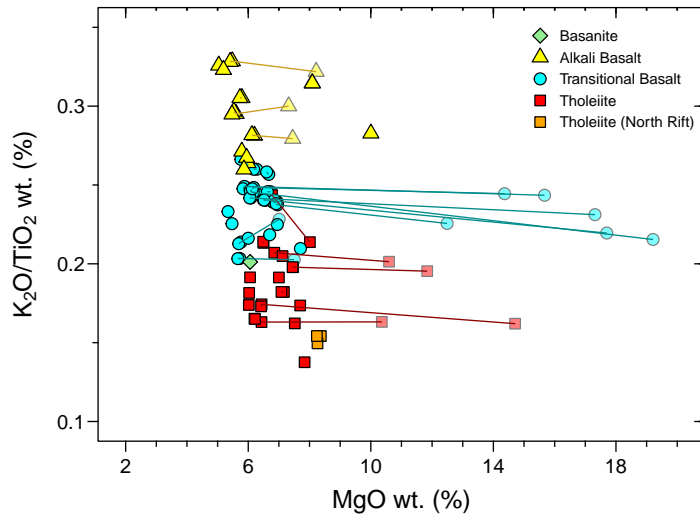
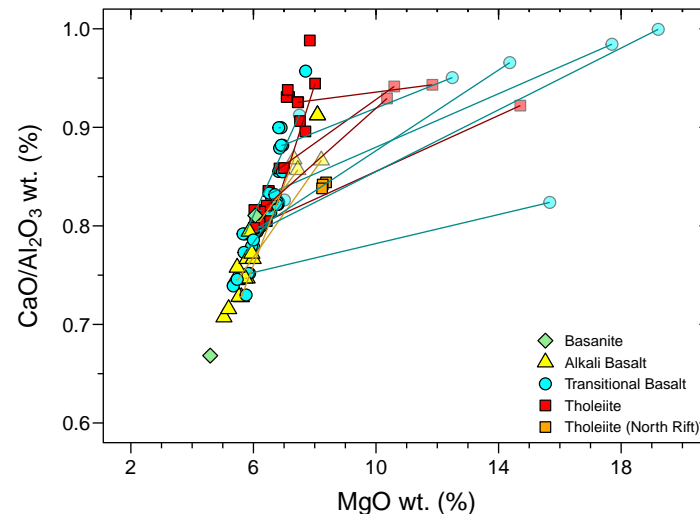
(a)  $K_2O/Al_2O_3$  vs.  $MgO$  wt. (%) for glass and whole rock.(b)  $CaO/Al_2O_3$  vs.  $MgO$  wt. (%)

Figure 2.10: Whole Rock and Glass Major Element Comparison. All data are shown in the same symbols indicating rock type based on glass. Symbols representing whole rock are more transparent than symbols for glass. Lines connecting available geochemical data of specific samples are shown. Data from this study, (Matvenkov and Sorokhtin, 1998; Ren et al., 2009) and Garcia (unpublished).

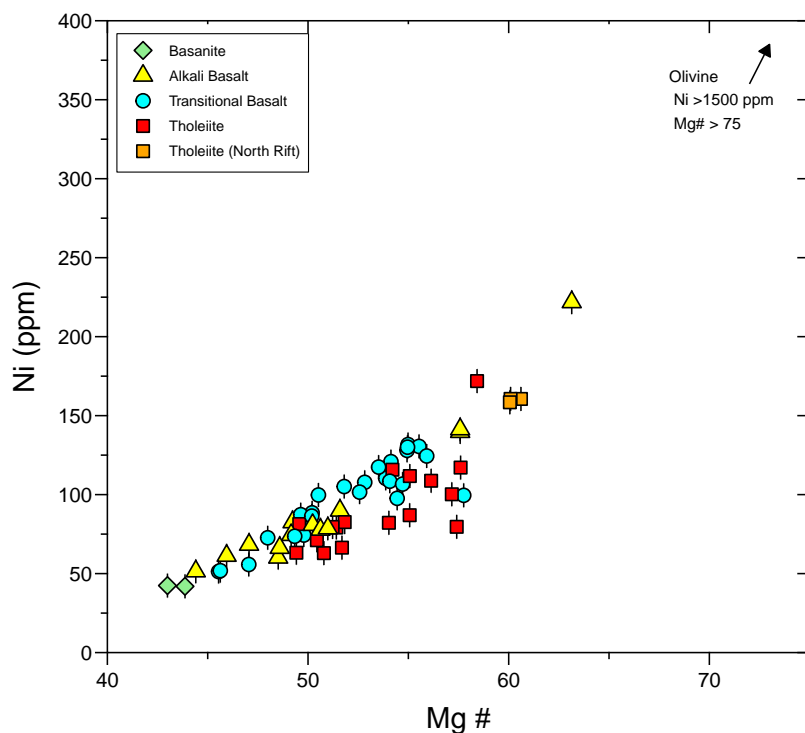


Figure 2.11: Ni (ppm) vs. Mg # (Number) of basaltic glasses from this study. Samples generally show linear relationship to high MgO and Ni (ppm) of olivine from Kama'ehuakanaloa lavas (GEOROC, <http://georoc.mpchmainz.gwdg.de/georoc/>)

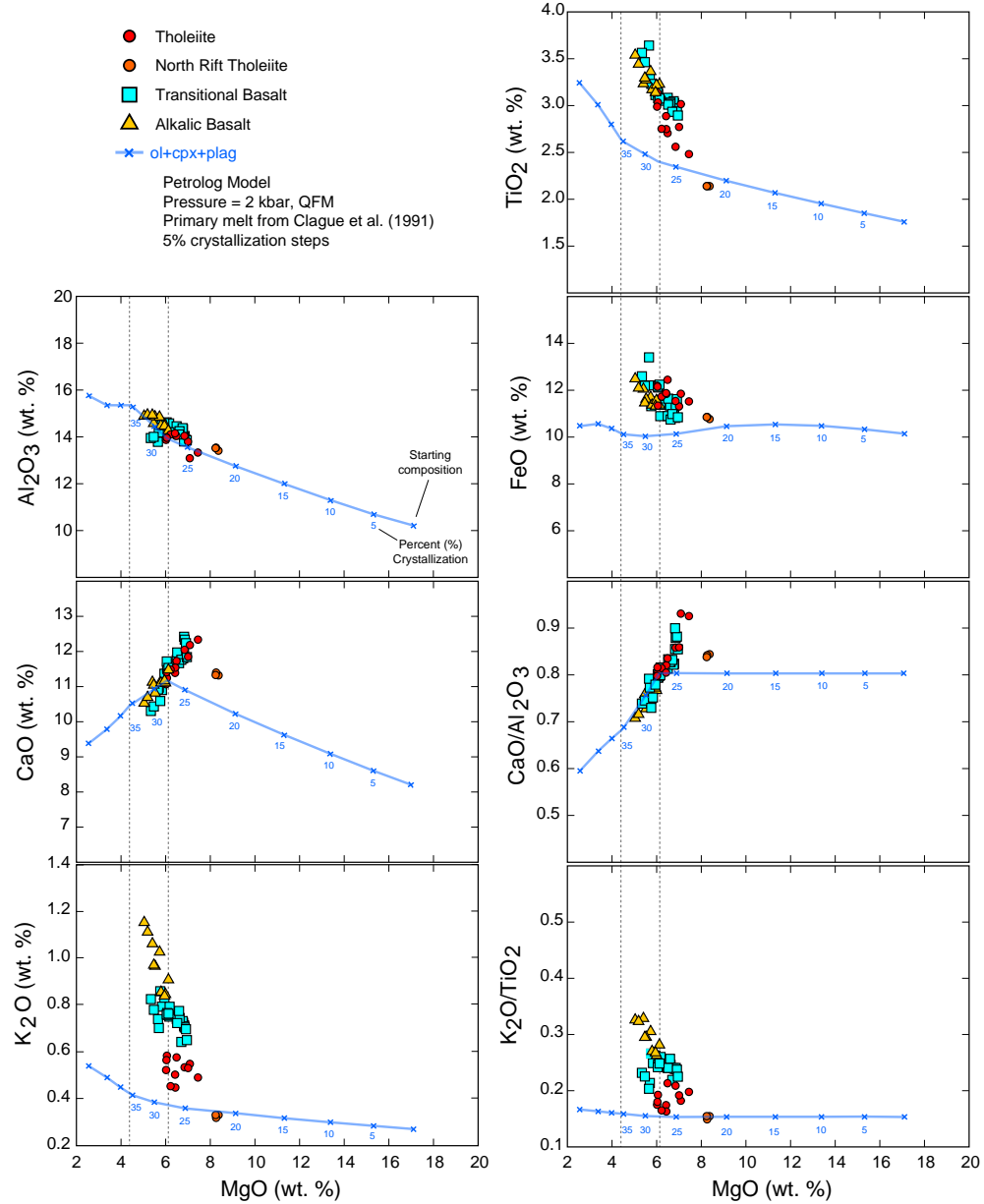
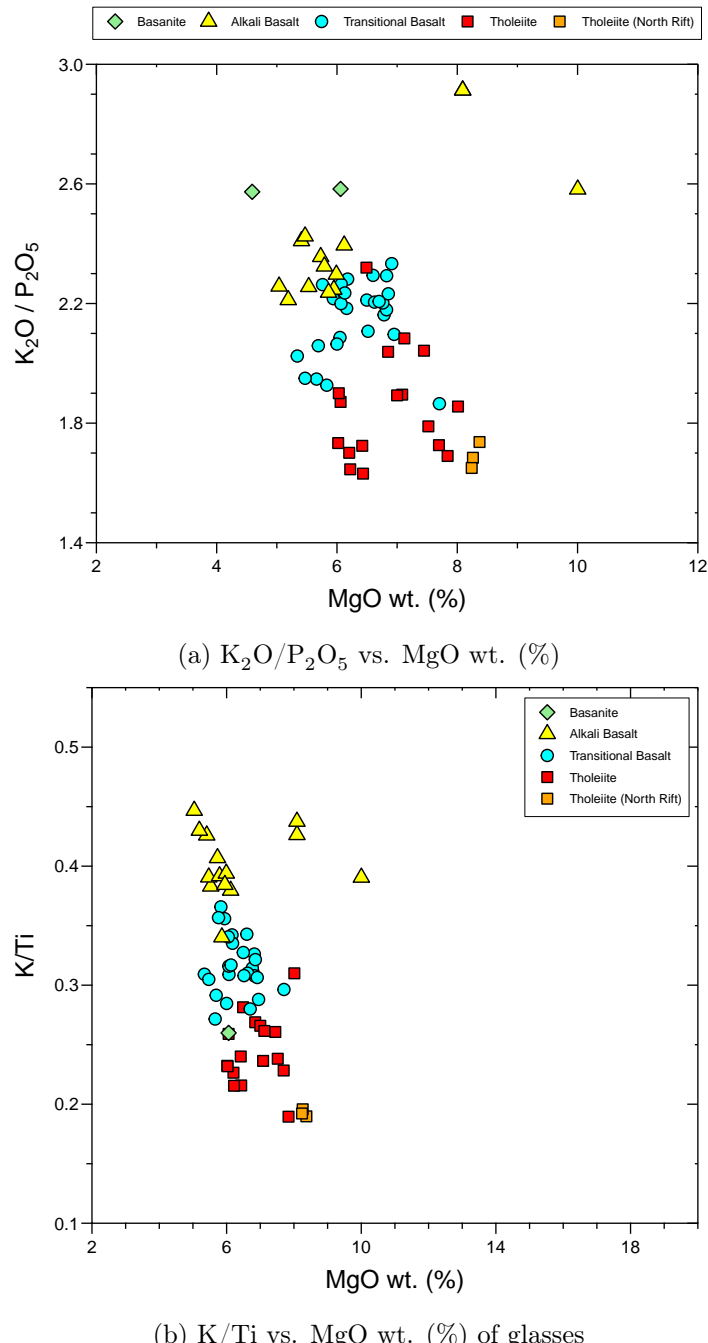


Figure 2.12: Fractional crystallization model produced in PETROLOG (Danyushevsky and Plechov, 2011). Starting composition from primary picritic melt composition from Clague et al. (1991). Model parameters were set to pressure of 2 kbar, oxygen fugacity at QFM, and 5% crystallization steps

Figure 2.13:  $\text{K}_2\text{O}/\text{P}_2\text{O}_5$  and  $\text{K}/\text{Ti}$  vs.  $\text{MgO}$  wt. (%)

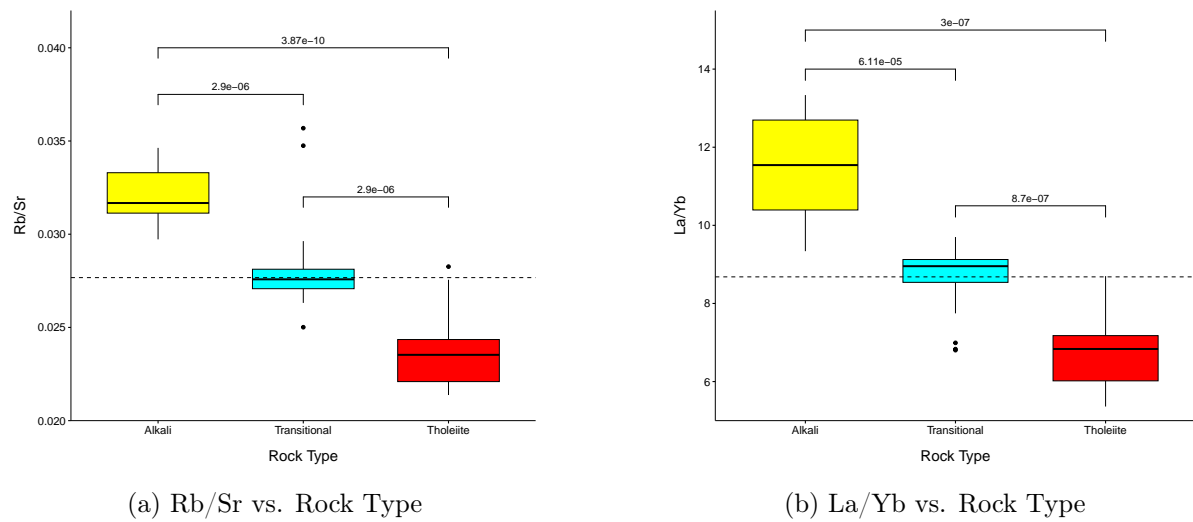


Figure 2.14: Boxplots showing t-test results and p-statistics for means, upper and low confidence intervals for various trace element ratios that are effective discriminants of South Rift lava types. Statistics shown for (a) Rb/Sr, (b) La/Yb vs. Rock Type in South Rift lavas, where Alkali basalts ( $n=10$ ) are shown in yellow, transitional basalts ( $n=26$ ) in cyan, and tholeiite basalts ( $n=14$ ) in red. Black dots are outliers, otherwise, specific points are not shown for each range. Narrow bracketed values are p-values comparing means of alkali-transitional basalt group pairs, and transitional-tholeiite basalt group pairs, respectively. Wide bracketed values are p-values comparing means of alkali-tholeiite basalt group pairs.

One way to assess overall geochemical trends at Kama‘ehuakanaloa in comparison to global OIB is to evaluate canonical mantle values for trace element ratios in MORB and OIB, e.g.  $\text{Ce}/\text{Pb} = 25\text{-}27$  and  $\text{Nb}/\text{U} = 25\pm 5$ ) (Hofmann et al., 1986). In this sample suite,  $\text{Nb}/\text{U}$  ranges from 58-61, deviating from canonical mantle values ( $47\pm 10$ ) (Hofmann et al., 1986). Elevated  $\text{Nb}/\text{U}$  may indicate retention of Nb in Ti oxides (like rutile phases) in subducted oceanic crust, which is further supported by positive  $\text{Ti}/\text{Ti}^*$ ,  $\text{Ta}/\text{Ta}^*$  and  $\text{Nb}/\text{Nb}^*$  anomalies in this suite. In addition, petrogenesis models of Hawaiian tholeiites suggest a higher amount of recycled crust in Kama‘ehuakanaloa’s mantle source compared to Kīlauea and Mauna Loa (Pietruszka et al., 2013). This is consistent with our finding of elevated  $\text{Nb}/\text{U}\sim 58$  relative to typical mantle ratio ( $47\pm 10$ ) (Hofmann et al., 1986). In general, this sample suite overlaps with typical global OIB  $\text{Nb}/\text{U}$ , including the lowest Nb samples (North Rift Tholeiites) (Fig. 2.15). A similar  $\text{Th}/\text{U}\sim 3.45\text{-}3.49$  for South Rift and North rift tholeiites suggests sources with similar extents of U+Th depletion. Overall, trace element ratio of diverse Kama‘ehuakanaloa lavas are consistent with a similar source that is closer to OIB than to MORB and experienced similar depletion events, despite the range of trace element concentrations.

A broader examination of trace element ratios at all Kama‘ehuakanaloa locations shows that  $\text{Rb}/\text{Sr}$  correlates with  $\text{K}_2\text{O}/\text{P}_2\text{O}_5$ . Variability within the brief stratigraphic sequence of East Flank lavas shows variation in trace element ratios like  $\text{Rb}/\text{Sr}$  (Fig. 2.16). Notably, some South Rift transitional basalts show the highest  $\text{Rb}/\text{Sr}$ , suggesting more crustal interaction compared to some alkalic basalts (Hofmann, 1988). Moderately compatible element ratios, e.g.  $\text{Sm}/\text{Yb}$  also shows correlations with  $\text{K}_2\text{O}/\text{P}_2\text{O}_5$  (Fig. 2.17).

$\text{Sm}/\text{Yb}$  ratios of oceanic lavas have been used as a proxy for lithospheric thickness

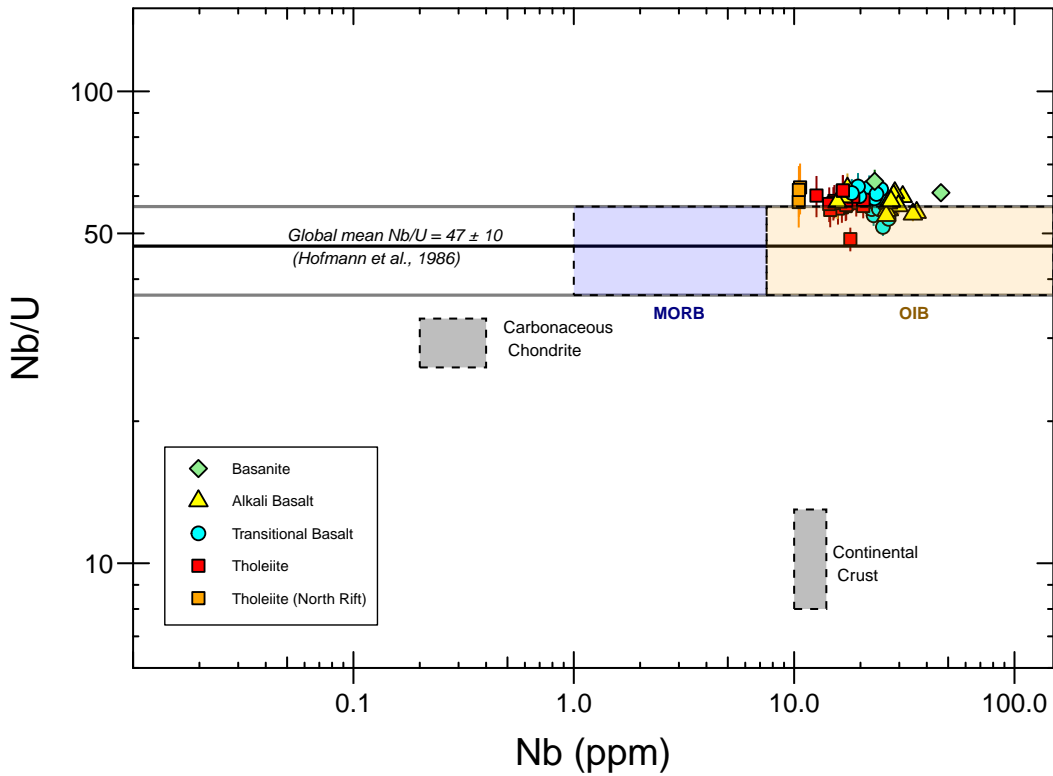


Figure 2.15: Nb/U vs. Nb (ppm) shown relative to values from [Hofmann et al. \(1986\)](#): Global mean  $\text{Nb}/\text{U} = 47 \pm 10$  ( $1\sigma$ ) shown with mean in bold line. The range of typical MORB and OIB values, range of carbonaceous chondrite, and continental crust values from [Hofmann et al. \(1986\)](#) are shown in dashed rectangles.

and estimating the depth of the lithosphere-asthenosphere boundary ([Niu et al., 2011](#); [Wu et al., 2018](#)). In this study, higher Sm/Yb is interpreted as higher pressure of melting under greater lithospheric thickness. Figure 2.17 shows that alkalic basalts and basanites exhibit higher Sm/Yb compared to tholeiites at the same locations. East Flank samples show a restricted range of Sm/Yb. A dredged Western Ridge alkalic basalt exhibits low Sm/Yb similar to North Rift tholeiites, but otherwise shares similar enrichment with other alkalic lavas. The Western Ridge is off axis away from the main rift zones,

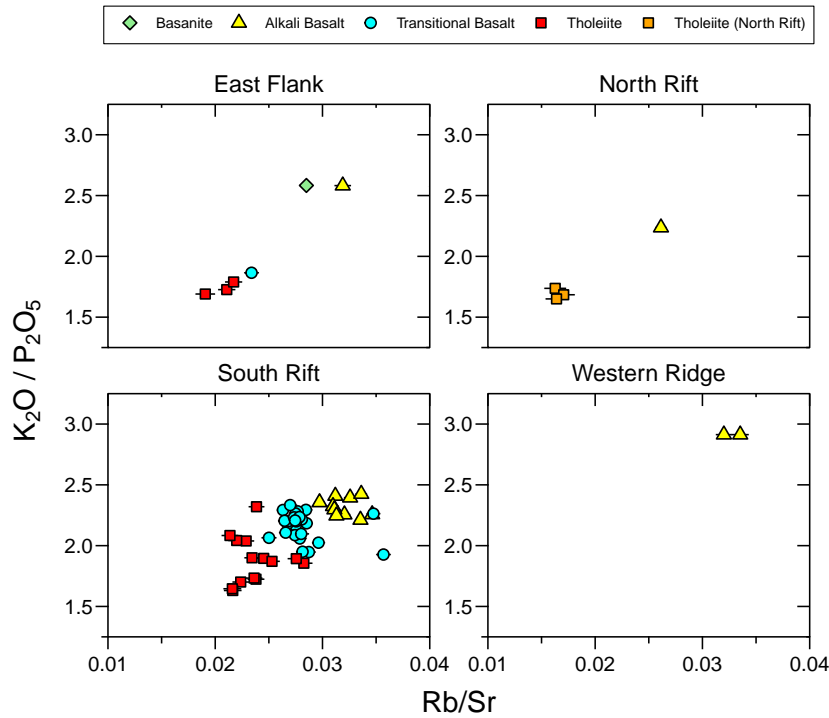


Figure 2.16:  $\text{K}_2\text{O}/\text{P}_2\text{O}_5$  vs.  $\text{Rb}/\text{Sr}$

hence, the lack of underlying intrusive material may produce less subsidence, accounting for shallow alkalic lava eruption. Furthermore, basanite, alkalic basalt, and transitional basalt Sm/Yb is elevated and separated from tholeiite values. South Rift transitional basalts overlap with tholeiites, and South Rift alkalic basalts vary to high Sm/Yb at a uniform  $\text{K}_2\text{O}/\text{P}_2\text{O}_5$ .

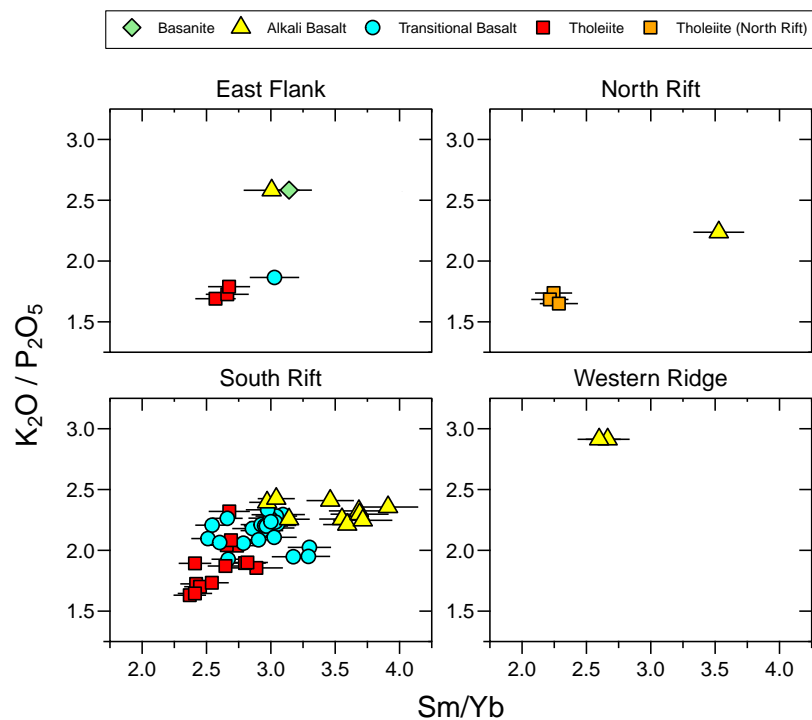


Figure 2.17:  $K_2O / P_2O_5$  vs.  $Sm/Yb$  for all Kama'ehuakanaloa locations and rock types.

### 2.5.3.1 Partial Melting and Mantle Source Lithology

Enrichment of large ion lithophile elements (LILE), and high ratios between light rare earth element (LREE) or medium rare earth elements (MREE) to heavy rare earth elements (HREE) are a common observation of intraplate oceanic lavas, especially at the Hawaiian Islands ([Clague and Frey, 1982](#)). Process identification diagrams ([Allègre and Minster, 1978](#)) with highly incompatible and relatively compatible elements can be used to evaluate source controls on trace element variation. La/Sm ratios compared to La contents exhibit a continuous trend between the entire suite (Fig. [2.18](#)), showing the role of partial melting and petrogenesis from a common source. At La  $\sim$ 15 ppm, East Flank alkalic basalts and South Rift tholeiites overlap in La contents but display higher La/Sm, which may indicate mixing between different sources. Overall, the dominant controls on the composition of the study suite during petrogenesis are variable degrees of partial melting of a common source, with some mixing between heterogeneous but similar sources.

To constrain differences in extent of source melting, the behavior of LREE (e.g. La) or MREE (e.g. Tb or Dy) to HREE (e.g. Yb) can be used to constrain mantle source lithology ([Feigenson et al., 2003](#)). Large variation in the ratio of Dy/Yb results from fractionation of Yb, which is highly compatible in garnet, and to a lesser extent, in clinopyroxene ([Blundy et al., 1998](#)). Such differences are observed in this study suite, most pronounced in the difference between alkaline and tholeiitic compositions (Fig. [2.6](#)) can be used to assess for differences in melting and the presence of residual garnet in the mantle source ([Clague and Frey, 1982; Sun and McDonough, 1989](#)).

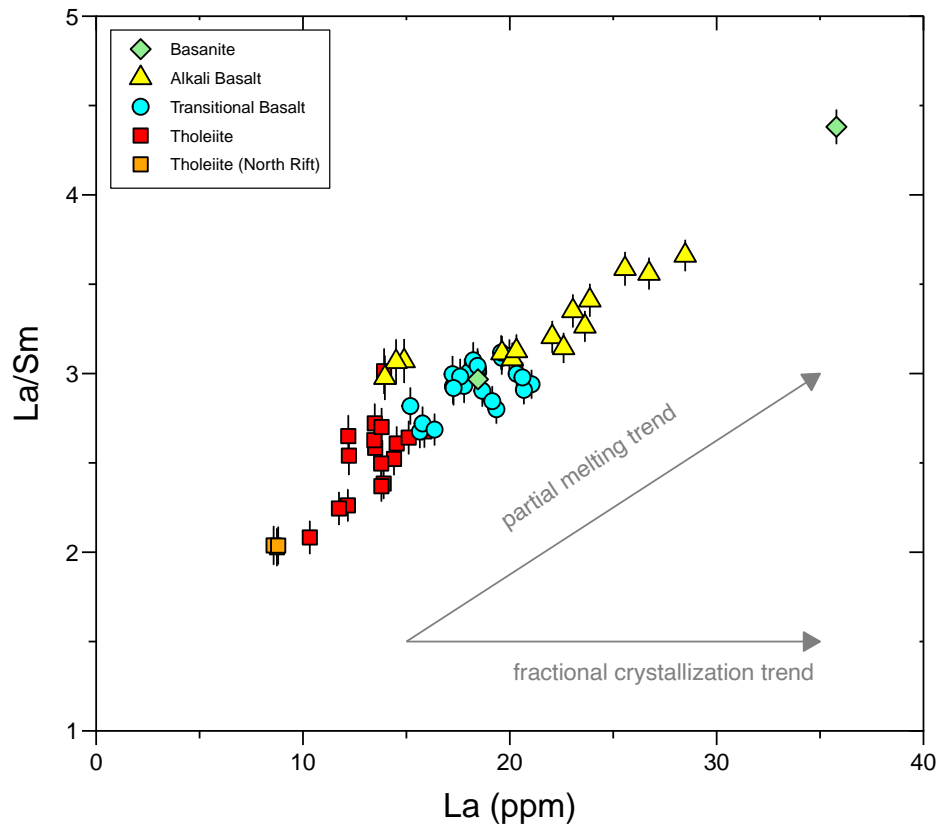


Figure 2.18: La/Sm vs. La (ppm) compositions, unnormalized

To assess if the Kama‘ehuakanaloa suite can be produced by varying fraction of melting of a garnet-bearing source and a shallower, spinel-bearing source, trace element compositions were compared to model calculations of non-modal equilibrium batch melting of mantle sources. The choice of non-modal melting reflects the likelihood that the proportion of mantle minerals and partition coefficients of trace elements will change as mantle melting proceeds during petrogenesis of Kama‘ehuakanaloa lavas. To calculate the concentration of each element in a resulting liquid from non-modal batch melting,

Equation 2.1 from Shaw (1970) was used:

$$\frac{C^l}{C^0} = \frac{1}{D_0 + F(1 - P)} \quad (2.1)$$

Explanation of the parameters used in Equation 2.1 are as follows:  $C^l$  = concentration of liquid,  $C^0$  = concentration of the source,  $D_0$  = Initial bulk distribution coefficient (Gast, 1968; Shaw, 1970),  $F$  = extent of melting as a percentage or fraction,  $P$  = melt reaction coefficient of each mineral. The source composition of primitive mantle from (Sun and McDonough, 1989) was used for  $C_0$  and partition coefficients for rare earth elements in mantle minerals are shown in Table 2.5 and used to calculate bulk  $D_0$ . Mineral modal abundances for garnet lherzolite and spinel lherzolite and resulting sum for D and P values are shown in Table 2.6.

Table 2.5: Partition Coefficients for Melting Model

Element	$C_0$ (ppm)	$D_{\text{ol}}$	$D_{\text{opx}}$	$D_{\text{cpx}}$	$D_{\text{gt}}$	$D_{\text{sp}}$
La	0.687	0	0.003	0.054	0.001	0.010
Tb	0.108	0.002	0.019	0.310	0.750	0.010
Dy	0.737	0.004	0.060	0.380	2.200	0.002
Yb	0.493	0.023	0.100	0.400	6.600	0.005

Concentrations of elements in primitive mantle are values from Sun and McDonough (1989). Partition coefficient  $D = (D_{\text{solid}}/D_{\text{melt}})$ . Values for partition coefficients from (Halliday et al., 1995; McKenzie and O’Nions, 1991; Johnson, 1998). Mineral abbreviations are as follows: ol = Olivine, opx = Orthopyroxene, cpx = Clinopyroxene, gt = Garnet, sp = Spinel.

Results showing primitive mantle normalized (Sun and McDonough, 1989) ratios of  $\text{Dy/Yb}_N$  and  $\text{La/Yb}_N$  within a range of modeled melt curves are shown in Figure 2.19. Solid tie lines indicate mixing between small fractions ( $F = 2, 4, 5, \text{ and } 10\%$ ) from the garnet lherzolite mantle with  $F = 10\%$  melting of spinel lherzolite. Note that tholeiite

Table 2.6: Modal Abundances and Melt Reaction Coefficients for Melting Model

Source	$X_{\text{ol}}$	$X_{\text{opx}}$	$X_{\text{cpx}}$	$X_{\text{gt}}$	$X_{\text{sp}}$	$\Sigma D_0$	$P_{\text{ol}}$	$P_{\text{opx}}$	$P_{\text{cpx}}$	$P_{\text{gt}}$	$P_{\text{sp}}$	$\Sigma P$
Garnet lherzolite	0.50	0.30	0.12	0.08	0	0.970	0.3	0.2	0.4	0.1	0	1.458
Spinel lherzolite	0.55	0.25	0.15	0	0.05	0.234	0.2	0.2	0.5	0	0.1	0.617

Mineral abbreviations are the same as in Table 2.5.  $X$  = proportion of mineral relative to all minerals in the rock source.  $P$  = melt reaction coefficient of each mineral. Mineral proportions/modal abundances for garnet lherzolite and spinel lherzolite and melt reaction coefficients from (McKenzie and O’Nions, 1991). Calculated  $\Sigma D_0$  and  $\Sigma P$  used with primitive mantle source  $C_0$  (Table 2.5) to calculate liquid concentration in Equation 2.1.

compositions are produced by larger F fractions, potentially F=15-20% of garnet lherzolite and F=10-20% spinel lherzolite but are not shown in Figure 2.19, which shows one F value (10%) for spinel lherzolite and variable F for garnet lherzolite.

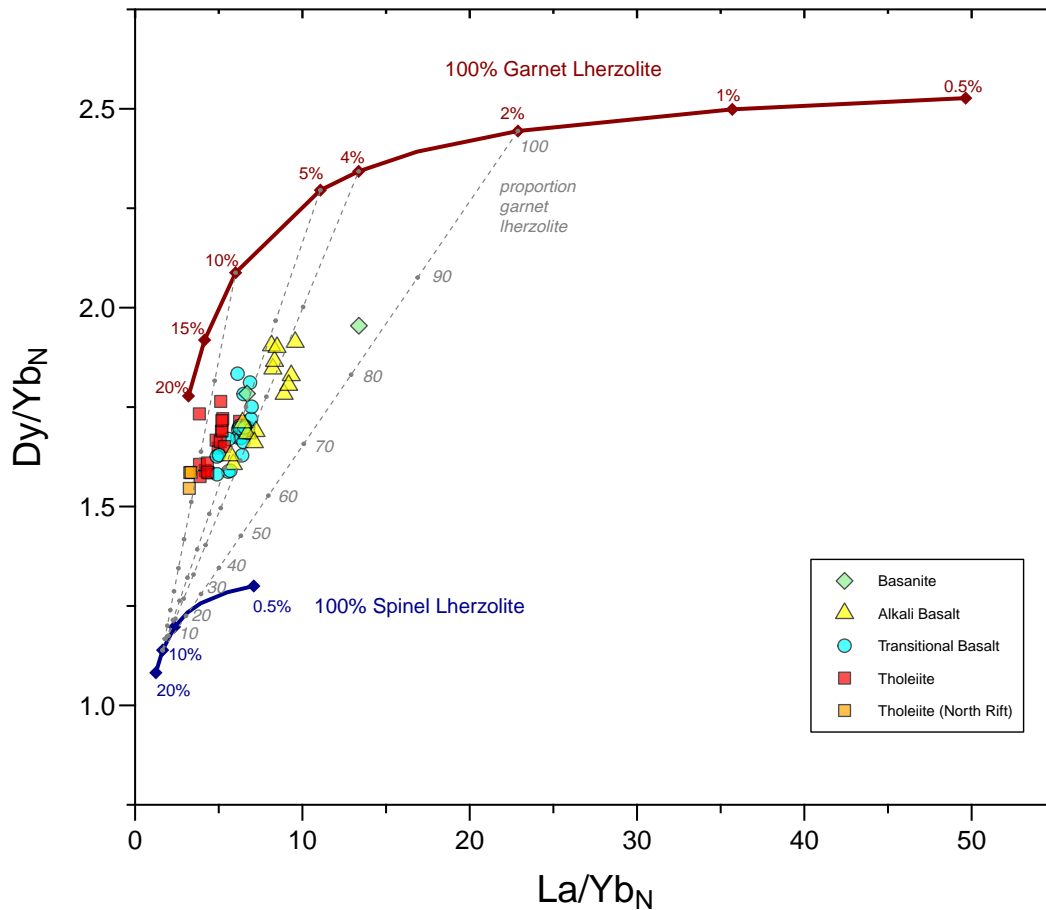


Figure 2.19:  $\text{Dy}/\text{Yb}_N$  vs.  $\text{La}/\text{Yb}_N$  concentrations and estimates of non-modal batch partial melting from garnet lherzoite and spinel lherzolite. Percentages of partial melt are shown in text annotations on plot, where 100% melting of garnet lherzolite is shown in dark red line and 100% melting of spinel lherzolite is shown in dark blue line. Tie lines connecting proportions for mixing between  $F = 10\%$  melting of spinel lherzolite and  $F = 2, 4, 5, 10\%$  melting of garnet lherzolite are shown in grey dashed lines. Relative proportions of mixing of garnet lherzolite shown in grey dots connected with dashed lines, where proportions are shown in increments of 0.10 between 0 to 1. Labeled proportions for one mixing line, between  $F = 2\%$  garnet lherzolite and  $F = 10\%$  spinel lherzolite is shown as an example. Source compositions from Sun and McDonough (1989).

In detail, REE modeling results basanites (Pisces 158-4 and 158-5) with overlapping compositions deriving from >2 to 5% melting of garnet lherzolite combined with 10% melting of spinel lherzolite. Their composition is consistent with a proportion of ~80-90% garnet lherzolite, whereas alkali basalts show a range of 70 to ~90% garnet lherzolite. A potential gap between a group alkali basalts with higher La/Yb and Dy/Yb and alkali basalts overlapping transitional basalts may indicate heterogeneous mixing within the alkaline magmas with more Si-saturated magmas, or a lack of data coverage. Transitional basalts show a more restricted range of ~ 5% garnet lherzolite melting combined with 10% spinel lherzolite melting. Similar to alkali basalts, the proportion of garnet lherzolite ranges from 70-85%. East Flank and South Rift tholeiites are produced by > 5 to 15-20% melting of garnet lherzolite combined with 10% melting of spinel lherzolite. North Rift tholeiites are produced by 10-20% melting of garnet lherzolite with 10-20% melting of spinel lherzolite. Similar to the transitional basalts, East Flank and South Rift tholeiite source proportions include roughly 70-90% garnet lherzolite, while North Rift tholeiite proportions correspond to proportions of 70-80% garnet lherzolite.

It would also be possible for an initial source to have an intermediate mineralogy due to overlapping stability depths for garnet and spinel. Aggregation of incremental non-modal melts of an intermediate source at varying F values could appropriately represent the pooling of melts in a vertical mantle melting column (Fram and Lesher, 1993). An intermediate source of 30-50% garnet lherzolite and 50-70% spinel lherzolite would match observed trends of some Kama'ehuakanaloa samples, however, varying proportions of garnet to spinel are still needed to explain the range of Dy/Yb in lower F rock types like the alkali basalts. Instead of an intermediate mineralogy, the range within each

rock type is consistent with mixing lines between garnet lherzolite and spinel lherzolite, which produce a linear array of compositions in Dy/Yb vs. La/Yb space. Hence, this discussion utilizes different extents of melting of spinel and garnet lherzolite, which mixes in different proportions to produce the range of Kama'ehuakanaloa compositions.

In summary, there is a range of melting from different proportions of garnet and spinel lherzolite in this study suite. An intermediate composition of 30-50% garnet lherzolite would match the curvature of some samples, however, the range of Dy/Yb is best matched by mixing between pure garnet lherzolite and spinel lherzolite melts which are generated at different depths and aggregated after formation. South Rift tholeiites and North Rift Tholeiites are produced by the largest degrees of partial melting, with the North Rift showing maximum melting of up to 20% of garnet and spinel lherzolite each, with relatively lower proportions of garnet lherzolite compared to South Rift basalts. Hence, North Rift tholeiites are more likely to derive from a mantle source within shallower spinel stability depths <90 km depth ([Green, 1970](#)). This is consistent with less enriched incompatible trace element signatures, and high SiO<sub>2</sub> from lower pressures of melting.

### 2.5.3.2 Parental/Primary Melts

Petrolog modeling results indicated that clinopyroxene started to crystallize at MgO~6.5 wt.% and continued for lower MgO concentrations. Estimates of primary magma compositions of ocean island lavas were determined using PRIMELT2 software ([Herzberg and Asimow, 2008](#)) by using sample compositions indicative of only olivine fractionation. Glass compositions with >6.5 wt.% MgO from the South and North Rift transitional and tholeiitic basalts were used to calculate primary magmas. After input into PRIMELT2 ([Herzberg and Asimow, 2008](#)), samples were filtered to remove samples with pyroxenite source warnings and FeO/MgO errors.

For the remaining samples, olivine addition was used to calculate a composition in equilibrium with mantle olivine  $\sim$ Fo<sub>90</sub>. [Clague \(1988\)](#) analyzed olivine in alkalic basalts recovered from KK dredges and found up to Fo<sub>92.6</sub>, the same maximum value determined by [Garcia et al. \(1995\)](#) in a study with East Flank alkalic basalts. In addition, [Garcia et al. \(1995\)](#) found olivines in East Flank tholeiites with Fo<sub>89.6</sub>, and Fo<sub>92.6</sub>. Hence, primary mantle olivine has been found across diverse chemical compositions at Kama‘ehuakanaloa. The percentage of mineral solid was used to calculate relative proportions of liquid melt fractions, which were averaged for each rock type to create a representative parental melt composition. In general, the parental melt concentrations for tholeiites and transitional are similar to estimates from [Garcia et al. \(1995\)](#) of East Flank samples, who contributed estimates for alkalic and tholeiitic basalts (Table 2.8).

Table 2.7: Estimates of trace elements for parental/primary melts<sup>[1]</sup>, corrected to Mg = 16 wt.%. Units are in ppm unless noted as wt.(%)

Parental Melts <sup>[1]</sup>	K	Rb	Sr	Y	Zr	Nb	Cs	Ba
South Rift Transitional <sup>[3]</sup>	4126	9.75	360	20.0	127.5	16.3	0.10	139.2
South Rift Tholeiite <sup>[2]</sup>	3209	7.25	299	18.8	107.5	12.8	0.07	107.5
North Rift Tholeiite <sup>[4]</sup>	2033	3.83	231	18.4	93.4	8.22	0.04	57.62
W	Pb	Th	U	La	Cl wt(%)	S wt(%)	F wt(%)	H <sub>2</sub> O wt(%)

<sup>[1]</sup> Selected trace elements of parental or primary melts after correction of MgO > 6.5 wt% composition to MgO = 16 wt.(%) or in equilibrium to mantle olivine with Fo<sub>90</sub>. Mantle source compositions calculated by determining olivine subtraction (%) from original lava with MgO = 16 wt.% needed to achieve MgO in representative samples (estimates given in footnotes 2, 3, 4). The % of olivine (ol) needed for representative samples was used to calculate liquid fractions (F), F = 1 - ol. The F value was used to calculate incompatible trace element values in the mantle source, assuming D = 0 in olivine during fractional crystallization.

<sup>[2]</sup> Representative sample MIR 2340-3: 25% olivine addition, F = 0.75

<sup>[3]</sup> Representative sample MIR 2343-10: 27% olivine addition, F = 0.73

<sup>[4]</sup> Representative sample TUNE 003D-A: 22% olivine addition, F = 0.78

Table 2.8: Literature Estimates for Parental Melt Compositions for East Flank Samples from Garcia et al. (1993, 1995).

Reference	Sample Name	Location	Rock Type	K (ppm)	Rb	La	Y
Garcia et al. (1993)	1804-1	Summit	Tholeiite	3178	7.56	9.99	17.89
Garcia et al. (1995)	187-5B	East Flank	Transitional Basalt	3846	7.81	11.32	17.57
Garcia et al. (1995)	187-1B	East Flank	Alkalic Basalt	4725	11.4	11.81	17.3

Following the parental melt estimates, source concentrations of highly incompatible elements were determined with  $F_{\text{liquid}}$  reflecting average extents of melting (range of 2.5-7.5% melting used from [Norman and Garcia \(1999\)](#)). The results of parental melt and mantle source concentrations are shown in Table [2.7](#).

Table 2.9: Estimates of trace elements for mantle source compositions. Units are in ppm unless noted as wt.(%)

Mantle Source <sup>[1]</sup>	K (ppm)	Rb	Sr	Y	Zr	Nb	Cs	Ba
South Rift Transitional	248	0.59	21.6	1.2	7.65	0.98	0.006	8.35
South Rift Tholeiite	257	0.58	24.0	1.5	8.60	1.02	0.006	8.60
North Rift Tholeiite	244	0.46	27.7	2.2	11.2	0.99	0.005	6.91
W	Pb	Th	U	L <sub>a</sub>	Cl wt(%)	S wt(%)	F wt(%)	H <sub>2</sub> O (%)
South Rift Transitional	0.011	0.073	0.061	0.017	0.78	0.034	0.008	0.003
South Rift Tholeiite	0.011	0.078	0.060	0.018	0.81	0.036	0.011	0.003
North Rift Tholeiite	0.010	0.079	0.056	0.016	0.82	0.010	0.012	0.003

<sup>[1]</sup> Calculated by using estimates of combined garnet and spinel Iherzolite melting as determined in Figure 2.19. South Rift Transitional, F = 6%. South Rift Tholeiite, F = 8%, North Rift Tholeiite, F = 12%.

The next section discusses the incompatible trace element composition of this study suite's parental source(s). Some volatile estimates are present in Table 2.9, and are further discussed in Chapter 3 instead.

## 2.5.4 Diagnostic Features of Kama‘ehuakanaloa Sample Suite

### 2.5.4.1 Compositional Differences: Alkalic vs. Tholeiitic

Hawaiian lavas generally exhibit less enrichment than global OIB, however within-volcano geochemical variability has been observed on short timescales of 10-100 years (Kurz et al., 2004). The magmatic system beneath Kama‘ehuakanaloa seamount is complex and has generated more evolved compositions relative to other Hawaiian volcanoes (Moore et al., 1982). However, identifying petrogenetic origin of the tholeiites and alkalic basalts is complicated by limited access to stratigraphic sequences at Kama‘ehuakanaloa.

Alkali basalt patterns exhibit steeper LREE/MREE and MREE/HREE slopes that suggest derivation by smaller degrees of melting at depth in the presence of residual garnet. Overall, the trace element characteristics of the alkali basalts (and the more enriched transitional basalts) resemble some of the late stage, post-erosional Honolulu Volcanic Series (HVS) on O‘ahu (Clague and Frey, 1982). The REE patterns for the HVS have been interpreted as evidence for small degree melts from a garnet-bearing source that were generated at greater depths than tholeiites (Clague and Frey, 1982). The HVS and Kama‘ehuakanaloa transitional to alkalic glasses also show a similar relationship between light REE enrichment and normative nepheline, although the Honolulu Series are SiO<sub>2</sub>-undersaturated lavas and strongly Ne-normative compared to Kama‘ehuakanaloa alkali basalts. In general, the mantle source of South Rift transitional basalts show higher highly incompatible Rb, Sr, Ba, and La compared to South Rift tholeiites. Trace element ratios are slightly elevated for transitional basalts, e.g. Th/U = 3.71 and Rb/Sr = 0.027, where South Rift tholeiite Th/U = 3.45 and Rb/Sr = 0.024. This is consistent with derivation

from the alkalic source.

North Rift tholeiites show the highest MgO contents of this study, and the lowest extents of olivine crystallization (Fig. 2.12, 2.11). Light REE enrichment of the North Rift tholeiite suggests derivation by slightly higher degrees of partial melting compared to the South Rift tholeiites (Fig. 2.7). Low values of La/Yb<sub>N</sub>, and La/Sm<sub>N</sub> suggest a source region that has experienced greater melt extraction, REE modeling is consistent with higher degrees of partial melting to generate the North Rift compositions. In addition, they show less heavy REE depletion than South Rift tholeiites, and suggesting origins at shallower mantle depths.

#### 2.5.4.2 Comparing the Kama‘ehuakanaloa mantle source to average Hawaiian shield basalts

Trace element ratios of lavas from several Hawaiian volcanoes often show overlap, e.g., melt inclusions and glasses from active Hawaiian volcanoes show lower Ba/Nb between 6-8 (Norman et al., 2002), compared to primitive mantle~9.8 (Sun and McDonough, 1989), suggesting similar mantle source enrichment among Hawaiian volcanoes. In this study, Kama‘ehuakanaloa south rift lavas shows higher Ba/Nb in alkali basalts up to 9.2, compared to tholeiites with variable, but lower Ba/Nb~8.1. This is consistent with observations of Mauna Kea post-shield alkalic lavas exhibiting higher in Ba/Nb than shield tholeiites (Norman et al., 2002). Hence, the difference between alkalic basalts and tholeiites at Kama‘ehuakanaloa derive from sources with varying proportions of mantle components, and the volcano exhibits these trends even in the earliest shield phase.

Another common feature of Hawaiian shield lavas is elevated W contents compared to the terrestrial average (Ireland et al., 2009), providing evidence for persistent differences in the Hawaiian mantle compared to primitive mantle, and depleted mantle. The distinct isotopic compositions of W and other refractory metals in global high-<sup>3</sup>He/<sup>4</sup>He lavas have been related to interaction with Earth's metallic core (Mundl-Petermeier et al., 2020; Jackson et al., 2020). W concentrations of Kama'ehuakanaloa glasses shown are similar to whole rock values found in Ireland et al. (2009), but mean values are lower (Fig. 2.20). Generally low-SiO<sub>2</sub> alkalic and transitional basalts show the highest W concentrations and significant variability.

Previous values for W and W/U at Kama'ehuakanaloa were distinctly higher compared to all other Hawaiian shields, and has been explained as evidence of contamination of Kama'ehuakanaloa basalts from enriched sources (Arevalo and McDonough, 2008; Ireland et al., 2009). However, in this study, after correcting for parental melt compositions and melting effects, the W/U ratio is essentially identical for different rock types ~0.61-0.65 (Table 2.9).

Of the South Rift glasses, W/U of TUNE-004 is highest. LO-02-02 measured at W = 265 ng/g and W/U = 0.79, and LO-02-04 at W = 313 ng/g and W/U = 0.86, significantly higher than other Hawaiian volcanoes (Ireland et al., 2009). Notably, both LO-02-02 and LO-04-04 are characterized as submarine picrite samples in previous studies (Valbracht et al., 1996). LO-02-04 is likely to be the same as TUNE-004 samples in this study. Though LO-02-04 has often been analyzed in OIB studies as a representative sample of the Kama'ehuakanaloa mantle source, it has not been explicitly identified as an alkalic basalt until now. Assimilation has been a proposed explanation for elevated W

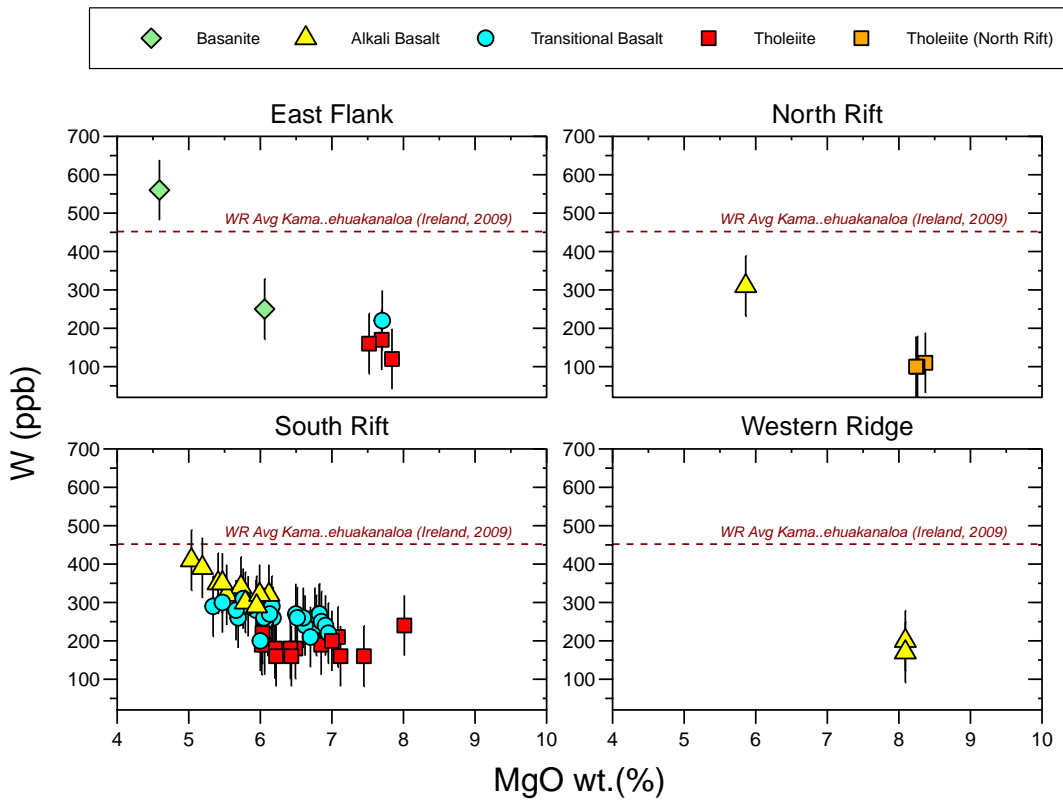


Figure 2.20: W (ppb, or ng/g) vs. MgO wt. (%) basaltic glasses. Values are shown according to geographic location at Kama'ehuakanaloa with the same rock type symbols are shown. Line representing average value from previous whole rock analyses of 452 ppb, or ng/g from [Ireland et al. \(2009\)](#)

in Kama'ehuakanaloa basalts ([Ireland et al., 2009](#)), consistent with interpreting results from transitional/alkalic basalts. The connection between W/U, W, and other trace elements with Helium isotopes are explored in Chapter 3

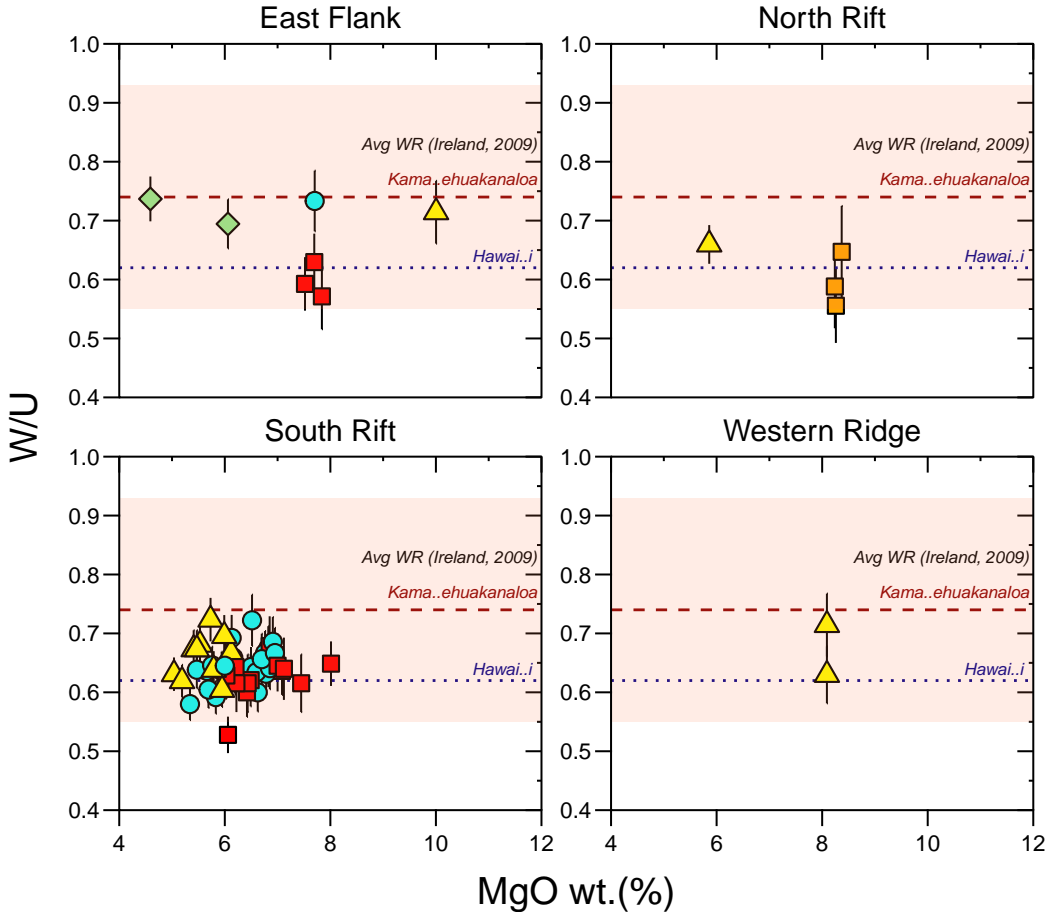


Figure 2.21:  $W/U$  vs.  $MgO$  wt. (%) basaltic glasses.  $W$  (ppb) and  $U$  (ppm) were used to calculate  $W/U$ . Values are shown according to geographic location at Kama'ehuakanaloa with the same rock type symbols from Figure 2.20. The dashed red line indicates average values from 6 whole rock Kama'ehuakanaloa samples, where  $W/U_{\text{average}} = 0.74 \pm 0.21$  ( $2\sigma$ ), in addition to from Ireland et al. (2009) for nine Hawaiian shield volcanoes. Hawaiian average  $0.62 \pm 0.19$  is shown from Arevalo and McDonough (2008).

## 2.6 Conclusion

This study contributed a dataset of trace element compositions for samples collected from a range of locations on Kama‘ehuakanaloa Seamount, predominantly along the rift zone portions which make up  $\sim 30$  km of the volcano’s length and from 2-5 km collection depth. In this chapter, I investigated the trace element geochemistry of 62 Kama‘ehuakanaloa basaltic glasses from rock samples to understand early stage volcanic processes and magma evolution occurring at a single volcano with exposures of the pre-shield to main shield transitional stage of oceanic island construction. Samples collected various topographic and geographic features of the volcano (including rift zones and exposed flanks) were used to uncover whether there are consistent patterns in petrogenetic series, parental melts, and mantle source expressed during the volcanic transition to shield-type volcanism. The limited coverage of some locations does not allow for constraints on long-term geochemical evolution of all portions of Kama‘ehuakanaloa. However, individual samples and groupings of rock types exhibit unique characteristics. The main findings are summarized below:

Crystal fractionation has extensively modified Kama‘ehuakanaloa submarine basalts. The deeply erupted south rift basalts at Kama‘ehuakanaloa seamount have witnessed a significant degree of crystallization during their evolution (between 20-30%). Basanite compositions show high enrichment in incompatible elements and North Rift tholeiites show the least enrichment (Figs. 2.5 and 2.3). Olivine fractionation was a dominant control on major element compositions. Co-precipitation of clinopyroxene and plagioclase account for additional fractionation of alkalic and transitional basalts (Fig. 2.12)

Indicators of mantle enrichment are observed in Kama‘ehuakanaloa suite and within rock types at several locations. Ratios that correspond to rock types include K/Ti (Fig. 2.13), Rb/Sr (Fig. 2.14), La/Sm (Fig. 2.18), with increasing ratios with Si-Saturation. Enrichment observed across rock types and locations, but not distinct among rock types include Nb/U (Fig 2.15) and W/U (Fig. 2.21).

The range of compositions are consistent with varying partial melting and a slightly heterogeneous source. Variation in REE contents and ratios are consistent with polybaric non-modal batch melting from garnet lherzolite and spinel lherzolite sources, with melt fractions between 6-12%. Lower melt fractions, higher Dy/Yb and Sm/Yb are consistent with deeper generation of melts of basanites and alkalic basalts. Tholeiites are generated by greater extents of melting, and compared to East Flank and South Rift tholeiites, a set of dredge samples from the North Rift have compositions consistent with the largest degree of melting. The potential for the North Rift and South Rift sources to differ in volatile elements are evaluated in Chapter 3.

## Chapter 3: Helium and Volatile ( $\text{H}_2\text{O}$ , $\text{CO}_2$ ) Geochemistry of Deep Rift Zone Lavas from Kama‘ehuakanaloa, Hawaiian Islands

### 3.1 Introduction

Kama‘ehuakanaloa’s summit platform reaches 975 meters below sea level (mbsl) relative to the depth of the surrounding seafloor. The height of the overlying water column is notable for producing high confining pressure of erupted basalts. Ocean island basalts erupt as pillow basalts in similar conditions as mid-ocean ridge basalts, with glassy rinds forming within seconds of seawater contact. Kama‘ehuakanaloa glass has notably exhibited “hyperquench” qualities, i.e., rapid cooling rates exceeding the maximum of natural materials (Potuzak et al., 2008).

Basaltic glasses, crystallized rocks, olivine and clinopyroxene minerals at Kama‘ehuakanaloa Seamount are marked by the highest  ${}^3\text{He}/{}^4\text{He}$  ratios observed in basalts sampled from the 80 million year history of the Hawaiian – Emperor volcanic chain, with values extending to  $> 30 \text{ R}_\text{A}$  ( $\text{R}_\text{A}$  is the atmospheric  ${}^3\text{He}/{}^4\text{He} = 1.39 \times 10^{-6}$ , Clarke et al., 1976). Kama‘ehuakanaloa basalts also display a significant range in  ${}^3\text{He}/{}^4\text{He}$ , extending down to 20  $\text{R}_\text{A}$  or lower (Kurz et al., 1983; Rison and Craig, 1983; Kaneoka et al., 1983, 2002; Hiyagon et al., 1992; Honda et al., 1993; Valbracht et al., 1994, 1996; Garcia, 1996; Loewen et al., 2019). The degree to which this variability represents melting of primordial and recycled components in the Hawaiian plume (Kurz et al., 1983; Garcia

et al., 1995; Dixon and Clague, 2001; Pietruszka et al., 2013), or to shallow level processes involving degassing and assimilation (Kent et al., 1999a,b) has not been fully evaluated. Additionally, most previous work has focused on volcanic eruptions sampled near the summit ( $\sim$ 1000 m water depth) where gas loss is expected to be more extensive.

Helium isotopes are central to the use of the Hawaiian Islands as a classic hotspot, or mantle plume example in geochemistry, as their structure, volume, and major element composition vary with isotope ratios in shield building lavas (Hauri, 1996). The high volumes of magma during the shield stage is interpreted as evidence of closest proximity of the volcano to the underlying hot spot, producing a robust magmatic system (Clague and Sherrod, 2014). Furthermore, Helium isotopes are central to the debate about mantle plumes, specifically due to  ${}^3\text{He}$  flux from the mantle in magmatic materials. The high  ${}^3\text{He}/{}^4\text{He}$  in early pre-shield submarine lavas located offshore of Hawai'i Island at Kama'ehuakanaloa volcano suggests proximity to the present-day center of the Hawaiian hotspot (Kurz et al., 1983, 2004; Kaneoka, 1987).

${}^3\text{He}/{}^4\text{He}$  variability in OIB has long been cited as the main inconsistency in mantle plume models. As described in Chapter 1, alternative explanations by plume skeptics in the “plate” model of volcanism generally invoke the melting properties of heterogeneities emplaced by subduction in a region just below the asthenosphere (Meibom et al., 2005; Smith, 2022). While these ideas are rarely explored in Hawaiian geochemical publications, they are often explored in textbooks (Foulger, 2011), scientific conference presentations (Foulger, 2020b), and public websites like [mantleplumes.org](http://mantleplumes.org) (Foulger, 2020a). Hence, a consideration for Helium isotope variability (and not solely maximum Helium isotope values), and explanations for such variability, has implications for consistency of mantle

plume model and geochemical data interpretation for non-specialists.

### 3.1.1 Study Aims and Research Questions

In this study, we present new volatile results for >60 submarine basalts from Kama‘ehuakanaloa Seamount, predominantly from the South Rift Zone (Fig. 1.9). The sample suite should be representative of the geographic extent of Kama‘ehuakanaloa Seamount away from the commonly studied summit region, and collection depths between 1.3 to 5 km promote the retention of magmatic volatiles. Samples have been analyzed for  $^{3}\text{He}/^{4}\text{He}$  and He and CO<sub>2</sub> concentration in both the vesicle and glass phase of the basalts. All glasses were also analyzed for H<sub>2</sub>O, Cl, F and S. The following research questions are addressed:

1. Do Helium isotope trends correspond to major element composition, i.e., between early alkali lavas and later tholeiitic lavas? Following up from Chapter 2, what is the trace element composition of the mantle hosting the high- $^{3}\text{He}/^{4}\text{He}$  component?
2. What are the systematic controls on Helium isotope variation?
3. When Helium results are contextualized with H<sub>2</sub>O-CO<sub>2</sub> concentrations in the same samples, can they be shown to have consistent decoupled noble gas signatures relative to trace elements?

## 3.2 Methods

A summary of all instrument and laboratory information, detection limits and blank values is in Table B.1. A summary of reference materials and standards used is in Table B.2.

### 3.2.1 Vesicle Helium and CO<sub>2</sub>

Analyses of <sup>3</sup>He/<sup>4</sup>He and vesicle He and CO<sub>2</sub> concentrations were carried out in the Noble Gas Laboratory at Oregon State University. Glassy rims were carefully chipped from rock samples. Large pieces with the fewest ruptured vesicles were lightly crushed and handpicked under a binocular microscope to eliminate adhering crystals and alteration. Typically 1-5 pieces of glass chips were picked on the basis of fresh and homogeneous appearance, yielding 300-400 mg for analyses. Glasses were subjected to 15 minute ultrasonic baths of ethanol and acetone, with rinsing in Milli-Q water between steps. They were subsequently air dried beneath a laminar flow hood, weighed to a precision of 0.1 mg, and loaded into stainless steel on-line crushers.

Vesicle He concentrations and <sup>3</sup>He/<sup>4</sup>He were determined by noble gas mass spectrometry and CO<sub>2</sub> concentrations were determined by manometry, both by in vacuo crushing. Analytical procedures follow methods described in [Graham et al. \(2014\)](#). Helium measurements were made using a Nu Instruments Noblesse mass spectrometer. The CO<sub>2</sub> and H<sub>2</sub>O liberated by crushing were condensed in a flow-through U-trap using liquid N<sub>2</sub>. The non-condensable gases (other reactive species plus He, Ne and Ar) were then processed through a series of heated and room temperature SAES getters to remove re-

maining reactive gas species before the noble gases were adsorbed onto activated charcoal at 10K using a Janis cryostat. Helium was then separated from the other noble gases and released directly to the mass spectrometer at 45°K.

### 3.2.2 Dissolved Helium

Dissolved (glass phase) helium concentrations were determined by melting at >1400°C in a high temperature Heine vacuum furnace on the powders retrieved from the crushing analyses. This dissolved He was extracted from approximately 150 mg of crushed rock powder (<0.1mm) retrieved from crushing the glass chips. Powders were loaded into tin foil boats and loaded into the sample carousel of the vacuum furnace and pumped overnight. The powders were then melted at 1410°C and helium was extracted in a similar fashion to the crushing extractions. Total concentrations and  ${}^3\text{He}/{}^4\text{He}$  were determined by combining the vesicles+glass results.

Line blanks were analyzed prior to each sample analysis. Average blanks were  $7.8 \times 10^{-11} \text{ cm}^3 \text{ STP } {}^4\text{He}$  and  $1.9 \times 10^{-16} \text{ cm}^3 \text{ STP } {}^3\text{He}$ , and are typically <1% of sample  ${}^4\text{He}$  and  ${}^3\text{He}$ . All  ${}^3\text{He}$  and  ${}^4\text{He}$  measurements reported in this study have been blank corrected. To monitor instrumental mass fractionation and drift, aliquots of the Helium Standard of Japan ([Matsuda et al., 2002](#)) were analyzed throughout the study. The HESJ standard has  ${}^3\text{He}/{}^4\text{He} = 20.4 \text{ R}_A$  relative to Oregon marine air (collected in 2007) based on calibration in the OSU lab, in agreement with the ratio determined earlier by Lupton and Evans (2004). Analytical uncertainties in  ${}^3\text{He}/{}^4\text{He}$  are reported here as  $\pm 2\sigma$ , which include the uncertainties summed in quadrature arising from sample ion counting,

blank correction, and reproducibility of the HESJ standard.

Vesicle CO<sub>2</sub> concentrations were determined from the gas released during crushing that was condensed in a stainless steel U-trap held at liquid N<sub>2</sub> temperature (77 K). CO<sub>2</sub> was distilled from any small amount of co-condensed H<sub>2</sub>O during the crushing, using a frozen isopropanol slush trap to retain the H<sub>2</sub>O and a liquid N<sub>2</sub> trap to transfer the CO<sub>2</sub> into a cold finger in a calibrated volume of the vacuum line. The partial pressure of CO<sub>2</sub> was then measured to high precision ( $\pm 0.2$  mtorr) using a 1-torr capacitance manometer after warming the cold finger to room temperature. The uncertainty calculated from repeated measurements of CO<sub>2</sub> was 0.35 ppm (Table B.2).

### 3.2.3 Dissolved H<sub>2</sub>O and CO<sub>2</sub>

Separate aliquots of the basalt glasses were polished into thin wafers and analyzed for dissolved H<sub>2</sub>O and CO<sub>2</sub> by FTIR at University of Tulsa following methods described in Michael and Graham (2015). The combined FTIR and manometric results can be used to compute the total (glass+vesicles) CO<sub>2</sub> concentration of a sample, as well the proportions of dissolved and exsolved gas.

### 3.2.4 F, S, Cl

The method used to determine F, S, and Cl by electron microprobe are described in Chapter 2 and Graham et al. (2023). Information about instrumentation are in Table B.1 and information about reference material measurements are in Table B.2.

### 3.3 Results

#### 3.3.1 Helium

Over 60 basalt glass samples were analyzed for  ${}^3\text{He}/{}^4\text{He}$  and Helium concentrations (Table 3.1). Analyses were initially carried out by crushing to extract the vesicle helium. The majority of crushed samples yielded powders suitable for analysis by melting to extract the dissolved glass helium. The amount of Helium released by crushing was typically below  $2 \times 10^{-6} \text{ cm}^3 \text{ STP/g}$ , and did not vary systematically with vesicle  ${}^3\text{He}/{}^4\text{He}$ . The  ${}^3\text{He}/{}^4\text{He}$  measured in vesicles ranged from 22.1-30.7 R<sub>A</sub>, with the exception of a single differentiated alkali basalt (MIR2337-b collected at 4795 m depth).

Table 3.1: Helium measurements from crushing and melting

ID	Sample	Type	[He]	${}^3\text{He}/{}^4\text{He}$	${}^2\sigma$	[He]	${}^3\text{He}/{}^4\text{He}$	${}^2\sigma$	[He]	${}^3\text{He}/{}^4\text{He}$	${}^2\sigma$
			(cc STP/g) Vesicle	(RA) Vesicle	(RA)	(cc STP/g) Glass	(RA)	(cc STP/g) Glass	(RA)	(RA)	Total
1	MIR 2335-2	TR	$3.92 \times 10^{-8}$	24.9	0.47	$4.48 \times 10^{-7}$	25.4	0.21	$4.87 \times 10^{-7}$	25.3	0.24
2	MIR 2335-5	TR	$6.47 \times 10^{-8}$	25.3	0.49	$5.21 \times 10^{-7}$	25.4	0.21	$5.85 \times 10^{-7}$	25.4	0.26
3	MIR 2335-6	TR	$9.13 \times 10^{-8}$	25.3	0.27						
4	MIR 2335-7	TR	$5.00 \times 10^{-8}$	24.3	0.28	$3.39 \times 10^{-7}$	25.2	0.22	$3.89 \times 10^{-7}$	25.1	0.23
5	MIR 2335-8	TR	$4.48 \times 10^{-8}$	24.4	0.31						
6	MIR 2335-9	TR	$5.09 \times 10^{-8}$	24.9	0.27						
7	MIR 2335-10	TR	$2.72 \times 10^{-8}$	24.4	0.37						
8	MIR 2335-11	TR	$2.63 \times 10^{-7}$	25.2	0.25	$4.14 \times 10^{-7}$	25.3	0.29	$6.77 \times 10^{-7}$	25.3	0.27
9	MIR 2335-12	TH	$1.59 \times 10^{-8}$	23.7	0.37	$1.38 \times 10^{-7}$	24.3	0.31	$1.54 \times 10^{-7}$	24.2	0.32
10	MIR 2336-2	TR	$1.41 \times 10^{-7}$	25.2	0.20	$6.13 \times 10^{-7}$	25.3	0.18	$7.53 \times 10^{-7}$	25.3	0.19
11	MIR 2336-4	TH	$3.38 \times 10^{-7}$	27.9	0.18	$3.88 \times 10^{-7}$	28.0	0.17	$7.26 \times 10^{-7}$	28.0	0.17
12	MIR 2336-5	TR	$1.17 \times 10^{-6}$	26.6	0.23	$2.77 \times 10^{-7}$	26.4	0.32	$1.45 \times 10^{-6}$	26.6	0.25
14	MIR 2337-2	TH	$7.18 \times 10^{-7}$	26.3	0.21	$5.38 \times 10^{-7}$	26.5	0.25	$1.26 \times 10^{-6}$	26.4	0.23
15	MIR 2337-3	TH	$6.23 \times 10^{-7}$	26.6	0.21	$8.41 \times 10^{-7}$	26.5	0.28	$1.46 \times 10^{-6}$	26.5	0.25
16	MIR 2338-1A	TR	$3.22 \times 10^{-7}$	25.6	0.20	$5.23 \times 10^{-7}$	25.3	0.18	$8.45 \times 10^{-7}$	25.4	0.19
17	MIR 2340-1	TH	$8.99 \times 10^{-8}$	26.3	0.21	$9.95 \times 10^{-8}$	26.2	0.36	$1.89 \times 10^{-7}$	26.3	0.30
18	MIR 2340-3	TH	$1.90 \times 10^{-8}$	26.1	0.61	$1.47 \times 10^{-7}$	26.5	0.35	$1.66 \times 10^{-7}$	26.4	0.39
19	MIR 2341-1	TR	$3.63 \times 10^{-7}$	25.7	0.22	$1.33 \times 10^{-7}$	24.9	0.36	$4.96 \times 10^{-7}$	25.5	0.27
20	MIR 2341-2	AB	$1.75 \times 10^{-7}$	24.4	0.24	$3.57 \times 10^{-8}$	22.7	0.43	$2.10 \times 10^{-7}$	24.1	0.29
21	MIR 2343-2	TR	$1.02 \times 10^{-7}$	29.1	0.23	$1.04 \times 10^{-8}$	25.9	0.68	$1.12 \times 10^{-7}$	28.8	0.32
22	MIR 2343-3	TR	$9.81 \times 10^{-8}$	24.0	0.23	$9.58 \times 10^{-8}$	23.4	0.28	$1.94 \times 10^{-7}$	23.7	0.26
23	MIR 2343-4	TR	$3.29 \times 10^{-7}$	24.1	0.15						
24	MIR 2343-5	TR	$4.39 \times 10^{-8}$	23.3	0.28						
25	MIR 2343-6	AB	$1.63 \times 10^{-7}$	23.2	0.17						
26	MIR 2343-7	TR	$5.06 \times 10^{-8}$	23.9	0.27	$6.36 \times 10^{-8}$	23.3	0.38	$1.14 \times 10^{-7}$	23.5	0.34
27	MIR 2343-8	TR	$5.46 \times 10^{-7}$	24.4	0.14	$2.21 \times 10^{-7}$	24.0	0.20	$7.68 \times 10^{-7}$	24.3	0.16
28	MIR 2343-10	TR	$1.29 \times 10^{-6}$	24.1	0.19	$5.54 \times 10^{-7}$	24.5	0.24	$1.84 \times 10^{-6}$	24.2	0.20
29	MIR 2343-11	TR	$4.12 \times 10^{-8}$	22.1	0.40	$1.91 \times 10^{-7}$	23.4	0.28	$2.32 \times 10^{-7}$	23.2	0.31

Helium measurements from crushing and melting (continued)

ID	Sample	Type	[He]	${}^3\text{He}/{}^4\text{He}$	${}^2\sigma$	[He]	${}^3\text{He}/{}^4\text{He}$	${}^2\sigma$	[He]	${}^3\text{He}/{}^4\text{He}$	${}^2\sigma$
			(cc STP/g) Vesicle	(R <sub>A</sub> ) Vesicle	Vesicle	(cc STP/g) Glass	(R <sub>A</sub> ) Glass	Glass	(cc STP/g) Total	(R <sub>A</sub> ) Total	(R <sub>A</sub> ) Total
30	MIR 2343-12	AB	$4.76 \times 10^{-7}$	25.3	0.18	$4.22 \times 10^{-8}$	23.2	0.42	$5.18 \times 10^{-7}$	25.1	0.22
31	MIR 2343-13	AB	$7.02 \times 10^{-7}$	25.3	0.17	$2.37 \times 10^{-7}$	25.0	0.22	$9.39 \times 10^{-7}$	25.3	0.18
32	Shinkai 490-8	TH	$2.14 \times 10^{-6}$	28.8	0.26	$9.30 \times 10^{-7}$	28.7	0.22	$3.07 \times 10^{-6}$	28.8	0.25
33	Shinkai 494-1	TR	$9.02 \times 10^{-8}$	23.6	0.44	8.48e-09	18.6	0.60	$9.87 \times 10^{-8}$	23.1	0.47
34	Shinkai 494-2	TR	$9.00 \times 10^{-8}$	24.1	0.33	7.58e-09	19.1	1.00	$9.76 \times 10^{-8}$	23.7	0.47
35	Shinkai 494-3	AB	$2.18 \times 10^{-7}$	24.6	0.16	4.07e-09	16.8	0.95	$2.22 \times 10^{-7}$	24.5	0.25
36	Shinkai 494-4	AB	$9.75 \times 10^{-9}$	22.7	0.44	4.55e-09	15.4	0.88	$1.43 \times 10^{-8}$	20.4	0.73
37	Shinkai 494-5	TH	$3.15 \times 10^{-7}$	26.5	0.16	$1.56 \times 10^{-7}$	25.1	0.22	$4.70 \times 10^{-7}$	26.0	0.18
38	Shinkai 494-6	TH	$2.33 \times 10^{-8}$	26.5	0.50	$1.03 \times 10^{-7}$	26.4	0.36	$1.26 \times 10^{-7}$	26.5	0.39
39	Shinkai 494-7	TH	$2.32 \times 10^{-8}$	25.9	0.40	$9.05 \times 10^{-8}$	26.2	0.36	$1.14 \times 10^{-7}$	26.1	0.37
40	Shinkai 494-8	TH	$1.44 \times 10^{-7}$	26.5	0.23	$8.42 \times 10^{-8}$	25.7	0.28	$2.28 \times 10^{-7}$	26.2	0.25
41	Shinkai 513-3	TH	$6.63 \times 10^{-7}$	29.9	0.24	$3.45 \times 10^{-7}$	29.7	0.23	$1.01 \times 10^{-6}$	29.8	0.24
42	Shinkai 513-4A	TR	$1.94 \times 10^{-6}$	26.3	0.19	$6.32 \times 10^{-8}$	24.5	0.36	$2.00 \times 10^{-6}$	26.2	0.20
43	Shinkai 513-5	TR	$1.45 \times 10^{-7}$	26.1	0.20	$2.09 \times 10^{-7}$	26.1	0.23	$3.54 \times 10^{-7}$	26.1	0.22
44	Shinkai 513-6	TR	$6.48 \times 10^{-7}$	26.1	0.21	$3.32 \times 10^{-7}$	26.1	0.21	$9.80 \times 10^{-7}$	26.1	0.21
45	Shinkai 513-7A	TH	$5.85 \times 10^{-7}$	27.4	0.22	$3.87 \times 10^{-7}$	27.3	0.21	$9.72 \times 10^{-7}$	27.3	0.22
46	Shinkai 515-1	AB	$4.92 \times 10^{-7}$	25.3	0.22	$1.06 \times 10^{-7}$	24.9	0.33	$5.98 \times 10^{-7}$	25.2	0.24
47	TUNE 003D-A	TH (N.)	$1.42 \times 10^{-6}$	30.6	0.22	$4.67 \times 10^{-7}$	30.6	0.33	$1.88 \times 10^{-6}$	30.6	0.25
48	TUNE 003D-B	TH (N.)	$7.94 \times 10^{-7}$	30.7	0.26	$5.34 \times 10^{-7}$	30.7	0.23	$1.33 \times 10^{-6}$	30.7	0.25
49	TUNE 003D-C	TH (N.)	$1.34 \times 10^{-6}$	30.7	0.24	$4.94 \times 10^{-7}$	30.7	0.23	$1.83 \times 10^{-6}$	30.7	0.24
50	TUNE 004D-A	AB	$1.80 \times 10^{-6}$	25.4	0.18	$2.45 \times 10^{-8}$	23.0	0.49	$1.82 \times 10^{-6}$	25.4	0.19
51	TUNE 004D-B	AB	$9.07 \times 10^{-7}$	25.3	0.16	9.61e-09	18.9	0.76	$9.17 \times 10^{-7}$	25.3	0.19
53	KK 17-2	AB	$4.18 \times 10^{-7}$	24.2		$1.66 \times 10^{-8}$	19.0		$4.35 \times 10^{-7}$	24.0	
54	KK 20-14	TH	$5.84 \times 10^{-7}$	26.7		$2.21 \times 10^{-7}$	26.4		$8.05 \times 10^{-7}$	26.6	
55	KK 25-4	TR	$4.82 \times 10^{-7}$	23.4		$7.63 \times 10^{-8}$	21.7		$5.58 \times 10^{-7}$	23.1	
56	KK 31-9	AB	$6.91 \times 10^{-7}$	20.6		$6.88 \times 10^{-8}$	18.7		$7.60 \times 10^{-7}$	20.4	
57	KK 31-12	AB	$1.31 \times 10^{-6}$	21.7		$2.77 \times 10^{-7}$	20.9		$1.59 \times 10^{-6}$	21.6	
58	Pisces 158-4	BS	$2.44 \times 10^{-7}$	22.3		5.78e-09	12.9		$2.50 \times 10^{-7}$	22.1	

## Helium measurements from crushing and melting (continued)

ID	Sample	Type	[He]	$^{3}\text{He}/^{4}\text{He}$	$^{2\sigma}$	[He]	$^{3}\text{He}/^{4}\text{He}$	$^{2\sigma}$	[He]	$^{3}\text{He}/^{4}\text{He}$	$^{2\sigma}$
			(cc STP/g)	(R <sub>A</sub> ) Vesicle	(R <sub>A</sub> ) Vesicle	(cc STP/g)	(R <sub>A</sub> ) Glass	(R <sub>A</sub> ) Glass	(cc STP/g)	(R <sub>A</sub> ) Total	(R <sub>A</sub> ) Total
59	Pisces 158-5	BS	1.20×10 <sup>-7</sup>	22.5		1.31×10 <sup>-8</sup>	19.3		1.33×10 <sup>-7</sup>	22.2	
60	Pisces 186-3	TH	7.94×10 <sup>-7</sup>	26.6							
61	Pisces 187-1A	AB	7.80×10 <sup>-7</sup>	22.8							
62	Pisces 187-5B	TR	4.27×10 <sup>-7</sup>	25.7							
63	Pisces 187-8	TH	5.02×10 <sup>-7</sup>	31.9		1.43×10 <sup>-7</sup>	30.6		6.45×10 <sup>-7</sup>	31.6	
64	Pisces 187-9	TH	1.02×10 <sup>-7</sup>	31.5							

[1] Rock types are abbreviated to BS = Basanite, AB = Alkali Basalt, TR = Transitional Basalt, and TH = Tholeiite Basalt, TH (N.) = Tholeiite Basalt (North Rift)

The range of  ${}^3\text{He}/{}^4\text{He}$  in other samples analyzed here lies within that of previous measurements for Kama‘ehuakanaloa glasses ( ${}^3\text{He}/{}^4\text{He} > 20 \text{ R}_\text{A}$ ) (Kaneoka et al., 1983; Kurz et al., 1983; Rison and Craig, 1983; Valbracht et al., 1996, 1997; Loewen et al., 2019). The North Rift tholeiite (TUNE 003-D) is distinct and has the highest value measured in this study; all three analyses yielded a uniform  ${}^3\text{He}/{}^4\text{He}$  of  $\sim 30.7 \text{ R}_\text{A}$ .

MIR 2337-b yielded a vesicle  ${}^3\text{He}/{}^4\text{He} = 4.5 \text{ R}_\text{A}$  and glass  ${}^3\text{He}/{}^4\text{He} = 3.0 \text{ R}_\text{A}$ . Kurz et al. (1983); Rison and Craig (1983) reported similarly low ratios in the vesicles of a differentiated alkali basalt (KK21-2, collected at 1092 m depth near the summit), having  ${}^3\text{He}/{}^4\text{He} = 4.6 \text{ R}_\text{A}$  and  $5.4 \text{ R}_\text{A}$ , respectively. The low  ${}^3\text{He}/{}^4\text{He}$  in KK21-2 was attributed to seawater or atmospheric interaction within the highly vesicular (25-35%) sample, despite the fresh appearance of the glass. MIR2337-b appears similarly fresh and glassy, but it has very low vesicularity. This sample is not representative of magmas being erupted at Kama‘ehuakanaloa Seamount, as the  $3\text{-}4.5 \text{ R}_\text{A}$   ${}^3\text{He}/{}^4\text{He}$  value and unusually high alkali content (Table A.1) is extremely dissimilar to other samples collected in MIR dive 2337, and we do not consider its volatile results further.

This study increases the existing data set for total  ${}^3\text{He}/{}^4\text{He}$  ratios (determined by crushing and melted, or crushing and step heating, see Fig. 3.1). Furthermore, the data set includes a larger contribution from transitional and alkali basalts whose  ${}^3\text{He}/{}^4\text{He}$  ratios are useful for assessing variable plume contribution to erupted lavas over time, during the pre-shield and/or shield transition. Figure 3.1 shows the distribution of total  ${}^3\text{He}/{}^4\text{He}$  values from combined glass crushing and melting experiments from previous literature with values from two sources (Kurz et al. (1983) n = 8; from Loewen et al. (2019), n=12) compared to this study.

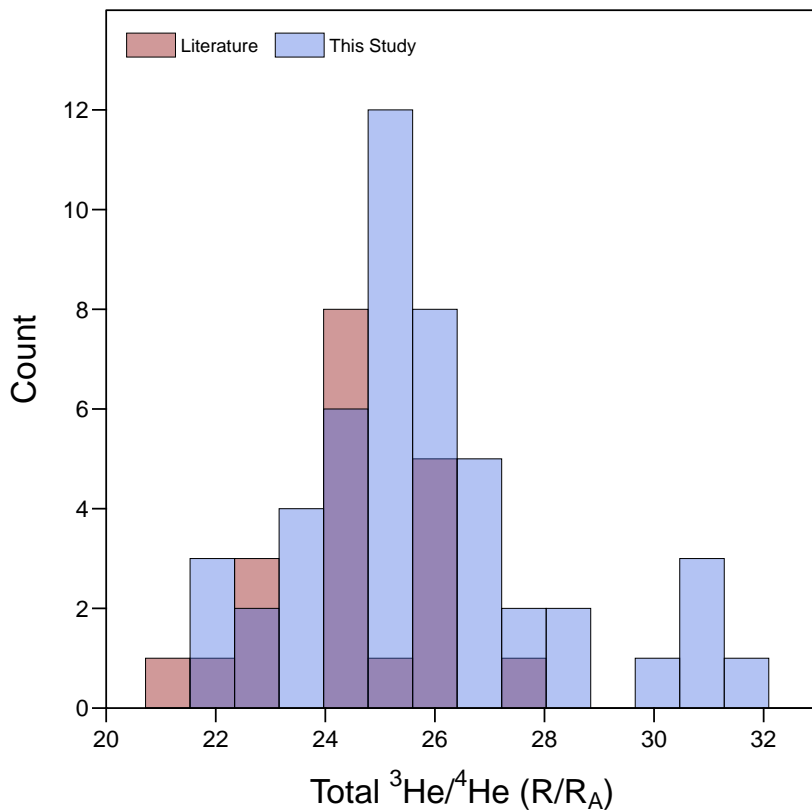
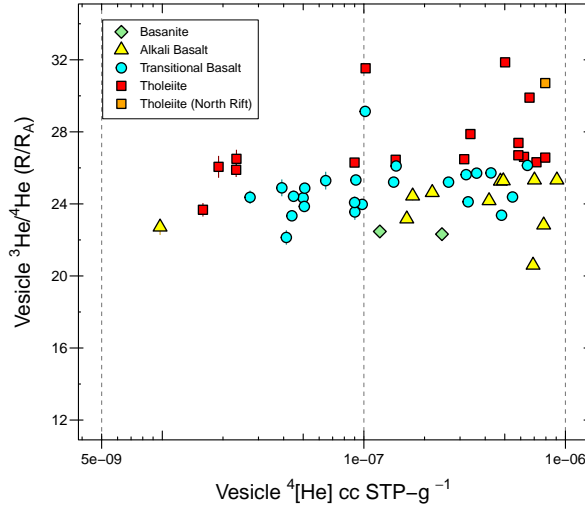


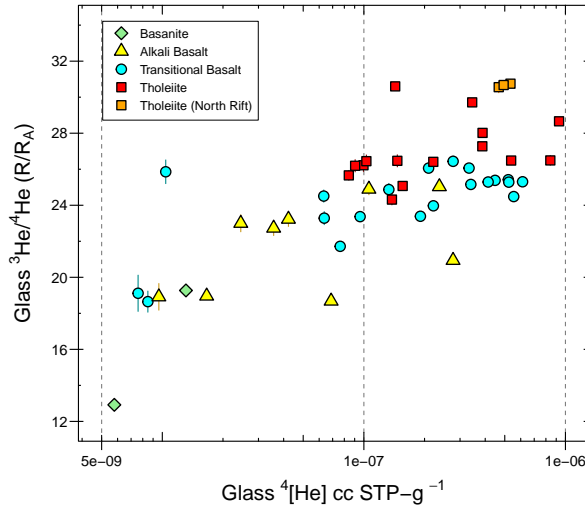
Figure 3.1: Histogram showing distribution of total  ${}^3\text{He}/{}^4\text{He}$  values from combined glass crushing and melting experiments. Red values are literature values from two studies: Kurz et al. (1983),  $n=8$ , and Loewen et al. (2019),  $n=12$ . Blue values are from this study,  $n=51$ .

Melting of the crushed powders yielded a larger range of  ${}^3\text{He}/{}^4\text{He}$  from 15.4–30.7  $\text{R}_A$ .

The amount of He released by melting was generally less than by crushing, typically below  $9 \times 10^{-7} \text{ cm}^3 \text{ STP/g}$  (Fig. 3.2). Samples with the lowest He isotope ratios in the glass ( $\sim 20 \text{ R}_A$ ) commonly had lower He concentrations, lying below  $9 \times 10^{-8} \text{ cm}^3 \text{ STP/g}$ . Helium isotope disequilibrium between vesicles and glass in basalts (Fig. 3.7) is discussed later in this chapter with a means to estimate eruption ages.



(a) Helium isotope ratios in vesicles vs. concentration of  ${}^4\text{He}$  in vesicles.



(b) Helium isotope ratios in vesicles vs. concentration of  ${}^4\text{He}$  in glass.

Figure 3.2: Helium isotope ratios in vesicles vs. concentration of  ${}^4\text{He}$  in vesicles compared between two different methods for vesicle measurement (crushing extraction) and glass measurement (melting extraction). Error bars are shown for  $2\sigma$  (standard deviation), though in most cases, are smaller than symbol size.

### 3.3.2 Major Volatiles: CO<sub>2</sub> and H<sub>2</sub>O

The glass H<sub>2</sub>O concentrations determined by FTIR range from 0.5-1.8 wt % (Table 3.2). The values overlap with concentrations previously reported for other Kama'ehuakanaloa basalts (Kent et al., 1999b; Dixon and Clague, 2001) and their melt inclusions (Kent et al., 1999a). Tholeiites span the narrowest range of H<sub>2</sub>O values and cluster around 0.6-0.9 wt.%, while the majority of alkali basalts typically exceed 1.0 wt %. Two deeply erupted alkali basalts (MIR2335-12 and TUNE 004-D) are anomalous and have H<sub>2</sub>O concentrations of 1.4 and 1.8 wt.%, respectively). H<sub>2</sub>O/Ce ratios (ppm/ppm) generally fall in a narrow range of 160-265, similar to the values of 155-237 reported previously by Dixon and Clague (2001).

Dissolved (glass) CO<sub>2</sub> concentrations determined by FTIR range from 40-260 ppm (Table 3.2). This range is similar to that of 53-258 for 4 South Rift basalts reported by Pietruszka et al. (2011) and larger than the range of 29-92 ppm reported for other Kama'ehuakanaloa basalts (Dixon and Clague, 2001). Vesicle CO<sub>2</sub> concentrations determined by capacitance manometry show large range from less than 1 ppm to 340 ppm. Combining both measurements yields total CO<sub>2</sub> contents (vesicles + glass) that range from 48 ppm to 510 ppm.

Concentrations of H<sub>2</sub>O in Kama'ehuakanaloa glass typically reaches a maximum of 1.01 wt. % (Byers et al., 1985; Garcia et al., 1989; Kent et al., 1999b). In our study, glass H<sub>2</sub>O contents reach a maximum value of 1.9 wt % and occurs in alkali basalt from the TUNE 004D dredge at 4 km. Pietruszka et al. (2011) reported H<sub>2</sub>O = 2.61 wt.% for a tholeiite from 4.7 km (6K 490 dive) and Wieser et al. (2020a) reported H<sub>2</sub>O =

1.87 wt. % for a sample from the same dive. The lowest H<sub>2</sub>O values ~0.48 wt.% occur at shallower depths, around 1-2 km depth in North Rift tholeiites (TUNE 003-D) and East Flank tholeiites (187-8 and 187-9). However, there appears to be little systematic relationship between higher H<sub>2</sub>O contents with depth, as 12 samples from deeper than 4.6 km have values of H<sub>2</sub>O between 0.66-0.94 wt%.

Table 3.2: CO<sub>2</sub>, H<sub>2</sub>O, Cl, S, K, Ti, F Measurements

ID	Sample	CO <sub>2</sub> cc STP/g Vesicle	CO <sub>2</sub> ppm Vesicle	CO <sub>2</sub> cc STP/g Glass	CO <sub>2</sub> ppm Glass	H <sub>2</sub> O ± Glass	Cl wt. (%)	S wt. (%)	K wt. (%)	Ti wt. (%)	F wt. (%)
1	MIR 2335-2	9.63×10 <sup>-4</sup>	1.89	0.129	253	6.40	0.89	0.028	0.078	0.16	0.56
2	MIR 2335-5	2.16×10 <sup>-3</sup>	4.24	0.119	234	16.0	0.88	0.025	0.093	0.17	0.61
3	MIR 2335-6	4.51×10 <sup>-3</sup>	8.85	0.126	248	10.5	0.89	0.027	0.097	0.16	0.61
4	MIR 2335-7	1.99×10 <sup>-3</sup>	3.91	0.124	243	3.42	0.76	0.010	0.079	0.17	0.59
5	MIR 2335-8	1.22×10 <sup>-3</sup>	2.39	0.135	265	2.64	0.79	0.018	0.083	0.18	0.58
6	MIR 2335-9	2.37×10 <sup>-3</sup>	4.65	0.122	239	5.51	0.80	0.009	0.085	0.17	0.58
7	MIR 2335-10	1.67×10 <sup>-4</sup>	0.33	0.125	245	4.19	0.77	0.008	0.083	0.17	0.59
8	MIR 2335-11	1.69×10 <sup>-2</sup>	33.2	0.122	239	21.1	0.94	0.034	0.101	0.18	0.65
9	MIR 2335-12	2.20×10 <sup>-3</sup>	4.32	0.059	115	7.00	1.43	0.040	0.102	0.17	0.40
10	MIR 2336-2	1.01×10 <sup>-2</sup>	19.8	0.113	222	6.00	0.86	0.002	0.095	0.17	0.64
11	MIR 2336-4	2.52×10 <sup>-2</sup>	49.5	0.095	186	7.26	0.98	0.021	0.062	0.19	0.45
12	MIR 2336-5	9.63×10 <sup>-2</sup>	189.0	0.092	180	11.9	0.97	0.006	0.089	0.18	0.63
14	MIR 2337-2	1.71×10 <sup>-2</sup>	33.6	0.066	129	3.20	0.66	0.015	0.082	0.21	0.45
15	MIR 2337-3	3.97×10 <sup>-2</sup>	77.9	0.101	199	2.10	0.75	0.040	0.043	0.19	0.41
16	MIR 2338-1A	2.82×10 <sup>-2</sup>	55.4	0.113	221	2.10	0.91	0.022	0.100	0.18	0.65
17	MIR 2340-1	5.75×10 <sup>-3</sup>	11.3	0.026	51	3.00	0.57	0.027	0.070	0.20	0.45
18	MIR 2340-3	4.86×10 <sup>-4</sup>	0.95	0.030	59	—	0.53	—	0.062	0.18	0.40
19	MIR 2341-1	2.35×10 <sup>-2</sup>	46.1	0.057	112	3.14	0.91	0.017	0.098	0.18	0.60
20	MIR 2341-2	1.49×10 <sup>-2</sup>	29.2	0.048	94	2.42	1.07	0.015	0.094	0.18	0.88
21	MIR 2343-2	6.09×10 <sup>-3</sup>	12.0	0.090	177	12.0	0.96	0.025	0.080	0.21	0.62
22	MIR 2343-3	5.83×10 <sup>-3</sup>	11.4	0.073	144	6.29	0.87	0.015	0.065	0.18	0.61
23	MIR 2343-4	2.96×10 <sup>-2</sup>	58.1	0.074	145	2.42	0.77	0.033	0.063	0.19	0.60
24	MIR 2343-5	1.84×10 <sup>-3</sup>	3.61	0.075	148	4.01	0.92	0.025	0.063	0.19	0.61
25	MIR 2343-6	1.40×10 <sup>-2</sup>	27.5	0.094	184	0.00	0.95	0.018	0.069	0.19	0.82
26	MIR 2343-7	2.28×10 <sup>-3</sup>	4.48	0.075	148	4.01	0.89	0.052	0.064	0.20	0.62
27	MIR 2343-8	5.04×10 <sup>-2</sup>	98.9	0.084	165	2.01	0.81	0.027	0.062	0.19	0.59
28	MIR 2343-10	1.19×10 <sup>-1</sup>	233.6	0.100	197	—	0.87	—	0.061	0.19	0.56
29	MIR 2343-11	4.19×10 <sup>-3</sup>	8.23	0.067	132	4.19	0.86	0.041	0.073	0.20	0.61

CO<sub>2</sub>, H<sub>2</sub>O, Cl, S, K, Ti, F Measurements (continued)

ID	Sample	CO <sub>2</sub> cc STP/g Vesicle	CO <sub>2</sub> ppm Vesicle	CO <sub>2</sub> cc STP/g Glass	CO <sub>2</sub> ppm Glass	H <sub>2</sub> O ± Glass	Cl wt. (%)	S wt. (%)	K wt. (%)	Ti wt. (%)	F wt. (%)
30	MIR 2343-12	4.66×10 <sup>-2</sup>	91.5	0.069	135	6.29	1.24	0.021	0.078	0.21	0.77
31	MIR 2343-13	6.94×10 <sup>-2</sup>	136.2	0.113	222	17.8	1.17	0.123	0.073	0.21	0.74
32	Shinkai 490-8	1.52×10 <sup>-1</sup>	298.4	0.090	176	8.38	0.91	0.087	0.100	0.20	0.46
33	Shinkai 494-1	7.76×10 <sup>-3</sup>	15.2	0.042	82	5.67	0.90	0.050	0.070	0.20	0.66
34	Shinkai 494-2	6.24×10 <sup>-3</sup>	12.2	0.036	70	7.00	0.84	0.010	0.069	0.19	0.65
35	Shinkai 494-3	2.70×10 <sup>-2</sup>	53.0	0.043	85	6.00	1.15	0.016	0.103	0.20	0.93
36	Shinkai 494-4	4.21×10 <sup>-4</sup>	0.83	0.041	81	2.01	1.10	0.028	0.102	0.20	0.91
37	Shinkai 494-5	2.31×10 <sup>-2</sup>	45.3	0.042	83	5.00	0.70	0.041	0.18	0.39	1.71
38	Shinkai 494-6	1.60×10 <sup>-3</sup>	3.14	0.024	48	7.55	0.72	0.009	0.037	0.18	0.36
39	Shinkai 494-7	5.29×10 <sup>-4</sup>	1.04	0.024	47	4.01	0.77	0.036	0.046	0.17	0.37
40	Shinkai 494-8	7.84×10 <sup>-3</sup>	15.4	0.034	66	2.00	0.83	0.084	0.040	0.19	0.41
41	Shinkai 513-3	5.07×10 <sup>-2</sup>	99.5	0.096	188	2.10	0.90	0.053	0.055	0.20	0.49
42	Shinkai 513-4A	1.73×10 <sup>-1</sup>	339.6	0.087	170	11.1	0.95	0.052	0.099	0.17	0.70
43	Shinkai 513-5	7.08×10 <sup>-3</sup>	13.9	0.094	184	4.84	0.80	0.022	0.065	0.17	0.51
44	Shinkai 513-6	5.43×10 <sup>-2</sup>	106.6	0.094	184	17.8	1.01	0.013	0.083	0.17	0.51
45	Shinkai 513-7A	3.90×10 <sup>-2</sup>	76.6	0.099	194	17.0	0.74	0.015	0.046	0.17	0.44
46	Shinkai 515-1	4.53×10 <sup>-2</sup>	88.9	0.062	121	4.36	1.17	0.052	0.077	0.21	0.79
47	TUNE 003D-A	6.08×10 <sup>-2</sup>	119.4	0.029	56	2.00	0.49	0.007	0.011	0.13	0.26
48	TUNE 003D-B	3.24×10 <sup>-2</sup>	63.6	0.021	41	5.00	0.50	0.019	0.010	0.13	0.26
49	TUNE 003D-C	5.64×10 <sup>-2</sup>	110.7	0.025	50	1.00	0.49	0.008	0.010	0.13	0.26
50	TUNE 004D-A	1.72×10 <sup>-1</sup>	337.6	0.052	102	3.63	1.88	0.046	0.097	0.17	0.72
51	TUNE 004D-B	8.39×10 <sup>-2</sup>	164.7	0.063	123	4.84	1.82	0.081	0.096	0.18	0.71
52	TUNE 004D-C	—	—	0.062	122	2.64	1.80	0.025	0.094	0.17	0.69
53	KK 17-2	5.45×10 <sup>-2</sup>	107.0	0.023	45	—	0.93	—	0.068	0.21	0.68
54	KK 20-14	4.42×10 <sup>-2</sup>	86.8	0.021	42	—	0.54	—	0.057	0.17	0.39
55	KK 25-4	3.31×10 <sup>-2</sup>	65.0	0.026	52	—	0.81	—	0.041	0.19	0.50
56	KK 31-9	7.35×10 <sup>-2</sup>	144.3	0.063	124	—	0.77	—	0.034	0.13	0.55
57	KK 31-12	1.13×10 <sup>-1</sup>	221.8	0.057	111	—	0.77	—	0.032	0.10	0.56

CO<sub>2</sub>, H<sub>2</sub>O, Cl, S, K, Ti, F Measurements (continued)

ID	Sample	CO <sub>2</sub> cc STP/g Vesicle	CO <sub>2</sub> ppm Vesicle	CO <sub>2</sub> cc STP/g Glass	CO <sub>2</sub> ppm Glass	H <sub>2</sub> O wt. (%) Glass	±	Cl wt. (%) Glass	S wt. (%) Glass	K wt. (%) Glass	Ti wt. (%) Glass	F wt. (%) Glass
58	Pisces 158-4	3.26×10 <sup>-2</sup>	64.0	0.066	130	—	1.14	—	0.110	0.21	1.44	2.00
59	Pisces 158-5	1.47×10 <sup>-2</sup>	28.9	0.029	57	—	0.86	—	0.043	0.29	0.62	2.30
60	Pisces 186-3	7.79×10 <sup>-2</sup>	152.9	0.025	50	—	0.48	—	0.032	0.21	0.30	1.53
61	Pisces 187-1A	8.30×10 <sup>-2</sup>	162.9	0.047	93	—	0.63	—	0.047	0.15	0.53	1.34
62	Pisces 187-5B	3.39×10 <sup>-2</sup>	66.5	0.024	48	—	0.87	—	0.046	0.17	0.45	1.57
63	Pisces 187-8	3.20×10 <sup>-2</sup>	62.8	0.018	36	—	0.49	—	0.052	0.14	0.35	1.51
64	Pisces 187-9	4.30×10 <sup>-3</sup>	8.44	0.015	30	—	0.48	—	0.049	0.15	0.35	1.51

Cl, S, K, Ti, F measured in glass

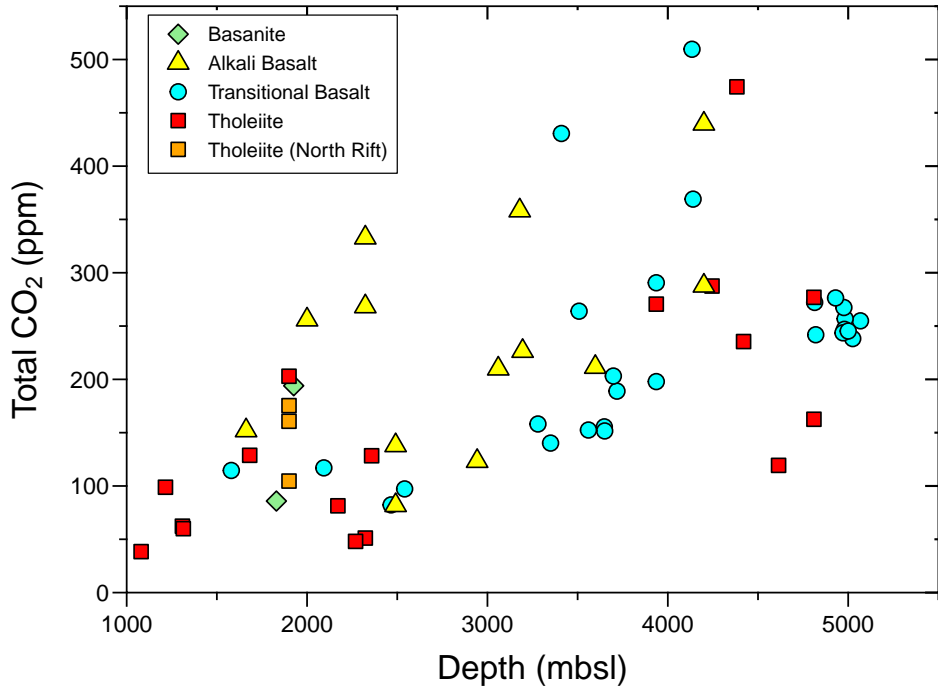


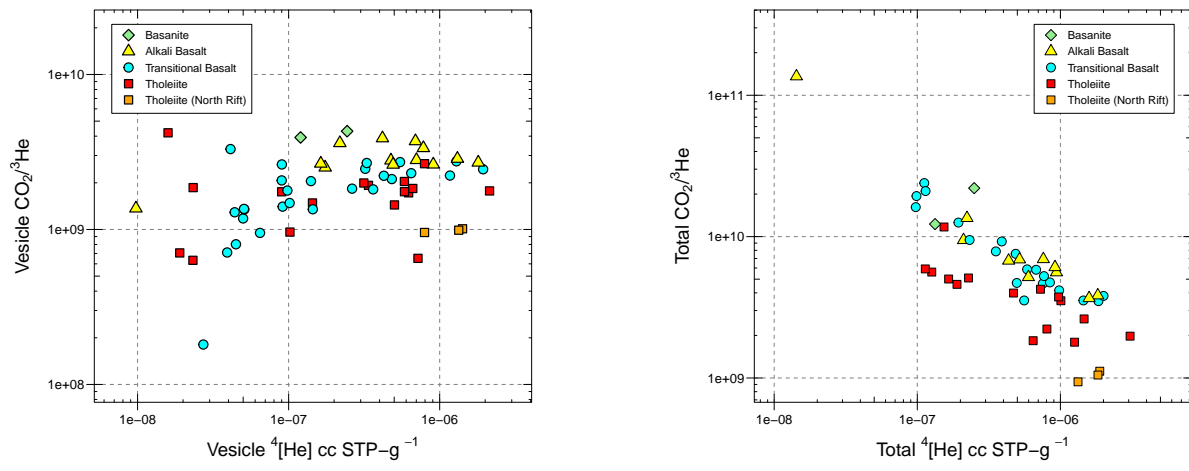
Figure 3.3: Total CO<sub>2</sub> concentrations (combined glass and vesicle), in ppm, vs. collection depth in meters below sea level

The equation to calculate CO<sub>2</sub>/<sup>3</sup>He of glass is described as follows in Equation 3.1:

$$\text{CO}_2/\text{He}_{\text{vesicle}} = \frac{\text{CO}_2 \text{ cc-STP/g, vesicle}}{(\text{He cc-STP/g, vesicle}) \times (1.39 \times 10^{-6})} \quad (3.1)$$

Total determinations are made by adding both together vesicle CO<sub>2</sub>/<sup>3</sup>He ratios, ranging from  $1.8 \times 10^8$  to  $3.6 \times 10^9$ , while glass CO<sub>2</sub>/<sup>3</sup>He ratios range from  $9.2 \times 10^8$  to  $4.6 \times 10^{11}$ . The vesicle CO<sub>2</sub>/<sup>3</sup>He ratios overlap the range of Kama'ehuakanaloa vent fluids from the summit ( $6 \times 10^8$  –  $8 \times 10^9$ ) and from the South Rift ( $2.7 \times 10^9$  –  $4.6 \times 10^9$ ), as reported by Hilton et al. (1998). The total CO<sub>2</sub>/<sup>3</sup>He ratio for the basalts shows an even larger

variation, ranging from  $9.4 \times 10^8$  to  $1.0 \times 10^{11}$ . The  $\text{CO}_2/{}^3\text{He}$  ratios above  $2 \times 10^{10}$  are restricted to samples having low total [He] ( $< 2 \times 10^{-7}$  ccSTP/g), with the highest  $\text{CO}_2/{}^3\text{He}$  ratio ( $> 1 \times 10^{11}$ ) occurring in the sample having the lowest [He] ( $< 2 \times 10^{-8}$  cm<sup>3</sup> STP/g). The lowest  $\text{CO}_2/{}^3\text{He}$  ratios of  $\sim 1 - 2 \times 10^9$  typically occur in samples having the highest He and  $\text{CO}_2$  contents and  ${}^3\text{He}/{}^4\text{He}$  ratios.



(a) Vesicle  $\text{CO}_2/{}^3\text{He}$  (vesicle + glass) vs. Vesicle  ${}^4\text{He}$  concentration

(b) Total  $\text{CO}_2/{}^3\text{He}$  (vesicle + glass) vs. Total  ${}^4\text{He}$  concentration

Figure 3.4:  $\text{CO}_2/{}^3\text{He}$  (vesicle and total) vs.  ${}^4\text{He}$  concentration.

All of the basalts are volatile-oversaturated based on the observed presence of vesicles. However, a few samples show dissolved  $\text{CO}_2+\text{H}_2\text{O}$  pressures estimated from VolatileCalc Newman and Lowenstern (2002) that are considerably less than the hydrostatic pressure at their collection depth. These exceptions are the TUNE 003D tholeiite from the North Rift area (sample volatile pressure =  $\sim 130$  bars vs. collection pressure =  $\sim 190$  bars) and several basalts recovered by Shinkai dive 494 ( $\sim 155$  bars vs.  $\sim 230$  bars). One possible explanation is that these lavas flowed downslope from their original eruption site.

If closed system degassing conditions can be assumed during the end stages of ascent and eruption, then an estimate can be made for the depth level in the crust where a basaltic magma may have last equilibrated. Under these conditions it is appropriate to use the total (vesicle + glass) gas contents measured in a basalt glass. Following this procedure, pressure estimates for the Kama‘ehuakanaloa basalts are shown in Figure 3.16. The measured amounts of  $\text{CO}_2 + \text{H}_2\text{O}$  show a large range, and basalts having the highest total volatile concentrations lie near 1.1-1.2 kbar (corresponding to  $\sim 2.7$  km depth in the crust). Clearly, however, many of the South Rift basalts degassed at shallow level where pressure were  $< 1$  kbar.

### 3.3.3 Other Volatiles (Cl, F)

Chlorine concentrations in the South Rift basalt glasses range from 370 ppm to 1025 ppm, within the range of literature values of 270-1700 ppm (Byers et al., 1985; Garcia et al., 1989; Kent et al., 1999b; Dixon and Clague, 2001). Chlorine values in alkali basalts (500-1025 ppm) and transitional basalts (600-1000 ppm) are often higher compared to tholeiites (370-1000 ppm) but there is overlap between all three groups. In general, there is an overall co-variation of Cl with K (Fig. 3.9). The lowest Cl concentration ( $\sim$ 100 ppm) and Cl/K ratio ( $\sim$ 0.04) occurs in the North Rift tholeiites.

Fluorine concentrations in Kama‘ehuakanaloa basalts range from 370-1040 ppm. F concentrations determined with the electron microprobe are highly uncertain and will not be evaluated further in this work. Early literature data shows a large range of F concentrations from 60-1300 ppm (Byers et al., 1985; Garcia et al., 1989), whereas recent determinations show a range of 342-946 ppm (Schipper et al., 2010; Pietruszka et al., 2011; Wieser et al., 2020a).

### 3.4 Discussion

The deeply erupted south rift basalts at Kama‘ehuakanaloa seamount have clearly witnessed a significant degree of volatile loss during their evolution, based on Helium and C concentrations (Fig. 3.3, 3.4). These processes present a challenge to reconstructing the volatile concentrations in Kama‘ehuakanaloa parental magmas. In the discussion below we employ a range of modeling tools and arguments to constrain volatile degassing and estimate key volatile characteristics of tholeiitic, transitional and alkali basalt compositional end-members at Kama‘ehuakanaloa. In the following discussion, I review the implications of this variability in terms of mixing between recycled and primordial components within the upwelling plume (Blichert-Toft et al., 2003; Kurz et al., 2004; Ren et al., 2005; Abouchami et al., 2005; Bryce et al., 2005; Pietruszka et al., 2013). In addition, I evaluate the possibility that the  ${}^3\text{He}/{}^4\text{He}$  and  $\text{CO}_2/\text{He}$  variations may be related to fractionation during degassing and/or assimilation that has occurred in the evolutionary history of Kama‘ehuakanaloa basalts. Our results have implications for the ultimate origin of volatiles in the deep mantle source of the Hawaiian islands.

#### 3.4.1 Helium Isotope Variability

##### 3.4.1.1 Lithophile Elements

Previous Sr-Nd-Pb isotope studies and trace element studies have been used to argue that both Kama‘ehuakanaloa tholeiitic and alkalic basalts were derived from similar sources (Staudigel et al., 1984; Garcia et al., 1995). However, some of these comparisons have

been limited to the summit and east flank of Kama‘ehuakanaloa (Garcia et al., 1995). Our results indicate a systematic difference between the mean values of  ${}^3\text{He}/{}^4\text{He}$  for South Rift tholeiites and transitional basalts.

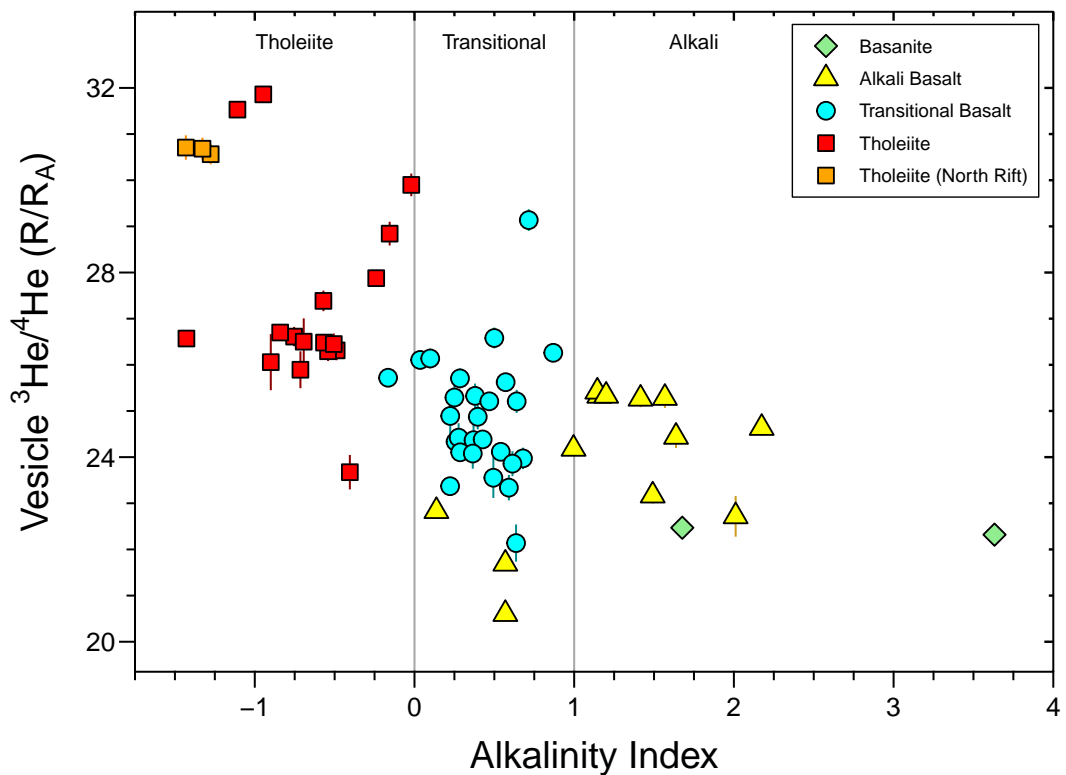


Figure 3.5: Vesicle  ${}^3\text{He}/{}^4\text{He}$  ( $R_A$ ) vs. Alkalinity Index. Equation =  $(\text{Na}_2\text{O} + \text{K}_2\text{O}) - (0.37 \times \text{SiO}_2 - 14.43)$  from (Carmichael et al., 1974)

The  ${}^3\text{He}/{}^4\text{He}$  in Kama‘ehuakanaloa basalts varies by  $\sim 10 R_A$ , and there appears to be a systematic difference between basalt types. The mean  ${}^3\text{He}/{}^4\text{He}$ , by group, for tholeiitic, transitional, and alkalic basalts of South Rift lavas are as follows:  $27.1 \pm 1.3 R_A$  ( $n=10$ ),  $24.9 \pm 1.5 R_A$  ( $n=20$ ), and  $24.6 \pm 0.9 R_A$  ( $n=7$ ), respectively (Fig. 3.6). An unpaired samples t-test for vesicle  ${}^3\text{He}/{}^4\text{He}$  in tholeiite and transitional basalt groups indicates that

they have significantly different mean values ( $p=0.004$ , two-tailed). The alkali basalts exhibit less variance than the transitional basalts, and the difference between their mean values is not statistically significant. However, the mean  ${}^3\text{He}/{}^4\text{He}$  ratio is different in tholeiites compared to both transitional and alkali basalts at the  $>95\%$  confidence level ( $p \leq 0.01$ ).

Table 3.3: Mean Vesicle  ${}^3\text{He}/{}^4\text{He}$  ratios and related statistics among rock types in South Rift

Rock Type	Number of samples	Mean Vesicle ${}^3\text{He}/{}^4\text{He}$	$\pm 1\sigma$	$\pm 2\sigma$
Alkali Basalt	9	24.62	1.02	2.03
Transitional Basalt	26	24.86	1.36	2.73
Tholeiite Basalt	14	26.78	1.45	2.90
Total (all South Rift lavas)	49	25.37	1.59	3.18

Table 3.4: Results from statistical method, two-sided t-test with pairwise comparison of mean values for Vesicle  ${}^3\text{He}/{}^4\text{He}$  of alkali-transitional, alkali-tholeiite, and transitional-tholeiite rock types in South Rift data set.

Group 1 [1]	Group 2 [1]	p-value	Significance level	Lower bound CI [2]	Upper bound CI [2]
Alkali	Transitional	0.583	Not Significant	-1.15	0.66
Alkali	Tholeiite	0.001	** ( $P \leq 0.01$ )	-3.24	-1.09
Transitional	Tholeiite	0.001	** ( $P \leq 0.01$ )	-2.89	-0.95

[1] Group means and number of samples are found in Table 3.3

[2] CI = confidence interval, set to 5% for the lower and 95% for the upper bound

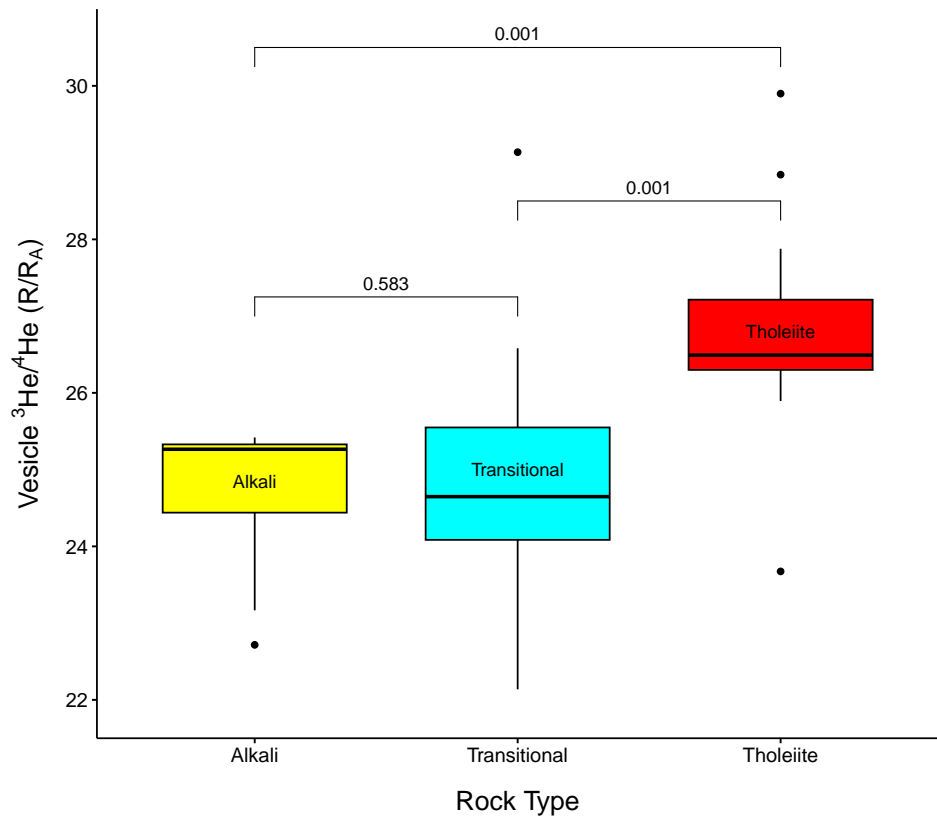


Figure 3.6: Boxplots showing vesicle  ${}^3\text{He}/{}^4\text{He}$  ratios for alkali basalts ( $n=9$ ), transitional basalts ( $n=26$ ), and tholeiite basalts ( $n=14$ ) in South Rift lavas at Kama'ehuakanaloa. The dashed center line shows the grand mean of  $25.4 \pm 1.6 R_A$ . Group means are indicated by the center line in each diamond, with CI0.95 and CI0.05 at top and bottom. Black diamonds show the data distribution of outliers from each group.

### 3.4.1.2 Disequilibrium Helium Isotopes and temporal constraints

The debate about Helium isotope variation in lavas is central to the mantle plume debate and the connection between global geodynamics and intraplate volcanism. While Kama‘ehuakanaloa has been a common representative locality for high- ${}^3\text{He}/{}^4\text{He}$  OIB in multi-isotopic component studies ((e.g., Eiler et al., 1997; Jackson et al., 2020)), the interpretation of  ${}^3\text{He}/{}^4\text{He}$  variation has changed since the early 1980s. Early studies of Kama‘ehuakanaloa lavas yielded isotopically indistinguishable values between vesicles/glass in oceanic basalts (Kurz and Jenkins, 1981; Lupton, 1983). However, disequilibrium between vesicles and glass in later studies (e.g., Rison and Craig, 1981) raised questions of isotope fractionation, precision about He solubility and partitioning, and vesicle/melt differences. Following experiments confirming He partitioning in gas more than melt, Rison and Craig (1981) determined that vesiculation was a factor in producing variable  ${}^3\text{He}/{}^4\text{He}$  ratios, which has significance to measurements determined by crushing and fusion. Isotope studies of other noble gas systems support the origin of Kama‘ehuakanaloa lavas from a unique and likely primitive reservoir, e.g., Valbracht et al. (1996) found mantle Helium and Neon ratios that had not been affected by secondary processes, and indicated different reservoirs than MORB. In summary,  ${}^3\text{He}/{}^4\text{He}$  isotope variation likely reflects a range of shallow processes, yet the signature reflects processes occurring deep mantle components. The following section explores differences in Helium isotopes within the study suite.

Estimated eruption ages can be computed for sample showing significant He isotope disequilibrium between vesicles and glass (Fig. 3.7). The largest extent of isotopic dise-

quilibrium between vesicles and glass occurs in alkalic basalt samples with low He concentrations. Disequilibrium in alkalic samples, exhibited by lower  $R_A$  would be explained by modification of  ${}^3\text{He}/{}^4\text{He}$  in glass by U+Th decay and post-eruptive  ${}^4\text{He}$  ingrowth (Graham et al., 1987). Using the method of Graham et al. (1987), eruption ages can be calculated by using the  ${}^3\text{He}/{}^4\text{He}$  in vesicles and glass, and Helium concentrations and Th/U ratio of the glass. The resulting age estimate is described by the following equation:

$$T = 3.58 \times 10^7 \{[\text{He}]_{\text{glass}}(1 - (R_{\text{glass}}/R_{\text{vesicle}}))(4.35 + \text{Th}/\text{U})\} \quad (3.2)$$

The largest extent of isotopic disequilibrium between vesicles and glass occurs in alkalic basalt samples with low He concentrations. The calculated eruption ages for eight South Rift samples yield a range of 9.1-40.7 kyrs (Table 3.5). The higher range of these estimates are older than the 7.3 kyr estimates for Kama‘ehuakanaloa summit samples from the same Helium isotope disequilibrium method Loewen et al. (2019).

Notably, samples that are assumed to be from the same lava flow (and can be grouped together using major, trace element, and isotopic compositions) show similar ages (e.g., Shinkai 494-3 and 494-4 show computed ages of  $9.1 \pm 1.4$  ( $2\sigma$ ) and  $10.7 \pm 1.7 \times 10^3$  yrs ago (ka), respectively. Two alkali basalt samples of the same lava flow (TUNE 004D dredge) exhibit vesicle  ${}^3\text{He}/{}^4\text{He}$  similar  $\sim 25.4$   $R_A$ . One sample, TUNE 004D-A has a glass  ${}^3\text{He}/{}^4\text{He}$  of 23  $R_A$  while TUNE 004D-B has glass  ${}^3\text{He}/{}^4\text{He}$  of 19  $R_A$ , the latter exhibiting nearly a 25% reduction from the vesicle value. Despite the variation in post-eruptive He addition among the two samples, their eruption ages are similar within error

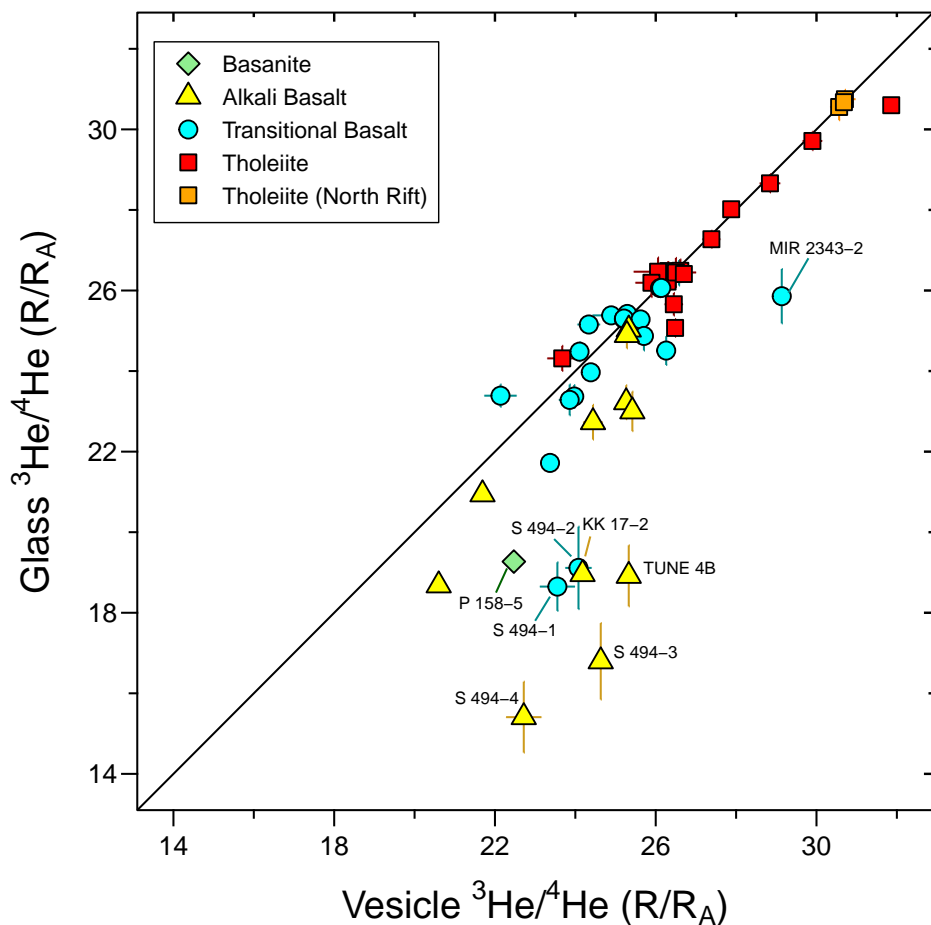


Figure 3.7: Comparison of  ${}^3\text{He}/{}^4\text{He}$  isotope ratios measured in glass (melted, furnace) versus in vesicles (gas extracted from crushing). A 1:1 line is shown for reference, where values plotting in equilibrium plot near the line. Most values that show disequilibrium show higher vesicle ratios than in glass. Detailed eruption age calculations are found in Table 3.5.

( $23.4 \pm 2.9$  ka and  $24.9 \pm 3.5$  ka), attesting to the utility of He isotope disequilibrium ages. Overall, the observed disequilibrium could be explained by modification of  ${}^3\text{He}/{}^4\text{He}$  in glass by U+Th decay and post-eruptive  ${}^4\text{He}$  in-growth in alkalic samples.

Table 3.5: Estimated eruption ages can be computed for samples showing significant He isotope disequilibrium between vesicles/glass

ID	Sample	Rock Type <sup>[1]</sup>	Th/U	$^{3}\text{He}/^{4}\text{He}$ (R <sub>A</sub> ) (vesicle)	$^{3}\text{He}/^{4}\text{He}$ (R <sub>A</sub> ) (glass)	Age (ka) <sup>[2]</sup>
59	Pisces 158-5	BS	3.92	22.47	19.27	22.4
35	Shinkai 494-3	AB	3.48	24.63	16.8	9.1
36	Shinkai 494-4	AB	3.44	22.72	15.4	10.7
51	TUNE 004-B	AB	3.28	25.33	18.92	24.8
53	KK 17-2	AB	3.72	24.18	18.96	33.8
21	MIR 2343-2	TR	3.36	29.14	25.86	12.3
33	Shinkai 494-1	TR	3.00	23.55	18.60	17.2
34	Shinkai 494-2	TR	3.32	24.08	19.11	15.5

<sup>[1]</sup> Rock types are abbreviated to BS = Basanite, AB = Alkali Basalt, TR = Transitional Basalt, and TH = Tholeiite Basalt

<sup>[2]</sup> ka = thousands of years ago. Eruption age is given by [Graham et al. \(1987\)](#) using Equation 3.2

### 3.4.2 Causes of Major Volatile Variations

#### 3.4.2.1 Secondary addition and seawater contamination

Magmas associated with enriched MORB and OIB environments displaying higher H<sub>2</sub>O may reflect fractional crystallization and/or assimilation of altered oceanic crust ([Wallace et al., 2015](#)). Previous studies finding elevated H<sub>2</sub>O in Kama‘ehuakanaloa picrites~1.5 wt.% have been hypothesized to reflect contributions from brines into melt in earlier stages of magmatic evolution ([Frey et al., 1997](#); [Norman and Garcia, 1999](#)). In this study, deeply erupted lavas (MIR2335-12 and TUNE 004-D) contain the highest dissolved H<sub>2</sub>O contents of 1.4 and 1.8 wt.%, respectively. In addition, they show H<sub>2</sub>O/Ce ratios~400 (Fig. 3.10), among the highest observed at Kama‘ehuakanaloa, and higher than the typical range of up to 300 observed in global MORB and OIB ([Wallace et al., 2015](#)). The ratio

of  $K_2O/P_2O_5$  is also elevated for alkalic and transitional basalts at Kama‘ehuakanaloa (Fig. 2.13a and correlates with MgO.

Elevated  $H_2O$  contents occurring from low degree melts or fractionation at previous Kama‘ehuakanaloa studies are consistent with 20% crystallization and up to 18% olivine fractionation. While Kent et al. (1999b) considered seawater alteration unlikely when the analyzed glasses appeared fresh under petrographic inspection, a seawater-derived phase may be incorporated prior to eruption in a magma chambers, possibly due to assimilation after crater collapse (Kent et al., 1999b). This signature would be consistent with elevated  $H_2O$  and Cl contents in glasses and olivine hosted melt inclusions.

$H_2O/K_2O$  in our sample set ranges from 0.93-2.72. Unlike Dixon and Clague (2001), there are no values lower than 0.50, which would indicate degassing of  $H_2O$ . Intermediate values of  $\sim 0.90$  are consistent with a mantle source that is depleted in  $H_2O$  (Davis et al., 2003). Davis et al. (2003) found that in submarine Kilauea, there was a slight correlation of Cl with water depth.

Assimilation (Cl/K) vs. source composition is evaluated by modeling results of seawater/brine and plume melts. Endmember compositions are shown in Table 3.6.

Table 3.6: Endmember compositions for brine assimilation model

	${}^4\text{He}$ (cc STP/g)	Cl (wt.%)	$\text{K}_2\text{O}$ (wt.%)	${}^3\text{He}/{}^4\text{He}$ (R <sub>A</sub> )	Cl/K
Lava [1]	$1.4 \times 10^{-6}$	0.01	0.26	32	0.031
Deep Seawater [2]	$4.5 \times 10^{-8}$	1.94	0.04	1.0	48.4
50 wt. % NaCl Brine 1 [3]	$4.0 \times 10^{-8}$	30.3	0.78	1.0	38.8
50 wt. % NaCl Brine 2 [3]	$4.0 \times 10^{-9}$	30.3	0.78	1.0	38.8

[1] Highest He concentration from TUNE 003 Tholeiite, and average tholeiite primary melt K (ppm) and Cl (wt.%) estimates in Table 2.7. Highest  ${}^3\text{He}/{}^4\text{He}$  from Kurz et al. (1983)

[2] He and  ${}^3\text{He}/{}^4\text{He}$  from Allègre et al. (1987). Chlorine and  $\text{K}_2\text{O}$  from Kent et al. (1999b)

[3] Kent et al. (1999a,b)

Results shown in Figure 3.8 show mixtures of Lava and Brine 1 at fractions of lava, f, with steps between 0.00-0.10 and 0.90-1.00 at increments of 0.01, and steps between 0.10-0.90 in increments of 0.10. A mixture of > 10% NaCl brine assimilation to plume-like melts shows an increase in Cl/K. However, brine assimilation has a negligible effect on  ${}^3\text{He}/{}^4\text{He}$  given what was measured (the glass Cl concentrations and  ${}^3\text{He}/{}^4\text{He}$ ), and hence, brine assimilation appears to play no role in the differences observed in  ${}^3\text{He}/{}^4\text{He}$ .

Kent et al. (1999a) measured high Cl contents in Kama‘ehuakanaloa pillow rim glasses and proposed shallow assimilation of variable amounts of seawater-derived hydrothermal brines. Hauri et al. (2002) also found systematically high Cl contents and high Cl/ $\text{K}_2\text{O}$  ratios in Kama‘ehuakanaloa melt inclusions, including one melt inclusion with higher Cl than the glass that indicated NaCl-saturation. Since high  $\text{H}_2\text{O}$  contents are not always found with excess Cl in Kama‘ehuakanaloa glasses, an assimilated hydrous component may not be common. Higher Cl can also signal the presence of deeply recycled crustal components, enriched in Cl from hydrothermal alteration and incorporated into a mantle

plume source Wallace et al. (2015). Water concentrations in the majority of our sample set are high enough and  $\text{H}_2\text{O}/\text{K}_2\text{O}$  is moderate, hence, significant shallow assimilation is not expected.

$\text{Cl}/\text{K}$  is expected to remain constant during crystallization and mantle melting, and increase with assimilation of altered material (Konrad et al., 2018a).  $\text{Cl}/\text{K}$  ratios of this study suite show that most samples lie between  $\text{Cl}/\text{K}$  of 0.04 to 0.21 (Fig. 3.9).  $\text{Cl}/\text{K}_2\text{O}$  ratios in the least contaminated Kama‘ehuakanaloa glasses are comparable to Mauna Loa glasses, and have similar mantle H isotope values, and high Cl may originate from lower degree of partial melting of Kama‘ehuakanaloa compared to Kīlauea and Mauna Loa, and not to a Cl-rich source (Davis et al., 2003). Mantle source estimates of Kama‘ehuakanaloa lavas in this study (Table 2.9) show the lowest Cl in North Rift tholeiite glasses, which formed from the highest degree of partial melting (Table 2.19). Though degassed in  $\text{CO}_2$ , low parental and mantle source estimates of  $\text{Cl H}_2\text{O}$ , with high He concentrations and high- ${}^3\text{He}/{}^4\text{He}$  in tholeiite glasses suggest an origin from less contaminated primitive, high- ${}^3\text{He}/{}^4\text{He}$  signature-bearing Kama‘ehuakanaloa mantle source.

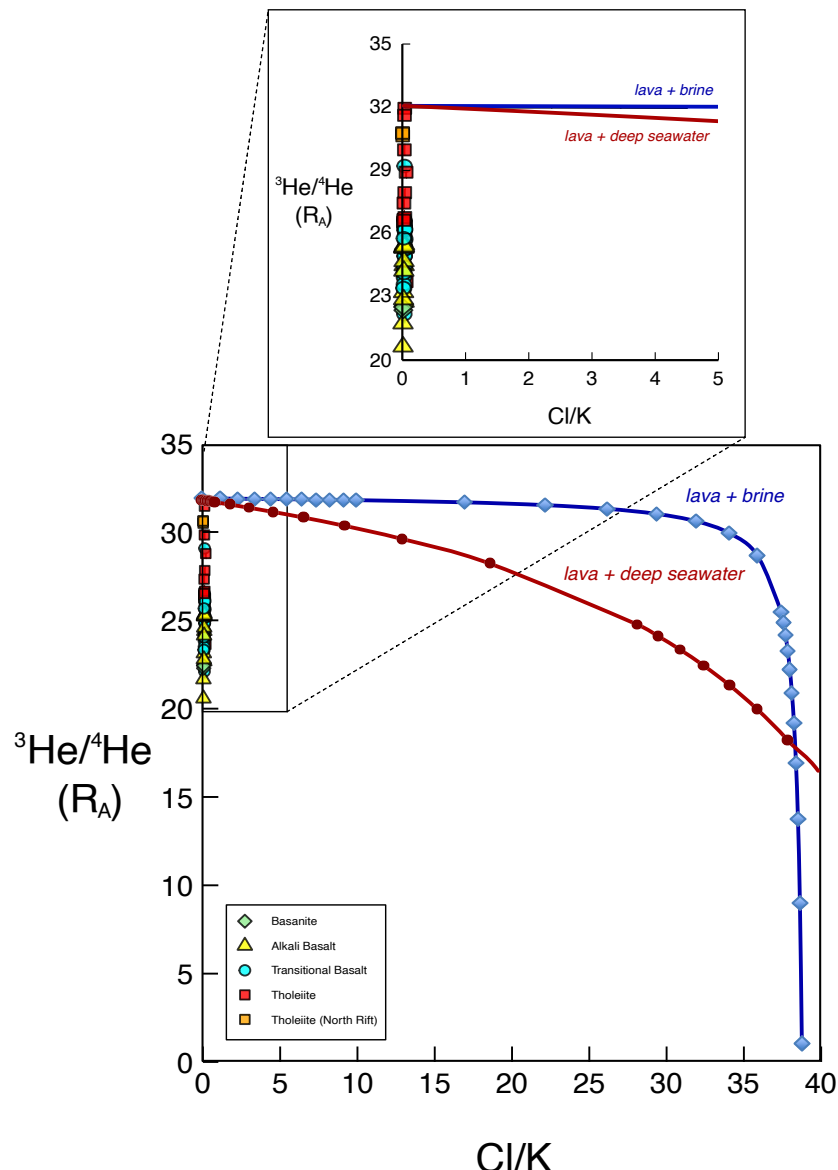


Figure 3.8: Modeling assimilation with Lava and Brine mixture (blue) and Lava and deep seawater (red). Endmember compositions used are in Table 3.6. Points indicate Lava-Brine mix at fractions of lava,  $f$ , where  $f=0$  indicates 100% lava. Steps between 0.00-0.10 and 0.90-1.00 at increments of 0.01, and steps between 0.10-0.90 in increments of 0.10. Full calculation results are in Table B.3.

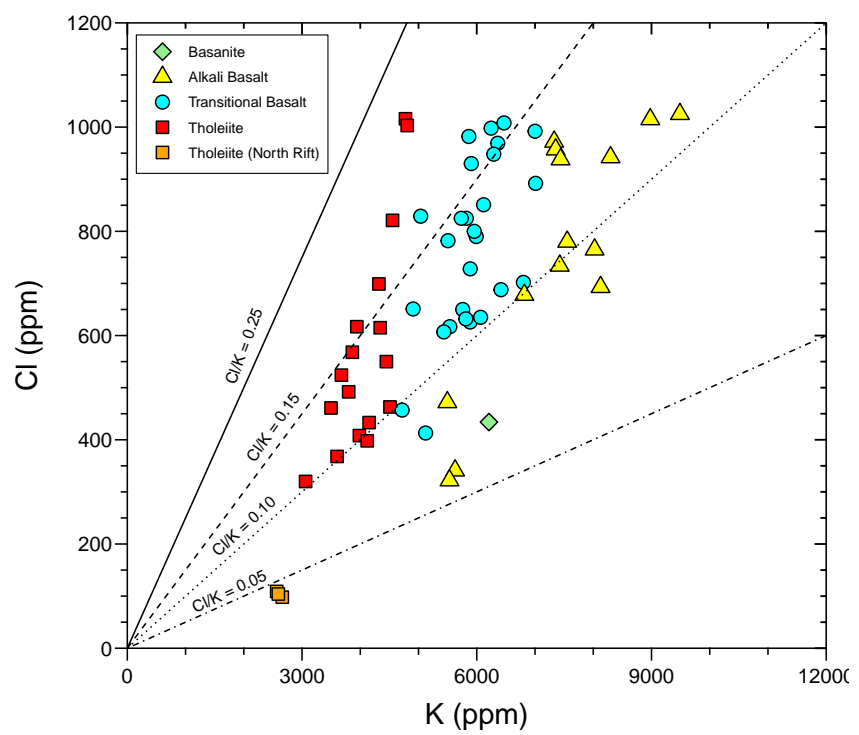


Figure 3.9: Cl (ppm) vs. K (ppm)

### 3.4.2.2 Source variation

High K/Ti can be used as an indicator of mantle enrichment (Michael and Cornell, 1998). Parental melt and mantle source estimates were calculated in Chapter 3 for South Rift transitional basalts and tholeiites, as well as North rift tholeiites.

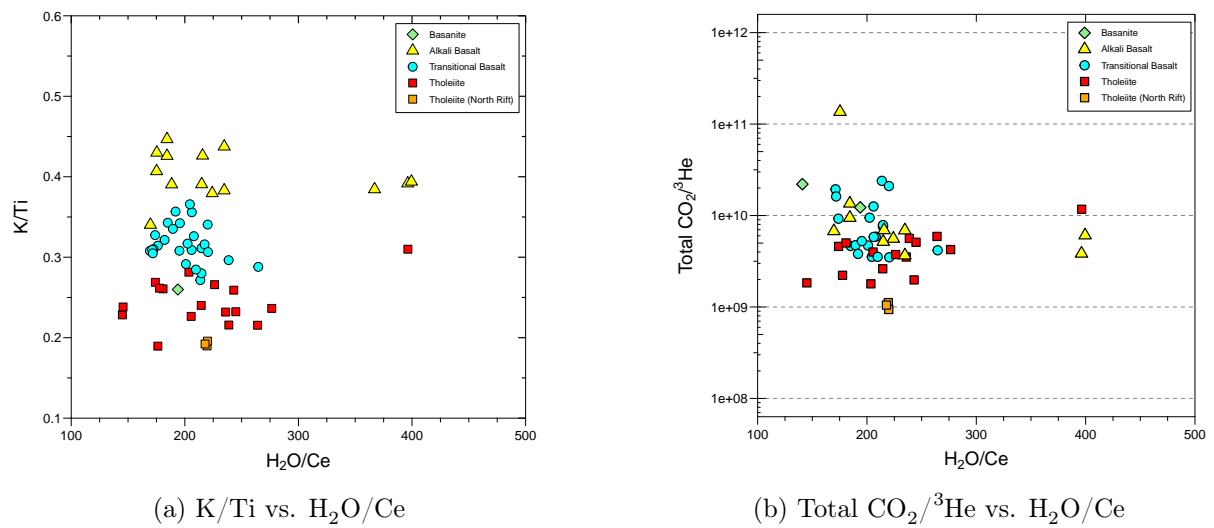


Figure 3.10: K/Ti vs.  $\text{H}_2\text{O}/\text{Ce}$  and total  $\text{CO}_2/\text{He}$  vs.  $\text{H}_2\text{O}/\text{Ce}$  both showing TUNE-4D (A,B,C) and MIR 2335-12 near maximum values of  $\text{H}_2\text{O}/\text{Ce} \sim 400$

The similar behavior among incompatible elements and  $\text{H}_2\text{O}$  during mantle melting and basaltic magma differentiation allows for the interpretation that Ba/Nb and  $\text{H}_2\text{O}/\text{Ce}$  represent mantle source values as per Dixon et al. (2017).

### 3.4.2.3 CO<sub>2</sub> degassing

The observed enrichment and heterogeneities of volatiles (noble gases, CO<sub>2</sub>, H<sub>2</sub>O, S) in plume locality basalts remains poorly understood, though extremely relevant to hypotheses about plume structure. Complex processes affecting volatile enrichment include migration from the plume in a separate liquid phase of CO<sub>2</sub> and H<sub>2</sub>O, mixing of source regions that have different volatile contents, and shallow-level assimilation or shallow-level degassing. The range of CO<sub>2</sub> and H<sub>2</sub>O concentrations in Kama‘ehuakanaloa lavas may also indicate underlying variations in primitive magmas and mantle sources. The majority of samples are CO<sub>2</sub>-oversaturated relative to hydrostatic pressure, and have experienced some amount of degassing from the original gas composition.

Inferred maximum CO<sub>2</sub>/Ba and CO<sub>2</sub>/Nb ratios in melt inclusions at Kama‘ehuakanaloa and other Hawaiian volcanoes are lower than typical global mantle domains (Tucker et al., 2019). The range of ratios indicate that most magmas have likely experienced variable, though large amounts of degassing. Earlier studies of major volatile variations (primarily H<sub>2</sub>O and CO<sub>2</sub>) showed that several stages of closed vs. open-system degassing occurred in the evolution of Kama‘ehuakanaloa summit magma Dixon and Clague (2001) and we follow and extend the arguments of that work to our new results for the deep rift basalts.

One method to calculate the extent of degassing by comparing the sample’s CO<sub>2</sub> to a non-volatile incompatible trace element, such as Ba. Kama‘ehuakanaloa basalts have Ba concentrations of up to 366 ppm, and measured CO<sub>2</sub>/Ba ratios ranging from <0.1-3.2 (Fig. 3.11). Assuming the mantle source has an original CO<sub>2</sub>/Ba = 105 typical of oceanic

basalts (Michael and Graham, 2015), the Kama‘ehuakanaloa samples have lost nearly all (up to 99.9%) of the original  $\text{CO}_2$  inventory, with the least degassed sample retaining 3% of pre-eruptive  $\text{CO}_2$  contents. Despite the high surrounding pressure, deeply erupted glasses that experienced shallow degassing show  $\text{CO}_2/\text{Ba} = 3.7$ , much lower than an undegassed reference ratio of  $\text{CO}_2/\text{Ba} = 105$  Michael and Graham (2015). The observed slope relative to the reference slope shows that the least degassed samples still lost >95% of original  $\text{CO}_2$ .

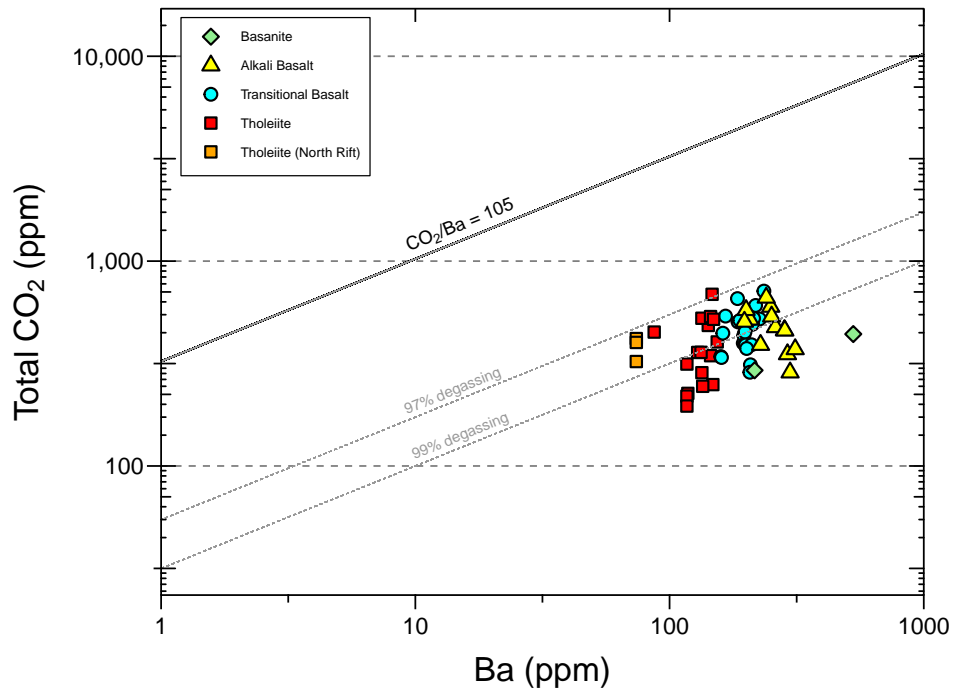


Figure 3.11: Total  $\text{CO}_2$  (ppm) vs.  $\text{Ba}$  (ppm) shown with undegassed reference line from compositions from Michael and Graham (2015) where an estimate of undegassed representative samples correspond to a  $\text{CO}_2/\text{Ba} = 105$ . Degassing line of 97% degassing corresponds to  $\text{CO}_2/\text{Ba} = 3$ , and 99% degassing corresponds to  $\text{CO}_2/\text{Ba} = 1$ .

A large amount of  $\text{CO}_2$  loss has occurred based on the occurrence of low  $\text{CO}_2/\text{Ba}$

ratios (order of 1) in the South Rift basalt glasses compared to a value that is generally accepted for the mantle (order of 100), and this complicates any simple reconstruction of primary volatile characteristics in the mantle plume source. The observed difference in  ${}^3\text{He}/{}^4\text{He}$  and  $\text{CO}_2/{}^3\text{He}$  ratios between tholeiitic/transitional basalt and alkali basalt magmas may be a fundamental feature of heterogeneity in the mantle plume source.

Comparing the  $\text{CO}_2/{}^3\text{He}$  ratio with the fraction of total  $\text{CO}_2$  in vesicles shows little relationship, hence, the ratio is controlled by  ${}^3\text{He}$ , which may reflect variations in the primitive magma/mantle source of the rocks. Hilton et al. (1998) proposed that large systematic changes in  $\text{CO}_2/{}^3\text{He}$  from vent fluids at Kama‘ehuakanaloa coincide with abrupt, and recent changes in the melting regime, where high ratios indicate recent alkalic magma (possibly by injection) in the summit region, instead of low  $\text{CO}_2/{}^3\text{He}$  ratios from previous tholeiitic magma degassing. However, the  $\text{CO}_2/{}^3\text{He}$  ratio is subject to fractionation because the solubility of  $\text{CO}_2$  is greater than solubility of He in water.

Dixon (1997) demonstrated that  $\text{CO}_2$  partitioning into the vapor phase relative to  $\text{H}_2\text{O}$  was weaker in alkalic melts during closed system degassing. Hence, they will lose less  $\text{CO}_2$  and lose more  $\text{H}_2\text{O}$  than tholeiitic magmas as volatiles are exsolved.

Magma ascent rates and lava flow emplacement times affect gas loss due to different cooling rates and hydrothermal interaction. Vesicularity,  $\text{CO}_2$  and combined  $\text{CO}_2/\text{He}$  have been related to syn-eruptive degassing, and variation in these can reflect differences in magmatic ascent rates and lava emplacement within co-genetic lava suites (Graham et al., 2018; Jones et al., 2018). For example, studies of a single East Pacific Rise eruption show that vesicle  $\text{CO}_2/{}^3\text{He}$  in glasses are higher in regions further from eruptive vents (Graham et al., 2018).

Volatile modeling in basalts requires considerations for major element compositions and solubility of major volatile species in order to generate appropriate estimates for equilibration depth. This study's major element compositions are shown with calculations for the North Arch compositional parameter according to Dixon (1997) in Figure 3.13, and shows good agreement with the trend of North Arch lavas. A comparison of total saturation pressures to compare results from MagmaSat (Ghiorso and Gualda, 2015) and VolatileCalc (Dixon, 1997; Newman and Lowenstern, 2002) from VESIcal (Iacovino et al., 2021; Wieser et al., 2022) are shown in Figure 3.12.

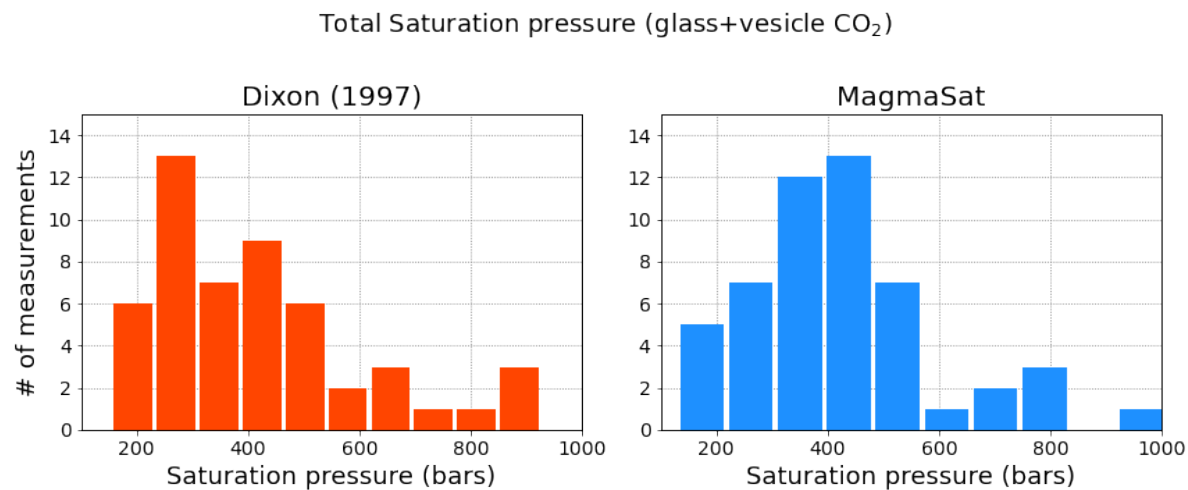


Figure 3.12: Histogram of Total Saturation Pressures to compare MagmaSat mixed-volatile solubility model in MELTS (Ghiorso and Gualda, 2015) and VolatileCalc (Dixon, 1997; Newman and Lowenstern, 2002). Output generated by thermodynamic solubility modeling tool VESIcal (Iacovino et al., 2021; Wieser et al., 2022)

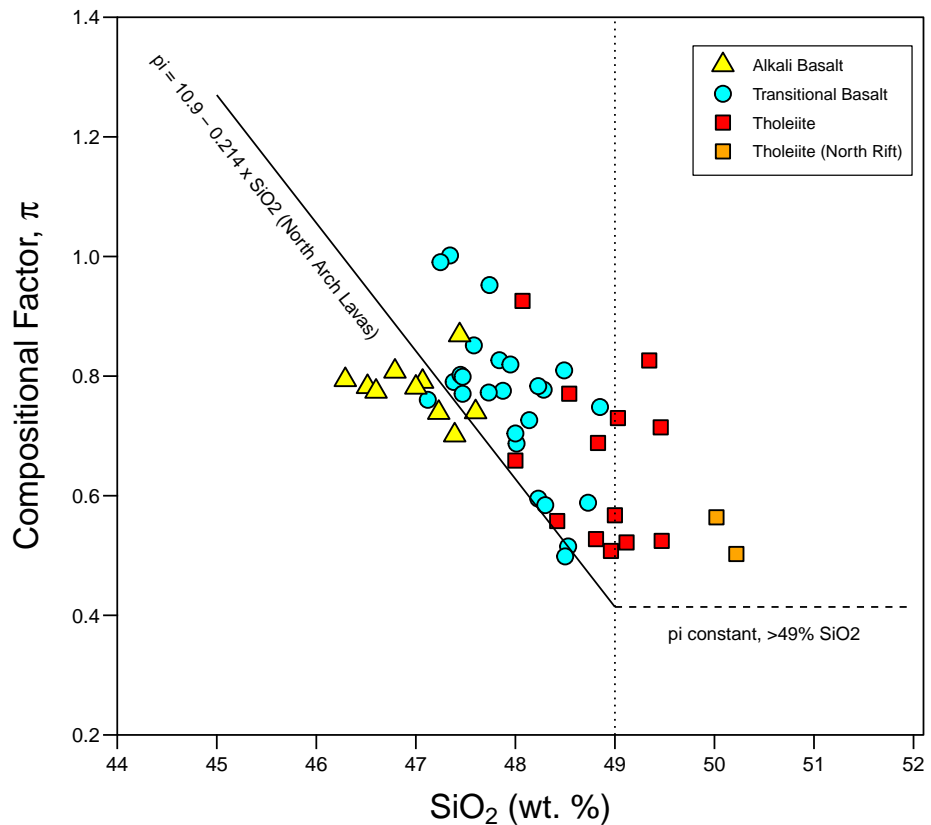


Figure 3.13: Values of  $\pi$  for Kama'ehuakanaloa glasses vs. SiO<sub>2</sub>, compared with best fit line calculated for glasses from the North Arch volcanic field from Dixon (1997). Equations to calculate  $\pi$  from same source. At SiO<sub>2</sub>>49 wt.%, the value is constant at ~0.4

### 3.4.2.4 Degassing and Vesicle-Melt Partitioning of He-CO<sub>2</sub>

Degassing regimes, specifically, kinetic disequilibrium effects, are revealed by partitioning of He and CO<sub>2</sub> between dissolved and vesicle phases due to solubility differences. Our results show that the CO<sub>2</sub>/<sup>3</sup>He ratio varies by a factor of 6X in vesicles and 500X in total CO<sub>2</sub>/<sup>3</sup>He (vesicles + glass) measurements. The difference suggests variable partitioning of He and CO<sub>2</sub> within the glass and vesicles. The relative behavior of He and CO<sub>2</sub> can be observed throughout the process of vesiculation, where they may preferentially partition into newly formed vapor phases. Hence, fractionation of the different gases may be observed as a byproduct of kinetic disequilibrium in Kama‘ehuakanaloa basalts, which vary in vesicularity from <1% up to 20%.

To evaluate the extent of vesicle-melt partitioning for the Kama‘ehuakanaloa suite, we compare the He and CO<sub>2</sub> concentrations in vapor vs. melt (Figure 3.14). According to vapor-melt partitioning by Henry’s Law, samples lying along a line with the slope of ~0.5-0.7 show joint He-CO<sub>2</sub> solubility equilibrium (slope is computed by the inverse solubility of He/CO<sub>2</sub>). A departure from plotting on the Henry’s law region indicates disequilibrium behavior of either He or CO<sub>2</sub>. Figure 3.14 shows that Kama‘ehuakanaloa basalts are not in solubility equilibrium, indicating the gas phase is relatively enriched in He relative to CO<sub>2</sub> (some samples show nearly 10-20X partitioning of He in vesicles). Tholeiites plot closest to the Henry’s Law field suggest more coherent behavior of gas species in the glass and vesicle phases, but still exhibit deviation from equilibrium conditions.

Non-equilibrium (kinetic) degassing has modified the CO<sub>2</sub>/<sup>3</sup>He ratio of Kama‘ehuakanaloa deep rift samples by preferential loss of <sup>3</sup>He. Hence, highly degassed samples

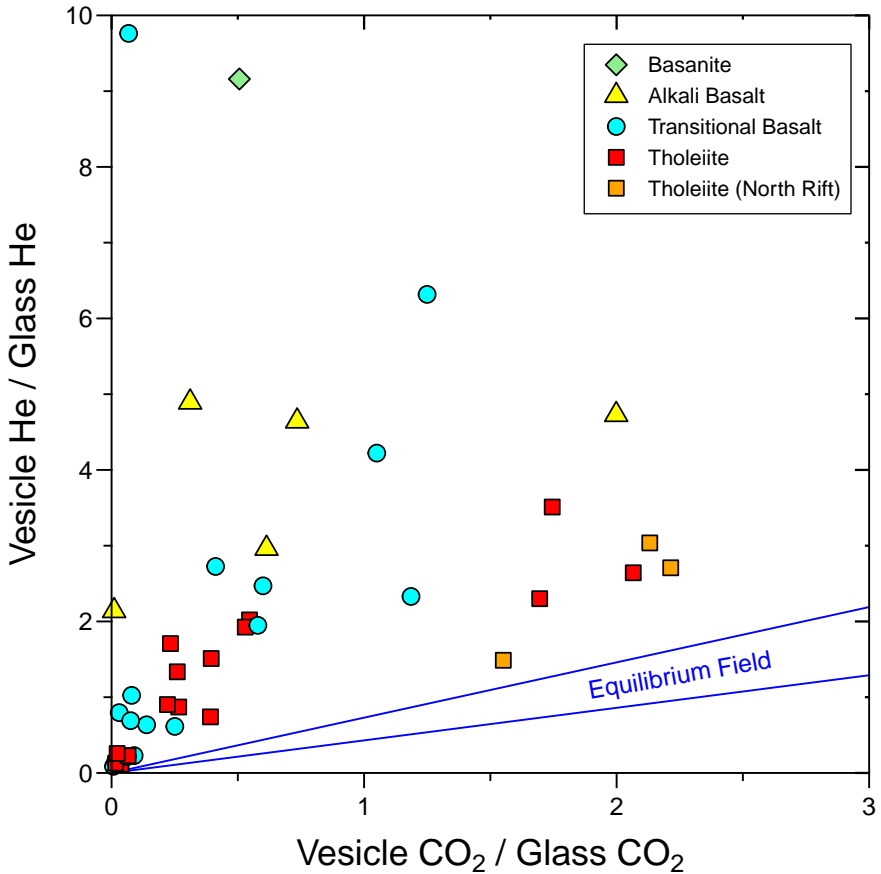


Figure 3.14: Vesicle He/Glass He vs. Vesicle CO<sub>2</sub>/Glass CO<sub>2</sub> and Equilibrium Partitioning Field, with solubility values explained in [Graham et al. \(2018\)](#)

likely show the highest CO<sub>2</sub>/<sup>3</sup>He due to this loss, and their ratio does not reflect the source. Low He concentrations are consistent with preferential loss of He during degassing, hence pre-eruptive bubble loss will result in residual magmas having higher CO<sub>2</sub>/<sup>3</sup>He. This is consistent with the proposal by [Gonnermann and Mukhopadhyay \(2007\)](#) that fractionation of CO<sub>2</sub> and <sup>3</sup>He is larger in ocean island basalts as a consequence of their higher CO<sub>2</sub> content and increased helium loss.

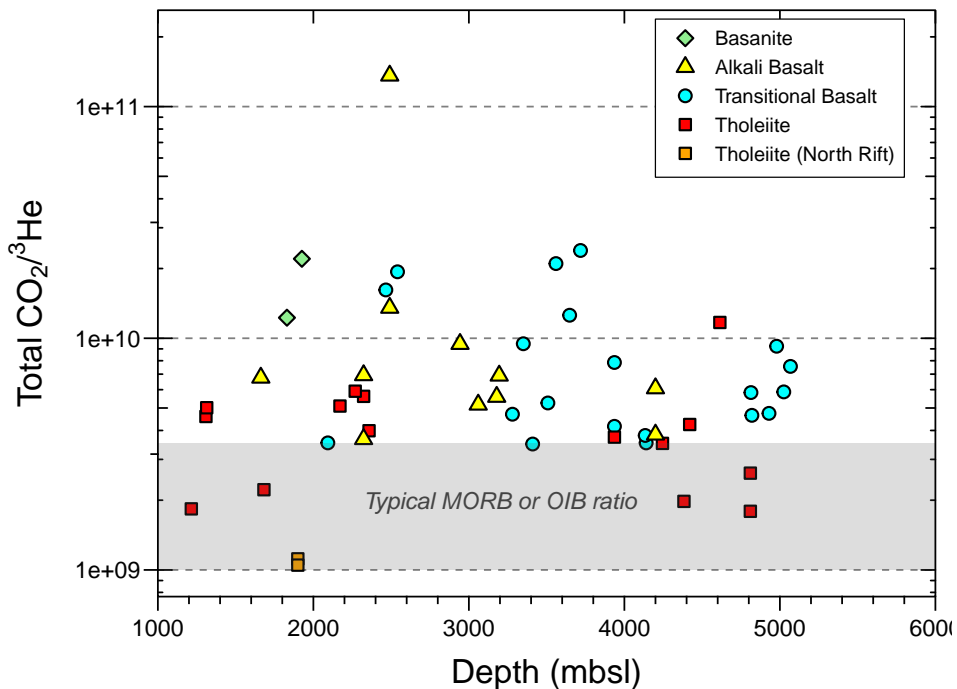


Figure 3.15: Total  $\text{CO}_2/\text{He}$  vs. Depth (meters below sea level), with typical MORB or OIB field between  $\times 10^9$  and  $3 \times 10^9$  (Marty and Jambon, 1987)

Isobars generated at 1200°C using VolatileCalc (Dixon et al., 1995; Dixon, 1997; Newman and Lowenstern, 2002) using total  $\text{CO}_2$  and dissolved  $\text{H}_2\text{O}$  contents show that Kama‘ehuakanaloa glasses plot near 0.5-1.0 kbar pressures. Samples with higher measured total  $\text{CO}_2$  plot closer to the 1.0 kbar curve. These indicate that Kama‘ehuakanaloa basalts degassed at pressures of <0.2-1.3 kbar (Fig. 3.16). The least degassed samples correspond to equilibration depths of 1.7-2.3 km, much shallower than the proposed magma chamber depth of 8 km by Garcia et al. (2006). This is consistent with the model of Dixon and Clague (2001) where during the pre-shield to shield transition, Kama‘ehuakanaloa melts originate from shallower, immature magma reservoirs at the base of the crust (cor-

responding to depths of 1-3 km below the summit), and mantle source, melting, and crystallization heterogeneity can be preserved despite rapid volcano growth. The range observed by tholeiites from high to low H<sub>2</sub>O with lower CO<sub>2</sub> and shallower equilibration depth is consistent with open-system degassing, whereas uniform H<sub>2</sub>O of transitional basalts is more consistent with closed-system degassing (Newman and Lowenstern, 2002). Significant quantities of CO<sub>2</sub> measured from hydrothermal fluids (Sedwick et al., 1992; Hilton et al., 1998) are consistent with persistent open-system degassing, and possible storage in shallow magmatic intrusions.

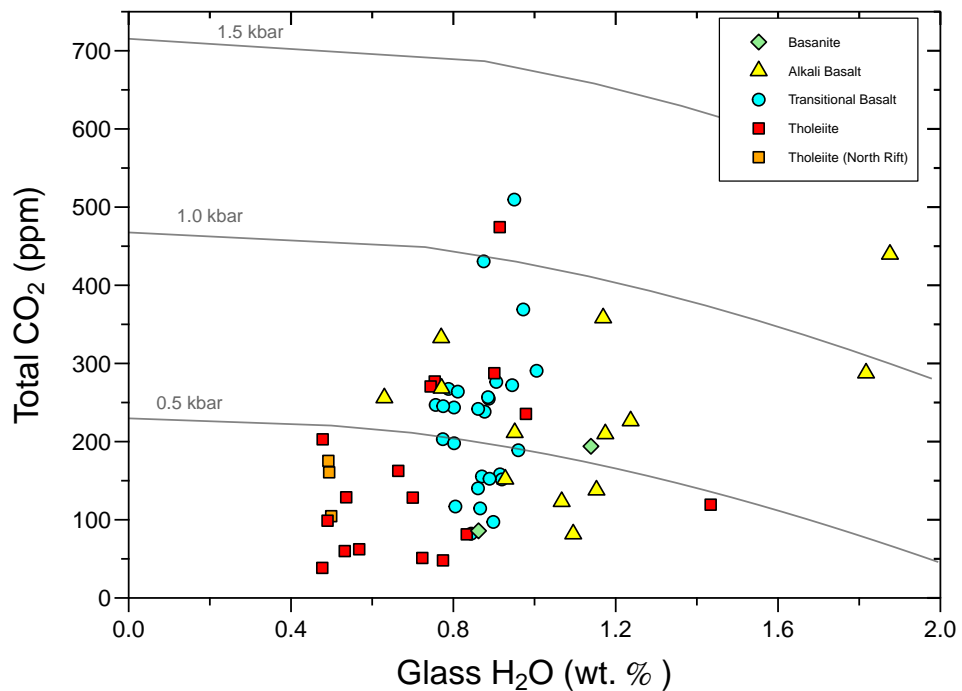


Figure 3.16: Total CO<sub>2</sub> (ppm) vs. glass H<sub>2</sub>O (wt.%) composition of glasses plotted with calculated VolatileCalc (Dixon et al., 1995; Dixon, 1997; Newman and Lowenstern, 2002) basalt isobars representing melt compositions of CO<sub>2</sub>-H<sub>2</sub>O at varying pressures of 0.5, 1.0, 1.5, and 2.0 kbars and T=1200°C.

### 3.4.3 Helium and Petrogenesis

REE modeling results from Chapter 2 suggest that South Rift lavas derive from a similar mantle source that experienced variable extents of depletion by prior melt extraction. Modeling indicates that South Rift and East Flank tholeiites were derived by 8-12% partial melting initiated at various depths within garnet and spinel lherzolite stability fields. Notably, a North Rift tholeiite was generated by higher amounts of melting, at least 12%. Moreover, other trace element ratios and indicators of enrichment were lowest for this sample. This sample is unique for high- ${}^3\text{He}/{}^4\text{He}$  30.7 R<sub>A</sub>, high CO<sub>2</sub> concentrations and low Cl despite the North Rift's relatively shallow depth and proximity to the summit. This contrasts with earlier ideas of increased asthenosphere input and lowering of  ${}^3\text{He}/{}^4\text{He}$  as shield-building proceeds.

#### 3.4.3.1 Refractory elements show evidence for and against recycling

The relationship of  ${}^3\text{He}/{}^4\text{He}$  with immobile, refractory trace elements has been used to evaluate the components hosted by the primitive reservoirs of high- ${}^3\text{He}/{}^4\text{He}$  localities, for example, positive anomalies in "TiTa<sub>N</sub>" (Ti, Ta, Nb) elements in OIB lavas may reflect rutile-bearing subducted oceanic crust in mantle plume-fed ocean islands (Jackson et al., 2008). Hawaiian lavas generally show poorer correlations for Ta anomalies ( $R^2 = 0.29$ ,  $n = 25$ ) compared to Ti and Nb ( $R^2$  up to 0.74,  $n = 32$ -35) (Peters and Day, 2014). Comparing this study's sample set for Ta/Ta\* (Jackson et al., 2008) anomalies vs. vesicle  ${}^3\text{He}/{}^4\text{He}$  in Figure 3.17 shows a slight positive trend with  $R^2 = 0.39$ , suggesting greater coherence between  ${}^3\text{He}/{}^4\text{He}$  and TiTa<sub>N</sub> anomalies. However, consideration for

partitioning behavior of trace elements, especially in clinopyroxene, is needed to evaluate if the mantle source of Kama'ehuakanaloa lavas retains a similar relationship.

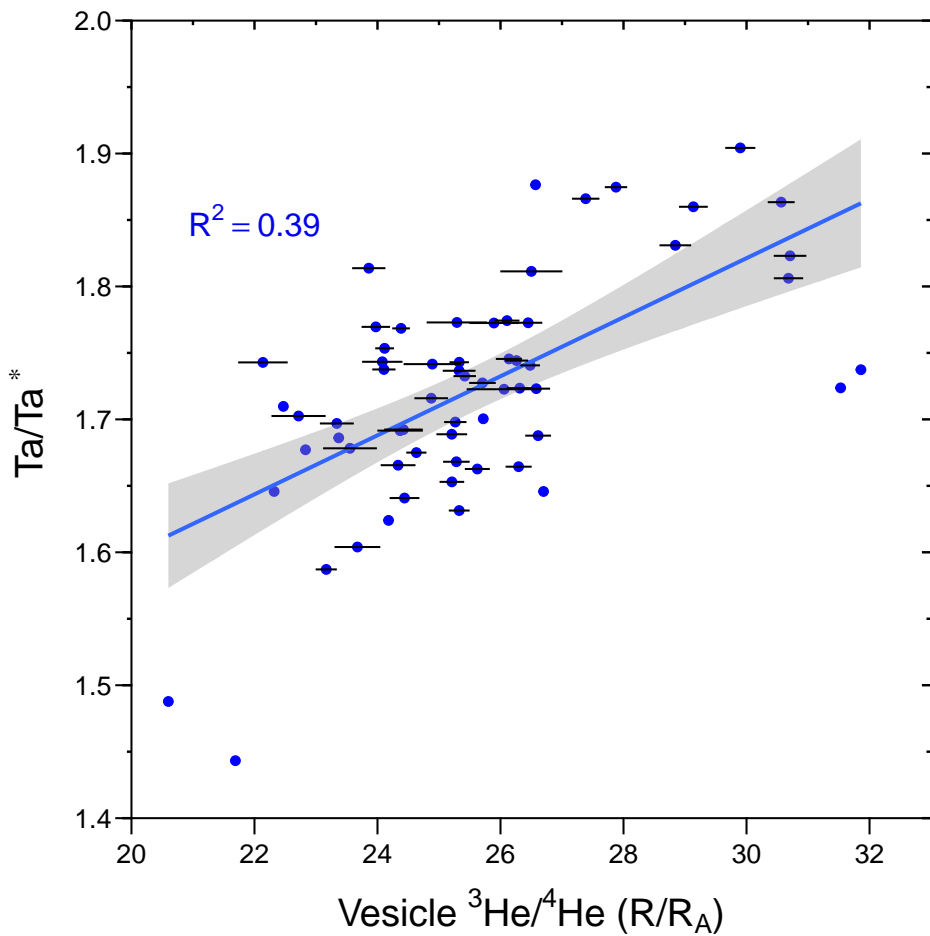


Figure 3.17:  $Ta/Ta^*$  anomaly vs. Vesicle  ${}^3\text{He}/{}^4\text{He}$  shown of all lavas in this study (n=62)

The noble gases (He, Ne, Ar, Xe) are notable because they provide conclusive evidence for the presence of an ancient (seemingly primordial) component trapped within the deep Earth. The elevated  ${}^3\text{He}/{}^4\text{He}$  ratios in some OIB coupled with distinct Ne, Xe

and W isotope signatures compared to MORB establish that this high  ${}^3\text{He}/{}^4\text{He}$  material has remained isolated from mixing and exchange with MORB source mantle for  $> 4.45$  Ga (Mukhopadhyay, 2012; Mundl-Petermeier et al., 2020). The coupled behavior of noble gases with other volatile species ( $\text{H}_2\text{O}$ ,  $\text{CO}_2$ , halogens, S and B) has become of fundamental importance because there is increasing evidence for significant recycling of volatile species to the mantle via the subduction of seawater, sediments and altered oceanic crust (Holland and Ballentine, 2006; Dixon et al., 2017; Hanyu et al., 2019; Graham and Michael, 2021).

The high- ${}^3\text{He}/{}^4\text{He}$  component sampled by OIB are generally associated with mantle enrichment. Indicators of mantle source composition like Nb/U among all Kama‘ehuakanaloa lavas (Fig. 2.15) are generally elevated, while W/U (Fig 2.21) is generally lower compared to other Hawaiian shields (Hofmann et al., 1986; Ireland et al., 2009). North Rift tholeiites show the lowest concentrations of incompatible lithophile elements (Rb, Sr) in parental melts (Table 2.7), however, they have among the highest  ${}^3\text{He}/{}^4\text{He}$  of Kama‘ehuakanaloa lavas. However, the composition of North Rift tholeiites provides support for the idea of high- ${}^3\text{He}/{}^4\text{He}$  mantle sources that are geochemically depleted, yet still arise from a distinct origin from MORB, as seen in Baffin-West Greenland which record different components of the proto-Iceland plume Willhite et al. (2019).

### 3.4.3.2 Is it a “dry” plume?

Dixon and Clague (2001) proposed a zoned plume model where the mantle components within the center of the plume are drier than the exterior, and strong enrichments in H<sub>2</sub>O are observed only ahead of the plume at South Arch. In their model, high <sup>3</sup>He/<sup>4</sup>He in Kama‘ehuakanaloa glasses are not the result of degassing of a volatile-rich plume, but of mixing along the outer rim of the plume with entrained lower mantle (FOZO) into the drier interior. The implications are explored by assessing volatile concentrations of the mantle source of South Rift transitional basalts and tholeiites, and North Rift tholeiites, as summarized in Table 3.7. Estimated H<sub>2</sub>O contents of the mantle source of North Rift tholeiites (0.046 wt.%) is similar to that of South Rift tholeiites (0.042 wt.%) (Table 3.7).

Table 3.7: Summary of Parental Melt/Mantle Source Volatiles summarized from Tables 2.8 and 2.9.

Model Result	Rock Type	Location	Cl (ppm)	S wt. (%)	F wt. (%)	H <sub>2</sub> O wt (%)
Parental Melts <sup>[1]</sup>	Th	South Rift	448.7	0.137	0.038	0.529
Parental Melts	Tr	South Rift	563.5	0.128	0.046	0.614
Parental Melts	Th (N.)	North Rift	80.87	0.100	0.024	0.386
Mantle Source <sup>[2]</sup>	Th	South Rift	35.9	0.011	0.003	0.042
Mantle Source	Tr	South Rift	33.8	0.008	0.003	0.037
Mantle Source	Th (N.)	North Rift	9.70	0.012	0.003	0.046

<sup>[1]</sup> See Table 2.8. Trace element abundances of parental magmas calculated using samples with MgO>6.5 wt% corrected for olivine fractionation to MgO=16 wt%

<sup>[2]</sup> See Table 2.9. Composition of mantle source region estimate if D=0, range of 6%, 8%, and 13% melting based on REE modeling (Fig. 2.19)

Davis et al. (2003) noted that inconsistent distribution of H<sub>2</sub>O and Cl in tholeiitic glasses from Kīlauea, Mauna Loa, and Kama‘ehuakanaloa complicate the concentrically zoned plume model of DePaolo et al. (2001). Estimated H<sub>2</sub>O contents of the mantle source of North Rift tholeiites (0.046 wt.%) is similar to that of South Rift tholeiites (0.042 wt.%)

(Table 3.7). However, Cl concentrations of the North Rift mantle source is much lower (10 ppm) compared to the the South Rift tholeiite source (36 ppm), suggesting differences in incorporating seawater or brines. Relatively uniform H<sub>2</sub>O in the Kama‘ehuakanaloa mantle source (Table 2.9), though varying Cl and trace element enrichment among North Rift tholeiites compared to East Flank and South Rift tholeiites suggest heterogeneity in volatile distributions in different portions of Kama‘ehuakanaloa.

### 3.5 Conclusion

Helium isotope trends correspond to major element composition, with the lowest  ${}^3\text{He}/{}^4\text{He}$  observed in samples with higher alkalinity index or alkalic composition (Fig. 3.5). South Rift alkali basalts show lower mean  ${}^3\text{He}/{}^4\text{He}$  compared to tholeiites (Fig. 3.3). Within South Rift lavas, the mean  ${}^3\text{He}/{}^4\text{He}$  ratio is different in tholeiites compared to both transitional and alkali basalts at the >95% confidence level ( $p \leq 0.01$ ). A possible control on lower  ${}^3\text{He}/{}^4\text{He}$  isotope in melt phases compared to the vesicle phase of alkalic glasses could be post-eruptive  ${}^4\text{He}$  ingrowth due to higher U+Th.

Tholeiites are interpreted as the most recent eruptives at Kama'ehuakanaloa Seamount, coinciding with expression of shield volcanism. In addition, if the elongate volcano grows northward, the observation of the high  ${}^3\text{He}/{}^4\text{He} \sim 30.5 \text{ R}_A$  in the North Rift tholeiites provides support for the high  ${}^3\text{He}/{}^4\text{He}$  source influencing magma chambers contributing to North and South Rifts. Plume-sourced Helium, interpreted in  ${}^3\text{He}/{}^4\text{He}$  isotopes, hence, is expected as the transition to shield volcanism continues. The observation of high- ${}^3\text{He}/{}^4\text{He} \sim 35 \text{ R}_A$  in a transitional basalt (Matsumoto et al., 2008) motivates further comparison of the plume signature in transitional basalt samples, which are considered less frequently for understanding Hawaiian shield source chemistry.

Total  $\text{CO}_2/{}^3\text{He}$  overlaps with mantle values, ranging upward from  $1 \times 10^9$ . Some elevated ratios may suggest the presence of recycled C within the mantle plume. However,  $\text{CO}_2/\text{Ba}$  indicates lavas lost >95% of their  $\text{CO}_2$  by degassing. Low Helium concentrations may reflect the preferential loss of He during degassing, which contribute to high  $\text{CO}_2/{}^3\text{He}$  in the study suite (Fig. 3.14 and 3.15). Similarity in trace element ratios like Nb/U and

W/U among North Rift and South Rift tholeiites suggests similar history of addition from recycled or subducted materials.

The average  $\text{H}_2\text{O}/\text{Ce} \sim 220$  of most Kama‘ehuakanaloa samples overlaps with typical mantle values. A few alkalic basalts show elevated values of  $\text{H}_2\text{O}/\text{Ce} \sim 400$ , and the estimated  $\text{H}_2\text{O}$  contents of the South Rift transitional basalt mantle source (0.037 wt.%) is lower than South Rift tholeiites (0.042 wt.%), suggesting variation as the degree of partial melting increases with shield volcanism. Estimated  $\text{H}_2\text{O}$  contents of the mantle source of North Rift tholeiites (0.046 wt.%) is similar to that of South Rift tholeiites (0.042 wt.%) (Table 3.7). However, Cl concentrations of the North Rift mantle source is much lower (10 ppm) compared to the the South Rift tholeiite source (36 ppm). Relatively uniform  $\text{H}_2\text{O}$  in the Kama‘ehuakanaloa mantle source with varying Cl and trace element enrichment among North Rift tholeiites compared to East Flank and South Rift tholeiites suggest heterogeneity in volatile distributions as sampled by the potentially different magma chambers supplying different portions of Kama‘ehuakanaloa.

## Chapter 4: Pb isotope variability at Kama‘ehuakanaloa Seamount: Constraints on the distribution of pre-shield and shield stage lavas

### 4.1 Introduction

Incipient plume melts comprise submarine Kama‘ehuakanaloa Seamount, one of few regions on Earth to show the pre-shield to shield transition. Tholeiitic flows have yet to cover older alkalic units, but poor mapping poses a challenge to placing spatial-temporal constraints on the transition. Major element data supports the idea that Kama‘ehuakanaloa’s pre-shield phase lasted 200 kyr ([Guillou et al., 1997](#)). Tholeiite accumulation at the summit suggests the transition to shield volcanism is nearly complete ([Loewen et al., 2019](#)), as the volcano has shifted closer to the hotspot center. Lava compositions are used to define the stages: Alkalic and tholeiitic elemental compositions indicate pre-shield and shield, respectively ([Garcia et al., 1995](#)). However, major element classification overlooks potential temporal trends from radiogenic and noble gas isotopes. Isotope compositions at Kama‘ehuakanaloa Seamount suggests lavas sample a rare mantle component ([Weis et al., 2020](#)), but most studies focus on the summit and neglect the deep rift (2-5 km depth, Fig. [4.3](#)).

In addition, Hawaiian shield lavas typically exhibit geographic and geochemical affinities to one of two trends of Loa or Kea type, named after the dominant shield volcanoes Mauna Loa and Mauna Kea (Fig. [4.2](#)) ([Abouchami et al., 2005](#); [Williamson et al., 2019](#)).

Previous work on Kama‘ehuakanaloa revealed Pb isotopes represent the Loa component, but less enriched Sr-Nd isotopes more consistent with Kea component (Abouchami et al., 2005; Weis et al., 2020). Hence, it is possible for a single volcano to display affinity towards a dominant Loa or Kea trend, while presenting unique compositions in specific isotopic systems. While Sr-Nd-Pb of Loa/Kea trend volcanoes are persistent regardless of volcanic stage,  $^3\text{He}/^4\text{He}$  measured in Hawaiian shield lavas is associated with early stage volcanism, and expected to decrease in subsequent post-shield, post-erosional, and rejuvenated lavas (Rison and Craig, 1983).

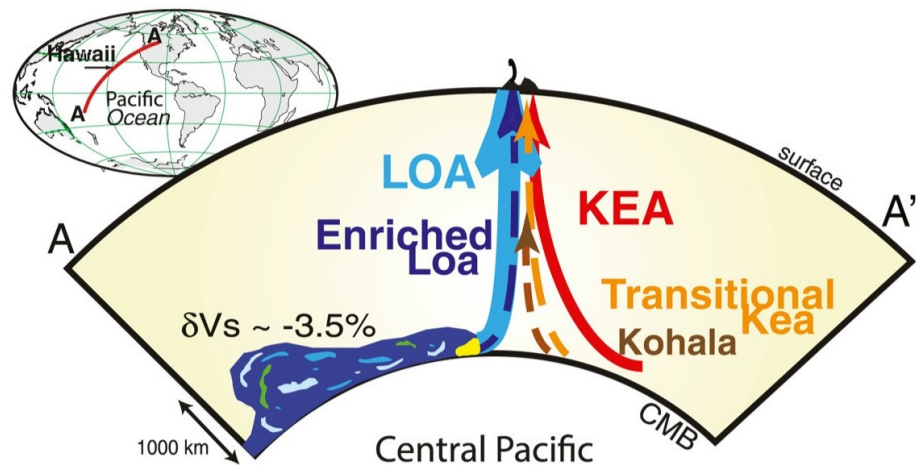


Figure 4.1: Figure from Weis et al. (2020). Transect A-A' shown in pink curved line on globe projection shown in cross section schematic of the mantle centered on the Central Pacific. Colored blobs representing Loa, Kea, Enriched Loa, Transitional Kea, Kohala, Lō'ihi (unlabeled, green) are geochemical groupings estimated by linear discriminant analyses in Weis et al. (2020). They are shown at different regions from the core-mantle boundary (CMB) to the surface.

Coupled Pb-He isotopes in Hawaiian volcanoes (Hanyu et al., 2010) and global OIBs (Eiler et al., 1997) are consistent with derivation from the same components. Kama‘ehu-

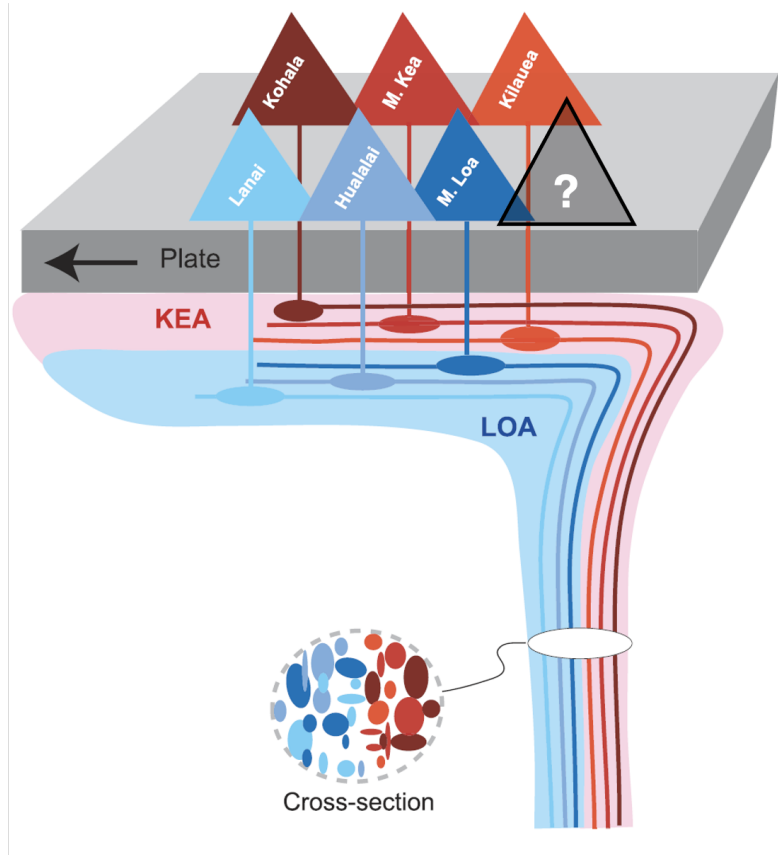


Figure 4.2: Modified figure from Abouchami et al. (2005) showing volcanoes of the Main Hawaiian Islands and Loa/Kea Affinities. Loa (blue): Lāna‘i, Hualālai, Mauna Loa. Kea (red): Kohala, Mauna Kea, Kīlauea. Additional unknown volcano in grey marked with "?" as Kama‘ehuakanaloa.

akanaloa's endmember exhibits high  $^{208}\text{Pb}/^{204}\text{Pb}$ , moderate  $^{206}\text{Pb}/^{204}\text{Pb}$  (Abouchami et al., 2005; Harrison and Weis, 2018; Staudigel et al., 1984), and is a rare Hawaiian source component (Weis et al., 2020; Harrison and Weis, 2018). Pb isotope variations in low-eruptive OIB indicate changes in plume direction and melt flux (Gerlach, 1990; Abouchami et al., 2005; Williamson et al., 2019). However, there is also evidence that  $^3\text{He}/^4\text{He}$  is decoupled or otherwise displaced from the solid plume phase due to volatile

dynamics, and low He, or the Helium paradox, suggests that plume Helium is not abundant [Gonnermann and Mukhopadhyay \(2007\)](#). Isotope variation studies may reveal such systematic changes in Kama‘ehuakanaloa’s evolution.

The deep South Rift lacks coverage of Pb isotope data available in geologic databases (e.g., GEOROC, <http://georoc.mpchmainz.gwdg.de/georoc/>) and the majority of previous measurements have been made on samples collected from the shallower, summit region (Fig. 4.3). The previous study allowed an examination of  ${}^3\text{He}/{}^4\text{He}$  isotope distribution among samples along Kama‘ehuakanaloa’s South Rift zone, in addition to a locality along the North Rift, and East Flank samples. Of particular interest was resolving the origin of North Rift Tholeiites versus South Rift tholeiites.

Previous Pb isotopes include double spike measurements on thermal ionization mass spectrometry (TIMS) ([Staudigel et al., 1984](#); [Valbracht et al., 1996](#); [Abouchami et al., 2005](#); [Weis et al., 2020](#)), and multi-collector (MC)-ICP-MS ([Weis et al., 2020](#)). Kama‘ehuakanaloa Seamount is one of the best studied Hawaiian volcanoes for individual measurements of Sr-Nd-Pb-He isotopes, yet few samples have full complementary analyses of combined isotopic systems. While spatial variation in geochemistry can occur on the scale of 50 km at different Hawaiian volcanic centers ([Ribe and Christensen, 1999](#)), few studies have evaluated if isotopic variability arises from the spatial scale of a single volcano like Kama‘ehuakanaloa (formerly Lō‘ihī) Seamount. This chapter examines the extent to which different pre-shield and shield phase mantle sources are conveyed in Kama‘ehuakanaloa lavas. This is accomplished by evaluating Pb isotope variation of North and South Rift lavas.

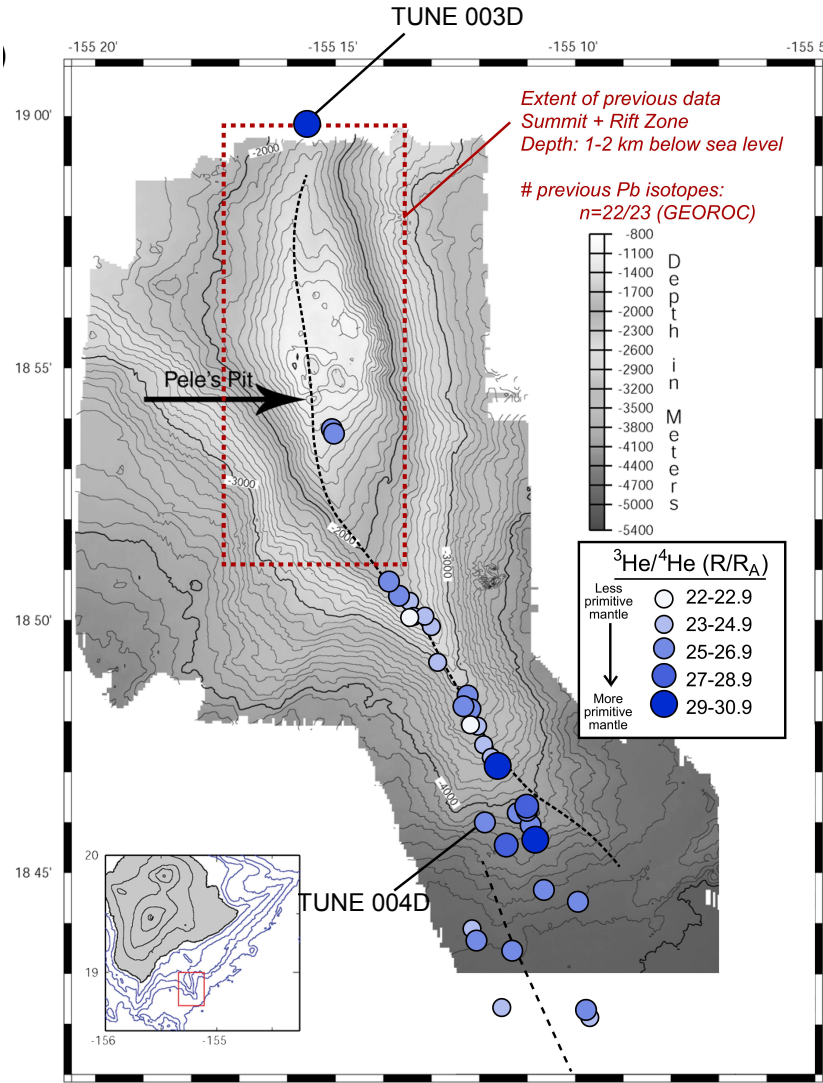


Figure 4.3: Bathymetric map with locations and vesicle  ${}^3\text{He}/{}^4\text{He}$  isotope distribution from South Rift basalts and North Rift tholeiites (East Flank and Western Ridge compositions not shown). Base map is a SeaBeam bathymetric map of in 100-m contours with sample locations from Vetter and Smith (2005). Dashed lines represent the approximate rift zone extents from Valbracht et al. (1997). Samples shaded according to vesicle ( $\text{R}_A$ ) from analyses in Chapter 3. Two samples from TUNE dredges are labeled.

#### 4.1.1 Study Aims and Research Questions

This study contributes Pb isotopes measured by multi-collector inductively coupled plasma mass spectrometry (MC-ICP-MS) to evaluate the distribution of rock types, isotopic signatures of basalts erupted along the 20-km long rift zone from depths of 1800 m to >5000 m. Specifically, insights from Pb isotopes of 28 diverse deep rift samples, in combination with empirical results from Chapters 2 and 3 allow an assessment of heterogeneity within Kama‘ehuakanaloa volcano, and possible indicators of the pre-shield to shield transition in context of Hawaiian volcanic systems and global OIB trends (DePaolo et al., 2001; Hanano et al., 2010). Data from major, trace element, and He isotope data from Chapter 2 and Chapter 3 are integrated in this study of 28 basalt glasses over a wide compositional range. The following research questions are addressed:

1. Are differences in major elements, trace element ratios, and  ${}^3\text{He}/{}^4\text{He}$  isotopes (Ch. 2- 3) observed in the Pb isotopes of Kama‘ehuakanaloa basalts?
2. Is the intermediate origin of South Rift transitional basalts supported by a similar range of Pb isotopes, or is there similar behavior or origin of alkalic vs. tholeiitic sources? Is there a difference in Pb isotopes of tholeiites from the South Rift vs. North Rift?
3. Is there a relationship between Pb and  ${}^3\text{He}/{}^4\text{He}$  isotopes? What are the implications for the growth of a single volcano from the pre-shield to early shield stage?
4. How does Pb isotope variation relate to long-term U-Th-Pb characteristics of the mantle source of Kama‘ehuakanaloa basalts? In addition to Loa/Kea affinities,

what are the implications for mantle source enrichment history and recycling?

## 4.2 Samples

This study increases the dataset for Kama‘ehuakanaloa lavas, particularly for analyses of basaltic glasses along the South Rift zone, and allows an assessment of previous analyses on sub-samples from the same dredge or dive. Precise sample coordinates and depths enable a study of variability along the ~20 km rift. Data will be compared with literature values, which ranges from  $\Delta^{206}\text{Pb} = 0.328$ ,  $\Delta^{208}\text{Pb} = 0.295$ , similar to whole rock values (Garcia et al., 1995; Staudigel et al., 1984). Pb concentrations from analyses in Chapter 4 range from 0.8-2.8 ppm and enabled a precise target concentration of 50 ng Pb/mL and ran at 20 ppb to eliminate sensitivity differences during MC-ICP-MS sessions.

## 4.3 Analytical Methods

All laboratory work was conducted at Oregon State University in the W.M. Keck Collaboratory for Plasma Spectrometry. Sample processing and elemental purification was conducted in a Class 100 clean room. Cleaning of all laboratory supplies and solutions were prepared with ultra-pure water obtained from a Milli-Q® IQ 7000 system (Millipore, Burlington, MA, USA) that deionizes reverse-osmosis water with resistivity of  $\geq 18.2 \text{ M}\Omega/\text{cm}$  at 25°C. Ultra-pure concentrated Fisher Scientific Optima™ grade hydrofluoric acid (HF), hydrobromic acid (HBr), distilled analytical grade hydrochloric acid (HCl) and nitric acid ( $\text{HNO}_3$ ) were used for all sample, standard, and solution prepara-

tion. All laboratory plastics were washed with aqua regia—analytical grade 4 M HCl, and 1 M HNO<sub>3</sub>). Each washing step was performed at 90°C for a minimum of 8 hours, usually overnight. Rinsing with Milli-Q® took place in between each heating step. Following the cleaning procedures, all plastics were dried in Class-100 laminar flow hoods.

Basaltic glass chips were inspected under binocular microscope and checked to be free of crystals, generally homogeneous and uniform appearance, minimal alteration, and fresh luster. Between 50-110 mg of glass material of 0.25-0.50 mm (35-60 mesh) grain size was loaded and weighed in acid-cleaned 15 mL Savillex® beakers. Leaching was achieved by placing samples with 2 M HCl in an ultrasonic bath at room temperature (20°C) for 10 minutes. The acid was decanted, and samples were rinsed with ultra-pure water, decanted, and rinsed twice more. After the third rinse, samples were subjected to three digestion steps to achieve complete dissolution of the basaltic glasses.

Each sample was first digested in a 3:1 mixture of concentrated 29 M HF:16 M HNO<sub>3</sub> solution, capped and heated overnight on a hotplate at 120°C for at least 24 hours to fully dissolve. The sample was evaporated to dryness at 120°C. Concentrated HNO<sub>3</sub> was added to the dry residue, and the sample was capped and left overnight to reflux on a hotplate at 120°C. The sample was evaporated until completely dry, and 6 N HCl was added. The samples were capped and dried overnight on a hot plate at 120°C. When nearly dry, 1 M HBr solution was added to redissolve the sample. Samples that were brought up in 1 N HBr solution were loaded into acid-cleaned 1.5 mL vials and centrifuged for 3 minutes at 13,500 RPM to separate insoluble precipitates. After centrifuging, most samples were not observed to contain undissolved precipitates unless original sample weights exceeded 90 mg.

Sample Pb was isolated using an anion exchange chromatography method similar to that described by Weis et al. (2006) and Melby (2020). Specifically, samples were processed in a “two-pass” procedure to improve Pb separation. For the first pass, a slurry of Dowex AG<sup>®</sup> 1-X8 (100-200 dry mesh, chloride form) analytical grade anion exchange resin was loaded into acid-cleaned Teflon columns with 500  $\mu$ L of resin and 3 mL reservoir capacity. The resin was rinsed in successive steps of Milli-Q<sup>®</sup> water and 6 M HCl before conditioning with 1 N HBr. After the sample was centrifuged in HBr, the clear supernatant was pipetted and loaded onto the column. The Sr-Nd-REE cut was washed from the column with 1 M HBr and 2 M HCl. Then, Pb was eluted 6 M HCl. The resin was discarded after this step and columns were cleaned in 2 N HNO<sub>3</sub> before the next use.

The second pass is an additional step to achieve purified Pb collection. The eluted Pb fraction was dried until evaporated, and brought up in 0.5 mL 1 N HBr. Columns were loaded halfway with  $\sim$ 200 $\mu$ L of AG<sup>®</sup> 1-X8 resin. The same sequence as the first pass was carried out, but with smaller volumes: after successive rinse steps of Milli-Q<sup>®</sup> water, 6 M HCl, and conditioning with 1 M HBr, the sample was loaded. The column was washed with 1 M HBr and 2 M HCl before Pb was eluted with 6 M HCl. The aliquot was dried completely and diluted with 2% HNO<sub>3</sub>. Each sample was additionally diluted before analysis on MC-ICP-MS, to approximate concentrations of 20 ng Pb/mL, which typically produces an instrument response of 20 total Pb volts.

Pb Isotope measurements were done on a Nu Instruments 3D Plasma Source Multi-Collector-ICP-MS at the W.M. Keck Collaboratory for Plasma Spectrometry. The machine is suited to measure Pb isotope ratios at 0.1-0.01% relative precision. The expo-

netional mass fractionation factor was calculated according to Equation C.1. NBS-981 was analyzed in-run, before and after every sample, and Pb isotopes were normalized for instrumental drift during the analytical session and for sample-standard bracketing.

Data includes  $^{206}\text{Pb}$ ,  $^{207}\text{Pb}$ ,  $^{208}\text{Pb}$  reported as ratios relative to  $^{204}\text{Pb}$ . Once corrected with the mass bias factor, values were normalized using a standard sample-standard bracketing (SSB) protocol using the double-spiked values of NBS 981 from [Ingle et al. \(2010\)](#):  $^{208}\text{Pb}/^{204}\text{Pb} = 36.72156$ ,  $^{207}\text{Pb}/^{204}\text{Pb} = 15.49741$ ,  $^{206}\text{Pb}/^{204}\text{Pb} = 16.94058$ . Comparing results of NBS-981 after normalizing to [Ingle et al. \(2010\)](#) shows values that are similar within error to other studies, and comparing to MC-ICP-MS data from [Weis et al. \(2005, 2006, 2020\)](#) show values of NBS-981 within error. During the analysis period, the method produced the following mean values for NBS-981 ( $n=63$ ) and  $\pm 2\sigma$  (SD):  $^{206}\text{Pb}/^{204}\text{Pb} = 16.94284 \pm 0.00928$ ,  $^{207}\text{Pb}/^{204}\text{Pb} = 15.50024 \pm 0.01119$  and  $^{208}\text{Pb}/^{204}\text{Pb} = 36.72846 \pm 0.03341$ .

Procedural blanks and reference materials were run using the same protocols as unknowns. Secondary standards/reference materials included USGS standards BHVO-1, BHVO-2 and Kil1919 (rock powders), and an in-house standard "Menehune", glass chips from Pu'u'ō'ō eruption ([Pietruszka et al., 2019](#)). Leached and unleached digestions of BHVO-1 were analyzed. Total procedural blanks were  $<87$  pg for Pb, with an average of  $<50$  pg for Pb. Hence, blanks account for less than 0.01% of Pb in the signal and values were not adjusted for blank signal.

#### 4.3.1 Reference Materials/Interlaboratory Comparison

Much attention has been paid to precise and simultaneous determinations of radiogenic isotopes in geologic materials. In recent years, multi-collector ICP-MS has shown that Pb isotopes are as stable and reproducible with MC-ICP-MS, with possible improvement compared to method comparisons on Sr-Nd isotopes ([Weis et al., 2006](#)).

While glass chips were leached for this study, fine powders supplied by USGS were not possible to leach without losing significant Pb concentration in the sample. Three analyses of a leached dissolution of BHVO-1 indicated Pb isotopic compositions that strongly differed from the accepted value, such that it appeared more similar to BHVO-2. After a second dissolution was performed on unleached BHVO-1 powder, Pb isotope results were within error to the accepted values (and values reported by [Weis et al. \(2005\)](#).

It is unexpected for the Pb isotope composition to be modified heavily by leaching. However, if the signature reflects modern seawater components, then we would expect to see more radiogenic Pb isotope composition in the residue. Instead, we see less radiogenic values that shift values towards lower  $^{208}\text{Pb}/^{204}\text{Pb}$  and  $^{206}\text{Pb}/^{204}\text{Pb}$ . Figure 4.5 shows that leached samples/leached residue ([Weis et al., 2005, 2006](#)), accepted values, and Pb ore source ([Reiners et al., 2017](#)) lie along a straight line in  $^{207}\text{Pb}/^{204}\text{Pb}$ - $^{206}\text{Pb}/^{204}\text{Pb}$  space. This suggests mixing between true BHVO-1 components and present-day sources. If this is the case, then this supports the presence of surficial contamination from steel milling, which was previously suggested to introduce metal contamination to first generation USGS reference materials. However, we did not measure trace element concentrations of the leachates or residues to confirm if the mixing is sensible for the gentle leach (2 N

HCl for 15 minutes without heat). This study provides additional observations consistent with Weis et al. (2005) where Pb isotopes of USGS reference materials vary depending on leaching protocol. The range of Pb isotopes are shown in Figure 4.6. The majority of 1 SD error bars of analyses from this study are smaller than symbol size on diagrams.

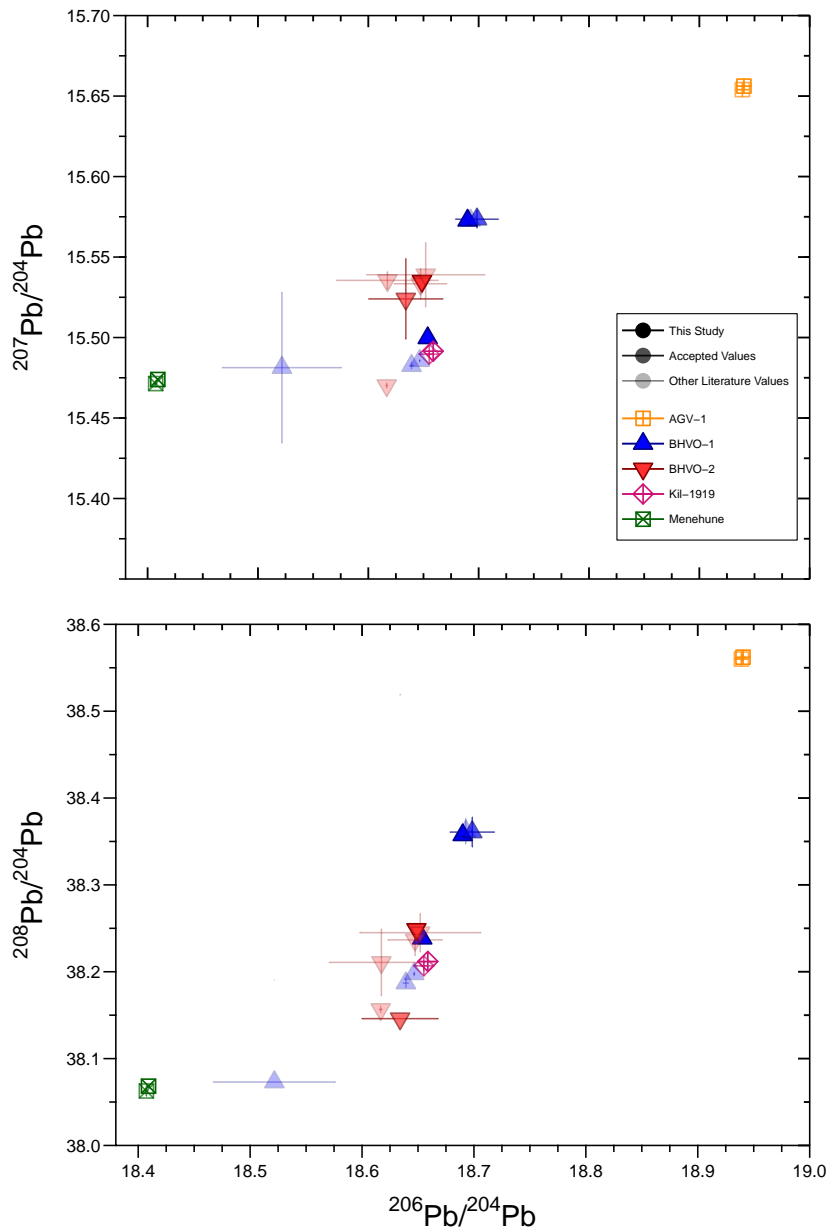


Figure 4.4:  $^{207}\text{Pb}/^{204}\text{Pb}$ - $^{206}\text{Pb}/^{204}\text{Pb}$  and  $^{208}\text{Pb}/^{204}\text{Pb}$ - $^{206}\text{Pb}/^{204}\text{Pb}$  diagrams for Reference Materials. Values are from Table C.1. Smaller, semi-transparent symbols represent literature values. Error bars on this study's values are for  $1\sigma$ .

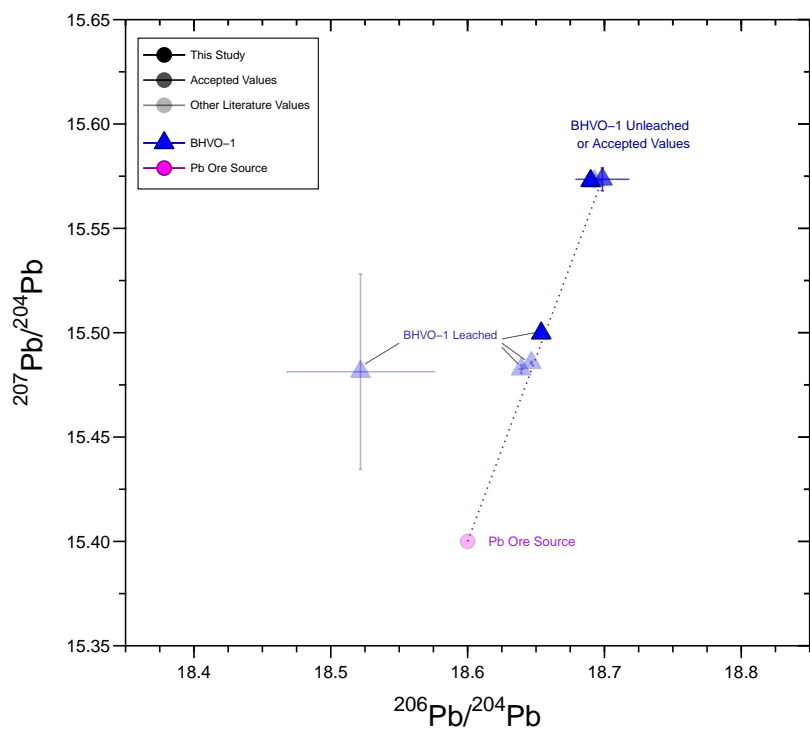


Figure 4.5:  $^{207}\text{Pb}/^{204}\text{Pb}$  vs.  $^{206}\text{Pb}/^{204}\text{Pb}$  of BHVO-1 and Pb ore source composition  $\sim 18.6$  from Reiners et al. (2017) associated with modern contamination. Accepted value of BHVO-1 from GeoReM. Leached values from this study and unleached and leached residue values of BHVO-1 are from Weis et al. (2005, 2006).

#### 4.4 Results

The Pb isotope compositions are listed in Table 4.1 and shown graphically in Pb-Pb-Pb plots in Figure 4.6. The range of previous Pb isotopes for all Kama'ehuakanaloa seamount rocks was  $^{206}\text{Pb}/^{204}\text{Pb} = 18.146 - 18.474$ ,  $^{207}\text{Pb}/^{204}\text{Pb} = 15.433-15.492$ , and  $^{208}\text{Pb}/^{204}\text{Pb} = 37.910 - 38.213$ . The ranges of the new data are  $^{206}\text{Pb}/^{204}\text{Pb} = 18.1726 - 18.4971$ ,  $^{207}\text{Pb}/^{204}\text{Pb} = 15.4457-15.4860$ , and  $^{208}\text{Pb}/^{204}\text{Pb} = 37.9512 - 38.2302$ . This study extends the higher boundary of  $^{206}\text{Pb}/^{204}\text{Pb}$  and  $^{208}\text{Pb}/^{204}\text{Pb}$  in the second decimal place. As a whole, the Pb isotope composition of Kama'ehuakanaloa is relatively limited compared to other ocean islands.

Table 4.1: Pb Isotope Compositions of Kana'ehuakanaloa Seamount samples

ID Sample	$^{208}\text{Pb}/^{204}\text{Pb}$	$^{207}\text{Pb}/^{204}\text{Pb}$	$1\sigma$	$^{206}\text{Pb}/^{204}\text{Pb}$	$1\sigma$	$^{208}\text{Pb}/^{206}\text{Pb}$	$1\sigma$	$^{206}\text{Pb}/^{207}\text{Pb}$	$1\sigma$	$^{208}\text{Pb}*/^{206}\text{Pb}^*$	$^{206}\text{Pb}*/^{207}\text{Pb}^*$	[1]
2 MIR-2335-05	38.1653	0.0006	15.4753	0.0002	18.3844	0.0003	2.0760	0.8418	0.9572			
6 MIR-2335-09 [2]	38.1516	0.0005	15.4725	0.0009	18.3757	0.0008	2.0762	0.8420	0.9567			
8 MIR-2335-11	38.1435	0.0005	15.4722	0.0002	18.3550	0.0002	2.0781	0.8429	0.9579			
11 MIR-2336-04 [2]	38.2162	0.0011	15.4750	0.0006	18.4841	0.0010	2.0675	0.8372	0.9524			
14 MIR-2337-02	38.1399	0.0006	15.4757	0.0003	18.3585	0.0003	2.0775	0.8430	0.9572			
16 MIR-2338-1a	38.1438	0.0006	15.4728	0.0002	18.3553	0.0003	2.0781	0.8430	0.9580			
18 MIR-2340-03	38.1317	0.0005	15.4741	0.0002	18.3498	0.0002	2.1102	0.8433	0.9572			
19 MIR-2341-01	38.1568	0.0007	15.4754	0.0003	18.4236	0.0003	2.0711	0.8400	0.9522			
20 MIR-2341-02	38.0142	0.0004	15.4599	0.0002	18.2603	0.0002	2.0818	0.8466	0.9536			
22 MIR-2343-03	38.2302	0.0005	15.4859	0.0002	18.4971	0.0002	2.0668	0.8372	0.9526			
23 MIR-2343-04 [3]	38.2219	0.0058	15.4848	0.0021	18.4895	0.0024	2.0672	0.8375	0.9525			
25 MIR-2343-06	38.1266	0.0006	15.4679	0.0002	18.3274	0.0003	2.0803	0.8440	0.9590			
28 MIR-2343-10 [2]	38.2255	0.0019	15.4860	0.0008	18.4910	0.0010	2.0672	0.8375	0.9527			
30 MIR-2343-12	38.0947	0.0006	15.4690	0.0002	18.3494	0.0003	2.0761	0.8430	0.9531			
32 Shinkai 490-8 [2]	38.1697	0.0015	15.4736	0.0007	18.4358	0.0000	2.0704	0.8393	0.9523			
33 Shinkai 494-1	38.1261	0.0006	15.4663	0.0002	18.3491	0.0003	2.0778	0.8429	0.9566			
34 Shinkai 494-2	38.1273	0.0006	15.4662	0.0002	18.3491	0.0003	2.0779	0.8429	0.9568			
35 Shinkai 494-3 [2]	38.0276	0.0016	15.4598	0.0009	18.2805	0.0008	2.0802	0.8457	0.9530			
33 Shinkai 494-4	38.0418	0.0006	15.4627	0.0003	18.2936	0.0003	2.0795	0.8452	0.9532			
37 Shinkai 494-7	38.0814	0.0007	15.4664	0.0003	18.3502	0.0003	2.0753	0.8428	0.9516			
40 Shinkai 494-8	38.0897	0.0006	15.4662	0.0002	18.3566	0.0003	2.0750	0.8425	0.9518			
41 Shinkai 513-3 [2]	38.2099	0.0027	15.4727	0.0001	18.4838	0.0025	2.0672	0.8371	0.9517			
42 Shinkai 513-4A [2]	38.1248	0.0014	15.4721	0.0003	18.3893	0.0014	2.0732	0.8414	0.9523			
44 Shinkai 513-6 [2]	38.1325	0.0024	15.4717	0.0013	18.3977	0.0024	2.0727	0.8409	0.9522			
45 Shinkai 513-7A	38.1636	0.0006	15.4739	0.0002	18.4389	0.0003	2.0697	0.8392	0.9513			
46 Shinkai 515-1 [2]	38.0937	0.0009	15.4694	0.0001	18.3482	0.0002	2.0762	0.8431	0.9532			
47 TUNE 003D-A [2]	37.9512	0.0033	15.4457	0.0015	18.1726	0.0019	2.0884	0.8499	0.9560			
50 TUNE 004D-A [2]	38.1185	0.0009	15.4679	0.0000	18.3628	0.0006	2.0919	0.8423	0.9544			

[1]  $^{208}\text{Pb}*/^{206}\text{Pb}^* = (^{208}\text{Pb}/^{204}\text{Pb} - 29.476) / (^{206}\text{Pb}/^{204}\text{Pb} - 9.307)$ , see Equation 4.1,[2], [3] Analysis reported as average of # measurements, where  $1\sigma$  is 1 standard deviation of the measurements

This study shows Kama‘ehuakanaloa lavas plotting above the Northern Hemisphere Reference Line when evaluating  $^{208}\text{Pb}/^{204}\text{Pb}$  vs.  $^{206}\text{Pb}/^{204}\text{Pb}$ , while plotting below the reference line in  $^{207}\text{Pb}/^{204}\text{Pb}$  vs.  $^{206}\text{Pb}/^{204}\text{Pb}$  space. Within rock type groupings of South Rift lavas, the range for alkalic basalts was  $^{206}\text{Pb}/^{204}\text{Pb} = 18.260 - 18.362$ ,  $^{207}\text{Pb}/^{204}\text{Pb} = 15.459 - 15.469$ ,  $^{208}\text{Pb}/^{204}\text{Pb} = 38.014 - 38.126$ ,  $^{208}\text{Pb}/^{206}\text{Pb} = 2.076 - 2.092$ ,  $^{207}\text{Pb}/^{206}\text{Pb} = 0.842 - 0.847$  (n=7). Overall, they demonstrated higher values compared to similar literature determinations of alkalic basalts (Fig. 4.6), plotting at nearly the highest value found at Kama‘ehuakanaloa for  $^{206}\text{Pb}/^{204}\text{Pb}$ . The range for transitional basalts was  $^{206}\text{Pb}/^{204}\text{Pb} = 18.349 - 18.497$ ,  $^{207}\text{Pb}/^{204}\text{Pb} = 15.466 - 15.486$ ,  $^{208}\text{Pb}/^{204}\text{Pb} = 38.124 - 38.230$ ,  $^{208}\text{Pb}/^{206}\text{Pb} = 2.067 - 2.078$ ,  $^{207}\text{Pb}/^{206}\text{Pb} = 0.837 - 0.843$  (n=12). The range for tholeiitic basalts was  $^{206}\text{Pb}/^{204}\text{Pb} = 18.349 - 18.484$ ,  $^{207}\text{Pb}/^{204}\text{Pb} = 15.466 - 15.476$ ,  $^{208}\text{Pb}/^{204}\text{Pb} = 38.082 - 38.216$ , and  $^{208}\text{Pb}/^{206}\text{Pb} = 2.067 - 2.110$ , and  $^{207}\text{Pb}/^{206}\text{Pb} = 0.837 - 0.843$  (n=8). The single North Rift Tholeiite basalt measurement recorded the lowest values of  $^{206}\text{Pb}/^{204}\text{Pb} = 15.445$ ,  $^{207}\text{Pb}/^{204}\text{Pb} = 18.172$ ,  $^{208}\text{Pb}/^{204}\text{Pb} = 37.951$ ,  $^{208}\text{Pb}/^{206}\text{Pb} = 2.088$ ,  $^{207}\text{Pb}/^{206}\text{Pb} = 0.8499$  (n=1).

#### 4.4.1 Previous Studies and Replicates

In general, few replicates exist for several types of isotopic analyses on Kama‘ehuakanaloa glasses. However, existing replicates are difficult to compare due to the lack of standardized naming and International Generic Sample Number (IGSN). In order to compare results of multi-isotopic analyses of key samples, information from replicates should be assessed. A literature comparison of samples named in original sources as originating

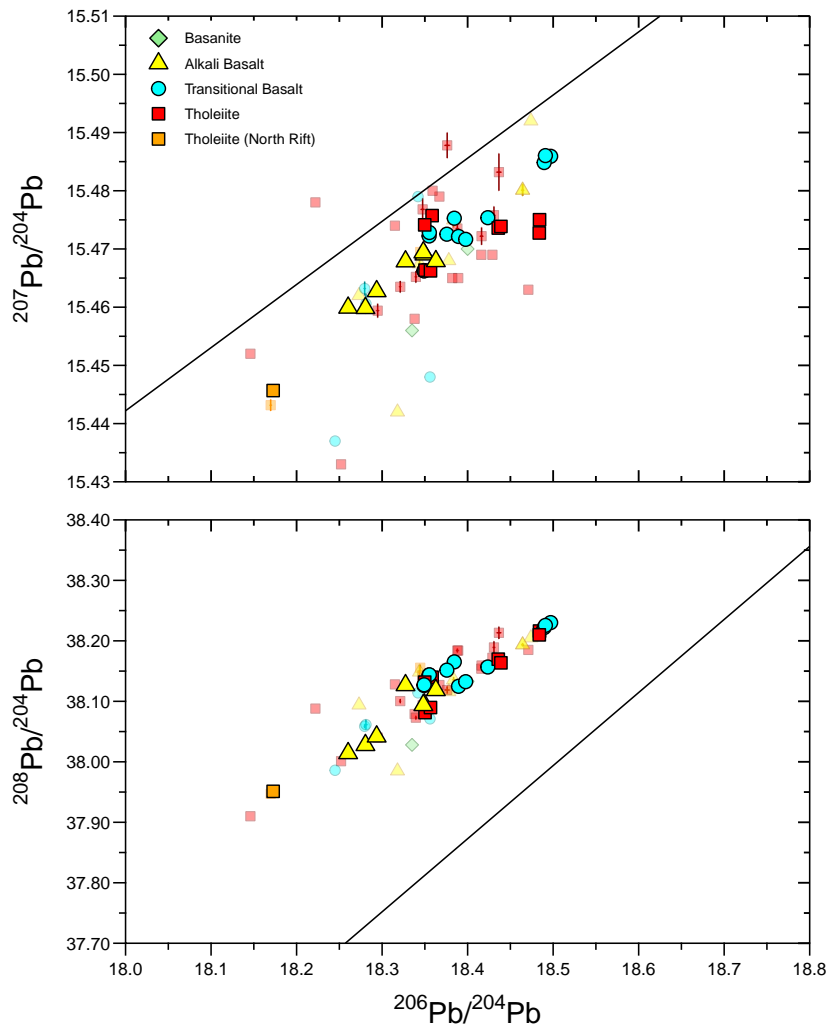


Figure 4.6:  $^{207}\text{Pb}/^{204}\text{Pb}$ - $^{206}\text{Pb}/^{204}\text{Pb}$  and  $^{208}\text{Pb}/^{204}\text{Pb}$ - $^{206}\text{Pb}/^{204}\text{Pb}$  diagrams for Kama'ehuakanaloa lavas. Values from this study have legend symbols matching the legend. Smaller, semi-transparent symbols represent literature values with the same rock types as this study, and are from the North Rift, East Flank, Summit/Crater Complex and South Rift Zone (Staudigel et al., 1984; Valbracht et al., 1996; Garcia et al., 1993, 1995; Abouchami et al., 2005; Weis et al., 2020). The Northern Hemisphere Reference Line (NHRL) from Hart (1984) is shown as linear arrays with slopes coinciding with 1.77 Ga age (Equation 4.2).

from the TUNE04WT expedition is shown in Figure 4.7.

Previous Pb isotope analyses on whole rock material from Valbracht et al. (1996) show similar to this study's results for TUNE-003D and TUNE-004D glasses (Fig. 4.7). Values for one whole rock analysis of TUNE-003D from Abouchami et al. (2005) is also in agreement, however, another whole rock value from that study for TUNE-003D is dissimilar, plotting nearly the same as TUNE-004D. Analyses of olivine and glass from "T4D4" in Valbracht et al. (1997) yield values of 30-33 R<sub>A</sub>, much higher than the vesicle determination of  $\sim$ 25.4 R<sub>A</sub> in this study for TUNE-004D (Table 3.1). However, the range observed in Valbracht et al. (1997) is similar to that of TUNE-003D.

This study contributes Pb isotope compositions of glasses for TUNE-003D and TUNE-004D within error to Valbracht et al. (1996), and with mixed agreement to Abouchami et al. (2005). This provides evidence for this study's glass samples as representative of the whole rock material used to determine Sr-Nd-Pb isotopes in Valbracht et al. (1996), and hence, can be interpreted as replicates of bulk or whole rock material. In contrast, TUNE-003D glasses Abouchami et al. (2005) and olivine/glass for TUNE-004D in Valbracht et al. (1997) result in different  ${}^3\text{He}/{}^4\text{He}$  and Pb isotopes compared to this study. If discrepancies originate from sub-sample or split errors, then studies utilizing TUNE04WT samples should validate sample characteristics with Valbracht et al. (1996), the first publication with geochemical results for the dredge hauls.

Data from several OIBs have been used to construct a possible global high- ${}^3\text{He}/{}^4\text{He}$  component with varying radiogenic isotope characteristics, including PREMA, PHEM (Farley et al., 1992), "C" (Han and Graham, 1996), FOZO (Hart et al., 1992; Stracke, 2012). Figure 4.8 depicts the  ${}^{208}\text{Pb}/{}^{204}\text{Pb}$ - ${}^{207}\text{Pb}/{}^{204}\text{Pb}$ - ${}^{206}\text{Pb}/{}^{204}\text{Pb}$  isotopic composition

of Kama‘ehuakanaloa basalts from this study relative to mantle endmembers (Zindler and Hart, 1986; Stracke, 2012). Kama‘ehuakanaloa compositions plot in the field of Hawaiian basalts (Weis et al., 2020), and do not overlap with enriched mantle endmembers (e.g. EMI or HIMU), nor with the central component “FOZO” (Hart et al., 1992; Stracke, 2012).

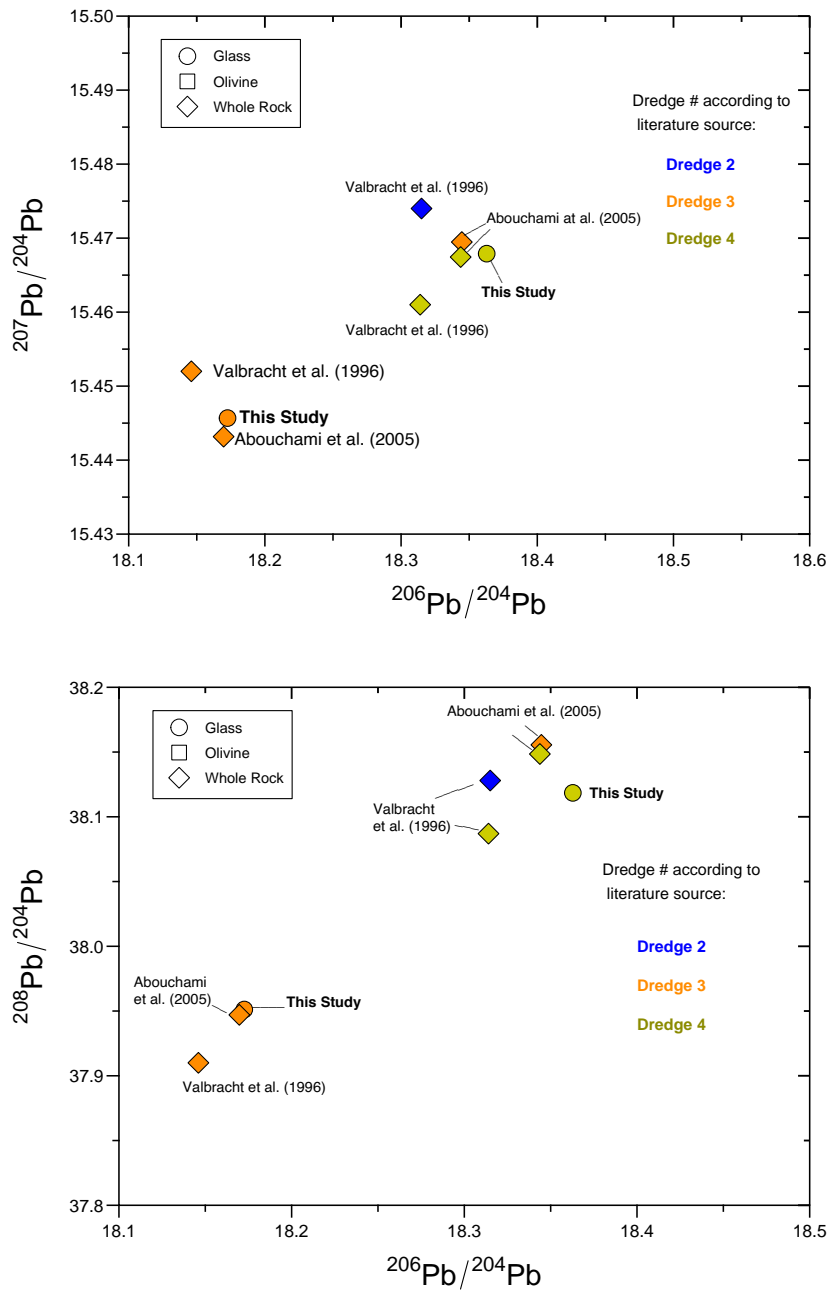


Figure 4.7:  $^{207}\text{Pb}/^{204}\text{Pb}$ - $^{206}\text{Pb}/^{204}\text{Pb}$  and  $^{208}\text{Pb}/^{204}\text{Pb}$ - $^{206}\text{Pb}/^{204}\text{Pb}$  Plot of literature values for samples from TUNE04WT expedition, named according to original data sources: Valbracht et al. (1996); Abouchami et al. (2005)

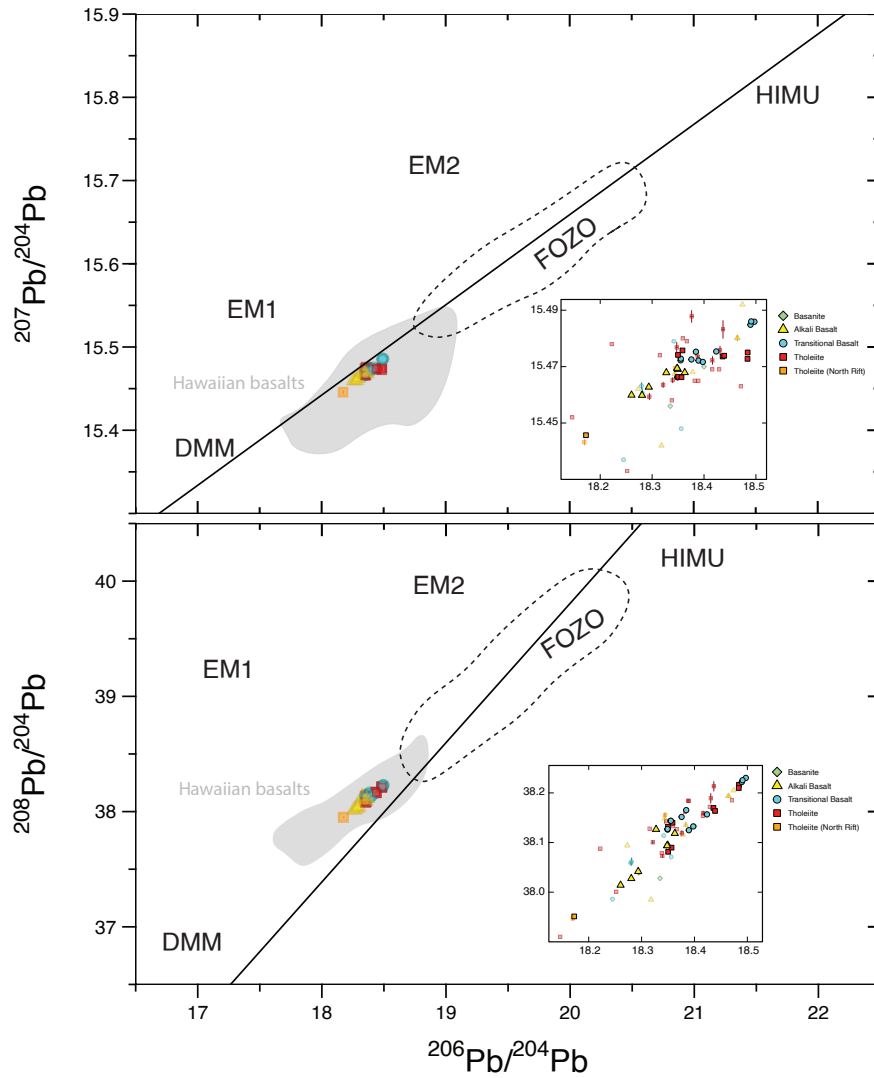


Figure 4.8:  $^{208}\text{Pb}/^{204}\text{Pb}$ - $^{207}\text{Pb}/^{204}\text{Pb}$ - $^{206}\text{Pb}/^{204}\text{Pb}$  isotopic composition of Kama'ehuakanaloa basalts from this study relative to mantle endmembers (Zindler and Hart, 1986; Stracke, 2012). A field of previous data for Hawaiian basalts include values from Weis et al. (2020). Insets show values in detail for this study and previous Kama'ehuakanaloa data from Staudigel et al. (1984); Valbracht et al. (1996); Garcia et al. (1993, 1995); Abouchami et al. (2005); Weis et al. (2020)

## 4.5 Discussion

This discussion explores aspects of Pb isotope variation in context of geographic distribution, possible degrees of radiogenic mantle sources, and integration with other isotope systems. Integrated datasets allow us to determine if the Kama‘ehuakanaloa mantle source is intrinsically heterogeneous and hosts both enriched and primordial components (DePaolo et al., 2001; Hanano et al., 2010).

### 4.5.1 Aspects of Pb Isotope Variation

Geographic variations may be useful for understanding how Kama‘ehuakanaloa’s mantle component manifests through time as the volcano enters the early shield. Few previous studies have evaluated isotopic variation with spatial distribution along the NW-SE trending  $\sim$ 20 km South Rift. The clustering of samples at 18.94-18.95°N in Figure 4.9a are samples collected by the ALVIN submersible in the summit/pit crater complex, and the precision of coordinate data are limited to 0.01 in decimal degrees (Garcia et al., 1993, 1995). The range of Pb isotopes along the South Rift zone are consistent with the range observed at a stratigraphic sequence observed at the pit crater complex.

Comparing ratios of trace elements K/Ti and La/Sm vs.  $^{206}\text{Pb}$  in Figure 4.10 shows different groupings of alkalic basalts, transitional basalts, and tholeiite basalts in trace element ratios. The groupings suggest source heterogeneity, even within different rock types from the same location.

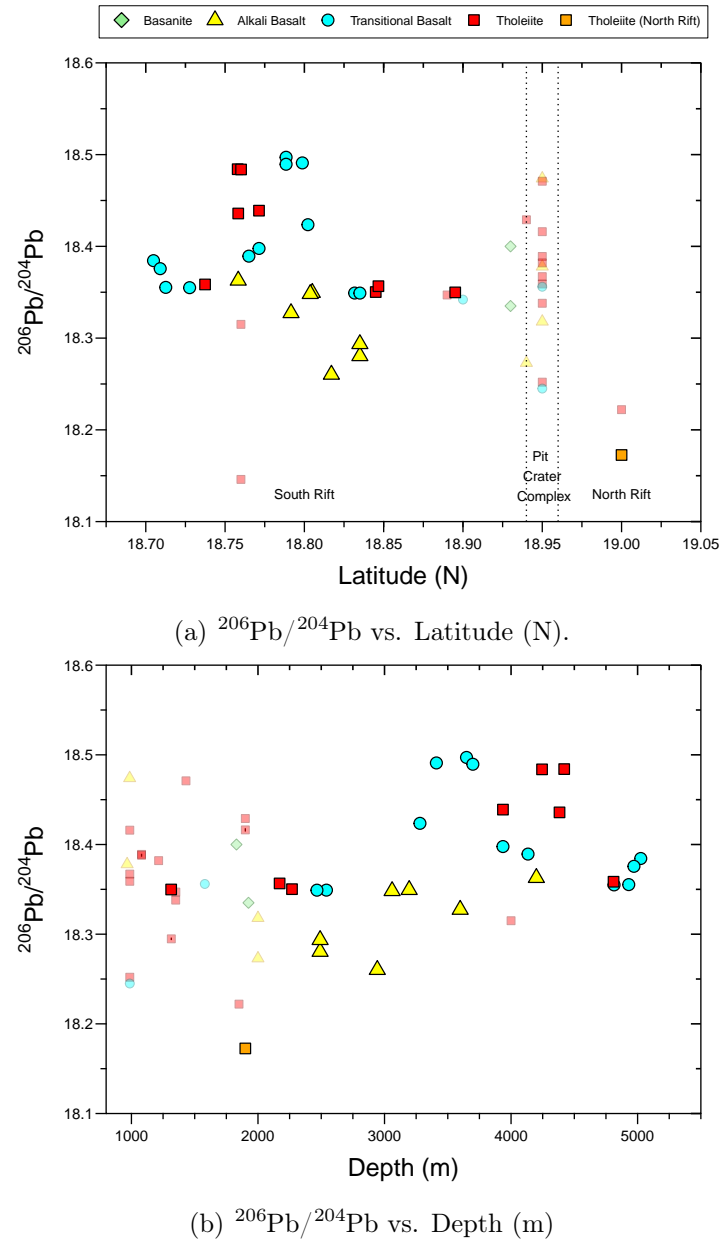
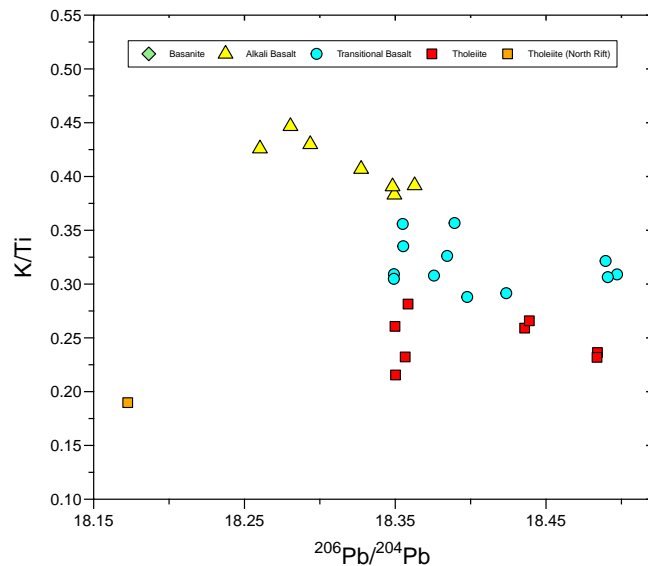
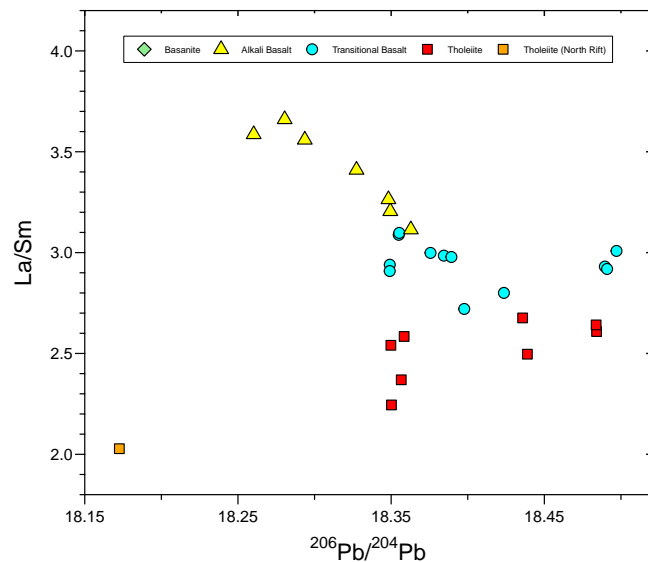


Figure 4.9:  $^{206}\text{Pb}/^{204}\text{Pb}$  vs. Latitude (N) and Depth (m). Smaller, semi-transparent symbols represent literature values with the same rock types as this study, from the same sources listed in Fig 4.6. Error bars for  $^{206}\text{Pb}/^{204}\text{Pb}$  are smaller than symbol sizes for all samples.

(a) K/Ti vs.  $^{206}\text{Pb}/^{204}\text{Pb}$ (b) La/Sm vs.  $^{206}\text{Pb}/^{204}\text{Pb}$ Figure 4.10: Major and Trace Element ratios vs.  $^{206}\text{Pb}/^{204}\text{Pb}$

#### 4.5.2 Radiogenic Sources and Loa/Kea Divide

The calculated radiogenic Pb value  $^{208}\text{Pb}^*/^{206}\text{Pb}^*$  is a measure of radiogenic Pb addition to initial Pb isotope ratios of the primordial Earth, and is shown in Equation 4.1) (Clague and Dalrymple, 1987).  $^{208}\text{Pb}^*/^{206}\text{Pb}^*$  represents the time-integrated  $^{232}\text{Th}/^{238}\text{U}$  of the original source, and is considered the best isotopic discriminator for Hawaiian mantle sources, as the ratio shows a difference between Loa and Kea trend volcanoes (Abouchami et al., 2005; Weis et al., 2011):

$$\frac{^{208}\text{Pb}^*/^{206}\text{Pb}^*}{^{206}\text{Pb}^*/^{204}\text{Pb}} = \frac{^{208}\text{Pb}/^{204}\text{Pb} - 29.476}{^{206}\text{Pb}/^{204}\text{Pb} - 9.307} \quad (4.1)$$

In this study, values of  $\Delta^{206}\text{Pb}/^{204}\text{Pb} = 0.328$ ,  $\Delta^{208}\text{Pb}/^{204}\text{Pb} = 0.295$  are similar to previously reported whole rock values at Kama‘ehuakanaloa (Garcia et al., 1995; Staudigel et al., 1984). Loa-trend volcanoes exhibit higher  $^{208}\text{Pb}^*/^{206}\text{Pb}^*$  ratios  $>0.9475$  than Kea-trend, however, show a large range among individual Loa volcanoes (Weis et al., 2011). Figure 4.11 shows that in this study, Kama‘ehuakanaloa’s  $^{208}\text{Pb}^*/^{206}\text{Pb}^*$  ranges from 0.951-0.959, consistent with previous values where Kama‘ehuakanaloa tends to cluster around 0.95 (Abouchami et al., 2005; Weis et al., 2011). Notably, despite the depleted trace element signature, the North Rift tholeiite basalt is not significantly less radiogenic than the average South Rift tholeiite, and often overlaps in  $^{208}\text{Pb}^*/^{206}\text{Pb}^*$ . Hence, the Pb isotopic signature, like the high- $^3\text{He}/^4\text{He}$  signature, is not consistent with MORB source origin, or the less radiogenic Kea-trend. This suggests derivation from a source with similar radiogenic U/Th and U/Pb ratios as the rest of Kama‘ehuakanaloa’s South Rift, and that tholeiite/shield lavas may derive from a more radiogenic source than early,

pre-shield lavas. Overall, Kama‘ehuakanaloa Pb isotope compositions are consistent with deriving from the Loa component in a bilaterally zoned plume ([Abouchami et al., 2005](#)).

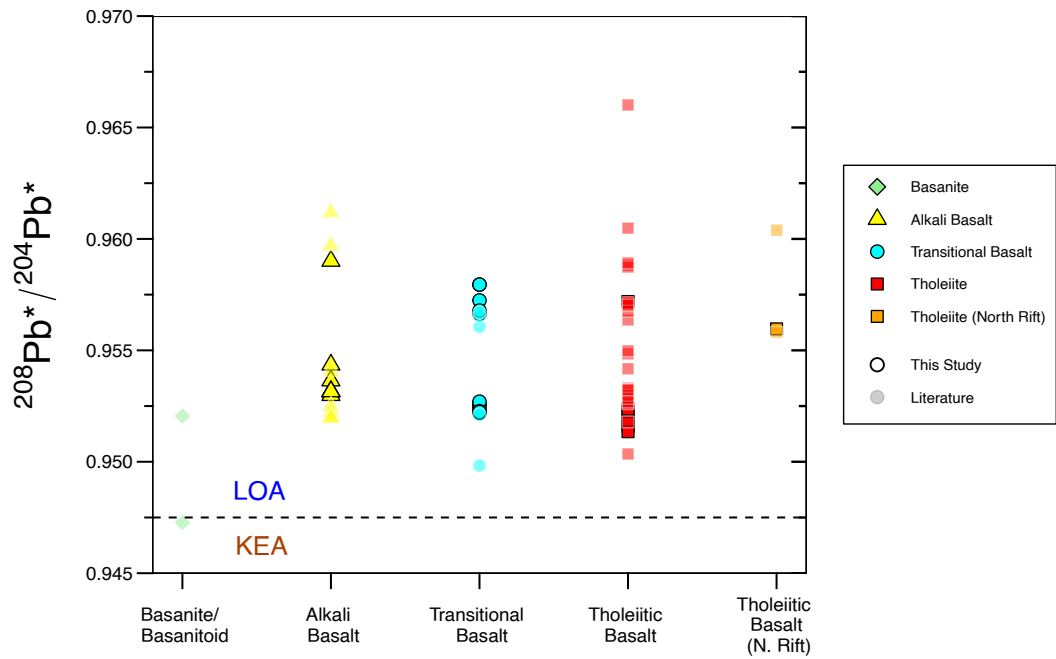


Figure 4.11: Radiogenic  $^{208}\text{Pb}^*/^{204}\text{Pb}^*$ , grouped by rock type. This Study glass values shown in opaque symbols with black borders. Literature samples shown in slightly transparent symbols with no border. Data sources include [Staudigel et al. \(1984\)](#); [Garcia et al. \(1993\)](#); [Valbracht et al. \(1996\)](#); [Abouchami et al. \(2005\)](#); [Weis et al. \(2020\)](#). Dashed line at 0.9475 depicts the Loa/Kea trend cutoff ([Weis et al., 2011](#)).

Enriched mantle sources of MORBs and OIBs were identified by their isotopic anomalies with respect to the Northern Hemisphere Reference Line (NHRL) by [Hart \(1984\)](#). The NHRL is plotted as linear arrays in  $^{207}\text{Pb}/^{204}\text{Pb}$ - $^{206}\text{Pb}/^{204}\text{Pb}$ - $^{208}\text{Pb}/^{204}\text{Pb}$  space, with the slope coinciding with 1.77 Ga age. Volcanic rocks plotting above the NHRL are

said to carry the signature of the DUPAL anomaly. The equations are shown below:

$$^{207}\text{Pb}/^{204}\text{Pb} = 0.1084(^{206}\text{Pb}/^{204}\text{Pb}) + 13.491 \quad (4.2)$$

$$^{208}\text{Pb}/^{204}\text{Pb} = 1.209(^{206}\text{Pb}/^{204}\text{Pb}) + 15.627 \quad (4.3)$$

Another way to show the anomaly is to calculate the vertical deviations from the NHRL for a given data set (DS) are given by the following equations:

$$\Delta 7/4 = [(^{207}\text{Pb}/^{204}\text{Pb})_{\text{DS}} - (^{207}\text{Pb}/^{204}\text{Pb})_{\text{NHRL}}] \times 100 \quad (4.4)$$

$$\Delta 8/4 = [(^{208}\text{Pb}/^{204}\text{Pb})_{\text{DS}} - (^{208}\text{Pb}/^{204}\text{Pb})_{\text{NHRL}}] \times 100 \quad (4.5)$$

Kama‘ehuakanaloa samples all plot above the NHRL in  $^{208}\text{Pb}/^{204}\text{Pb}$ - $^{206}\text{Pb}/^{204}\text{Pb}$  space, including the North Rift tholeiite, which is consistent with enrichments in OIB lavas. In  $^{207}\text{Pb}/^{204}\text{Pb}$ - $^{206}\text{Pb}/^{204}\text{Pb}$  space, all Kama‘ehuakanaloa samples plot below the NHRL, though the deviations are smaller than the ones in the 8/4 plot. This is consistent with the observation that Pb isotopes of Hawaiian lavas often overlap with MORB composition and rarely show isotopic characteristics from enriched mantle.

#### 4.5.3 Integrating ${}^3\text{He}/{}^4\text{He}$ Isotopes to understand volcanic evolution

This study found that there is a statistically significant difference between Pb-He isotopes from the two dredges (TUNE-003D, classified as North Rift tholeiites, and TUNE-004D, South Rift alkali basalts). The distinction between the major element and isotopic composition is rarely clarified, and the two are often interpreted as petrologically similar based on picritic texture (Valbracht et al., 1996; Kent et al., 1999b; Abouchami et al., 2005). However, they represent different major rock types, and it is necessary to distinguish between unique and representative tholeiitic samples in order to appropriately interpret characteristics of Kama‘ehuakanaloa’s shield stage. There is some separation of South Rift lavas and  ${}^{206}\text{Pb}/{}^{204}\text{Pb}$  compositions, but not for  ${}^{207}\text{Pb}/{}^{204}\text{Pb}$  or  ${}^{208}\text{Pb}/{}^{204}\text{Pb}$  (Fig. 4.12). Similar to trace element ratios, the North Rift tholeiites are dissimilar to South Rift tholeiites by showing the least radiogenic Pb values.

At Kama‘ehuakanaloa, Pb isotope variation likely relates to long-term U-Th-Pb characteristics of the mantle sources. Additional endmember types for components only present in the pre-shield stage have been observed at Kama‘ehuakanaloa, while post-shield components have been observed at Kohala and Haleakalā (Weis et al., 2020). The radiogenic isotope geochemistry, or Sr-Nd-Pb-Hf isotope signature of Hawaiian shield basalts reveals several mantle isotope components, and drill cores indicate rapid variation and mantle component mixing (Weis et al., 2020; Kurz et al., 2004). Isotope diversity reflects melting heterogeneities that are (1) irregularly distributed in the upper mantle, or (2) intrinsically plume-hosted (Weis et al., 2020; DePaolo et al., 2001; Hanano et al., 2010).

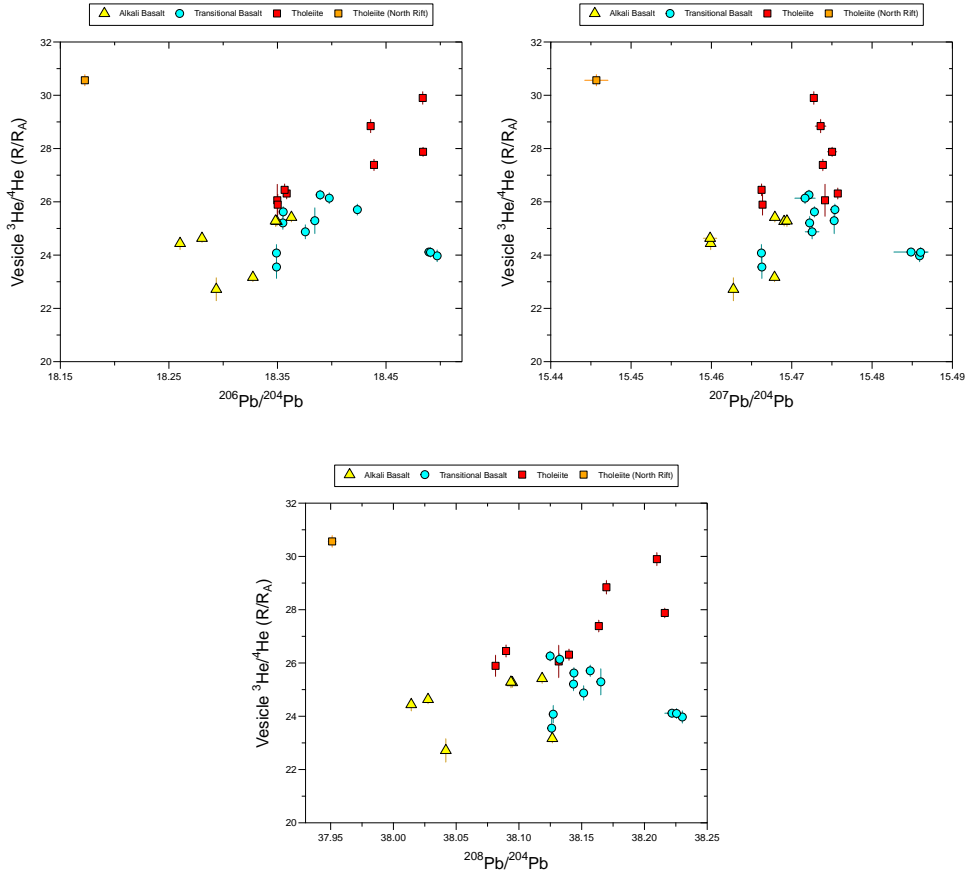


Figure 4.12: Vesicle  ${}^3\text{He}/{}^4\text{He}$  ( $R_A$ ) vs.  ${}^{206}\text{Pb}/{}^{204}\text{Pb}$ - ${}^{207}\text{Pb}/{}^{204}\text{Pb}$ - ${}^{208}\text{Pb}/{}^{204}\text{Pb}$

Though Sr-Nd isotopes are not part of the empirical dataset of this study, the Pb isotope analyses of whole rock material in Valbracht et al. (1996) match the results of glasses from this study, and it can be assumed that "T4D3" and 'T4D4" represent TUNE-003D and TUNE-004D samples in this study, respectively. The next section will examine previously determined Sr-Nd results in context of this study's Pb-He isotope contributions. TUNE-003D samples show less enriched Sr~0.703634 compared to TUNE-004D Sr~0.703716 (Valbracht et al., 1996). Typically, Sr-Nd has a negative relationship in

global OIB (Stracke, 2012), but TUNE-003D  $^{143}\text{Nd}/^{144}\text{Nd} = 0.512935$  exhibits a slightly more enriched signature compared to TUNE-004D  $^{143}\text{Nd}/^{144}\text{Nd} = 0.512959$  (Valbracht et al., 1996). Hence, North Rift tholeiites show less radiogenic Sr-Pb isotopes, but similar or slightly enriched Nd isotopes relative to South Rift basalts.

Results from chapter 3 revealed different mean  $^3\text{He}/^4\text{He}$  for Kama‘ehuakanaloa tholeiites compared to transitional basalts, and alkalic basalts, and alkalic basalts exhibited less variance in  $^3\text{He}/^4\text{He}$  than transitional basalts. Higher  $^3\text{He}/^4\text{He}$  in Kama‘ehuakanaloa tholeiites suggests a greater proportion of a primordial source in shield lavas. The same statistical treatment can be done with Pb isotopes. Figure 4.13 shows how the depleted mantle source often overlaps with Pb isotopes for Kama‘ehuakanaloa and Mauna Loa type lavas. However, Kama‘ehuakanaloa samples and the representative mantle composition extend to high- $^3\text{He}/^4\text{He}$ . A possible mixing line between Kama‘ehuakanaloa could be consistent with the transitional basalt composition.

Hawaiian shield to post-shield isotope trends evolve along  $^{208}\text{Pb}/^{204}\text{Pb}$ - $^{206}\text{Pb}/^{204}\text{Pb}$  lineaments, and volcanoes from the same trend can sample more and less radiogenic Pb with time. (Hanano et al., 2010). Figure 4.14 shows a linear trend drawn through South Rift alkali basalts to transitional basalts consistent with the evolution of other Hawaiian volcanoes from shield/late-shield to post-shield stage, particularly Mahukona lavas. Similar to the observations in Figure 4.11 of radiogenic  $^{208}\text{Pb}^*/^{206}\text{Pb}^*$ , the evolution within the Kama‘ehuakanaloa suite is consistent with evolution of the Loa component in a bi-laterally zoned plume (Abouchami et al., 2005). Overall, Kama‘ehuakanaloa Pb isotopes are consistent with the pre-shield to shield transition as proceeding in a similar way of shield to post-shield, though  $^3\text{He}/^4\text{He}$  isotope evolution does not proceed in a similar

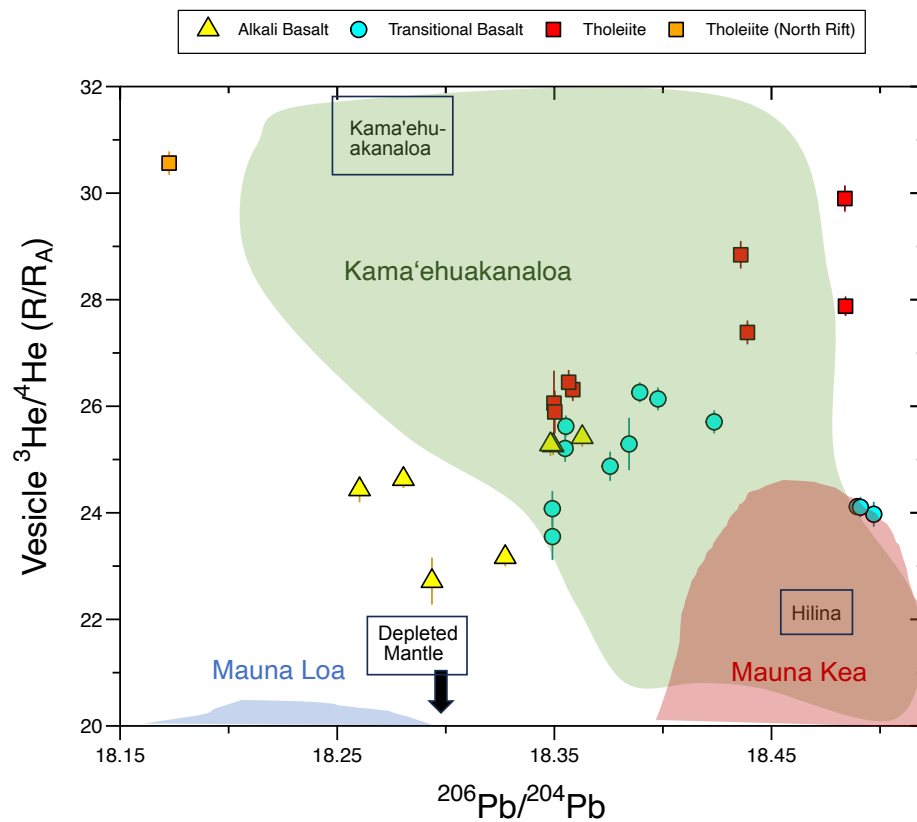


Figure 4.13: Vesicle  ${}^3\text{He}/{}^4\text{He}$  ( $R_A$ ) vs.  ${}^{206}\text{Pb}/{}^{204}\text{Pb}$ . Compilation from Hanyu et al. (2010) of major Hawaiian volcanoes Kama'ehuakanaloa, Mauna Kea and Mauna Loa shown in colored fields, and components for Kama'ehuakanaloa, Depleted Mantle, and Hilina shown in boxes.

way.

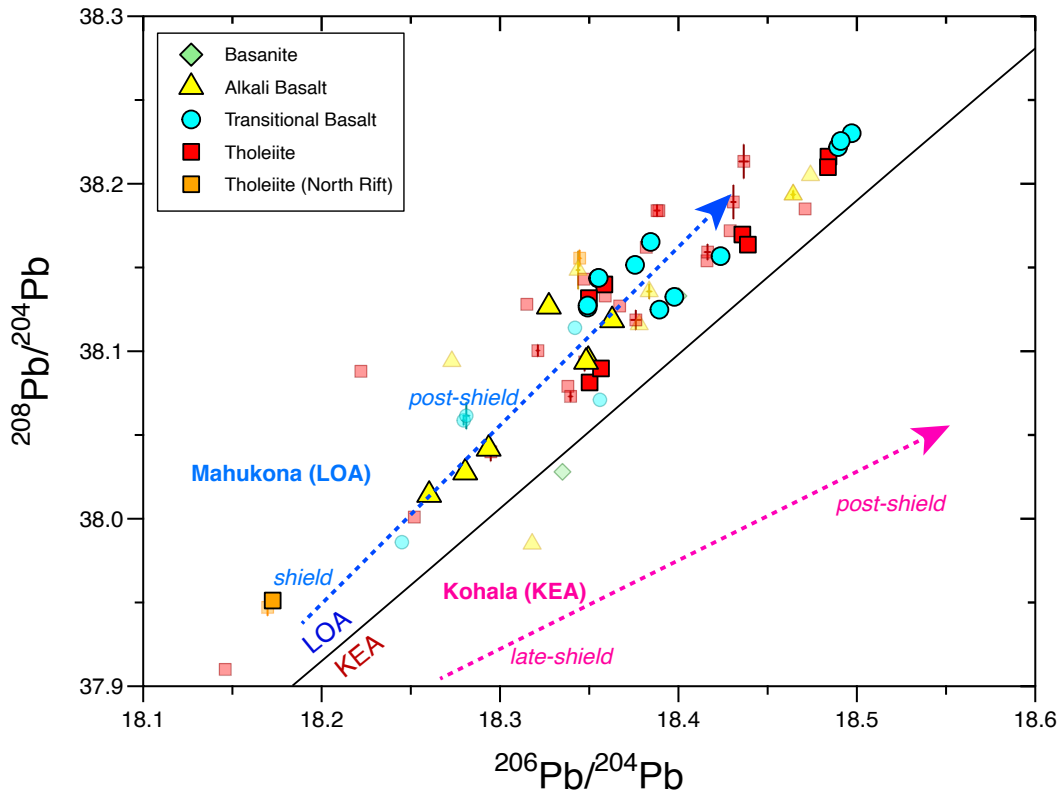


Figure 4.14:  $^{208}\text{Pb}/^{204}\text{Pb}$  vs.  $^{206}\text{Pb}/^{204}\text{Pb}$  of this study shown in comparison with trendlines of Loa and Kea volcano evolution from Hanano et al. (2010). Mahukona (LOA) trend shown in blue dashed arrow with approximate locations of shield and post-shield samples. Kohala (KEA) trend shown in pink dashed line with approximate locations of late-shield to post-shield

## 4.6 Conclusions

The range of Pb isotopes along the South Rift zone (from depths of 2-5 km depth) are comparable to the range observed at a stratigraphic sequence observed at the pit crater complex. Overall, tholeiites from either North or South Rift zone show less radiogenic signatures ( $^{208}\text{Pb}/^{204}\text{Pb}$ ,  $^{207}\text{Pb}/^{204}\text{Pb}$ ,  $^{206}\text{Pb}/^{204}\text{Pb}$ ) compared to alkali basalts. However, transitional basalts, which are transitional in trace elements and  $^3\text{He}/^4\text{He}$  isotopes (Ch. 2 and 3) do not display intermediate Pb isotope compositions between the range of tholeiites and alkali basalts. Instead, they share the range of alkali basalts, even extending to higher  $^{206}\text{Pb}/^{204}\text{Pb}$ - $^{207}\text{Pb}/^{204}\text{Pb}$ - $^{208}\text{Pb}/^{204}\text{Pb}$  than alkali basalts in this study, and most previous data in  $^{206}\text{Pb}/^{204}\text{Pb}$ - $^{208}\text{Pb}/^{204}\text{Pb}$  (Fig. 4.6).

The compositions of transitional basalts add complexity to the interpretation of less radiogenic Pb isotopes with strictly pre-shield stage, and radiogenic Pb isotopes with early shield. However, Pb isotopes generally appear to be indicators of Kama‘ehuakanaloa’s temporal evolution, similar to the evolution at other Hawaiian volcanoes (both Loa and Kea trend affinities), where increasingly radiogenic  $^{206}\text{Pb}/^{204}\text{Pb}$  and  $^{208}\text{Pb}/^{204}\text{Pb}$  are observed after the shield (or late-shield) to post-shield stage affinities (Fig. 4.14).

The relationship of Pb-He was explored by comparing vesicle  $^3\text{He}/^4\text{He}$  isotope ratios (Ch. 3) with new Pb isotope results. South Rift tholeiites show positive trends between  $^3\text{He}/^4\text{He}$  and all Pb isotopes, most significantly when comparing alkali basalts and tholeiites, where alkali basalts exhibit the lowest  $^3\text{He}/^4\text{He}$  and radiogenic Pb isotopes, and tholeiites show the highest  $^3\text{He}/^4\text{He}$  and overlap in radiogenic Pb isotopes with transitional basalts. An exception to this trend is the North Rift tholeiites, which

have among the highest  ${}^3\text{He}/{}^4\text{He}$ , but the lowest radiogenic isotope compositions.

This study found that there is a statistically significant difference between Pb-He isotopes from two dredges from the same expedition, TUNE-003D and TUNE-004D. Though their isotopic compositions are within the range of known Kama‘ehuakanaloa compositions, they do not represent the same mantle source composition, as North Rift tholeiites exhibit trace element and isotopic characteristics unlike the South Rift tholeiites. Future work should continue to replicate measurements and compare characteristics to test whether or not these samples, in addition to TUNE-002D (not included in this study) consistently overlap in isotopic composition, or if there are differences that should be examined further.

## Chapter 5: Conclusions

Volcanic transitions are an important issue in understanding the different ways in which intraplate volcanism proceeds with the evolution of a mantle plume. Two key problems are the frequency of data gaps from hiatuses in volcanic activity and inaccessible early stage lavas due to complete coverage by later stage productive phases.

The rationale for revisiting prior data stems from the observation that classification of alkaline compositions (including transitional) based on modal mineralogy is necessary for basalt classification. Data selection and compilation efforts have resulted in a binary classification of samples into tholeiitic/primitive and alkaline/evolved, where presumed tholeiitic samples are targeted for geochemical measurements, and hence, have higher potential for replication studies and data reuse. Filtered datasets, however, may result in an averaging out of heterogeneity among Kama'ehuakanaloa sample groups or locations and a biased focus toward the tholeiitic/primitive compositions. This practice leaves a "long tail" of data ([Heidorn, 2008](#)), where alkaline and transitional basalts are rarely used to examine spatial/temporal trends, where field relationships and structural morphology are unknown. The legacy of such classification limits to the degree to which such samples are re-used for analysis, and which data passes certain criteria for future research questions.

This study contributed a dataset of trace element compositions for samples collected from a range of locations on Kama'ehuakanaloa Seamount, predominantly along the rift

zone portions which make up  $\sim 30$  km of the volcano's length and from 2–5 km collection depth, which provide insights into pre-shield and early shield evolution at a single volcano.

Differences in trace element enrichment of the relatively evolved compositions observed within this study suite can be attributed to predominantly olivine crystallization (and to a lesser extent, clinopyroxene and plagioclase) from parental melts. The range of variation in most trace element ratios observed in South Rift glasses overlaps with compositions observed in the Western Ridge and East Flank regions, regardless of depth of collection (dive samples). However, the North Rift tholeiites exhibit differences compared to tholeiites of other regions. Hence, lavas erupted in the North Rift likely originate from different magma chambers than tholeiites from the South Rift zone.

Kama'ehuakanaloa's geochemical transition has been known to be gradational. Transitional basalts likely represent intermediate products from alkalic and tholeiite magma generation, overlapping with both types in concentrations and source ratios. The differences between alkalic and subalkalic/tholeiite parental melts can be attributed to differences in partial melting. There appears to be a relatively heterogeneous common origin to all Kama'ehuakanaloa basalts in this study. The range of trace element enrichment and diagnostic mantle source ratios may be related to polybaric melting from a range of mantle source depths with both garnet and spinel lherzolite contributions.

Helium isotope trends correspond to major element composition, with the lowest  ${}^3\text{He}/{}^4\text{He}$  observed in samples with alkalic compositions. Tholeiites are interpreted as the most recent eruptives at Kama'ehuakanaloa seamount, coinciding with expression of shield volcanism. In addition, if the elongate volcano grows northward, the observation of the high  ${}^3\text{He}/{}^4\text{He} \sim 30.5 \text{ R}_\text{A}$  in the North Rift tholeiites provides support for

the high  $^3\text{He}/^4\text{He}$  source influencing magma chambers contributing to North and South Rifts. Plume-sourced Helium, interpreted in  $^3\text{He}/^4\text{He}$  isotopes, hence, is expected as the transition to shield volcanism continues.

Possible controls on Helium concentrations include preferential loss of He during degassing. Similarity in estimated  $\text{H}_2\text{O}$  contents of the mantle source of North Rift tholeiites and South Rift tholeiites, Nb/U, W/U among North Rift and South Rift tholeiites suggests similar history of addition from recycled or subducted materials. The high- $^3\text{He}/^4\text{He}$ , high  $^3\text{He}/^4\text{He}$  concentrations, and low mantle source Cl concentrations of the North Rift samples suggests a mantle source that is relatively free of influence from incorporating of recycled, seawater and/or atmospheric components.

The distribution of Pb isotopes at Kama‘ehuakanaloa was examined to assess indicators of mantle source variation at the youngest Hawaiian shield volcano. Glasses from Kama‘ehuakanaloa South and North rift zones exhibit some variation despite likely similar timescales of eruption, and the range of Pb isotopes along the South Rift zone (from depths of 2-5 km depth) are comparable to the range observed at a stratigraphic sequence observed at the pit crater complex.

South Rift tholeiites exhibit more radiogenic Pb isotope ratios than South Rift alkalic basalts and North Rift tholeiites. Replicates of dredged whole rock analyses of glass material in this study confirms that the North Rift tholeiites exhibit the least radiogenic Pb isotope ratios. The compositions of transitional basalts add complexity to the interpretation of less radiogenic Pb isotopes with strictly pre-shield stage, and radiogenic Pb isotopes with early shield. Transitional basalts do not display intermediate Pb isotope compositions between tholeiites and alkali basalts, but extend to higher  $^{206}\text{Pb}/^{204}\text{Pb}$ -

$^{207}\text{Pb}/^{204}\text{Pb}$ - $^{208}\text{Pb}/^{204}\text{Pb}$  than alkali basalt values. Kama‘ehuakanaloa Pb isotope compositions and  $^{208}\text{Pb}^*/^{206}\text{Pb}^*$  are consistent with the Loa component in a bilaterally zoned plume, and the temporal evolution of Pb isotopes from alkalic to tholeiitic is similar to observations of shield to post-shield compositions of other Hawaiian volcanoes.

Additional petrographic analyses to constrain mineral and melt proportions can be used to evaluate rock type differences and explore magma chamber dynamics. The observation of high- $^3\text{He}/^4\text{He}$   $\sim 35 \text{ R}_\text{A}$  in a transitional basalt (Matsumoto et al., 2008) motivates further comparison of the plume signature in transitional basalt samples, which are considered less frequently for understanding Hawaiian shield source chemistry.

## APPENDICES

## Appendix A: Chapter 0

### Expedition Descriptions

#### 1981 Kana Keoki

The first collection, from expedition KK1-HW-81, were collected by dredge in 1981 cruise on the R/V *Kana Keoki*. The expedition yielded 18 dredge stations total. Sample locations, general petrographic descriptions, and chemical compositions were provided in [Moore et al. \(1982\)](#). A designation of maximum possible flow units per dredge station were also included, based on lava morphology, glass characteristics, characteristics of hydrothermal deposits. Microprobe glass analyses were presented in [Moore et al. \(1982\)](#) in addition to modal data for olivine, clinopyroxene, plagioclase, titanomagnetite, and vesicles.

#### MIR 1990

MIR samples were collected in 1990 during dives with the Russian submersible MIR (Russian for “world”). Samples collected by MIR in 1990 were mostly taken from pillow basalts along exposed portions of the rift zone using a cm-wide knife-edge tool that sampled fresh glass ([Valbracht et al., 1996](#)). MIR samples have the least metadata available. Major element glass compositions and sampling notes were provided by Garcia (unpub-

lished), originally from Alexander Malahoff and shipboard scientists. Water depths for the MIR sample locations are taken from unpublished data tables, and in some cases, precise sample locations are not available. Some locations and depths may be an average of the start/stop transect recorded for an entire dive. Locations for each MIR dive sample should therefore be viewed as approximations based on the reported dive start/end locations and sample collection depths. This study includes the majority of dive stations from the expedition.

### 1991 Pisces V

Pisces V samples collected in 1991 by the Pisces submersible at a deeply dissected section from the east flank near the summit region. Sampling information, glass microprobe analyses, and trace elements are reported in [Garcia et al. \(1995\)](#). Though the samples represent a limited range of depth, they include a range of compositions including tholeiitic, weakly alkalic and strongly alkalic. The sample set includes two basanites, which are the most differentiated samples of the study's sample suite.

### TUNE04WT 1991

TUNE04WT dredge samples were collected in October 1991 during the Tunes IV expedition, Leg 4, on the R/V *Thomas Washington*. In this study, these are the only samples with International Generic Sample Number (IGSN) assignments ([SIO Geological Data Center, 2018](#)). However, each dredge varied in collection weight up to hundreds of kilo-

grams, hence, the same IGSN cannot be assumed to represent identical sub-samples. Splits were sent to ANU and SIO repositories, and are usually named "LO-02" or "T4-D2" with the latter digit indicating dredge haul number (range of 1-4), e.g. in [Valbracht et al. \(1996\)](#); [Bennett et al. \(1996\)](#); [Kent et al. \(1999a\)](#). This study includes half of the dive stations from the expedition, from dredge 3 and dredge 4.

### Shinkai 6500 1999

Dives/manned submersible of Shinkai 6500 during the 1999 YK-99-07 expedition. The Shinkai 6500. or 6K, submersible (Japanese for "deep sea") is known to be the most capable of sampling the deepest water depths of any known submersibles. Sample collection depths and precise locations for Shinkai 6500 dives during August and September 1999 are taken from the cruise report ([Shipboard Scientists, 1999](#)). These samples have the most documentation of media and video in the JAMSTEC archive. These samples have the highest amount of location metadata and media available. This study includes the majority of the dive stations from the expedition.

Table A.1: Electron Microprobe Measurements of Major Elements determined by JEOL JXA 8200 by P.J. Michael at University of Tulsa

ID	Sample	SiO <sub>2</sub> <sup>[1]</sup>	TiO <sub>2</sub>	Al <sub>2</sub> O <sub>3</sub>	FeO	MnO	MgO	CaO	Na <sub>2</sub> O	K <sub>2</sub> O	P <sub>2</sub> O <sub>5</sub>	Sum
13	MIR 2337-b <sup>[2]</sup>	50.3	2.25	16.9	7.34	0.14	7.18	10.7	3.05	1.17	0.52	99.58
17	MIR 2340-1	49.0	2.56	14.0	11.5	0.18	6.85	12.1	2.64	0.53	0.26	99.68
47	TUNE 003D-A	49.8	2.14	13.4	10.8	0.14	8.37	11.3	2.39	0.33	0.19	98.86
48	TUNE 003D-B	50.2	2.14	13.5	10.9	0.18	8.26	11.4	2.40	0.32	0.19	99.51

Electron Microprobe Measurements of Major Elements determined by JEOL JXA 8200 by P.J. Michael at University of Tulsa

ID	Sample	SiO <sub>2</sub> <sup>[1]</sup>	TiO <sub>2</sub>	Al <sub>2</sub> O <sub>3</sub>	FeO	MnO	MgO	CaO	Na <sub>2</sub> O	K <sub>2</sub> O	P <sub>2</sub> O <sub>5</sub>	Sum
49	TUNE 003D-C	50.0	2.14	13.5	10.9	0.18	8.24	11.3	2.42	0.33	0.20	99.23
50	TUNE 004D-A	47.2	3.17	14.5	11.4	0.15	5.79	11.1	3.33	0.86	0.37	97.84
51	TUNE 004D-B	47.0	3.22	14.5	11.6	0.16	5.99	11.1	3.31	0.85	0.37	98.05
56	KK 31-9	46.3	2.13	13.7	11.8	0.18	8.09	12.5	2.60	0.67	0.23	98.20

<sup>[1]</sup> All units are in weight percent (%). All UT analyses have been multiplied by a factor of 0.90 to minimize inter-laboratory bias factors when comparing with major element compositions previously reported by University of Hawai'i

<sup>[2]</sup> MIR 2337-b is a highly differentiated alkali basalt of unusual composition with unknown original parent sample. It was not included in the rest of this study.

Table A.2: Location Metadata for Dive/Submersible Collected Samples

ID	Sample Name	Location	Depth (m)	Latitude (N°)	Longitude (W°)
1	MIR 2335-2 <sup>[1]</sup>	South Rift	5068	18.70231	-155.1604
2	MIR 2335-5	South Rift	5025	18.70487	-155.1619
3	MIR 2335-6	South Rift	4983	18.70061	-155.1833
4	MIR 2335-7	South Rift	4979	18.70568	-155.1909
5	MIR 2335-8	South Rift	4976	18.70696	-155.1915
6	MIR 2335-9	South Rift	4971	18.70911	-155.1909
7	MIR 2335-10	South Rift	5000	18.69363	-155.1643
8	MIR 2335-11	South Rift	4814	18.72764	-155.2000
9	MIR 2335-12	South Rift	4614	18.72000	-155.1900
10	MIR 2336-2	South Rift	4820	18.74055	-155.1647

## Location Metadata for Dive/Submersible Collected Samples (continued)

ID	Sample Name	Location	Depth (m)	Latitude (N°)	Longitude (W°)
11	MIR 2336-4	South Rift	4420	18.75794	-155.1767
12	MIR 2336-5	South Rift	4140	18.76991	-155.1858
13	MIR 2337-b	South Rift	4795	18.73000	-155.1600
14	MIR 2337-2	South Rift	4810	18.73738	-155.1730
15	MIR 2337-3	South Rift	4810	18.73738	-155.1730
16	MIR 2338-1a	South Rift	4930	18.71259	-155.1905
17	MIR 2340-1	South Rift	1309	18.89648	-155.2504
18	MIR 2340-3	South Rift	1314	18.89511	-155.2497
19	MIR 2341-1	South Rift	3280	18.80223	-155.2047
20	MIR 2341-2	South Rift	2943	18.81704	-155.2111
21	MIR 2343-2	South Rift	3718	18.78532	-155.1927
22	MIR 2343-3	South Rift	3648	18.78845	-155.1948
23	MIR 2343-4	South Rift	3698	18.78845	-155.1948
24	MIR 2343-5	South Rift	3650	18.78845	-155.1948
25	MIR 2343-6	South Rift	3598	18.79159	-155.1954
26	MIR 2343-7	South Rift	3560	18.79244	-155.1978
27	MIR 2343-8	South Rift	3508	18.79444	-155.1981
28	MIR 2343-10	South Rift	3410	18.79872	-155.1996
29	MIR 2343-11	South Rift	3350	18.79900	-155.2023
30	MIR 2343-12	South Rift	3195	18.80499	-155.2047
31	MIR 2343-13	South Rift	3179	18.80499	-155.2047
32	Shinkai 490-8 [2]	South Rift	4383	18.75830	-155.1900
33	Shinkai 494-1	South Rift	2541	18.83170	-155.2183
34	Shinkai 494-2	South Rift	2466	18.83500	-155.2200

## Location Metadata for Dive/Submersible Collected Samples (continued)

ID	Sample Name	Location	Depth (m)	Latitude (N°)	Longitude (W°)
35	Shinkai 494-3	South Rift	2491	18.83500	-155.2250
36	Shinkai 494-4	South Rift	2491	18.83500	-155.2267
37	Shinkai 494-5	South Rift	2358	18.84000	-155.2267
38	Shinkai 494-6	South Rift	2323	18.84170	-155.2300
39	Shinkai 494-7	South Rift	2269	18.84500	-155.2317
40	Shinkai 494-8	South Rift	2171	18.84670	-155.2333
41	Shinkai 513-3	South Rift	4245	18.76010	-155.1789
42	Shinkai 513-4A	South Rift	4134	18.76500	-155.1803
43	Shinkai 513-5	South Rift	3936	18.77020	-155.1817
44	Shinkai 513-6	South Rift	3936	18.77140	-155.1817
45	Shinkai 513-7A	South Rift	3936	18.77140	-155.1817
46	Shinkai 515-1	South Rift	3060	18.80370	-155.2030
58	Pisces V 158-4 [3]	East Flank	1926	18.93000	-155.2400
59	Pisces V 158-5	East Flank	1830	18.93000	-155.2400
60	Pisces V 186-3	East Flank	1900	18.94000	-155.2500
61	Pisces V 187-1A	East Flank	2000	18.95000	-155.2500
62	Pisces V 187-5B	East Flank	1580	18.95000	-155.2500
63	Pisces V 187-8	East Flank	1215	18.95000	-155.2500
64	Pisces V 187-9	East Flank	1080	18.95000	-155.2500

[1] Reference for all MIR samples may be in Matvenkov and Sorokhtin (1998) but the publication is not accessible at the present time. A few locations are shown in Valbracht et al. (1997)

[2] Expedition information for Shinkai samples is Shipboard Scientists (1999)

[3] Expedition and sampling information Pisces V samples in Garcia et al. (1995)

Table A.3: Location Metadata for Dredge Samples

ID	Sample Name	Location	Depth start (m)	Depth end (m)	Latitude start (N°)	Latitude end (N°)	Longitude start (W°)	Longitude end (W°)
47	TUNE 003D-A [1]	North Rift	1900	1830	19.0000	19.0017	-155.2683	-155.26
48	TUNE 003D-B	North Rift	1900	1830	19.0000	19.0017	-155.2683	-155.26
49	TUNE 003D-C	North Rift	1900	1830	19.0000	19.0017	-155.2683	-155.26
50	TUNE 004D-A	South Rift	4200	3900	18.7583	18.7733	-155.2083	-155.19
51	TUNE 004D-B	South Rift	4200	3900	18.7583	18.7733	-155.2083	-155.19
52	TUNE 004D-C	South Rift	4200	3900	18.7583	18.7733	-155.2083	-155.19
53	KK 17-2 [3]	North Rift	1662	1572	18.9800	18.9900	-155.2700	-155.28
54	KK 20-14	South Rift	1682	1351	18.8900	18.8900	-155.2600	-155.27
55	KK 25-4	South Rift	2093	1913	18.8600	18.8600	-155.2400	-155.26
56	KK 31-9	Western Ridge	2323	2049	18.9400	18.9500	-155.2900	-155.32
57	KK 31-12	Western Ridge	2323	2049	18.9400	18.9500	-155.2900	-155.32

[1] Reference for location for all TUNE samples from SIO Geological Data Center (2018). Separate rocks from a single dredge haul (either dredge 3 for “TUNE 003D” or dredge 4 for “TUNE 004D”) are originally classified as unique samples because of unknown degree of sample splitting from parent rocks.

[2] Reference for locations for all KK samples from Moore et al. (1982)

### A.1 Chapter 1

Table A.4: CIPW Normative Compositions

ID	Sample Name	Rock Type [1]	Or	Ab	An	Ne	Di	En	OI	Mt	Il	Ap	Normative Index <sup>[2]</sup>	Alkalinity Index <sup>[3]</sup>
1	MIR 2335-2	TR	4.3	24.4	23.9	0.3	26.9		12.0	1.8	5.8	0.7	0.2	
2	MIR 2335-5	TR	4.3	23.8	23.8	0.2	28.1		11.7	1.8	5.8	0.7	0.3	
3	MIR 2335-6	TR	4.5	25.2	24.6	0.1	26.1		11.1	1.8	5.9	0.8	0.4	
4	MIR 2335-7	TR	4.4	24.8	24.5	0.0	26.4	0.1	11.5	1.8	5.9	0.7	-0.1	0.3
5	MIR 2335-8	TR	4.4	24.1	23.9	0.6	26.9		11.9	1.8	5.8	0.7	0.3	
6	MIR 2335-9	TR	4.2	20.5	23.4	1.7	30.3		11.7	1.9	5.7	0.7	0.4	
7	MIR 2335-10	TR	4.5	24.2	24.0	0.4	27.2		11.5	1.8	5.8	0.7	0.4	
8	MIR 2335-11	TR	4.9	25.0	23.5	1.1	25.6		11.5	1.9	6.0	0.8	0.6	
9	MIR 2335-12	TH	4.4	24.3	24.1	0.3	26.8		11.8	1.8	5.9	0.8	-0.4	
10	MIR 2336-2	TR	4.6	23.8	22.9	1.0	27.3		12.0	1.8	5.8	0.8	0.5	
11	MIR 2336-4	TH	3.3	22.0	22.8	0.0	29.9	4.5	9.3	1.9	5.8	0.6	-4.5	-0.2
12	MIR 2336-5	TR	4.7	28.2	22.5	0.0	24.1	0.2	11.4	1.9	6.1	0.9	-0.2	0.5
14	MIR 2337-2	TH	3.4	21.8	25.1	0.0	26.1	8.6	7.3	2.0	5.1	0.5	-8.6	-0.5
15	MIR 2337-3	TH	3.0	22.2	25.4	0.0	24.1	14.7	2.6	1.9	5.5	0.6	-14.7	-0.8
16	MIR 2338-1a	TR	4.8	24.3	23.3	0.9	27.0		11.4	1.9	5.9	0.8	0.6	
18	MIR 2340-3	TH	2.9	20.7	24.0	0.0	29.3	9.7	6.4	1.9	4.7	0.5	-9.7	-0.9
19	MIR 2341-1	TR	4.2	25.7	23.5	0.0	24.3	4.8	8.6	2.0	6.3	0.8	-4.8	0.3
20	MIR 2341-2	AB	6.4	21.0	22.4	4.7	25.4		11.1	2.0	6.2	1.0	1.6	
21	MIR 2343-2	TR	4.4	25.5	22.3	0.0	24.9	0.5	12.4	2.2	7.0	0.8	-0.5	0.7
22	MIR 2343-3	TR	4.6	23.1	24.0	1.4	25.9		12.3	2.0	6.0	0.7	0.7	
24	MIR 2343-5	TR	4.5	23.4	24.3	1.0	25.8		12.4	2.0	5.9	0.8	0.6	
25	MIR 2343-6	AB	6.1	21.9	22.2	4.1	25.2		11.1	1.9	6.5	1.0	1.5	
26	MIR 2343-7	TR	4.5	22.7	24.4	1.4	26.1		12.1	2.0	6.0	0.8	0.6	
27	MIR 2343-8	TR	4.3	22.4	24.3	1.2	27.4		12.1	1.9	5.8	0.8	0.4	
28	MIR 2343-10	TR	4.2	21.6	23.3	1.3	29.4		12.1	1.9	5.6	0.7	0.3	
29	MIR 2343-11	TR	4.6	23.1	23.9	1.4	26.1		12.5	2.0	5.9	0.8	0.6	
30	MIR 2343-12	AB	5.8	24.1	22.1	3.4	24.4		11.1	1.9	6.3	0.9	1.4	
31	MIR 2343-13	AB	5.4	22.2	21.4	3.6	27.8		10.8	1.9	6.2	0.8	1.2	
32	Shinkai 490-8	TH	3.5	23.8	24.6	0.0	25.0	10.4	4.3	1.9	5.9	0.7	-10.4	-0.2

CIPW Normative Compositions (continued)

ID	Sample Name	Rock Type [1]	Or	Ab	An	Ne	Di	En	OI	Mt	II	Ap	Normative Index[2]	Alkalinity Index[3]
33	Shinkai 494-1	TR	4.9	27.3	21.6	0.0	22.8	6.3	7.5	2.1	6.8	0.9	-6.3	0.5
34	Shinkai 494-2	TR	4.7	26.6	22.3	0.0	22.8	7.7	6.4	2.0	6.7	0.9	-7.7	0.4
35	Shinkai 494-3	AB	6.9	21.5	20.9	5.7	24.0		11.1	2.0	6.8	1.1		2.2
36	Shinkai 494-4	AB	6.7	21.7	21.3	5.4	24.3		11.0	2.0	6.6	1.1		2.0
37	Shinkai 494-5	TH	2.8	22.2	25.6	0.0	24.1	14.5	2.8	2.0	5.5	0.6	-14.5	-0.6
38	Shinkai 494-6	TH	2.7	21.8	25.8	0.0	24.9	13.8	3.3	1.9	5.3	0.6	-13.8	-0.7
39	Shinkai 494-7	TH	2.7	22.0	25.9	0.0	24.7	14.9	2.1	1.9	5.3	0.6	-14.9	-0.7
40	Shinkai 494-8	TH	3.1	22.8	24.7	0.0	23.9	14.9	2.2	2.0	5.7	0.7	-14.9	-0.5
41	Shinkai 513-3	TH	3.4	23.6	24.5	0.0	25.5	7.1	7.3	2.0	6.1	0.7	-7.1	0.0
42	Shinkai 513-4A	TR	5.2	27.9	21.9	0.9	23.8		11.5	1.9	6.2	0.8		0.9
43	Shinkai 513-5	TR	3.8	25.9	23.1	0.0	27.5	0.2	11.5	1.8	5.6	0.6	-0.2	0.0
44	Shinkai 513-6	TR	3.9	25.2	22.8	0.0	28.2		11.9	1.8	5.6	0.7		0.1
45	Shinkai 513-7A	TH	3.1	23.4	23.7	0.0	27.3	7.6	7.2	1.8	5.3	0.6	-7.6	-0.6
46	Shinkai 515-1	AB	5.9	22.5	22.2	3.8	25.9		10.5	1.9	6.4	0.9		1.6
47	TUNE 003D-A	TH (N)	2.0	20.2	24.9	0.0	24.5	17.8	3.3	1.7	4.1	0.4	-17.8	-1.3
48	TUNE 003D-B	TH (N)	1.9	20.3	25.2	0.0	24.6	18.9	2.5	1.7	4.1	0.4	-18.9	-1.4
49	TUNE 003D-C	TH (N)	2.0	20.5	25.1	0.0	24.4	18.2	3.0	1.7	4.1	0.4	-18.2	-1.3
50	TUNE 004D-A	AB	5.1	23.6	22.0	2.5	25.2		10.8	1.8	6.0	0.8		1.1
51	TUNE 004D-B	AB	5.0	22.8	22.1	2.8	25.1		11.4	1.9	6.1	0.8		1.2
52	TUNE 004D-C	AB	5.0	24.1	22.0	2.3	25.5		11.1	1.8	6.0	0.8		1.0
53	KK 17-2	AB	5.0	23.5	21.7	1.9	25.9		11.4	1.9	6.2	0.8		1.0
54	KK 20-14	TH	3.0	20.9	22.6	0.0	29.4	11.5	4.4	1.9	4.6	0.5	-11.5	-0.8
55	KK 25-4	TR	3.8	25.0	23.1	0.0	24.4	4.6	9.5	2.0	5.6	0.7	-4.6	0.2
56	KK 31-9	AB	4.0	15.3	23.7	3.6	30.2		15.1	1.9	4.0	0.5		0.6
57	KK 31-12	AB	4.0	15.3	23.7	3.6	30.2		15.1	1.9	4.0	0.5		0.6
58	Pisces V 158-4	Bas	10.3	13.0	19.7	12.5	24.4		9.5	1.9	6.4	1.5		3.6
59	Pisces V 158-5	Bas	4.5	13.2	25.0	5.6	26.3		14.9	2.5	7.2	0.6		1.7
60	Pisces V 186-3	TH	2.1	17.6	24.1	0.0	29.9	17.3	1.2	1.9	4.9	0.5	-17.3	-1.4
61	Pisces V 187-1A	AB	3.9	12.3	21.4	3.8	35.1		16.3	1.9	4.4	0.6		0.1

## CIPW Normative Compositions (continued)

ID	Sample Name	Rock Type [1]	Or	Ab	An	Ne	Di	En	OI	Mt	Il	Ap	Normative Index <sup>[2]</sup>	Alkalinity Index <sup>[3]</sup>
62	Pisces V 187-5B	TR	3.3	21.0	23.3	0.2	31.0		12.6	1.8	5.1	0.7		-0.2
63	Pisces V 187-8	TH	2.6	20.1	24.5	0.0	27.2	12.8	4.9	1.8	4.9	0.6	-12.8	-0.9
64	Pisces V 187-9	TH	2.5	19.9	24.8	0.0	27.8	14.2	3.2	1.8	4.9	0.5	-14.2	-1.1

[1] Rock types are abbreviated to BS = Basanite, AB = Alkali Basalt, TR = Transitional Basalt, and TH = Tholeiite Basalt

[2] Normative Index calculated by CIPW calculation

[3] Alkalinity Index =  $(\text{Na}_2\text{O} + \text{K}_2\text{O}) - (0.37 \times \text{SiO}_2 - 14.43)$  from (Carmichael et al., 1974)

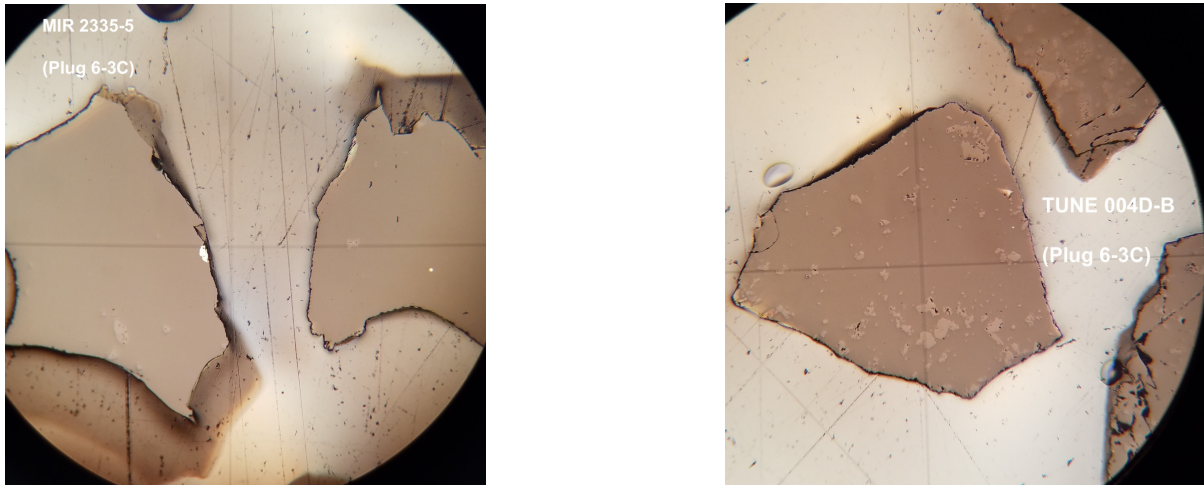


Figure A.1: Grain mount photos taken during the polishing process (a) MIR2335-5, a sparsely olivine-phyric transitional basalt. (b) TUNE04-04B, an olivine-phyric alkalic basalt. Chips are typically 0.25-1.0 mm across.

In the beginning of each analytical session, BCR-2G was measured several times. The bracketing standards were measured before and after each measurement of standards and unknown samples (glasses) for the purpose of correcting external mass bias, but they also demonstrate the machine stability during the analytical sessions.

Table A.5: LA-ICP-MS Standards

Reference Material	Material	Composition	Ref.
GSD-1G	Glass, synthetic	Basalt	Jochum et al. (2005)
GSA-1G	Glass, synthetic	Basalt	Jochum et al. (2005)
BCR-2G <sup>[1]</sup>	Glass, geological	Basalt	Jochum and Nohl (2008)
BHVO-2G <sup>[2]</sup>	Glass, geological	Basalt	Jochum and Nohl (2008)

<sup>[1]</sup> Used as primary calibration standard

<sup>[2]</sup> Used as reference standard

Table A.6: Summary of LA-ICP-MS Analytical Accuracy and Reproducibility: BHVO-2G Standard & Instrument Detection Limit

	BHVO-2G (measurements, n = 12)					LA-ICP-MS
	Accepted/Lit. Value [1]	Measured Mean Value (ppm)	1 $\sigma$ (ppm)	1 $\sigma$ %	Accuracy [2] %	Detection Limit [3] (ppb)
K	4270	4077.9	129.0	3.16	-4.50	252
Rb	9.2	8.75	0.298	3.41	-4.93	5.70
Sr	396	394.4	3.586	0.91	-0.39	4.60
Y	26	25.6	0.795	3.10	-1.41	5.50
Zr	170	171.2	5.400	3.15	0.70	11.60
Nb	18.3	18.0	0.306	1.70	-1.37	7.20
Mo	3.8	4.17	0.135	3.23	9.79	22.10
Sn	2.6	2.09	0.064	3.07	-19.6	18.10
Cs	0.1	0.09	0.004	4.09	-7.60	4.70
Ba	131	130.0	4.051	3.12	-0.73	31.20
Hf	4.32	4.41	0.151	3.42	2.14	13.30
Ta	1.15	1.16	0.020	1.70	0.59	5.10
W	0.23	0.25	0.079	31.6	8.13	16.30
Tl		0.02	0.002	9.98		
Pb	1.7	1.69	0.079	4.67	-0.87	8.90
Th	1.22	1.22	0.031	2.53	-0.10	5.00
U	0.403	0.41	0.020	5.03	0.72	3.20
Sc	33.0	29.8	0.602	0.020	-9.61	15.80
Ti	16300	16688	146.41	0.009	2.38	91.80
V	308.0	334.8	17.93	0.054	8.72	6.30
Mn	1316.6	1369.8	63.32	0.046	4.04	11.10
Ni	116.0	132.8	7.596	0.057	14.4	40.78
La	15.2	14.3	0.307	0.022	-6.17	3.60
Ce	37.6	37.8	1.157	0.031	0.43	3.10
Pr	5.35	5.10	0.036	0.007	-4.60	2.70
Nd	24.5	23.53	0.456	0.019	-3.97	15.40
Sm	6.10	5.79	0.167	0.029	-5.03	15.40
Eu	2.07	1.99	0.026	0.013	-3.63	3.80
Gd	6.16	5.71	0.209	0.037	-7.35	18.30
Tb	0.92	0.84	0.031	0.037	-8.96	3.40
Dy	5.28	4.86	0.206	0.042	-7.92	10.60
Ho	0.98	0.88	0.044	0.050	-10.0	2.90
Er	2.56	2.32	0.114	0.049	-9.26	10.30
Tm	0.34	0.30	0.013	0.046	-12.9	2.60
Yb	2.01	1.86	0.098	0.053	-7.41	13.50
Lu	0.28	0.26	0.011	0.043	-8.54	3.20

[1] Literature - accepted values from GeoReM (<http://georem.mpch-mainz.gwdg.de/>)

[2] Accuracy =  $100 \times [ (\text{Measured Mean Value} - \text{Accepted Value}) / \text{Accepted Value} ]$

[3] ThermoScientific iCap RQ ICP-MS at Oregon State University, 2020

## Appendix B: Chapter 2

Table B.1: Summary of Volatiles Instrumentation

Parameter	Name (Type)	Detection Limit	Blank
$^3\text{He}/^4\text{He}$ [1]	Nu Instruments Noblesse (MS) <sup>[2]</sup>		
$\text{He}^{[1]}$	Nu Instruments Noblesse (MS) <sup>[2]</sup>	$5.00 \times 10^{-11}$ cc STP	$1.00 \times 10^{-10}$ cc STP
$\text{CO}_2$	MKS Baratron Capacitance (Manometry) <sup>[2]</sup>	$5.00 \times 10^{-6}$ cc STP	$1.00 \times 10^{-5}$ cc STP
$\text{CO}_2$	Nicolet 520 (FTIR) <sup>[3]</sup>	15 ppm	
$\text{H}_2\text{O}$	Nicolet 520 (FTIR) <sup>[3]</sup>	0.03 wt.%	
Cl	JEOL JXA 8200 (EMP) <sup>[3]</sup>	0.0008 %	0.0010 %
S	JEOL JXA 8200 (EMP) <sup>[3]</sup>	0.0027 %	0.0005 %
K	JEOL JXA 8200 (EMP) <sup>[3]</sup>	0.0035 %	0.0005 %
Ti	JEOL JXA 8200 (EMP) <sup>[3]</sup>	0.0058 %	
F	JEOL JXA 8200 (EMP) <sup>[3]</sup>	0.021 %	

<sup>[1]</sup> For both vesicle (crushing) and glass (melting) experiments

<sup>[2]</sup> Oregon State University (2020)

<sup>[3]</sup> University of Tulsa (2020)

Table B.2: Summary of Volatiles Reference Materials

Parameter	Name	Measured Value	$\pm 1\sigma$	N=
${}^3\text{He}/{}^4\text{He}$ [1]	HESJ <sup>[5]</sup>	20.37 R <sub>A</sub>	0.06 R <sub>A</sub>	22
He <sup>[1]</sup>	HESJ <sup>[5]</sup>	$1.49 \times 10^{-7}$ cc STP	$3.45 \times 10^{-10}$ cc STP	22
CO <sub>2</sub> <sup>[2]</sup>	CO <sub>2</sub>	$1.77 \times 10^{-2}$ cc STP	$1.8 \times 10^{-4}$ cc STP	4
CO <sub>2</sub> <sup>[3]</sup>	VE32	184 ppm	15 ppm	10
H <sub>2</sub> O	VE32	0.275 wt.%	0.010 wt.%	14
Cl <sup>[4]</sup>	Scapolite USNM R6600-1 <sup>[6]</sup>	1.44 %	0.02 %	10
S <sup>[4]</sup>	Pyrite UC 21334	53.30 %	0.80%	10
K <sup>[4]</sup>	Microcline USNM 143966 <sup>[6]</sup>	12.65 %	0.40 %	10
Ti <sup>[4]</sup>	Ilmenite USNM 96189 <sup>[6]</sup>	27.38 %	0.40 %	10
F	F-Phlogopite Synthetic	9.01 %	0.50 %	10

[1] For both vesicle (crushing) and glass (melting) experiments

[2] Determined by Manometry

[3] Determined by FTIR

[4] Samples normalized by reference material TR154 21D-3

[5] Helium Standard of Japan, from Matsuda et al. (2002)

[6] From Jarosewich et al. (1980)

Table B.3: Model Results for  ${}^3\text{He}/{}^4\text{He}$  and Cl/K for Lava, Seawater, Brine Mixtures

Mixture <sup>[1]</sup>	Fraction Lava <sup>[2]</sup>	${}^4\text{He}$ (cc STP/g)	Cl (wt.%)	$\text{K}_2\text{O}$ (wt.%)	${}^3\text{He}/{}^4\text{He}$ (R <sub>A</sub> )	Cl/K
Lava + Seawater	0	$1.37 \times 10^{-6}$	0.01	0.26	32.0	0.03
	0.1	$1.24 \times 10^{-6}$	0.20	0.24	31.9	0.84
	0.2	$1.11 \times 10^{-6}$	0.39	0.22	31.7	1.82
	0.3	$9.73 \times 10^{-7}$	0.59	0.19	31.6	3.02
	0.4	$8.40 \times 10^{-7}$	0.78	0.17	31.3	4.53
	0.5	$7.08 \times 10^{-7}$	0.97	0.15	31.0	6.48
	0.6	$5.75 \times 10^{-7}$	1.16	0.13	30.5	9.10
	0.7	$4.43 \times 10^{-7}$	1.36	0.11	29.8	12.80
	0.8	$3.10 \times 10^{-7}$	1.55	0.08	28.4	18.45
	0.9	$1.78 \times 10^{-7}$	1.74	0.06	24.9	28.10
	1.0	$4.55 \times 10^{-8}$	1.94	0.04	1.0	48.38
Lava + Brine	0	$1.37 \times 10^{-6}$	0.01	0.26	32.0	0.03
	0.1	$1.24 \times 10^{-6}$	3.04	0.31	31.9	9.73
	0.2	$1.10 \times 10^{-6}$	6.07	0.36	31.8	16.67
	0.3	$9.71 \times 10^{-7}$	9.10	0.42	31.6	21.86
	0.4	$8.38 \times 10^{-7}$	12.12	0.47	31.4	25.91
	0.5	$7.05 \times 10^{-7}$	15.15	0.52	31.1	29.14
	0.6	$5.72 \times 10^{-7}$	18.18	0.57	30.7	31.79
	0.7	$4.39 \times 10^{-7}$	21.21	0.62	30.0	33.99
	0.8	$3.06 \times 10^{-7}$	24.24	0.68	28.8	35.86
	0.9	$1.73 \times 10^{-7}$	27.27	0.73	25.5	37.46
	1.0	$4.00 \times 10^{-8}$	30.30	0.78	1.0	38.85

<sup>[1]</sup> Endmember details in Table 3.6. Results shown in Figure 3.8.

<sup>[2]</sup> Note that Figure 3.8 also shows fractions in increments of 0.01 between 0-0.1 and 0.9-1.0 in the mixing curves, but results have been simplified here.

## Appendix C: Chapter 3

The exponential mass fractionation factor was calculated with masses of  $^{204}\text{Pb}$ ,  $^{206}\text{Pb}$ ,  $^{207}\text{Pb}$ ,  $^{208}\text{Pb}$  ([Emsley, 1998](#); [Sansonetti and Martin, 2005](#)):

$$^{208}\text{Pb} = 207.976627$$

$$^{207}\text{Pb} = 206.975872$$

$$^{206}\text{Pb} = 205.97444$$

$$^{204}\text{Pb} = 203.97302$$

Example equation for calculating mass bias factor for  $^{208}\text{Pb}/^{204}\text{Pb}$ , using isotope masses of  $^{204}\text{Pb}$  and  $^{208}\text{Pb}$ , "Run Measurements" for Pb isotope ratios were corrected with reference to "True" measurements of NBS-981 for  $^{206}\text{Pb}/^{204}\text{Pb}$ ,  $^{207}\text{Pb}/^{204}\text{Pb}$ ,  $^{208}\text{Pb}/^{204}\text{Pb}$  from [Ingle et al. \(2010\)](#):

$$\begin{aligned} \text{Mass Bias Factor for } ^{208}\text{Pb}/^{204}\text{Pb} &= \ln \frac{\frac{^{208}\text{Pb}/^{206}\text{Pb}_{(\text{True Measurement})}}{^{208}\text{Pb}/^{206}\text{Pb}_{(\text{Run Measurement})}}}{\ln \frac{^{208}\text{Pb}_{\text{Mass}}}{^{204}\text{Pb}_{\text{Mass}}}} \\ &= \ln \left( \frac{36.72156}{\text{Run Measurement}} \right) / \ln \left( \frac{207.976627}{203.97302} \right) \end{aligned}$$

Table C.1: Pb Isotope Compositions of Reference Materials

Sample	$^{208}\text{Pb}/^{204}\text{Pb}$	$1\sigma$	$^{207}\text{Pb}/^{204}\text{Pb}$	$1\sigma$	$^{206}\text{Pb}/^{204}\text{Pb}$	$1\sigma$
AGV-1 leached	38.5622	0.0038	15.6562	0.0014	18.9404	0.0017
Menehune leached	38.0682	0.0013	15.4739	0.0005	18.4092	0.0009
BHVO-1-leached	38.2385	0.0034	15.4997	0.0014	18.6538	0.0024
BHVO-1-unleached	38.3575	0.0005	15.5728	0.0002	18.6899	0.0002
BHVO-2-unleached	38.2489	0.0006	15.5350	0.0003	18.6486	0.0003
Kil1919-unleached	38.2119	0.0006	15.4915	0.0002	18.6588	0.0003

## Bibliography

- Abouchami, W., Hofmann, A. W., Galer, S. J. G., Frey, F. A., Eisele, J., and Feigenson, M. (2005). Lead isotopes reveal bilateral asymmetry and vertical continuity in the Hawaiian mantle plume. *Nature*, 434(7035):851–856.
- Allègre, C. and Minster, J. (1978). Quantitative models of trace element behavior in magmatic processes. *Earth and Planetary Science Letters*, 38(1):1–25.
- Allègre, C. J. (2008). *Isotope Geology*. Cambridge University Press, Cambridge, UK ; New York.
- Allègre, C. J., Staudacher, T., and Sarda, P. (1987). Rare gas systematics: Formation of the atmosphere, evolution and structure of the Earth's mantle. *Earth and Planetary Science Letters*, 81(2):127–150.
- Allègre, C. J., Staudacher, T., Sarda, P., and Kurz, M. (1983). Constraints on evolution of Earth's mantle from rare gas systematics. *Nature*, 303(5920):762–766.
- Arevalo, R. and McDonough, W. F. (2008). Tungsten geochemistry and implications for understanding the Earth's interior. *Earth and Planetary Science Letters*, 272(3):656–665.
- Bellieni, G., Justin Visentin, E., Le Maitre, RW., Piccirillo, E., and Zanettin, B. (1983). Proposal for a division of the basaltic (B) field of the TAS diagram. *IUGS Subcommission on the Systematics of Igneous Rocks. Circular 38, Contribution 102*.
- Bennett, V. C., Esat, T. M., and Norman, M. D. (1996). Two mantle-plume components in Hawaiian picrites inferred from correlated Os–Pb isotopes. *Nature*, 381(6579):221–224.
- Blichert-Toft, J., Weis, D., Maerschalk, C., Agranier, A., and Albarède, F. (2003). Hawaiian hot spot dynamics as inferred from the Hf and Pb isotope evolution of Mauna Kea volcano. *Geochemistry, Geophysics, Geosystems*, 4(2):8704.
- Blundy, J., Robinson, J., and Wood, B. (1998). Heavy REE are compatible in clinopyroxene on the spinel lherzolite solidus. *Earth and Planetary Science Letters*, 160(3–4):493–504.

- Bottinga, Y. and Weill, D. F. (1972). The viscosity of magmatic silicate liquids; a model calculation. *American Journal of Science*, 272(5):438–475.
- Bryce, J. G., DePaolo, D. J., and Lassiter, J. C. (2005). Geochemical structure of the Hawaiian plume: Sr, Nd, and Os isotopes in the 2.8 km HSDP-2 section of Mauna Kea volcano. *Geochemistry, Geophysics, Geosystems*, 6(9):Q09G18.
- Byers, C. D., Garcia, M. O., and Muenow, D. W. (1985). Volatiles in pillow rim glasses from Loihi and Kilauea volcanoes, Hawaii. *Geochimica et Cosmochimica Acta*, 49(9):1887–1896.
- Calvert, A. T. and Lanphere, M. A. (2006). Argon geochronology of Kilauea's early submarine history. *Journal of Volcanology and Geothermal Research*, 151(1-3):1–18.
- Campbell, I. H. (2005). Large Igneous Provinces and the Mantle Plume Hypothesis. *Elements*, 1(5):265–269.
- Campbell, I. H. (2007). Testing the plume theory. *Chemical Geology*, 241(3-4):153–176.
- Campbell, I. H. and Griffiths, R. W. (1990). Implications of mantle plume structure for the evolution of flood basalts. *Earth and Planetary Science Letters*, 99(1-2):79–93.
- Carmichael, I. S., Turner, F. J., Verhoogen, J., Carmichael, I. S. E., and Turner, F. J. (1974). *Igneous Petrology*. McGraw-Hill International Series in the Earth and Planetary Sciences. McGraw-Hill, New York, NY.
- Clague, D. A. (1987). Hawaiian alkaline volcanism. *Geological Society, London, Special Publications*, 30(1):227–252.
- Clague, D. A. (1988). Petrology of Ultramafic Xenoliths from Loihi Seamount, Hawaii. *Journal of Petrology*, 29(6):1161–1186.
- Clague, D. A., Batiza, R., Head III, J. W., and Davis, A. S. (2003). Pyroclastic and Hydroclastic Deposits on Loihi Seamount, Hawaii. In *Explosive Subaqueous Volcanism*, pages 73–95. American Geophysical Union (AGU).
- Clague, D. A. and Dalrymple, G. B. (1987). The Hawaiian–Emperor volcanic chain Part 1. Geologic evolution. In Decker, R. W., Wright, T. L., and Stauffer, P. H., editors, *Volcanism in Hawaii*, volume 1 of *U.S. Geological Survey Professional Paper 1350*, pages 5–54. USGS.

- Clague, D. A. and Dixon, J. E. (2000). Extrinsic controls on the evolution of Hawaiian ocean island volcanoes. *Geochemistry, Geophysics, Geosystems*, 1(4):1010.
- Clague, D. A. and Frey, F. A. (1982). Petrology and Trace Element Geochemistry of the Honolulu Volcanics, Oahu: Implications for the Oceanic Mantle below Hawaii. *Journal of Petrology*, 23(3):447–504.
- Clague, D. A., Paduan, J. B., Caress, D. W., Moyer, C. L., Glazer, B. T., and Yoerger, D. R. (2019). Structure of Lō‘ihī Seamount, Hawai‘i and Lava Flow Morphology From High-Resolution Mapping. *Frontiers in Earth Science*, 7.
- Clague, D. A. and Sherrod, D. R. (2014). Growth and Degradation of Hawaiian Volcanoes. In Poland, M. P., Takahashi, T. J., and Landowski, C. M., editors, *Characteristics of Hawaiian Volcanoes*, number 1801 in Professional Paper, pages 97–146. U.S. Geological Survey, Reston, VA.
- Clague, D. A., Weber, W. S., and Dixon, J. E. (1991). Picritic glasses from Hawaii. *Nature*, 353(6344):553–556.
- Clarke, W., Jenkins, W., and Top, Z. (1976). Determination of tritium by mass spectrometric measurement of  $^3\text{He}$ . *The International Journal of Applied Radiation and Isotopes*, 27(9):515–522.
- Clocchiatti, R., Schiano, P., Ottolini, L., and Bottazzi, P. (1998). Earlier alkaline and transitional magmatic pulsation of Mt Etna volcano. *Earth and Planetary Science Letters*, 163(1):399–407.
- Courtillot, V., Davaille, A., Besse, J., and Stock, J. (2003). Three distinct types of hotspots in the Earth’s mantle. *Earth and Planetary Science Letters*, 205(3-4):295–308.
- Crisp, J. A. (1984). Rates of magma emplacement and volcanic output. *Journal of Volcanology and Geothermal Research*, 20(3-4):177–211.
- Daly, R. A. (1925). The Geology of Ascension Island. *Proceedings of the American Academy of Arts and Sciences*, 60(1):3–80.
- Dana, J. D. (1849). Geology. In *United States Exploring Expedition: During the Years 1838, 1839, 1840, 1841, 1842 Under the Command of Charles Wilkes, U. S. N.*, volume 10. Geo. P. Putnam, New York.

- Danyushevsky, L. V. and Plechov, P. (2011). Petrolog3: Integrated software for modeling crystallization processes. *Geochemistry, Geophysics, Geosystems*, 12(7):Q07021.
- Darwin, C. (1891). *Geological Observations on the Volcanic Islands, and Parts of South America Visited during the Voyage of H.M.S. Beagle*. D. Appleton and Company, New York, 3rd edition.
- Davis, M. G., Garcia, M. O., and Wallace, P. (2003). Volatiles in glasses from Mauna Loa Volcano, Hawai'i: Implications for magma degassing and contamination, and growth of Hawaiian volcanoes. *Contributions to Mineralogy and Petrology*, 144(5):570–591.
- DePaolo, D. J., Bryce, J. G., Dodson, A., Shuster, D. L., and Kennedy, B. M. (2001). Isotopic evolution of Mauna Loa and the chemical structure of the Hawaiian plume. *Geochemistry, Geophysics, Geosystems*, 2(7).
- DePaolo, D. J. and Stolper, E. M. (1996). Models of Hawaiian volcano growth and plume structure: Implications of results from the Hawaii Scientific Drilling Project. *Journal of Geophysical Research: Solid Earth*, 101(B5):11643–11654.
- Dixon, J. E. (1997). Degassing of alkalic basalts. *American Mineralogist*, 82(3-4):368–378.
- Dixon, J. E., Bindeman, I. N., Kingsley, R. H., Simons, K. K., Le Roux, P. J., Hajewski, T. R., Swart, P., Langmuir, C. H., Ryan, J. G., Walowski, K. J., Wada, I., and Wallace, P. J. (2017). Light Stable Isotopic Compositions of Enriched Mantle Sources: Resolving the Dehydration Paradox. *Geochemistry, Geophysics, Geosystems*, 18(11):3801–3839.
- Dixon, J. E. and Clague, D. A. (2001). Volatiles in Basaltic Glasses from Loihi Seamount, Hawaii: Evidence for a Relatively Dry Plume Component. *Journal of Petrology*, 42(3):627–654.
- Dixon, J. E., Stolper, E. M., and Holloway, J. R. (1995). An Experimental Study of Water and Carbon Dioxide Solubilities in Mid-Ocean Ridge Basaltic Liquids. Part I: Calibration and Solubility Models. *Journal of Petrology*, 36(6):1607–1631.
- Dolphin, G. and Dodick, J. (2014). Teaching Controversies in Earth Science: The Role of History and Philosophy of Science. In Matthews, M. R., editor, *International Handbook of Research in History, Philosophy and Science Teaching*, pages 553–599. Springer Netherlands, Dordrecht.
- Dziewonski, A. M. and Anderson, D. L. (1981). Preliminary reference Earth model. *Physics of the Earth and Planetary Interiors*, 25(4):297–356.

- Eiler, J. M., Farley, K. A., Valley, J. W., Hauri, E., Craig, H., Hart, S. R., and Stolper, E. M. (1997). Oxygen isotope variations in ocean island basalt phenocrysts. *Geochimica et Cosmochimica Acta*, 61(11):2281–2293.
- Emsley, J. (1998). *The Elements*. Oxford University Press, New York, NY, 3rd ed edition.
- Farley, K., Natland, J., and Craig, H. (1992). Binary mixing of enriched and undegassed (primitive?) mantle components (He, Sr, Nd, Pb) in Samoan lavas. *Earth and Planetary Science Letters*, 111(1):183–199.
- Farnetani, C. G. and Samuel, H. (2005). Beyond the thermal plume paradigm. *Geophysical Research Letters*, 32(7):L07311.
- Feigenson, M. D., Bolge, L. L., Carr, M. J., and Herzberg, C. T. (2003). REE inverse modeling of HSDP2 basalts: Evidence for multiple sources in the Hawaiian plume. *Geochemistry, Geophysics, Geosystems*, 4(2):8706.
- Fornari, D. J., Garcia, M. O., Tyce, R. C., and Gallo, D. G. (1988). Morphology and structure of Loihi Seamount based on Seabeam Sonar Mapping. *Journal of Geophysical Research: Solid Earth*, 93(B12):15227–15238.
- Foulger, G. R. (2011). *Plates vs Plumes: A Geological Controversy*. John Wiley & Sons, Hoboken.
- Foulger, G. R. (2020a). Do plumes exist? <http://www.mantleplumes.org>.
- Foulger, G. R. (2020b). Involving Students From Day One: Teaching Geological Controversy. In *GSA 2020 Connects Online*, volume 52.
- Fram, M. S. and Lesher, C. E. (1993). Geochemical constraints on mantle melting during creation of the North Atlantic basin. *Nature*, 363(6431):712–715.
- Francek, M. (2013). A Compilation and Review of over 500 Geoscience Misconceptions. *International Journal of Science Education*, 35(1):31–64.
- Frey, F. A. and Clague, D. A. (1983). Geochemistry of diverse basalt types from Loihi Seamount, Hawaii: Petrogenetic implications. *Earth and Planetary Science Letters*, 66:337–355.
- Frey, F. A., Rhodes, J. M., Cox, K. G., McKenzie, D. P., and White, R. S. (1997). Inter-shield geochemical differences among Hawaiian volcanoes: Implications for source compositions, melting process and magma ascent paths. *Philosophical Transactions of the Royal Society A*, 352(1718):133–152.

*Royal Society of London. Series A: Physical and Engineering Sciences*, 342(1663):121–136.

Frey, F. A., Wise, W. S., Garcia, M. O., West, H., Kwon, S.-T., and Kennedy, A. (1990). Evolution of Mauna Kea Volcano, Hawaii: Petrologic and geochemical constraints on postshield volcanism. *Journal of Geophysical Research*, 95(B2):1271.

Garcia, M. O. (1996). Petrography and olivine and glass chemistry of lavas from the Hawaii Scientific Drilling Project. *Journal of Geophysical Research: Solid Earth*, 101(B5):11701–11713.

Garcia, M. O., Caplan-Auerbach, J., De Carlo, E. H., Kurz, M., and Becker, N. (2006). Geology, geochemistry and earthquake history of Lō'ihi Seamount, Hawaii's youngest volcano. *Geochemistry*, 66(2):81–108.

Garcia, M. O., Foss, D. J., West, H., and Mahoney, J. J. (1995). Geochemical and Isotopic Evolution of Loihi Volcano, Hawaii. *Journal of Petrology*, 36(6):1647–1674.

Garcia, M. O., Jorgenson, B. A., Mahoney, J. J., Ito, E., and Irving, A. J. (1993). An evaluation of temporal geochemical evolution of Loihi Summit Lavas: Results from Alvin submersible dives. *Journal of Geophysical Research: Solid Earth*, 98(B1):537–550.

Garcia, M. O., Muenow, D. W., Aggrey, K. E., and O'Neil, J. R. (1989). Major element, volatile, and stable isotope geochemistry of Hawaiian submarine tholeiitic glasses. *Journal of Geophysical Research: Solid Earth*, 94(B8):10525–10538.

Garcia, M. O., Rubin, K. H., Norman, M. D., Rhodes, J. M., Graham, D. W., Muenow, D. W., and Spencer, K. (1998). Petrology and geochronology of basalt breccia from the 1996 earthquake swarm of Loihi seamount, Hawaii: Magmatic history of its 1996 eruption. *Bulletin of Volcanology*, 59(8):577–592.

Gast, P. W. (1968). Trace element fractionation and the origin of tholeiitic and alkaline magma types. *Geochimica et Cosmochimica Acta*, 32(10):1057–1086.

Gast, P. W., Tilton, G. R., and Hedge, C. (1964). Isotopic Composition of Lead and Strontium from Ascension and Gough Islands. *Science*, 145(3637):1181–1185.

Gerlach, D. C. (1990). Eruption rates and isotopic systematics of ocean islands: Further evidence for small-scale heterogeneity in the upper mantle. *Tectonophysics*, 172(3–4):273–289.

- Ghiorso, M. S. and Gualda, G. A. R. (2015). An H<sub>2</sub>O–CO<sub>2</sub> mixed fluid saturation model compatible with rhyolite-MELTS. *Contributions to Mineralogy and Petrology*, 169(6):53.
- Gonnermann, H. M. and Mukhopadhyay, S. (2007). Non-equilibrium degassing and a primordial source for helium in ocean-island volcanism. *Nature*, 449(7165):1037–1040.
- Graham, D. W., Hanan, B. B., Hémond, C., Blachert-Toft, J., and Albarède, F. (2014). Helium isotopic textures in Earth's upper mantle. *Geochemistry, Geophysics, Geosystems*, 15(5):2048–2074.
- Graham, D. W., Jenkins, W. J., Kurz, M. D., and Batiza, R. (1987). Helium isotope disequilibrium and geochronology of glassy submarine basalts. *Nature*, 326(6111):384–386.
- Graham, D. W., Michael, P., Truong, T., and Garcia, M. (2024). Helium and Carbon Isotopes, Volatiles, and Trace Elements in Submarine Basalt Glasses from Loihi Seamount.
- Graham, D. W. and Michael, P. J. (2021). Predominantly Recycled Carbon in Earth's Upper Mantle Revealed by He-CO<sub>2</sub>-Ba Systematics in Ultradepleted Ocean Ridge Basalts. *Earth and Planetary Science Letters*, 554:116646.
- Graham, D. W., Michael, P. J., and Rubin, K. H. (2018). An investigation of mid-ocean ridge degassing using He, CO<sub>2</sub>, and  $\delta^{13}\text{C}$  variations during the 2005–06 eruption at 9°50'N on the East Pacific Rise. *Earth and Planetary Science Letters*, 504:84–93.
- Graham, D. W., Michael, P. J., and Truong, T. B. (2023). Carbon isotope composition of basalts from Loihi Seamount: Primordial or recycled carbon in the Hawaiian mantle plume? *Earth and Planetary Science Letters*, 617:118248.
- Green, D. H. (1970). A review of experimental evidence on the origin of basaltic and nephelinitic magmas. *Physics of the Earth and Planetary Interiors*, 3:221–235.
- Guillou, H., Garcia, M. O., and Turpin, L. (1997). Unspiked K-Ar dating of young volcanic rocks from Loihi and Pitcairn hot spot seamounts. *Journal of Volcanology and Geothermal Research*, 78(3-4):239–249.
- Halliday, A. N., Lee, D.-C., Tommasini, S., Davies, G. R., Paslick, C. R., Godfrey Fitton, J., and James, D. E. (1995). Incompatible trace elements in OIB and MORB and source enrichment in the sub-oceanic mantle. *Earth and Planetary Science Letters*, 133(3-4):379–395.

- Hanan, B. B. and Graham, D. W. (1996). Lead and Helium Isotope Evidence from Oceanic Basalts for a Common Deep Source of Mantle Plumes. *Science*, 272(5264):991–995.
- Hanano, D., Weis, D., Scoates, J. S., Aciego, S., and DePaolo, D. J. (2010). Horizontal and vertical zoning of heterogeneities in the Hawaiian mantle plume from the geochemistry of consecutive postshield volcano pairs: Kohala-Mahukona and Mauna Kea-Hualalai. *Geochemistry, Geophysics, Geosystems*, 11(1):Q01004.
- Hanyu, T., Kimura, J.-I., Katakuse, M., Calvert, A. T., Sisson, T. W., and Nakai, S. (2010). Source materials for inception stage Hawaiian magmas: Pb-He isotope variations for early Kilauea. *Geochemistry, Geophysics, Geosystems*, 11(3):Q0AC01.
- Hanyu, T., Shimizu, K., Ushikubo, T., Kimura, J.-I., Chang, Q., Hamada, M., Ito, M., Iwamori, H., and Ishikawa, T. (2019). Tiny droplets of ocean island basalts unveil Earth's deep chlorine cycle. *Nature Communications*, 10(1).
- Harrison, L. N. and Weis, D. (2018). The Size and Emergence of Geochemical Heterogeneities in the Hawaiian Mantle Plume Constrained by Sr-Nd-Hf Isotopic Variation Over ~47 Million Years. *Geochemistry, Geophysics, Geosystems*, 19(8):2823–2842.
- Hart, S. R. (1984). A large-scale isotope anomaly in the Southern Hemisphere mantle. *Nature*, 309(5971):753–757.
- Hart, S. R., Hauri, E. H., Oschmann, L. A., and Whitehead, J. A. (1992). Mantle Plumes and Entrainment: Isotopic Evidence. *Science*, 256(5056):517–520.
- Hauri, E., Wang, J., Dixon, J. E., King, P. L., Mandeville, C., and Newman, S. (2002). SIMS analysis of volatiles in silicate glasses. *Chemical Geology*, 183(1-4):99–114.
- Hauri, E. H. (1996). Major-element variability in the Hawaiian mantle plume. *Nature*, 382(6590):415–419.
- Hawai'i Board on Geographic Names (2021). Minutes for the 05/04/2021 Meeting of the Hawai'i Board on Geographic Names. [https://files.hawaii.gov/dbedt/op/gis/bgn/HBGN\\_Minutes\\_2021-05-04\\_Approved.pdf](https://files.hawaii.gov/dbedt/op/gis/bgn/HBGN_Minutes_2021-05-04_Approved.pdf).
- Hawaiian Volcano Observatory (2022). Kama'ehuakanaloa — the volcano formerly known as Lo'ihi Seamount. *Volcano Watch*.

- Heidorn, P. B. (2008). Shedding Light on the Dark Data in the Long Tail of Science. *Library Trends*, 57(2):280–299.
- Helmberger, D., Ni, S., Wen, L., and Ritsema, J. (2000). Seismic evidence for ultralow-velocity zones beneath Africa and eastern Atlantic. *Journal of Geophysical Research: Solid Earth*, 105(B10):23865–23878.
- Helz, R. T. and Thornber, C. R. (1987). Geothermometry of Kilauea Iki lava lake, Hawaii. *Bulletin of Volcanology*, 49(5):651–668.
- Herzberg, C. and Asimow, P. D. (2008). Petrology of some oceanic island basalts: PRIMELT2.XLS software for primary magma calculation. *Geochemistry, Geophysics, Geosystems*, 9(9):Q09001.
- Hilton, D. R., McMurtry, G. M., and Goff, F. (1998). Large variations in vent fluid CO<sub>2</sub>/<sup>3</sup>He ratios signal rapid changes in magma chemistry at Loihi seamount, Hawaii. *Nature*, 396(6709):359–362.
- Hiyagon, H., Ozima, M., Zashu, S., and Sakai, H. (1992). Noble gases in submarine glasses from mid-oceanic ridges and Loihi seamount: Constraints on the early history of the Earth. *Geochimica et Cosmochimica Acta*, 56(3):1301–1316.
- Hofmann, A., Jochum, K., Seufert, M., and White, W. (1986). Nb and Pb in oceanic basalts: New constraints on mantle evolution. *Earth and Planetary Science Letters*, 79(1-2):33–45.
- Hofmann, A. W. (1988). Chemical differentiation of the Earth: The relationship between mantle, continental crust, and oceanic crust. *Earth and Planetary Science Letters*, 90(3):297–314.
- Hofmann, A. W. (1997). Mantle geochemistry: The message from oceanic volcanism. *Nature*, 385(6613):219–229.
- Hofmann, A. W. and White, W. M. (1982). Mantle plumes from ancient oceanic crust. *Earth and Planetary Science Letters*, 57(2):421–436.
- Holland, G. and Ballentine, C. J. (2006). Seawater subduction controls the heavy noble gas composition of the mantle. *Nature*, 441(7090):186–191.
- Honda, M., McDougall, I., Patterson, D. B., Doulgeris, A., and Clague, D. A. (1993). Noble gases in submarine pillow basalt glasses from Loihi and Kilauea, Hawaii: A solar component in the Earth. *Geochimica et Cosmochimica Acta*, 57(4):859–874.

- Iacovino, K., Matthews, S., Wieser, P. E., Moore, G. M., and Bégué, F. (2021). VESIcal Part I: An Open-Source Thermodynamic Model Engine for Mixed Volatile ( $H_2O-CO_2$ ) Solubility in Silicate Melts. *Earth and Space Science*, 8(11).
- Ingle, S., Ito, G., Mahoney, J. J., Chazey, W., Sinton, J., Rotella, M., and Christie, D. M. (2010). Mechanisms of geochemical and geophysical variations along the western Galápagos Spreading Center. *Geochemistry, Geophysics, Geosystems*, 11(4):Q04003.
- Ireland, T. J., Arevalo, R., Walker, R. J., and McDonough, W. F. (2009). Tungsten in Hawaiian picrites: A compositional model for the sources of Hawaiian lavas. *Geochimica et Cosmochimica Acta*, 73(15):4517–4530.
- Irvine, T. N. and Baragar, W. R. A. (1971). A Guide to the Chemical Classification of the Common Volcanic Rocks. *Canadian Journal of Earth Sciences*, 8(5):523–548.
- Jackson, M. G., Blichert-Toft, J., Halldórsson, S. A., Mundl-Petermeier, A., Bizimis, M., Kurz, M. D., Price, A. A., Harðardóttir, S., Willhite, L. N., Breddam, K., Becker, T. W., and Fischer, R. A. (2020). Ancient Helium and Tungsten Isotopic Signatures Preserved in Mantle Domains Least Modified by Crustal Recycling. *Proceedings of the National Academy of Sciences*, 117(49):30993–31001.
- Jackson, M. G., Hart, S. R., Saal, A. E., Shimizu, N., Kurz, M. D., Blusztajn, J. S., and Skovgaard, A. C. (2008). Globally elevated titanium, tantalum, and niobium (TITAN) in ocean island basalts with high  $^3He/ ^4He$ . *Geochemistry, Geophysics, Geosystems*, 9(4):Q04027.
- Jarosewich, E., Nelen, J., and Norberg, J. A. (1980). Reference Samples for Electron Microprobe Analysis\*. *Geostandards Newsletter*, 4(1):43–47.
- Johnson, K. T. M. (1998). Experimental determination of partition coefficients for rare earth and high-field-strength elements between clinopyroxene, garnet, and basaltic melt at high pressures. *Contributions to Mineralogy and Petrology*, 133(1):60–68.
- Jones, M. P., Soule, S. A., Gonnermann, H. M., Le Roux, V., and Clague, D. A. (2018). Magma ascent and lava flow emplacement rates during the 2011 Axial Seamount eruption based on CO<sub>2</sub> degassing. *Earth and Planetary Science Letters*, 494:32–41.
- Judd, J. W. (1881). Volcanoes, their Action and Distribution. In *Popular Science Monthly*, volume 20, pages 43–56. D. Appleton & Co., New York.

- Kaneoka, I. (1987). Constraints on the characteristics of magma sources for Hawaiian volcanoes based on noble gas systematics. In Decker, R. W., Wright, T. L., and Stauffer, P. H., editors, *Volcanism in Hawaii*, volume 1 of *Professional Paper*, pages 745–757. U.S. Geological Survey.
- Kaneoka, I., Hanyu, T., Yamamoto, J., and Miura, Y. N. (2002). Noble gas systematics of the Hawaiian volcanoes based on the analysis of Loihi, Kilauea and Koolau submarine rocks. In Takahashi, E., Lipman, P. W., Garcia, M. O., Naka, J., and Aramaki, S., editors, *Geophysical Monograph Series*, volume 128, pages 373–389. American Geophysical Union, Washington, D. C.
- Kaneoka, I., Takaoka, N., and Clague, D. A. (1983). Noble gas systematics for coexisting glass and olivine crystals in basalts and dunite xenoliths from Loihi Seamount. *Earth and Planetary Science Letters*, 66:427–437.
- Kay, R., Hubbard, N. J., and Gast, P. W. (1970). Chemical characteristics and origin of oceanic ridge volcanic rocks<sup>1</sup>. *Journal of Geophysical Research*, 75(8):1585–1613.
- Kent, A. J., Clague, D. A., Honda, M., Stolper, E. M., Hutcheon, I. D., and Norman, M. D. (1999a). Widespread assimilation of a seawater-derived component at Loihi Seamount, Hawaii. *Geochimica et Cosmochimica Acta*, 63(18):2749–2761.
- Kent, A. J., Norman, M. D., Hutcheon, I. D., and Stolper, E. M. (1999b). Assimilation of seawater-derived components in an oceanic volcano: Evidence from matrix glasses and glass inclusions from Loihi seamount, Hawaii. *Chemical Geology*, 156(1-4):299–319.
- Kent, A. J. R., Stolper, E. M., Francis, D., Woodhead, J., Frei, R., and Eiler, J. (2004). Mantle heterogeneity during the formation of the North Atlantic Igneous Province: Constraints from trace element and Sr-Nd-Os-O isotope systematics of Baffin Island picrites. *Geochemistry, Geophysics, Geosystems*, 5(11):Q11004.
- Konrad, K., Graham, D. W., Kent, A. J., and Koppers, A. A. (2018a). Spatial and temporal variability in Marquesas Islands volcanism revealed by  ${}^3\text{He}/{}^4\text{He}$  and the composition of olivine-hosted melt inclusions. *Chemical Geology*, 477:161–176.
- Konrad, K., Koppers, A. A. P., Steinberger, B., Finlayson, V. A., Konter, J. G., and Jackson, M. G. (2018b). On the relative motions of long-lived Pacific mantle plumes. *Nature Communications*, 9(1):854.

- Koppers, A. A. P., Becker, T. W., Jackson, M. G., Konrad, K., Müller, R. D., Romanowicz, B., Steinberger, B., and Whittaker, J. M. (2021). Mantle plumes and their role in Earth processes. *Nature Reviews Earth & Environment*, 2(6):382–401.
- Koppers, A. A. P. and Watts, A. B. (2010). Intraplate Seamounts as a Window into Deep Earth Processes. *Oceanography*, 23(1):42–57.
- Kress, V. C. and Carmichael, I. S. E. (1988). Stoichiometry of the iron oxidation reaction in silicate melts. *American Mineralogist*, 73(11-12):1267–1274.
- Kurz, M. and Jenkins, W. (1981). The distribution of helium in oceanic basalt glasses. *Earth and Planetary Science Letters*, 53(1):41–54.
- Kurz, M. D., Curtice, J., Lott, D. E., and Solow, A. (2004). Rapid helium isotopic variability in Mauna Kea shield lavas from the Hawaiian Scientific Drilling Project. *Geochemistry, Geophysics, Geosystems*, 5(4):Q04G14.
- Kurz, M. D., Jenkins, W. J., and Hart, S. R. (1982). Helium isotopic systematics of oceanic islands and mantle heterogeneity. *Nature*, 297(5861):43–47.
- Kurz, M. D., Jenkins, W. J., Hart, S. R., and Clague, D. (1983). Helium isotopic variations in volcanic rocks from Loihi Seamount and the Island of Hawaii. *Earth and Planetary Science Letters*, 66:388–406.
- Lange, R. A. and Carmichael, I. S. (1987). Densities of Na<sub>2</sub>O-K<sub>2</sub>O-CaO-MgO-FeO-Fe<sub>2</sub>O<sub>3</sub>-Al<sub>2</sub>O<sub>3</sub>-TiO<sub>2</sub>-SiO<sub>2</sub> liquids: New measurements and derived partial molar properties. *Geochimica et Cosmochimica Acta*, 51(11):2931–2946.
- Langseth, M. G., Le Pichon, X., and Ewing, M. (1966). Crustal structure of the mid-ocean ridges: 5. Heat flow through the Atlantic Ocean floor and convection currents. *Journal of Geophysical Research*, 71(22):5321–5355.
- Laske, G., Morgan, J. P., and Orcutt, J. A. (1999). First results from the Hawaiian SWELL Pilot Experiment. *Geophysical Research Letters*, 26(22):3397–3400.
- Lay, T. and Garnero, E. J. (2011). Deep Mantle Seismic Modeling and Imaging. *Annual Review of Earth and Planetary Sciences*, 39(1):91–123.
- Le Bas, M. J., Le Maitre, R. W., Streckeisen, A., Zanettin, B., and IUGS Subcommission on the Systematics of Igneous Rocks (1986). A Chemical Classification of Volcanic Rocks Based on the Total Alkali-Silica Diagram. *Journal of Petrology*, 27(3):745–750.

- Le Maitre, R. W., Streckeisen, A., Zanettin, B., Le Bas, M. J., Bonin, B., and Bateman, P., editors (2004). *Igneous Rocks: A Classification and Glossary of Terms: Recommendations of the International Union of Geological Sciences, Subcommission on the Systematics of Igneous Rocks*. Cambridge University Press, Cambridge ; New York, 2nd ed edition.
- Lipman, P. W., Sisson, T. W., Ui, T., and Naka, J. (2000). In search of ancestral Kilauea volcano. *Geology*, 28(12):1079–1082.
- Loewen, M. W., Graham, D. W., Bindeman, I. N., Lupton, J. E., and Garcia, M. O. (2019). Hydrogen isotopes in high  ${}^3\text{He}/{}^4\text{He}$  submarine basalts: Primordial vs. recycled water and the veil of mantle enrichment. *Earth and Planetary Science Letters*, 508:62–73.
- Loewen, M. W. and Kent, A. J. R. (2012). Sources of elemental fractionation and uncertainty during the analysis of semi-volatile metals in silicate glasses using LA-ICP-MS. *Journal of Analytical Atomic Spectrometry*, 27(9):1502.
- Lupton, J. E. (1983). Terrestrial Inert Gases: Isotope Tracer Studies and Clues to Primordial Components in the Mantle. *Annual Review of Earth and Planetary Sciences*, 11(1):371–414.
- Macdonald, G. A. and Katsura, T. (1964). Chemical Composition of Hawaiian Lavas. *Journal of Petrology*, 5(1):82–133.
- Malahoff, A., Kolotyrkina, I. Y., Midson, B. P., and Massoth, G. J. (2006). A decade of exploring a submarine intraplate volcano: Hydrothermal manganese and iron at Lō‘ihī volcano, Hawai‘i. *Geochemistry, Geophysics, Geosystems*, 7(6):Q06002.
- Malahoff, A., McMurtry, G. M., Smith, J. R., and Hunneke, W. (1987). Neovolcanism, neotectonics, and hydrothermal activity on Loihi submarine volcano, Hawaii. *Eos, Transactions American Geophysical Union*, 68(44):1553.
- Malahoff, A., McMurtry, G. M., Wiltshire, J. C., and Yeh, H.-W. (1982). Geology and chemistry of hydrothermal deposits from active submarine volcano Loihi, Hawaii. *Nature*, 298(5871):234–239.
- Marty, B. and Jambon, A. (1987). C $\{\text{He}$  in volatile fluxes from the solid Earth: Implications for carbon geodynamics. *Earth and Planetary Science Letters*, 83(1-4):16–26.

- Matsuda, J., Matsumoto, T., Sumino, H., Nagao, K., Yamamoto, J., Miura, Y., Kaneoka, I., Takahata, N., and Sano, Y. (2002). The  ${}^3\text{He}/{}^4\text{He}$  ratio of the new internal He Standard of Japan (HESJ). *Geochemical Journal*, 36(2):191–195.
- Matsumoto, T., Orihashi, Y., Matsuda, J.-I., and Yamamoto, K. (2008). Argon isotope ratio of the plume-source deduced from high-resolution stepwise crushing extraction. *Geochemical Journal*, 42(1):39–49.
- Matvenkov, V. and Sorokhtin, O. (1998). Petrological characteristics of the initial stages of interplate volcanism Loihi (Hawaii, Pacific Ocean). *Okeanologiya*, 38(5):742–749.
- McKenzie, D. and O’Nions, R. K. (1991). Partial Melt Distributions from Inversion of Rare Earth Element Concentrations. *Journal of Petrology*, 32(5):1021–1091.
- McLennan, S. M. (1989). Rare earth elements in sedimentary rocks: Influence of provenance and sedimentary processes. In Lipin, B. R. and McKay, G., editors, *Geochemistry and Mineralogy of Rare Earth Elements*, volume 21 of *Reviews in Mineralogy*, pages 169–200. Mineralogical Society of America, Washington, D. C.
- Meibom, A. and Anderson, D. L. (2004). The statistical upper mantle assemblage. *Earth and Planetary Science Letters*, 217(1-2):123–139.
- Meibom, A., Sleep, N. H., Zahnle, K., and Anderson, D. L. (2005). *Models for Noble Gases in Mantle Geochemistry: Some Observations and Alternatives*, pages 347–363. Number 388 in Special Paper. Geological Society of America.
- Melby, K. M. (2020). *Evaluating Spatial Patterns of Heavy Metal Levels and Pb Isotopic Compositions of Peat Soils along the Red Dog Mine Haul Road in Northwest Alaska*. M.S. Thesis, Oregon State University.
- Menard, H. W. (2014). *The Ocean of Truth: A Personal History of Global Tectonics*. Princeton University Press.
- Merz, D. K., Caplan-Auerbach, J., and Thurber, C. H. (2019). Seismicity and Velocity Structure of Lō’ihī Submarine Volcano and Southeastern Hawai’i. *Journal of Geophysical Research: Solid Earth*, 124(11):11380–11393.
- Michael, P. J. and Cornell, W. C. (1998). Influence of spreading rate and magma supply on crystallization and assimilation beneath mid-ocean ridges: Evidence from chlorine and major element chemistry of mid-ocean ridge basalts. *Journal of Geophysical Research: Solid Earth*, 103(B8):18325–18356.

- Michael, P. J. and Graham, D. W. (2015). The behavior and concentration of CO<sub>2</sub> in the suboceanic mantle: Inferences from undegassed ocean ridge and ocean island basalts. *Lithos*, 236–237:338–351.
- Moore, J., Normark, W. R., and Lipman, P. W. (1979). Loihi Seamount – a young submarine Hawaiian volcano. In *Hawaii Symposium on Intraplate Volcanism and Submarine Volcanism*, page 127, Hilo.
- Moore, J. G. and Clague, D. A. (1981). Loihi Seamount Lavas: Volatile Contents. *Eos, Transactions American Geophysical Union*, 62(45):1083.
- Moore, J. G., Clague, D. A., and Normark, W. R. (1982). Diverse basalt types from Loihi seamount, Hawaii. *Geology*, 10(2):88.
- Morgan, W. J. (1968). Rises, trenches, great faults, and crustal blocks. *Journal of Geophysical Research*, 73(6):1959–1982.
- Morgan, W. J. (1972). Deep Mantle Convection Plumes and Plate Motions. *AAPG Bulletin*, 56.
- Mukhopadhyay, S. (2012). Early differentiation and volatile accretion recorded in deep-mantle neon and xenon. *Nature*, 486(7401):101–104.
- Mukhopadhyay, S., Lassiter, J. C., Farley, K. A., and Bogue, S. W. (2003). Geochemistry of Kauai shield-stage lavas: Implications for the chemical evolution of the Hawaiian plume. *Geochemistry, Geophysics, Geosystems*, 4(1):1009.
- Mundl-Petermeier, A., Walker, R., Fischer, R., Lekic, V., Jackson, M., and Kurz, M. (2020). Anomalous 182W in high 3He/4He ocean island basalts: Fingerprints of Earth's core? *Geochimica et Cosmochimica Acta*, 271:194–211.
- National Oceanic and Atmospheric Administration National Centers for Environmental Information (2022). ETOPO 2022 15 Arc-Second Global Relief Model.
- Newman, S. and Lowenstern, J. B. (2002). VolatileCalc: A silicate melt–H<sub>2</sub>O–CO<sub>2</sub> solution model written in Visual Basic for excel. *Computers & Geosciences*, 28(5):597–604.
- Niu, Y., Wilson, M., Humphreys, E. R., and O'Hara, M. J. (2011). The Origin of Intraplate Ocean Island Basalts (OIB): The Lid Effect and its Geodynamic Implications. *Journal of Petrology*, 52(7-8):1443–1468.

- Norman, M. D. and Garcia, M. O. (1999). Primitive magmas and source characteristics of the Hawaiian plume: Petrology and geochemistry of shield picrites. *Earth and Planetary Science Letters*, 168(1):27–44.
- Norman, M. D., Garcia, M. O., Kamenetsky, V. S., and Nielsen, R. L. (2002). Olivine-hosted melt inclusions in Hawaiian picrites: Equilibration, melting, and plume source characteristics. *Chemical Geology*, 183(1-4):143–168.
- O'Connor, C., Weatherall, J. O., and Mohseni, A. (2023). The Best Paper You'll Read Today: Media Bias and the Public Understanding of Science. Preprint, MetaArXiv.
- Oggier, F., Widiwijayanti, C., and Costa, F. (2023). Integrating global geochemical volcano rock composition with eruption history datasets. *Frontiers in Earth Science*, 11:1108056.
- O'Hara, M. J. (1973). Non-Primary Magmas and Dubious Mantle Plume beneath Iceland. *Nature*, 243(5409):507–508.
- Oreskes, N. (2018). *Plate Tectonics: An Insider's History Of The Modern Theory Of The Earth*. CRC Press.
- Peeters, M. and Maeseele, P. (2023). The Interpretive Interface: Where Journalistic and Pluralistic Discourses (Don't) Meet. *Digital Journalism*, pages 1–19.
- Peters, B. J. and Day, J. M. D. (2014). Assessment of relative Ti, Ta, and Nb (TITAN) enrichments in ocean island basalts. *Geochemistry, Geophysics, Geosystems*, 15(11):4424–4444.
- Pietruszka, A. J., Heaton, D. E., Garcia, M. O., and Marske, J. P. (2019). Explosive summit collapse of Kīlauea Volcano in 1924 preceded by a decade of crustal contamination and anomalous Pb isotope ratios. *Geochimica et Cosmochimica Acta*, 258:120–137.
- Pietruszka, A. J., Keyes, M. J., Duncan, J. A., Hauri, E. H., Carlson, R. W., and Garcia, M. O. (2011). Excesses of seawater-derived  $^{234}\text{U}$  in volcanic glasses from Loihi Seamount due to crustal contamination. *Earth and Planetary Science Letters*, 304(1-2):280–289.
- Pietruszka, A. J., Norman, M. D., Garcia, M. O., Marske, J. P., and Burns, D. H. (2013). Chemical heterogeneity in the Hawaiian mantle plume from the alteration and dehydration of recycled oceanic crust. *Earth and Planetary Science Letters*, 361:298–309.

- Pitman, W. C. and Heirtzler, J. R. (1966). Magnetic Anomalies over the Pacific-Antarctic Ridge. *Science*, 154(3753):1164–1171.
- Potuzak, M., Nichols, A. R., Dingwell, D. B., and Clague, D. A. (2008). Hyperquenched volcanic glass from Loihi Seamount, Hawaii. *Earth and Planetary Science Letters*, 270(1-2):54–62.
- Presnall, D. C. and Gudfinnsson, G. H. (2011). Oceanic Volcanism from the Low-velocity Zone – without Mantle Plumes. *Journal of Petrology*, 52(7-8):1533–1546.
- Reiners, P. W., Carlson, R. W., Renne, P. R., Cooper, K. M., Granger, D. E., McLean, N. M., and Schoene, B. (2017). Analytical methods. In *Geochronology and Thermochronology*, pages 39–64. John Wiley & Sons, Ltd, Chichester, UK.
- Ren, Z.-Y., Hanyu, T., Miyazaki, T., Chang, Q., Kawabata, H., Takahashi, T., Hirahara, Y., Nichols, A. R. L., and Tatsumi, Y. (2009). Geochemical Differences of the Hawaiian Shield Lavas: Implications for Melting Process in the Heterogeneous Hawaiian Plume. *Journal of Petrology*, 50(8):1553–1573.
- Ren, Z.-Y., Ingle, S., Takahashi, E., Hirano, N., and Hirata, T. (2005). The chemical structure of the Hawaiian mantle plume. *Nature*, 436(7052):837–840.
- Ribe, N. and Christensen, U. (1999). The dynamical origin of Hawaiian volcanism. *Earth and Planetary Science Letters*, 171(4):517–531.
- Richards, M. A., Duncan, R. A., and Courtillot, V. E. (1989). Flood Basalts and Hot-Spot Tracks: Plume Heads and Tails. *Science*, 246(4926):103–107.
- Rison, W. and Craig, H. (1981). Loihi Seamount: Mantle volatiles in the basalts. *Eos, Transactions American Geophysical Union*, 62(1083).
- Rison, W. and Craig, H. (1983). Helium isotopes and mantle volatiles in Loihi Seamount and Hawaiian Island basalts and xenoliths. *Earth and Planetary Science Letters*, 66:407–426.
- Robinson, J. E. and Eakins, B. W. (2006). Calculated volumes of individual shield volcanoes at the young end of the Hawaiian Ridge. *Journal of Volcanology and Geothermal Research*, 151(1-3):309–317.
- Sansonetti, J. E. and Martin, W. C. (2005). Handbook of Basic Atomic Spectroscopic Data. *Journal of Physical and Chemical Reference Data*, 34(4):1559–2259.

- Schilling, J.-G. (1973a). Afar Mantle Plume: Rare Earth Evidence. *Nature Physical Science*, 242(114):2–5.
- Schilling, J.-G. (1973b). Iceland Mantle Plume: Geochemical Study of Reykjanes Ridge. *Nature*, 242(5400):565–571.
- Schilling, J.-G. and Winchester, J. W. (1966). Rare Earths in Hawaiian Basalts. *Science*, 153(3738):867–869.
- Schipper, C. I., White, J. D., Houghton, B., Shimizu, N., and Stewart, R. B. (2010). Explosive submarine eruptions driven by volatile-coupled degassing at Lo‘ihi Seamount, Hawai‘i. *Earth and Planetary Science Letters*, 295(3-4):497–510.
- Sedwick, P., McMurtry, G., and Macdougall, J. (1992). Chemistry of hydrothermal solutions from Pele’s Vents, Loihi Seamount, Hawaii. *Geochimica et Cosmochimica Acta*, 56(10):3643–3667.
- Shaw, D. M. (1970). Trace element fractionation during anatexis. *Geochimica et Cosmochimica Acta*, 34(2):237–243.
- Sherrod, D. R., Sinton, J. M., Watkins, S. E., and Brunt, K. M. (2007). *Geologic Map of the State of Hawai‘i*. U.S. Geological Survey Open-File Report 2007-1089.
- Shipboard Scientists (1999). Shinkai 6500/Yokosuka Cruises (YK99-07,-08) Around Hawaiian Islands: Onboard Report. Technical report, Japan Marine Science and Technology Center, Yokosuka.
- SIO Geological Data Center (2018). TUNE04WT Tunes Expedition Leg 04 - Cruise Report.
- Sleep, N. H. (1990). Hotspots and mantle plumes: Some phenomenology. *Journal of Geophysical Research*, 95(B5):6715.
- Smith, A. D. (2022). B" not D" as the source of intraplate volcanism. In Foulger, G. R., Hamilton, L. C., Jurdy, D. M., Stein, C. A., Howard, K. A., and Stein, S., editors, *In the Footsteps of Warren B. Hamilton: New Ideas in Earth Science*, pages 371–378. Geological Society of America.
- Smith, G. A. and Bermea, S. B. (2012). Using Students’ Sketches to Recognize Alternative Conceptions About Plate Tectonics Persisting From Prior Instruction. *Journal of Geoscience Education*, 60(4):350–359.

- Staudigel, H., Zindler, A., Hart, S. R., Leslie, T., Chen, C. Y., and Clague, D. (1984). The isotope systematics of a juvenile intraplate volcano: Pb, Nd, and Sr isotope ratios of basalts from Loihi Seamount, Hawaii. *Earth and Planetary Science Letters*, 69(1):13–29.
- Stolper, E., Sherman, S., Garcia, M., Baker, M., and Seaman, C. (2004). Glass in the submarine section of the HSDP2 drill core, Hilo, Hawaii. *Geochemistry, Geophysics, Geosystems*, 5(7).
- Stracke, A. (2012). Earth's heterogeneous mantle: A product of convection-driven interaction between crust and mantle. *Chemical Geology*, 330–331:274–299.
- Stracke, A. (2021). A process-oriented approach to mantle geochemistry. *Chemical Geology*, 579:120350.
- Sun, S.-s. and McDonough, W. F. (1989). Chemical and isotopic systematics of oceanic basalts: Implications for mantle composition and processes. *Geological Society, London, Special Publications*, 42(1):313–345.
- Tarduno, J., Bunge, H.-P., Sleep, N., and Hansen, U. (2009). The Bent Hawaiian-Emperor Hotspot Track: Inheriting the Mantle Wind. *Science*, 324(5923):50–53.
- Tatsumoto, M. (1978). Isotopic composition of lead in oceanic basalt and its implication to mantle evolution. *Earth and Planetary Science Letters*, 38(1):63–87.
- Tucker, J. M., Hauri, E. H., Pietruszka, A. J., Garcia, M. O., Marske, J. P., and Trusdell, F. A. (2019). A high carbon content of the Hawaiian mantle from olivine-hosted melt inclusions. *Geochimica et Cosmochimica Acta*, 254:156–172.
- Valbracht, P., Honda, M., Staudigel, H., McDougall, I., and Trost, A. (1994). Noble Gas Partitioning in Natural Samples: Results from Coexisting Glass and Olivine Phenocrysts in Four Hawaiian Submarine Basalts. In Matsuda, J., editor, *Noble Gas Geochemistry and Cosmochemistry*, pages 373–381. Terra Scientific Publishing Company (TERRAPUB), Tokyo.
- Valbracht, P., Staudigel, H., Honda, M., McDougall, I., and Davies, G. (1996). Isotopic tracing of volcanic source regions from Hawaii: Decoupling of gaseous from lithophile magma components. *Earth and Planetary Science Letters*, 144(1-2):185–198.
- Valbracht, P. J., Staudacher, T., Malahoff, A., and Allègre, C. J. (1997). Noble gas systematics of deep rift zone glasses from Loihi Seamount, Hawaii. *Earth and Planetary Science Letters*, 150(3):399–411.

- Vetter, E. W. and Smith, C. R. (2005). Insights into the ecological effects of deep ocean CO<sub>2</sub> enrichment: The impacts of natural CO<sub>2</sub> venting at Loihi seamount on deep sea scavengers. *Journal of Geophysical Research*, 110(C9):C09S13.
- Vine, F. J. (1966). Spreading of the Ocean Floor: New Evidence: Magnetic anomalies may record histories of the ocean basins and Earth's magnetic field for 2x10<sup>8</sup> years. *Science*, 154(3755):1405–1415.
- Wallace, P. J., Plank, T., Edmonds, M., and Hauri, E. H. (2015). Volatiles in Magmas. In *The Encyclopedia of Volcanoes*, pages 163–183. Elsevier.
- Weaver, J. and Langmuir, C. H. (1990). Calculation of phase equilibrium in mineral-melt systems. *Computers & Geosciences*, 16(1):1–19.
- Weis, D., Garcia, M. O., Rhodes, J. M., Jellinek, M., and Scoates, J. S. (2011). Role of the deep mantle in generating the compositional asymmetry of the Hawaiian mantle plume. *Nature Geoscience*, 4(12):831–838.
- Weis, D., Harrison, L. N., McMillan, R., and Williamson, N. M. B. (2020). Fine-Scale Structure of Earth's Deep Mantle Resolved Through Statistical Analysis of Hawaiian Basalt Geochemistry. *Geochemistry, Geophysics, Geosystems*, 21(11).
- Weis, D., Kieffer, B., Maerschalk, C., Barling, J., de Jong, J., Williams, G. A., Hanano, D., Pretorius, W., Mattielli, N., Scoates, J. S., Goolaerts, A., Friedman, R. M., and Mahoney, J. B. (2006). High-precision isotopic characterization of USGS reference materials by TIMS and MC-ICP-MS. *Geochemistry, Geophysics, Geosystems*, 7(8):Q08006.
- Weis, D., Kieffer, B., Maerschalk, C., Pretorius, W., and Barling, J. (2005). High-precision Pb-Sr-Nd-Hf isotopic characterization of USGS BHVO-1 and BHVO-2 reference materials: Pb-Sr-Nd-Hf Characterization. *Geochemistry, Geophysics, Geosystems*, 6(2).
- White, W. (2015). Probing the Earth's Deep Interior Through Geochemistry. *Geochemical Perspectives*, pages 95–251.
- Whitehead Jr., J. A. and Luther, D. S. (1975). Dynamics of laboratory diapir and plume models. *Journal of Geophysical Research (1896-1977)*, 80(5):705–717.
- Wieser, P. E., Edmonds, M., MacLennan, J., and Wheeler, J. (2020a). Microstructural Constraints on Magmatic Mushes under Kīlauea Volcano, Hawai'i. *Nature Communications*, 11(1).

- Wieser, P. E., Iacovino, K., Matthews, S., Moore, G., and Allison, C. M. (2022). VESIcal: 2. A Critical Approach to Volatile Solubility Modeling Using an Open-Source Python3 Engine. *Earth and Space Science*, 9(2).
- Wieser, P. E., Jenner, F., Edmonds, M., MacLennan, J., and Kunz, B. E. (2020b). Chalcophile elements track the fate of sulfur at Kīlauea Volcano, Hawai'i. *Geochimica et Cosmochimica Acta*, 282:245–275.
- Wilkinson, M. D., Dumontier, M., Aalbersberg, I. J., Appleton, G., Axton, M., Baak, A., Blomberg, N., Boiten, J.-W., da Silva Santos, L. B., Bourne, P. E., Bouwman, J., Brookes, A. J., Clark, T., Crosas, M., Dillo, I., Dumon, O., Edmunds, S., Evelo, C. T., Finkers, R., Gonzalez-Beltran, A., Gray, A. J. G., Groth, P., Goble, C., Grethe, J. S., Heringa, J., 't Hoen, P. A. C., Hooft, R., Kuhn, T., Kok, R., Kok, J., Lusher, S. J., Martone, M. E., Mons, A., Packer, A. L., Persson, B., Rocca-Serra, P., Roos, M., van Schaik, R., Sansone, S.-A., Schultes, E., Sengstag, T., Slater, T., Strawn, G., Swertz, M. A., Thompson, M., van der Lei, J., van Mulligen, E., Velterop, J., Waagmeester, A., Wittenburg, P., Wolstencroft, K., Zhao, J., and Mons, B. (2016). The FAIR Guiding Principles for scientific data management and stewardship. *Scientific Data*, 3(1):160018.
- Willhite, L. N., Jackson, M. G., Blichert-Toft, J., Bindeman, I., Kurz, M. D., Halldórsson, S. A., Harðardóttir, S., Gazel, E., Price, A. A., and Byerly, B. L. (2019). Hot and Heterogenous High-  ${}^3\text{He}/{}^4\text{He}$  Components: New Constraints From Proto-Iceland Plume Lavas From Baffin Island. *Geochemistry, Geophysics, Geosystems*, 20(12):5939–5967.
- Williams, Q. and Garnero, E. J. (1996). Seismic Evidence for Partial Melt at the Base of Earth's Mantle. *Science*, 273(5281):1528–1530.
- Williamson, N. M. B., Weis, D., Scoates, J. S., Pelletier, H., and Garcia, M. O. (2019). Tracking the Geochemical Transition Between the Kea-Dominated Northwest Hawaiian Ridge and the Bilateral Loa-Kea Trends of the Hawaiian Islands. *Geochemistry, Geophysics, Geosystems*, 20(9):4354–4369.
- Wilson, J. T. (1963). A possible origin of the Hawaiian Islands. *Canadian Journal of Physics*, 41(6):863–870.
- Wu, Z., Barosh, P. J., Zhang, Q., Wu, J., and Yang, Y. (2018). A Thickness Gauge for the Lithosphere Based on Ce/Yb and Sm/Yb of Mantle-Derived Magmatic Rocks. *Acta Geologica Sinica - English Edition*, 92(6):2120–2135.

- Yoder, H. S. and Tilley, C. E. (1962). Origin of Basalt Magmas: An Experimental Study of Natural and Synthetic Rock Systems. *Journal of Petrology*, 3(3):342–532.
- Zindler, A. and Hart, S. (1986). Chemical Geodynamics. *Annual Review of Earth and Planetary Sciences*, 14(1):493–571.